

1980 NRL REVIEW

NRL
Review
1980
c.1

LOAN COPY: RETURN TO
AFWL TECHNICAL LIBRARY
KIRTLAND AFB, N. M.

0056425



TECH LIBRARY KAFB, NM



Issued 1 July 1981
NAVAL RESEARCH LABORATORY
WASHINGTON, D.C.

Approved for public release; distribution unlimited



0056425

1980

N **AVAL**
R **RESEARCH** **VIEW**
L **ABORATORY**
WASHINGTON, D.C. 20375



Issued 1 July 1981

20080303068



Mission . . .

To conduct a broadly based multidisciplinary program of scientific research and advanced technological development directed toward new and improved materials, equipment, techniques, systems, and related operational procedures for the Navy. In fulfillment of this mission, the Naval Research Laboratory:

Initiates and conducts scientific research of a basic and long-range nature in scientific areas of special interest to the Navy.

Conducts exploratory and advanced technological development deriving from or appropriate to the scientific program areas.

Within areas of technological expertise, develops prototype systems applicable to specific projects.

Performs scientific research and development for other Naval commands and, where specially qualified, for other agencies of the Department of Defense and, in defense-related efforts, for other Government agencies.

Upon request from appropriate Naval commands, assumes responsibility as the Navy's principal R&D center in areas of unique professional competence.

Provides to the Navy and its contractors standardized techniques and procedures for measurements and the accurate calibration of standard instruments in areas of special Navy needs.

Furnishes scientific consultative services for the Navy and, where specially qualified, for other agencies of the Department of Defense and, in defense-related efforts, for other Government agencies.

Provides to the Navy determinations of performance characteristics of developmental and prototype devices through limited engineering test and evaluation services.

PREFACE

This *NRL Review* is just that—a review of the major unclassified research and development efforts and accomplishments of the Naval Research Laboratory (NRL) during 1980. As such, it is an important source document for other Navy and DoD organizations, academia, and industry, and has been since its inception in 1967.

NRL's principal task is the development and orderly flow of research results for Navy applications and technology transfer. The Laboratory interacts strongly with science and technology performers and users both in and outside of the Navy and the Department of Defense. Readership response indicates that the *Review* plays a significant role in the success of this information exchange. The *Review* also provides part of the comprehensive record of Laboratory accomplishments for archival purposes.

It has been nearly six decades since the Naval Research Laboratory opened its doors of science for the Navy and the nation. In the past 57 years, NRL has grown from a handful of small buildings to a complex of specialized laboratories housed in some 150 buildings along the banks of the Potomac River in Washington, D.C. with field stations located in Maryland, Florida, Virginia, and West Virginia.

From its beginning, the Laboratory has continuously grown to meet the needs of the Navy and the country. This growth and subsequent change has resulted in progress. A number of NRL's significant events of the past year are discussed in this *Review*. From outer space to the depths of the world's oceans, NRL was there with its expertise and know-how, sharing its knowledge with the scientific communities here and abroad through the transfer of technology.

NRL's multidisciplinary research endeavors and past achievements embrace nearly all of the physical sciences. There are other research facilities in the Navy, but each is primarily concerned with a specific range of problems for a specific product of naval technology. NRL's position is unique. The Laboratory operates directly under the Chief of Naval Research, who reports to the Assistant Secretary of the Navy for Research, Engineering and Systems. This direct link fosters the most diversified research programs of any military or commercial laboratory.

The Naval Research Laboratory is often referred to as the Navy's corporate laboratory, a designation confirming that NRL not only performs basic research leading to future naval materials and systems, but also acts as one of the major points of focus for research and development in the Navy if not the nation.

But to bring it all into perspective—NRL is *people* and creativity. It begins with a single scientist or a small group of researchers with their ideas and goals fostered by the backing of a well-managed scientific and support organization where managers put a premium on excellence and create a climate for inventiveness. This is NRL.

The articles contained in the *Review* represent the wide-ranging unclassified research conducted at the Laboratory during 1980 and are indicative of NRL's continuous mission to serve the Navy, the Department of Defense, and the nation. We hope that as you read the *Review*, the quality and significance of our work will become apparent.



Capt. E.E. Henifin, USN
Commanding Officer
Naval Research Laboratory



CONTENTS

MISSION	ii
PREFACE	
Capt. E.E. Henifin, USN	iii
THE LABORATORY—PAST AND PRESENT	1
PLANNING THE NRL CORE RESEARCH PROGRAM	10
LABORATORY PEOPLE AND THEIR RESEARCH	12
THE NRL PROGRAM—RESEARCH AND PROGRESS	
Dr. Alan Berman	17
INFORMATION PROCESSING, TRANSMISSION, AND ANALYSIS	22
Adaptive Processing	
B.L. Lewis, F.M. Staudaher, and W.F. Gabriel	23
Microwave Optical Lenses	
J.P. Shelton	26
Microwave GaAs Field-effect Transistor Oscillators	
C. Rauscher	28
Surface Acoustic Wave (SAW) Convolvers	
K.L. Davis and J.F. Weller	29
Survivable Intra-Task-Force Communications	
D.J. Baker	31
Automation of Military Message Handling	
C.L. Heitmeyer and S.H. Wilson	33
Conversational Tests for Evaluating Voice Systems	
A. Schmidt-Nielson and S.S. Everett	34
Inverse Scattering Method for Measurements of Sinusoidal Surfaces	
A.K. Jordan	36
DETECTION AND DEFENSE	40
A Microcomputer Aided Tracking System	
D.C. Cross, A.B. Mays, and P.M. Thiebaud	41
Scenario Generator for Radar Environment Simulations	
B. McGhee and W. Morris	43
RF Environment Simulation via Matrix Array	
B.W. Edwards	45
Real-time Image Analysis Architecture	
R.H. Evans, T.R. Husson, and E.F. Williams	47
Granular, Niobium Nitride Weak Link SQUIDS	
E.J. Cukauskas, J.H. Claassen, and M. Nisenoff	49

MARINE GEOSCIENCE	54
Lagrangian Oceanographic Measurements	
C.M. Gordon and D. Greenewalt	55
Mapping Ocean Currents with Over-the-horizon Radar	
D.B. Trizna	57
Modeling of Isothermal, Upper-ocean Water Masses	
R.P. Mied, J.P. Dugan, and A.F. Schuetz	61
Coherent Radar Observations of Breaking Shoaling Waves	
W.C. Keller, W.J. Plant, and G.R. Valenzuela	63
Crustal Geophysics Studies in the South Atlantic Ocean	
R.K. Perry	65
Portable Systems for Oceanographic Data Acquisition	
D. Steiger	67
Automated Aerosol Sampling System	
F.K. Lepple, D.J. Bressan, and R.E. Larson	68
Bioluminescence in the World's Oceans	
R.V. Lynch	70
ACOUSTIC PROPERTIES AND APPLICATIONS	76
Microparticle Detection Using Focused Ultrasound	
J. Jarzynski	77
Low-frequency Sonic Reflectivity of Ice	
T.C. Yang and C.W. Votaw	78
Sound Propagation Through Fluids in Piping Systems	
R.A. Skop and M.P. Horne	80
Applications of Acoustic Holography in Nondestructive Evaluation	
A.V. Clark, Jr.	82
Phase Calibration of Hydrophones	
L.D. Luker and A.L. Van Buren	84
New Omnidirectional Standard Transducers	
L.E. Ivey	85
A New Underwater Shock-wave Sensor	
S.W. Meeks	87
OPTICAL RESEARCH AND APPLICATIONS	92
Accurate Phase Measurement for Fiber-optic Interferometers	
I.J. Bush	93
Fiber-optic Gyroscopes	
W.K. Burns	94
Circumventing the Spatial-Resolution—Wavelength Barrier in Microscopy	
J. Reintjes, T.J. Manuccia, and R. Waynant	96
Local Instances of Good Seeing	
H.H. Szu and J.A. Blodgett	99
ATMOSPHERIC BEHAVIOR AND PROPERTIES	104
Reduced-density Channels in Gases at Atmospheric Pressure	
R.E. Pechacek, M. Raleigh, and K.A. Gerber	105
Convective Cooling of Lightning Channels	
J.M. Picone and J.P. Boris	106
Starlight and the Nighttime Ionosphere	
R.R. Meier, D.F. Strobel, and C.B. Opal	108
Modeling the Equatorial Spread-<i>F</i> Scintillation Environment	
S.L. Ossakow and S.T. Zalesak	109
Finite-element Modeling of Convection-diffusion Problems	
G.A. Keramidas	111

SOLAR SCIENCE AND SATELLITES	114
The Sun as a Variable Star	
J.W. Cook, G.E. Brueckner, and E. VanHoosier	115
Solar Ultraviolet Spectral Irradiance Monitoring Program	
M.E. VanHoosier, J.-D.F. Bartoe, and D.K. Prinz	116
High-resolution X-ray Spectra of Solar Flares	
R.W. Kreplin, G.A. Doschek, and U. Feldman	119
Modeling of Solar Wind Interaction with the Earth's Magnetosphere	
J.A. Fedder and P.J. Palmadesso	121
Semianalytic Method for Satellite Orbit Determination	
B. Kaufman	122
Parametric Wave-spectra Measurements from Aerospace Platforms	
D.T. Chen	124
HIGH-POWER TECHNOLOGY AND ASTROPHYSICS	128
SS433—A Peculiar Galactic Object	
K.J. Johnston	129
New Payload for Far-infrared Sky Survey	
D.P. McNutt, K. Shivanandan, and M. Daehler	131
Rapid Variability from X-ray Emitting Galaxies	
K.S. Wood and W.A. Snyder	132
XUV Radiation Modeling of Dense Plasmas	
D. Duston and J. Davis	135
An Ultra-high-power Magnetron for Air Breakdown Studies	
R.K. Parker and W.M. Black	138
MATERIALS MODIFICATION AND BEHAVIOR	142
A New Metal-surface Cleaning Method	
D.L. Venezky and R. Panayappan	143
Ion Implantation, a New Method to Modify Polymers	
D.C. Weber, P. Brant, and C. Carosella	144
Corrosion Behavior of Laser-processed Metal Surfaces	
E. McCafferty, P.G. Moore, and J.D. Ayers	146
Ion Implantation for Improved Corrosion Resistance	
G.K. Hubler and J.K. Hirvonen	147
A New Class of Amorphous Magnetic Alloys	
N.C. Koon and B.N. Das	149
InP Planar Transferred-electron Devices	
R.L. Henry, K.J. Slegner, and H.B. Dietrich	150
MATERIALS ANALYSIS AND PROPERTIES	156
Anomalous-scattering Analysis of Macromolecular Structure	
W.A. Hendrickson	157
Signal-enhanced NMR for Materials Analysis	
B.S. Holmes and G.C. Chingas	158
Partially Stabilized Zirconia Crystals	
R.P. Ingel and R.W. Rice	159
The As Antisite Defect in GaAs	
R.J. Wagner, J.J. Krebs, and G.H. Stauss	161
Toward a Red Blood Cell Surrogate	
B.P. Gaber and J.P. Sheridan	163
STRESS AND RADIATION EFFECTS	166
Creep-fatigue Crack Propagation in Stainless Steel	
D.J. Michel	167

CONTENTS

Prediction of High-temperature Fatigue Crack Growth	
K. Sadananda and P. Shahinian	168
Low-cycle Fatigue Life of Titanium Alloys	
J.M. Krafft	170
Sulfur Trioxide Factor in Low-temperature Hot Corrosion	
R.L. Jones and S.T. Gadomski	171
Damage Cascades in Semiconducting Material	
G.D. Mueller and C.S. Guenzer	174
Cosmic-ray Effects on Microelectronics	
J.H. Adams, Jr., R. Silberberg, and C.H. Tsao	175
RECOGNITION—Honors, Awards, and Training	181
CONTRIBUTIONS—Papers, Reports, and Patents	196
NRL REVIEW STAFF	226
KEY OFFICES AND PERSONNEL	227

THE LABORATORY—PAST AND PRESENT

Historical Background

At a time when government and science seem inextricably linked, when virtually no one questions the dependence of national defense on the excellence of national technical capabilities, it is instructive to recall that in-house defense research is rather recent. The Naval Research Laboratory (NRL), the first modern research institution created within the United States Navy, began operations only 57 years ago.

NRL was a war baby. In a pattern that is almost ritual in American history, it took the threat of armed conflict to bring scientific leadership and political power together in decisive action for national defense. The first step came in May 1915, a time when Americans were deeply worried over the great European war. Thomas Edison, asked by a *New York Times* correspondent to comment on the conflict, argued that the nation should look to science. "The Government," he proposed in a published interview, "should maintain a great research laboratory.... In

this could be developed...all the technique of military and naval progression without any vast expense." Secretary of the Navy Josephus Daniels seized the opportunity of Edison's public comments to enlist his support. Edison agreed to serve as the head of a new body of civilian experts, named the Naval Consulting Board, to advise the Navy on science and technology. The Board's most ambitious plan was the creation of a modern research facility for the Navy. A defense-minded Congress allocated \$1.5 million for the institution in 1916, but wartime delays and disagreements within the Naval Consulting Board postponed construction until 1920. NRL finally opened in 1923.

In the years before World War II, the Laboratory was a small institution with limited capabilities. There was then little Congressional support for maintaining a strong Navy and even less for naval research. Nonetheless, with its few resources NRL made great strides. Its two original divisions, Radio and Sound, pioneered the fields of high-frequency radio and underwater



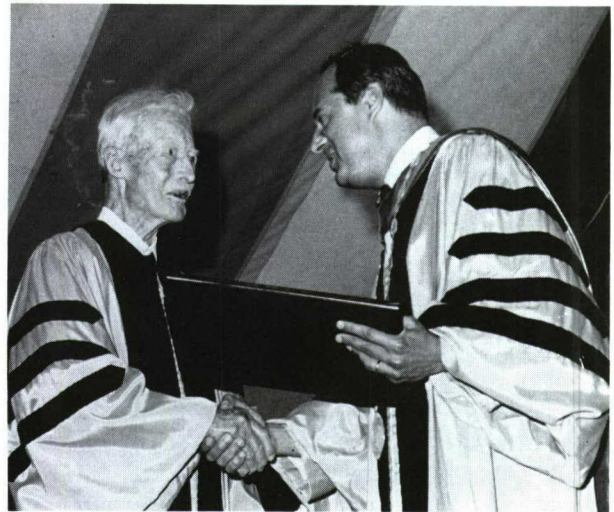
The new laboratory for electronic warfare research
in the final stage of construction

sound propagation. They produced communications equipment, direction-finding devices, sonar sets, and, perhaps most significant of all, the first practical radar equipment built in this country. They even managed some basic research, participating, for example, in the discovery and early exploration of the ionosphere. In addition, the Laboratory was able to work gradually toward its goal of becoming a truly general research facility. By World War II, five new divisions had been added to Radio and Sound: Physical Optics, Chemistry, Metallurgy, Mechanics and Electricity, and Internal Communications. Although they were few and were always short of funds, the workers in these areas also made numerous contributions to the technical expertise of the Navy.

World War II changed NRL as had nothing before. Total employment jumped from 396 in 1941 to 4400 in 1946, expenditures from \$1.7 million to \$13.7 million, the number of buildings from 23 to 67, and the number of projects from 200 to about 900. During the conflict, scientific activities necessarily were concentrated almost entirely on applied research. Much new electronics equipment—radio, radar, sonar—was developed. Countermeasures were devised. New lubricants were produced, as were antifouling paints, luminous identification tapes, and a "sea marker" to help save men lost in the ocean. A thermal diffusion process was conceived and used to supply some of the ^{235}U isotope needed for one of the first atomic bombs. NRL also labored as a watchdog, type-testing a host of new devices that poured from booming wartime industry before they were certified as reliable for the fleet.

After the war, there was no thought of regression to the old NRL. Scientific research was now widely recognized as a vital national resource, and the Laboratory had a major and continuing role to play in providing it. When the Office of Naval Research was created in 1946, NRL was transferred to it; it thus became the "corporate laboratory" of the Navy, as it was later to be called.

The demands of this new position necessitated substantial reorganization. Rapid expansion had met wartime demands, but had left NRL improperly structured to address long-term Navy requirements. One major task—neither easily nor rapidly accomplished—was reshaping research management, that is, transforming a group of largely autonomous scientific divisions into a unified institution with a clear mission and a fully coordinated research program. The first attempt

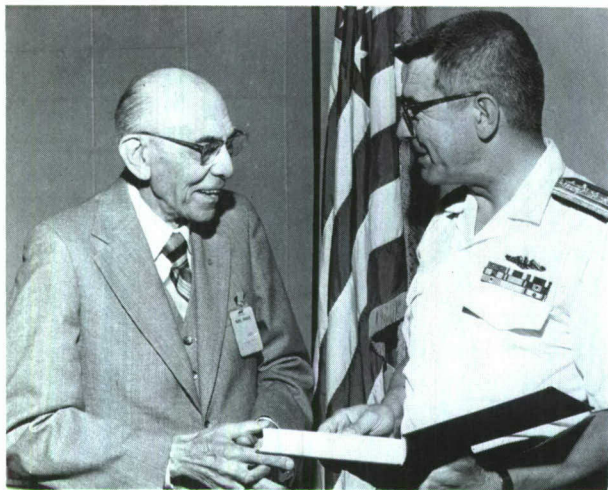


Dr. E.O. Hulburt, NRL's first civilian Director of Research, receiving an honorary degree from Dr. Steven Muller, President of Johns Hopkins University

at reorganization vested power in a committee composed of all the division superintendents. This proved unwieldy, so in 1949 a civilian Director of Research was named and given full authority over the program. Associate directors were added in 1954, and under strong leadership in recent years, this structure has provided effective, centralized management.

NRL's scientific program during the past 34 years has been characterized by continual achievement and flexibility. Naturally, some areas of study have persistently been on the Laboratory's agenda because of their continuing importance to the Navy. These include basic research concerning the Navy's environment of sea, sky, and space. Investigations have ranged widely, from monitoring the sun's behavior, to analyzing marine atmospheric conditions, to measuring parameters of the deep oceans. Detection and communications capabilities have benefited by research that has exploited new portions of the electromagnetic spectrum, extended ranges to outer space, and provided means of transferring information reliably and securely even through massive jamming. Sound in the sea, submarine habitability, lubricants, shipbuilding materials, fire fighting, and other subjects have also been steadfast concerns.

Yet, while not neglecting traditional subjects, the Laboratory has been keen to move into new areas opened by the advance of science. It



Dr. Louis A. Gebhard presenting a copy of his revised book to Rear Adm. Baciocco.

pioneered naval research into space, from atmospheric probes with captured V-2 rockets, through direction of the Vanguard project—America's first satellite program—up to involvement in such ongoing projects as the Navy Global Positioning System. It is today, in fact, the Navy's leading laboratory in space research. NRL has been quick to recognize and use new technological advances such as computers, solid-state electronics, lasers, composite materials, and optical fibers. Finally, it has evaluated serious new threats, such as the effects of intense radiation or new forms of shock and vibration, on components or on aircraft, ships, and satellites.

Guiding NRL's diverse activities through the years has been a single aim: to conduct pioneering scientific research and development that will provide improved materials, equipment, techniques, systems, and operations. In the future, as in the past, the Laboratory will continue to contribute to and exploit scientific progress in order to meet the ever-changing technical needs of the Navy.

Organization and Administration

The position of NRL within the Navy is diagrammed on the organization chart inside the front cover of this report. As a field command of the Office of Naval Research, the Laboratory is under general direction of the Chief of Naval Research.

Heading the Laboratory with joint responsibilities are the naval commanding officer and the civilian director of research. Directly under them

are staff functions that provide central services such as security and personnel management. Line authority passes from the commanding officer and director of research to five associate directors of research in the following areas: technical services, general science and technology, systems research and technology, material science and component technology, and space and communications technology. The first of these provides centralized technical support, the other four are the research directorates responsible for executing NRL's research and development program. Further details of the organization of the Laboratory are given on the organization chart that follows this article.

Administering the organization and operation of NRL to ensure it runs effectively and efficiently is a dynamic process that requires continual attention from managers at all levels. One clear indication of concern for sound administration appears in the number of reorganizations made in 1980: significant changes were made in 11 of the Laboratory's 23 divisions. Thus, the Laboratory's structure kept fully attuned to the evolving functions. A related alteration was made in the organization of Laboratory work. At the beginning of fiscal year 1980, the whole program administration system was overhauled and a new means of documenting scientific projects was instituted. The new system replaced one that had not been significantly changed since 1966, and whose basic format dated back to 1946.

In the area of personnel, the implementation of the Civil Service Reform Act of 1978 continued, bringing further modification to the way supervisors and management officials in General Schedule grades 13 through 15 are evaluated, compensated, and promoted. All such civilian employees of the Department of the Navy now work under a merit-based system that uses techniques of management-by-objectives to make performance goal-oriented rather than function-oriented. Equal employment opportunity continued to receive close attention, especially since the first objective of every employee under the new merit system must be related to equal employment. One significant action in this area was the promulgation of definite policy on sexual harassment.

Financially, NRL operates under the system of Naval Industrial Funding, which requires that all research projects include charges for overhead costs as well as direct research costs. Appropriations for scientific projects in 1980 came from the

Office of Naval Research, the Navy Systems Commands, the Navy Material Command, and other government agencies, such as the Defense Advanced Research Projects Agency, the Department of Energy, and the National Aeronautics and Space Administration. To clarify NRL's relationship to its sponsoring agencies, both inside and outside the Department of Defense, a comprehensive policy on interagency support agreements was drafted and promulgated. It provided sound legal guidance for making the NRL expertise available in the appropriate way and in the appropriate balance to all the parts of the government that need it.

Besides funding for scientific work, NRL received some Navy monies for general construction, maintenance, and operations. In fiscal year 1980, the Laboratory's budget totaled \$248.5 million.

Personnel

The distribution of regular full-time NRL employees as of December 31, 1980 was:

Military	
Officers	33
Enlisted	<u>99</u>
Total	132
Civilian	
Senior Executive Service	23
Scientific and engineering Professionals	1223
Scientific and engineering Subprofessionals	339
Support professionals	79
Support subprofessionals	198
Clerical, administrative, and other General Schedule	725
Wage Board	<u>568</u>
Total	3155

The highest university degrees held by permanent employees as of December 31, 1980, were as follows:

Bachelors	525
Masters	318
Doctors	<u>593</u>
Total	1436

Further information concerning opportunities of NRL employees for higher education may

be found in the section "Continuing Education and Training" at the back of this report.

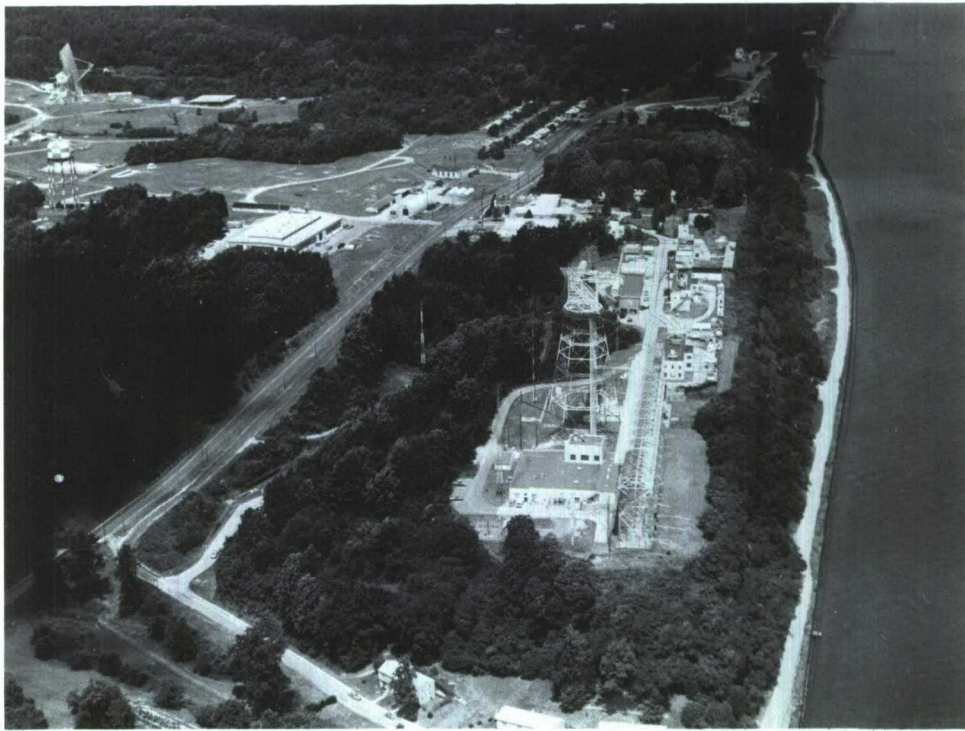
Field Stations

NRL's main laboratory complex in Washington, D.C., houses the major portion of its extensive facilities and supporting services. Some of these are described below under "Main Laboratory Facilities." For research that cannot be conducted in Washington, NRL has acquired or made arrangements over the years to use a variety of field sites or auxiliary facilities. They are located in Maryland, Virginia, California, Florida, and Puerto Rico. The two largest are the Chesapeake Bay Detachment (CBD) and the Underwater Sound Reference Detachment (USRD).

The Chesapeake Bay Detachment, which occupies 68.1 hectares near Chesapeake Beach, Maryland, provides facilities and services for research in radar, fire-control equipment, optical devices, materials, communications, and other subjects. It has a 45.7-m steerable parabolic microwave antenna; a hypervelocity gun for studying ballistics penetration into various materials; several radars, including NRL's long-range, over-the-horizon radar; a ship motion simulator; a fire test facility for research on the behavior and extinguishment of large fires in unconfined areas; and other equipment. For measurements over the water, CBD uses several small research vessels, including a jack-up barge that can provide a stable research platform in shallow depths.

The Underwater Sound Reference Detachment, located at Orlando, Florida, functions in many ways like a standards bureau of underwater sound. Its semitropical climate and two clear, tranquil lakes are distinct assets to its research and development on underwater reference standards and its improvement of techniques to calibrate, test, and evaluate underwater acoustic devices. USRD boasts an anechoic tank for simulating ocean depths to 700 m and smaller pressure tanks for simulating depths to 7000 m. It has employed its sophisticated capabilities to provide acoustic equipment and calibration services not only to hundreds of Navy activities and their contractors, but also to allied governments.

Some field sites have been chosen primarily because they provide favorable conditions for the operation of specific antennas and electronic subsystems. Maryland Point, Maryland, has two radio telescopes with antennas 25.6 m and 26 m



Chesapeake Bay Detachment, located in southern Maryland



Active use of Chesapeake Bay Detachment's fire test facility



Underwater Sound Reference Detachment. test site for underwater acoustic devices near Orlando, Florida

in diameter for radio astronomy research; NRL's Waldorf facility has an 18.3 m X-band antenna and an S-band antenna of the same size for space and communications research. Pomonkey, a third field site in Maryland, has a free-space antenna range for the development and testing of a variety of antenna types. Another facility used in improving communications is the Antenna

Model Measurement Range in Brandywine, Maryland. Here, scaled model ships can be set up and rotated in the center of a range 305 m in diameter to provide data that aid in theoretical and experimental antenna design. The Laboratory has installations for satellite tracking in Blossom Point, Maryland, and at Vandenberg Air Force Base in California.



NRL's Tilghman Island test site

At a few other small sites it either owns or leases, NRL conducts specialized investigations in accordance with the current requirements of its sponsors.

Research Platforms

NRL's principal research vessel, USNS HAYES, is a 75-m ocean-going catamaran packed with scientific instruments. Operated by the Military Sealift Command and named for Harvey C. Hayes, the initial head of NRL's Sound Division and a pioneer in underwater acoustics, HAYES has served as the Laboratory's research ship for nine years. In 1980, she sailed on major cruises to investigate acoustic bathymetry and geophysics research in the South Atlantic in conjunction with the Brazilian Navy, environmental chemistry in the Caribbean, and bioluminescence studies in the gulf stream off the east coast of the United States. The ship was placed in reduced operational status for the period May through September, and during December underwent Coast Guard recertification.

For airborne research, NRL has three four-engine turboprop P-3 *Orions* and a two-engine S-2E *Tracker*. In 1980, these airplanes logged around 1300 hours of flying time on projects ranging from magnetic bathymetry off the coast of California, to electronic countermeasure research over Maryland, to studies of radar signal reflections from ships in the Atlantic, Pacific, and Caribbean.

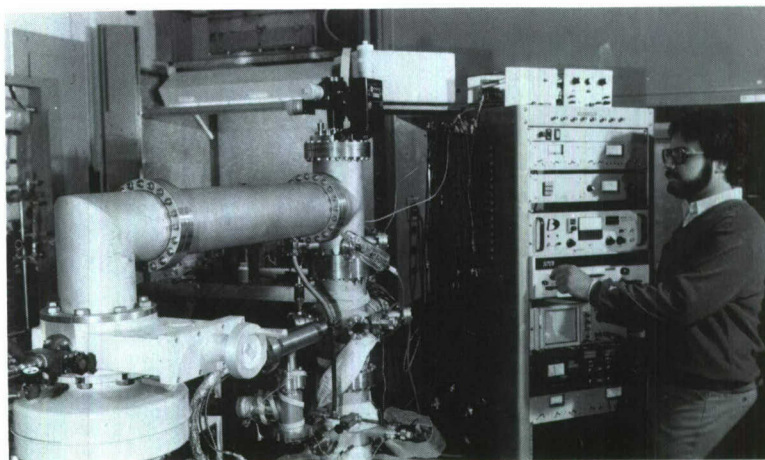
Main Laboratory Facilities

At its main location in Washington, D.C., NRL has a wide variety of sophisticated facilities for advanced research. The following description, while by no means complete, gives an illustrative glimpse of some of these tools of modern science and technology.

A prerequisite for most current research is high-speed data processing and numerical computation. To provide it, NRL uses over 200 computer systems. The largest and most powerful of them, a Texas Instruments Advanced Scientific Computer located in the Research Computation Division, has a two-pipe central processor, a high-speed bipolar central memory with a million-word capacity, and a disk storage capacity of over 450 million words. In addition, researchers may utilize an optimizing Fortran compiler and other software packages to facilitate their programming tasks. The Research Computation Division also has a DEC System-10 that furnishes data management support to the whole Laboratory on a time-shared basis.

In its role as the Navy's leading center for space research, NRL not only conducts scientific investigations of the phenomena of outer space, but also builds and assists in launching Navy satellites. Hence, it possesses such facilities as anechoic chambers, clean rooms, and various devices for studying effects of shock and vibration, noise, solar radiation, and other factors. Moreover, it has equipment for telemetry, tracking, and data reduction. To process data from the SEASAT space vehicle, the Laboratory has developed, jointly with Bendix Corporation, a Synthetic Radar Data Preprocessing System that relies on a 42-track high-density digital tape recorder.

For studies in plasma physics, NRL has high-powered magnetic compression devices that can excite matter to a plasma state. Experimental studies of the interactions between plasma and electron beams are made with several types of electron beam generators. The largest of them, named Gamble II, is also employed for investigating such phenomena as high-current beam interactions and for the simulation of x rays for weapons effects tests. Related research involves lasers. NRL's two-beam neodymium glass laser can generate powerful beams for examining laser-matter interactions. This facility is supplemented by a UV excimer laser designed specifically to examine wavelength effects in



Dr. Benjamin M. DeKoven, an NRC/NRL postdoctoral research associate, adjusting the controls of the supersonic molecular beam apparatus designed by research scientists in the optical diagnostics section of the Chemistry Division. Research topics include the elucidation of primary steps in the dissociation of energetic materials and studies involving molecular ion production and ion molecule reactions. Also being developed is a program involving the study of gas-surfaces interactions in electroactive polymers.

laser-matter interactions. And in the Laser Materials Applications Center, researchers utilize a 20-kW CO₂ electric discharge laser to study welding, various surface treatments, and the deterioration of materials under high irradiance. Lasers are equally important in other parts of the research program. Chemists examine their power to effect novel types of chemical synthesis, while optical scientists investigate their employment in fiber-optic systems and as weapons.

To support studies in radiation technology, NRL has a 60-MeV Linear Electron accelerator, a 5-MV positive-ion Van de Graaff accelerator, a 2-MV electron Van de Graaff accelerator, a high-fluence 200-kV ion implantation system, and a cobalt 60 source. Taken together, these versatile radiation facilities, capable of producing a wide spectrum of radiations, are unique in the Department of Defense. They are used for a variety of experiments, including the modification of materials by means of ion implantation and experiments on the radiation vulnerability and hardening of components for Navy ships and satellites.

The field of electronic warfare is a growing concern at NRL. The major area of expansion is the use of various forms of facilities and techniques for simulation studies. As electronic hardware becomes more expensive and sophisticated, simulation not only eliminates many costly

field measurements, but also permits rigorous and repeatable analysis in a controlled environment. As research tools, NRL has a Mobile Infrared Signature Measurement and Simulation Facility and a Missile Seeker Simulation Facility. A complex, computer supported Central Target Simulator is now operating with good results and its capabilities are being expanded to accommodate a broader range of EW problems.

Another installation that supports NRL contributions to the continuing evolution of electronics is the new Microelectronics Facility. In its humidity-controlled, dust-free environment, photolithography or chemical etching techniques are used to produce custom microelectronic devices and circuits on semiconductor chips.

In the related microcircuit testing facility, NRL performs comprehensive evaluations of systems, such as microprocessors, that include large numbers of integrated circuits. For its versatility and sophistication, this facility is unique within the Department of Defense. Its capabilities are being employed to ensure that critical parts of defense hardware are fully reliable.

For acoustical investigations, NRL uses three large research tanks, instrumented for studying echo characteristics and for device development. Experimental studies in fluid mechanics can be made in a multipurpose wave-wind channel. Measuring 30 m long by 1.2 m

wide by 1.8 m deep, the channel is equipped with a mechanical bulkhead to generate regular waves and a special fan to make wind waves. An associated water tunnel has a large blowdown channel with a 15-m test section for acoustic and flow-induced vibration studies of towed line arrays and flexible cables.

Fires in confined spaces, such as surface ships and submarines, are a continuing Navy problem. To help find solutions, NRL has recently built a 325 m³ pressurizable chamber that is both highly instrumented and automated. The chamber is being used for research on the formation and control of toxic products emanating from fires and other uncontrolled stresses in closed environments.

The characteristics of materials can be examined with a number of instruments. NRL has several scanning-electron microscopes as well as capabilities for x-ray analysis and electron and Auger spectroscopy. It has a high-performance secondary ion mass spectrometer that represents a standard for surface analysis and significantly extends the diagnostic capability of the technique. A high-resolution, high-performance, reverse-geometry mass spectrometer is employed for probing reactions between ions and molecules. NRL has a variety of machines with capacity up to 272,000 kg for testing fatigue and fracture of new materials. One facility that uses superconducting magnets produces very high magnetic fields—over 200 kOe—and allows the study of electrical, optical, and other properties of material under magnetic stress.

The high-quality instrumentation required by a diverse institution such as the Naval Research Laboratory is expensive. The major facilities presently in operation represent a capital investment of over \$100 million.

Maintenance and Construction

As a major national laboratory, NRL requires an energy-efficient plant that has modern technical facilities and provides a pleasant and productive work environment for its employees. Guiding development is a master plan covering all aspects of NRL's facilities and their use, from construction to physical organization of research work in laboratory buildings to landscaping and parking. A new edition of the plan was finished and approved in 1980 and will be published in 1981. One of its principal features is abandon-

ment of the idea of future expansion of NRL's main site. Moreover, far more emphasis is placed on adaptive reuse of existing structures than on erection of new buildings.

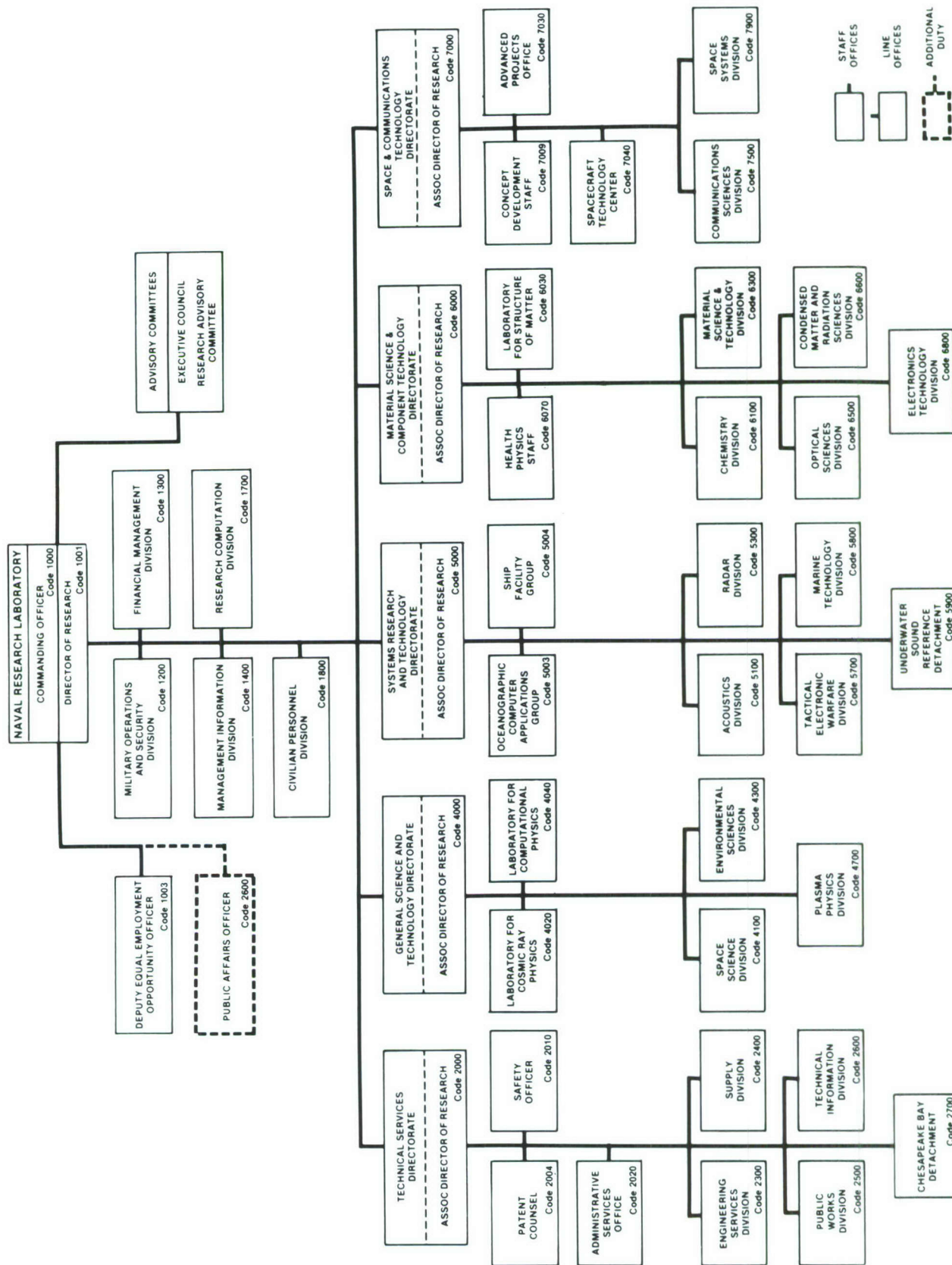
A number of significant construction projects were carried out at NRL during 1980. Road improvements of the central mall area were completed, and a number of parking lots were repaved. Cafeteria and recreation facilities were refurbished. A new wave tank was installed for the Marine Technology Division. NRL's oil storage capacity was increased to 30 day's supply by construction of a large oil tank. Construction of the newest research facility, the Electromagnetic Development Laboratory, went on throughout the year; the building is now scheduled for completion in 1981.

Increased energy efficiency was the goal of other plant modifications. Old windows were replaced, insulation laid, and better thermostatic controls installed. The payoff of such efforts appeared clearly in statistics, as NRL's energy use dropped 7.5% below the level recorded in 1979. A project to use methane gas from the adjacent Blue Plains Wastewater Treatment Plant for generating heat progressed substantially; it should be finished in 1981. Within two years, it will be saving the Government over half a million dollars per year. Finally, a solar energy facility to heat the main administrative building received final approval in 1980; contracts for construction will be let in 1981. Because of the number, variety, and scope of these and other energy efficiency measures, NRL was nominated in 1980 for the Secretary of the Navy's Energy Conservation Award.

Further Information

The *NRL Fact Book* gives more details about the Laboratory and its operations. It lists important equipment, current fields of research, field sites, and outlying facilities and presents information about the responsibilities, organization, key personnel, and funding of the divisions, detachments, and other major organizational units. Copies are available by request from:

Commanding Officer
Attention Code 2628
Naval Research Laboratory
Washington, DC 20375



Organizational Chart, December 1980

PLANNING THE NRL CORE RESEARCH PROGRAM

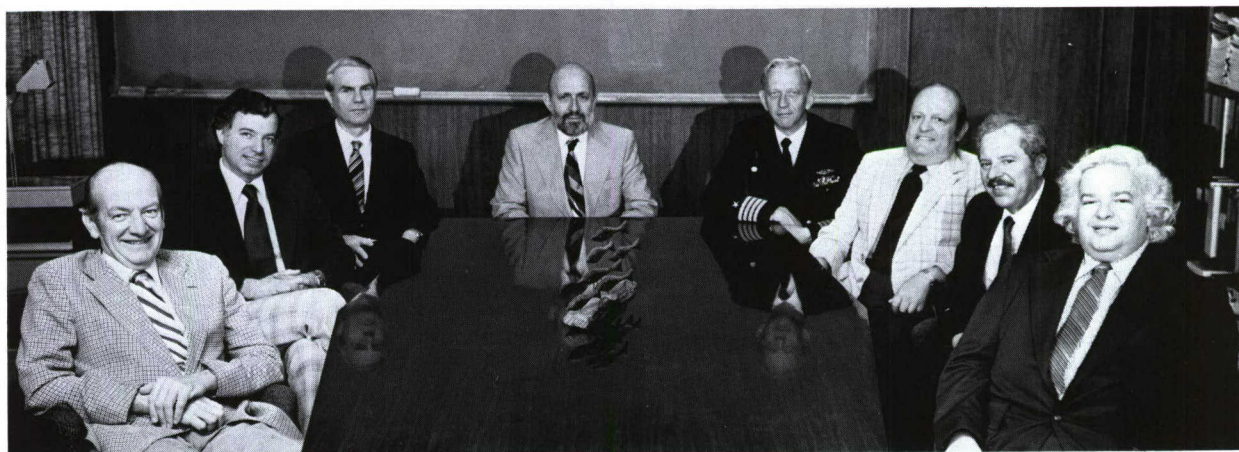
Basic research is a principal component of NRL's mission that provides the foundation for the Laboratory's scientific program. Although most other Navy laboratories also conduct some basic research, none has the NRL mandate for a large, broad-ranging effort that covers virtually all areas of physical science of interest to the Navy.

The sponsor for the core research program, which supports more than 25% of NRL's scientific work force, is the Office of Naval Research (ONR). Contrary to a common notion, the funds it provides the Laboratory for the program are not an allocation. Because NRL operates totally under the Naval Industrial Fund, the program must receive full approval from its sponsor. NRL devotes significant management effort to the formulation of the core program each year.

The organization of the program derives from the structure of the Department of Defense budget. A single budgetary program element, entitled "61153N—Defense Research Sciences (Navy)" includes, among other expenditures, funding that pays for the NRL core program.

This element is subdivided into 14 subelements, and these categories, which bear titles such as General Physics, Chemistry, Electronics, and Energy Conversion, define the Naval Research areas. NRL conducts some work in 13 of the 14 areas (excepting Behavioral and Social Sciences). The subelements are further subdivided into task areas and, finally, into work units. Work units provide the skeletal structure for all NRL research and development activity.

Although the core program is reviewed continually throughout the year, there is a formal review process that provides the basis for the Claimaint Program Proposal (CPP) submitted to the Chief of Naval Research (CNR) by NRL. In the formal process, qualified NRL staff members are assigned oversight responsibilities at each level to monitor progress and provide administrative guidance. There is a monitor for each subelement, a coordinator for each task area, and a principal investigator for each work unit. The core program evolves, in essence, by establishing or revising work units so that, within fiscal guidance, all of them taken together constitute a



The Research Advisory Committee, responsible for the scientific program and administration, meets frequently with the Commanding Officer. Pictured at an early 1981 meeting are (from left) Dr. H. North, Dr. T. Coffey, Mr. R.E. Ellis, Dr. A. Berman, Director of Research, Capt. E. E. Henifin, Dr. A.I. Schindler, Mr. R.R. Rojas, and Dr. B. Wald. Dr. North, Dr. Coffey, Dr. Schindler, Mr. Rojas, and Dr. Wald are respectively, Associate Director of Research for Technical Services, General Science and Technology, Material Science and Component Technology, Systems Research and Technology, and Space and Communications Technology. Mr. Ellis, a senior staff member, is Head of the Management Information Division.

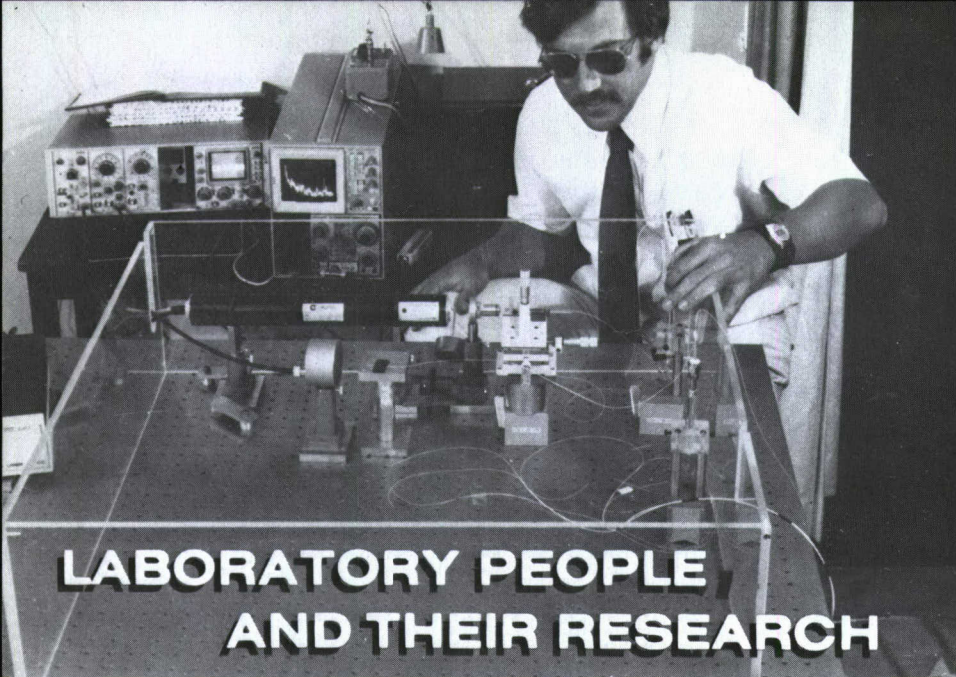
well-coordinated whole. The work units are then arranged into the appropriate task area and subelement groupings.

Like most planning in the Department of Defense, the NRL core program is projected not only for the current fiscal year, but also for five years beyond it. Thus the formal review and planning done each year updates and extends the plans of the previous year. Even so, the process is lengthy and time consuming. It begins around October when the Director of Research issues a memorandum giving guidance for the upcoming cycle. Based on previous guidance from the CNR, this memorandum sets budgetary levels for each subelement and task area for the planning period. Subsequently, program reviews are conducted and explanatory documentation written in the appropriate form at the lower levels.

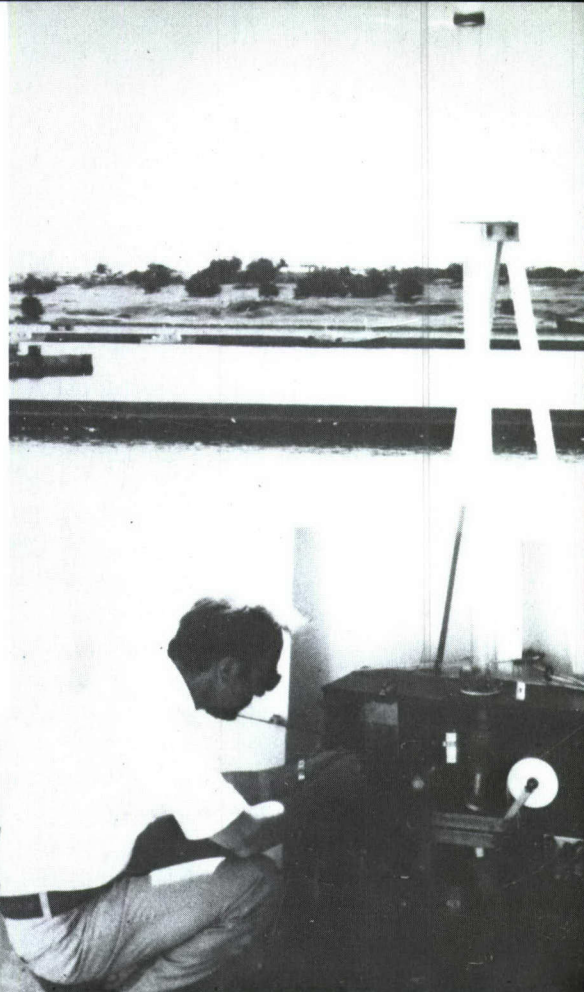
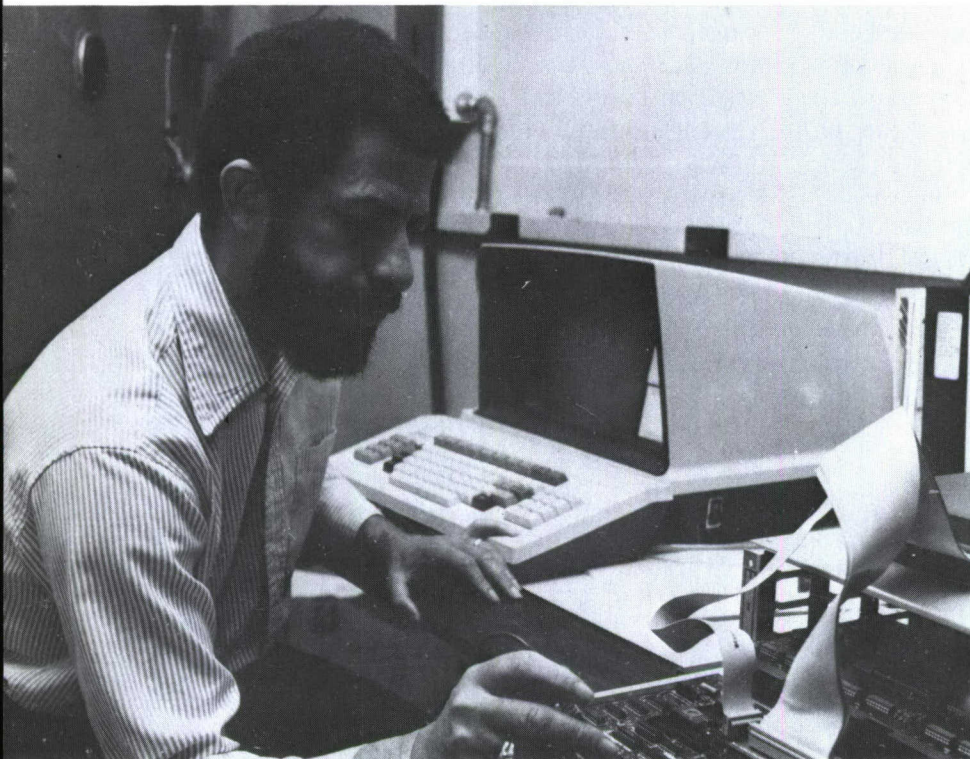
The next step is a comprehensive, Laboratory-wide review. In formal sessions during January and February, oral presentations to supplement the written material are made on each task area to NRL's Research Advisory Committee (RAC). This body, the senior policy reviewing board of the Laboratory, consists of the commanding officer, the director of research, the five associate directors of research, and the head of the Management Information Division. After

having heard the presentations and with the written explanations in hand, the RAC meets in executive session at the week-long "RAC retreat" to make the hard decisions on which Laboratory projects will be increased, decreased, reorganized, or terminated. The results are based primarily on scientific merit and potential value to the Navy with some leavening by fiscal guidance, program balance and capability considerations. Program documentation is then revised to reflect the decisions. The considered result forms the core research program package, which is prepared and sent to the CNR for his inspection, modification, and approval.

In the last few years, "special focus" programs have been added to the core research program. ONR, to balance the broad support it provides to NRL for the coordinated effort that was explained above, has adopted this new approach to facilitate coordination of closely related research efforts and to increase the probability of their transition and transfer to more applied programs. Although funded from the same program element and organized into task areas and work units similar to those for the regular core program, the "special focus" efforts allow greater management attention by the Chief of Naval Research.



LABORATORY PEOPLE AND THEIR RESEARCH



Reading clockwise from upper left:

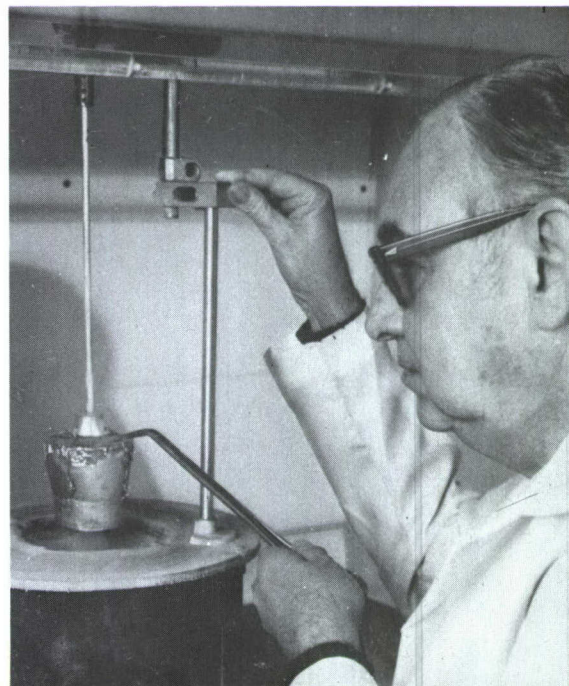
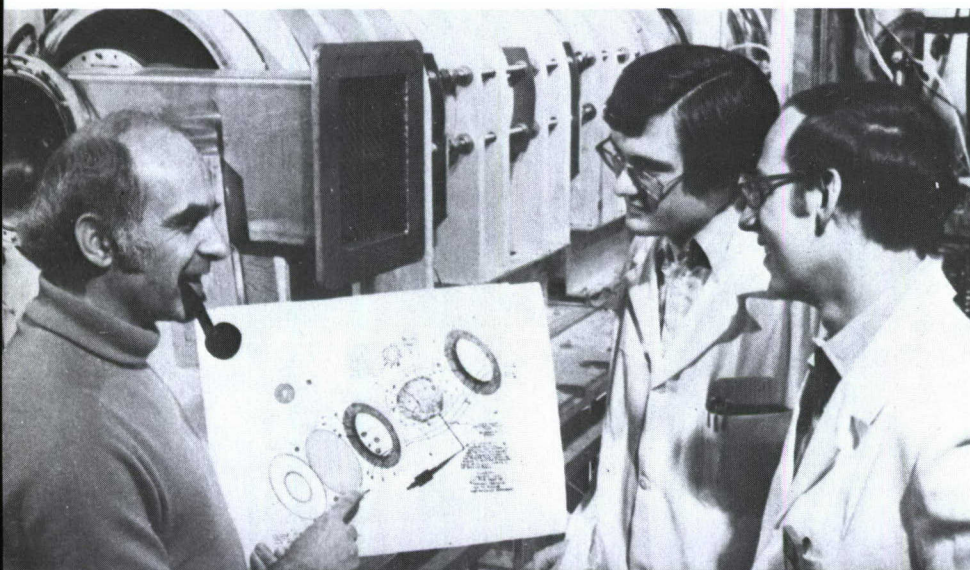
J. Cole with the optical fiber interferometer.

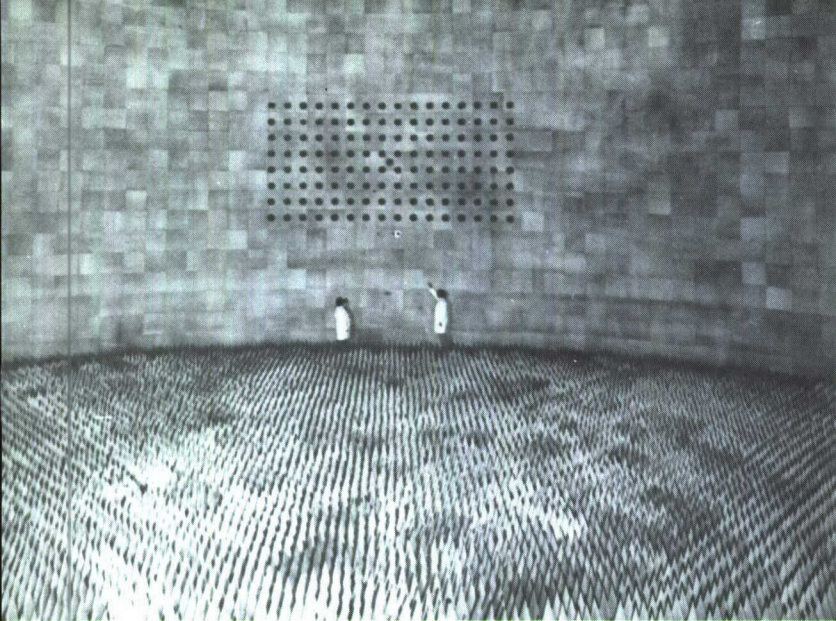
F. Lepple making adjustments to the ARCAS aerosol sampling unit. See page 68.

R. Ginther positioning the crucible before lowering it into the high-purity-glass melting furnace.

C. Kapetanakos explaining the ion ring experiment to two associates.

J. Phillips operating the memory tester that has been used to test all memories of a particular class flown on space missions.





Reading clockwise from upper left:

R. Schoppet and G. Farmer, dwarfed by the huge anechoic chamber that comprises part of the Central Target Simulator, point out a matrix array. See page 45.

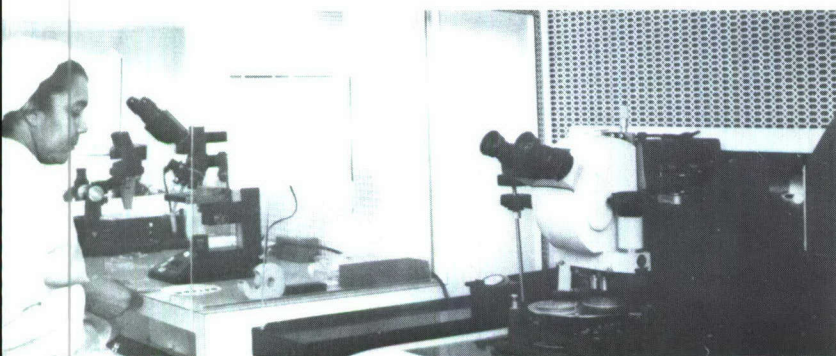
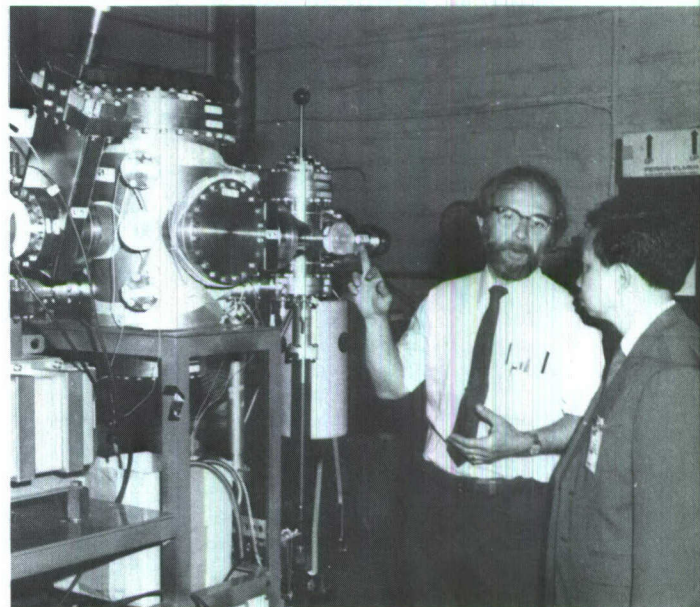
R. Panayappan and D. Venezky demonstrating the ease of rust removal with the newly developed cleaning compound. See page 143.

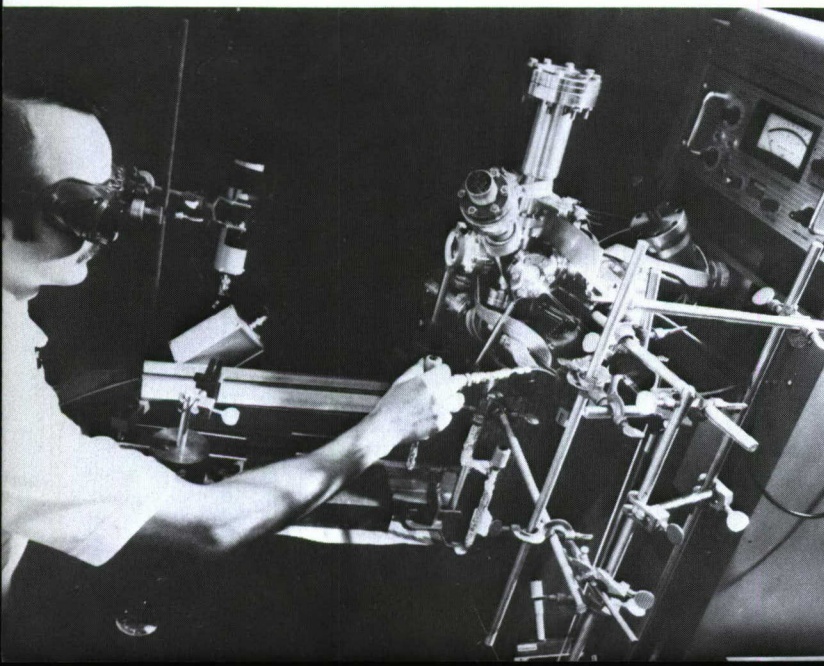
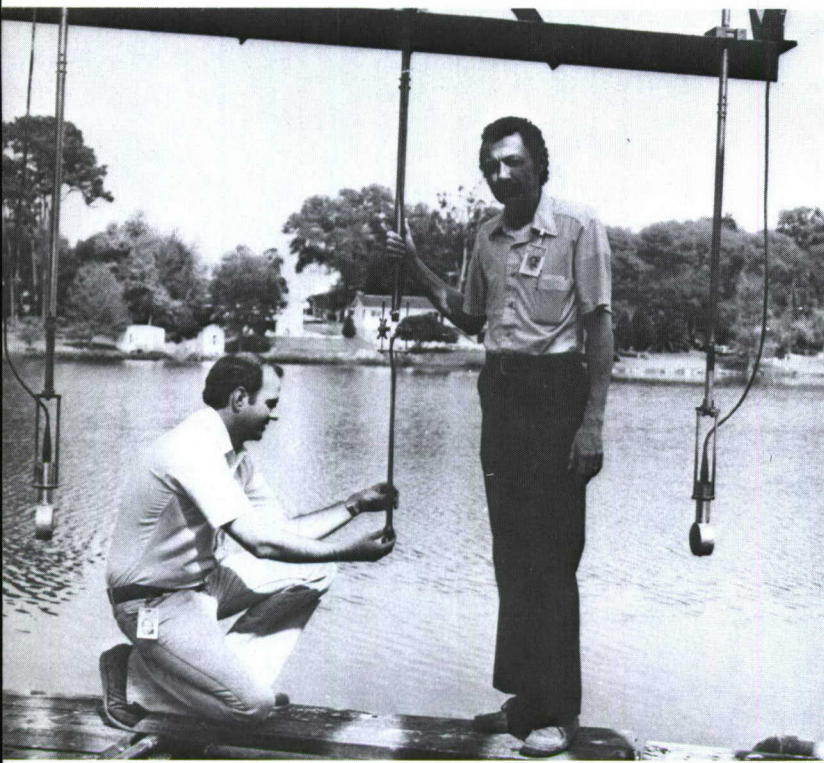
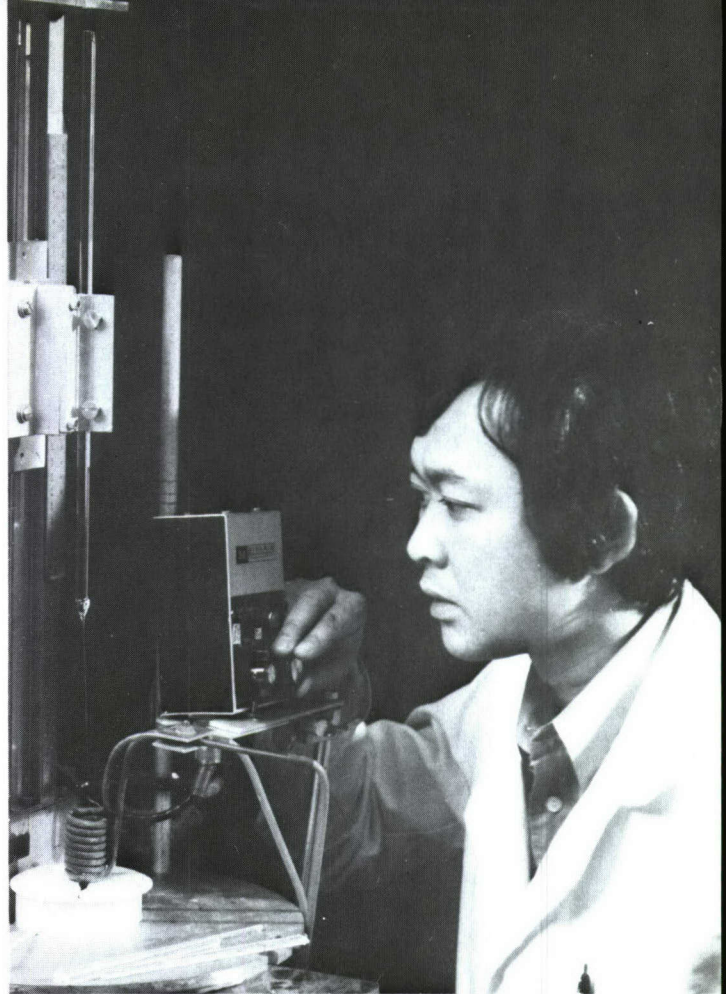
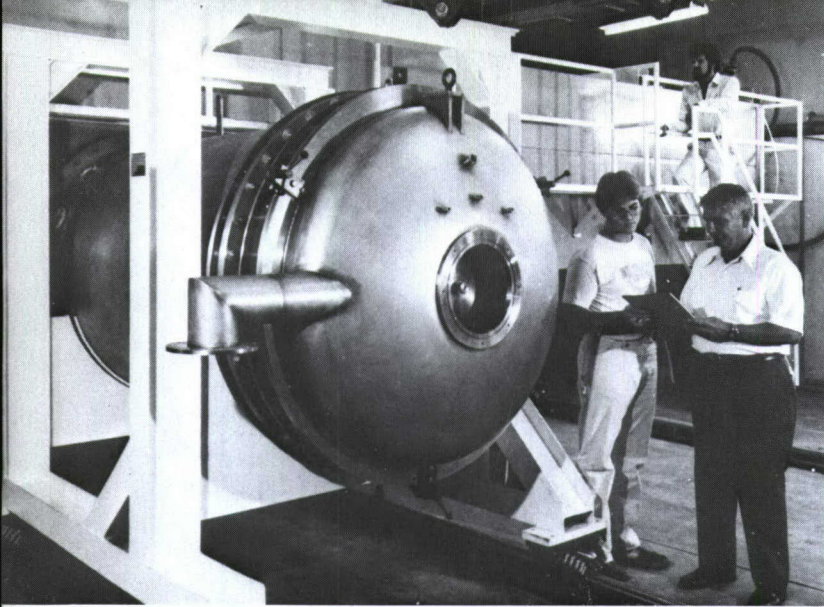
A. Knudson explaining the target chamber used for studies of ion-induced light emission to a distinguished Chinese visitor.

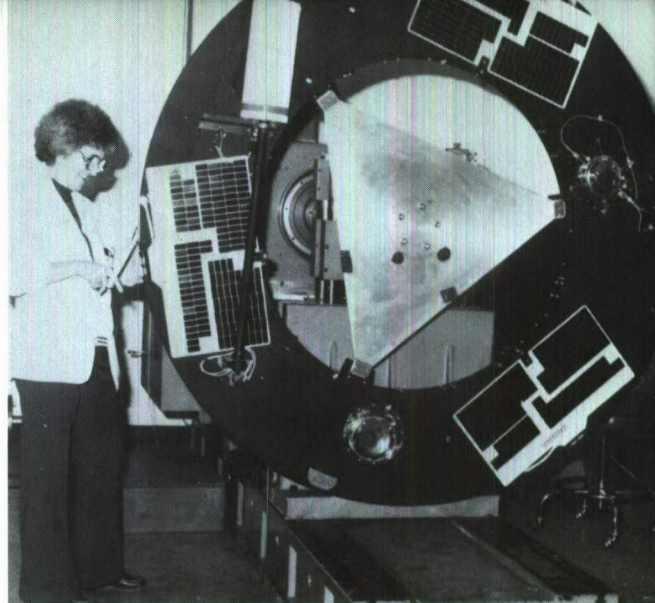
R.E. Taylor (left) with M. Fitzpatrick lowering a "daisy chain" of test specimens into corrosion fatigue test chamber.

B. Holmes setting up the *J* cross-polarization spectrometer. See page 158.

G. Hodge inspecting integrated circuits during processing in the photolithography section of the new microelectronics facility.







Reading clockwise from upper left:

L. Colquitt with the new PVF_2 acoustic shock sensor. See page 87.

J. Oliver making last-minute adjustments to the wire harness of the transponder experiment during a lull in spin balancing.

J. Griffith demonstrating easy removal of barnacles from a newly developed fouling release coating.

A. DeFonzo with laser source used for generating subpicosecond pulses of light for the study of semiconductors

C. Buhler (left) with W. Collins, Jr., installing thermal control coatings during gravity-gradient subsystem installation at the satellite launch site.

Opposite page (reading clockwise from upper left):

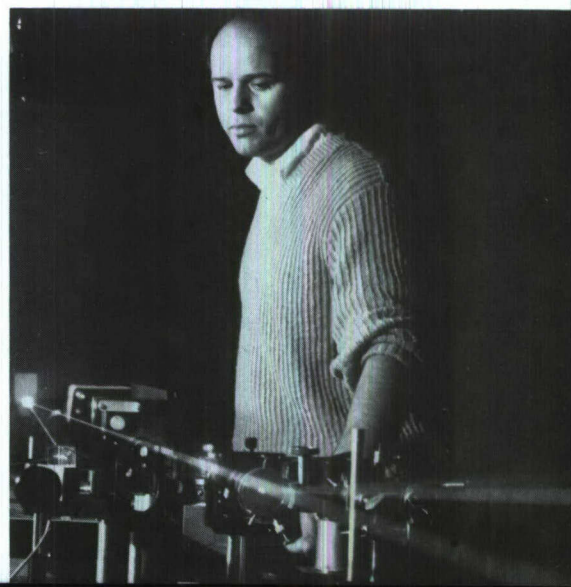
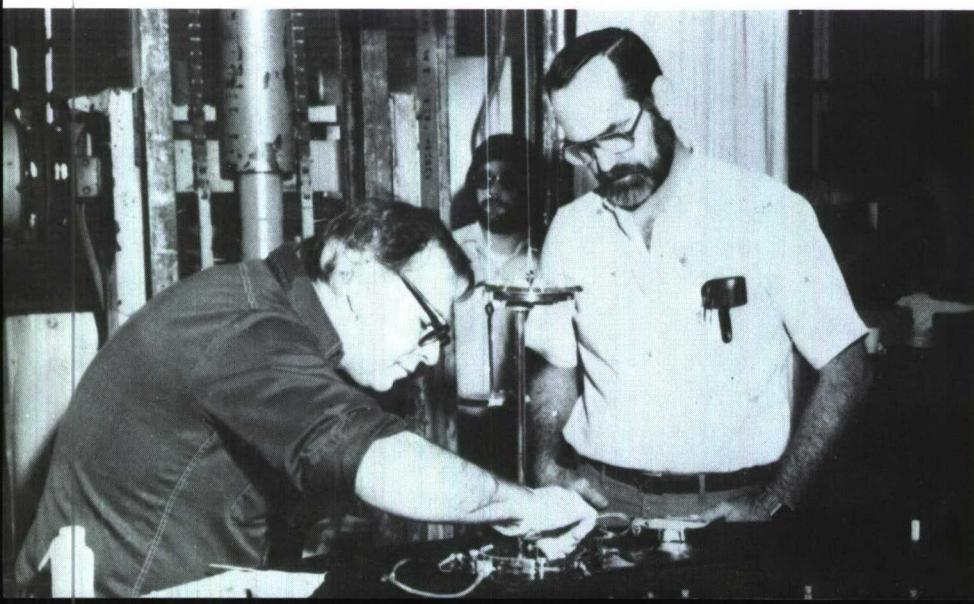
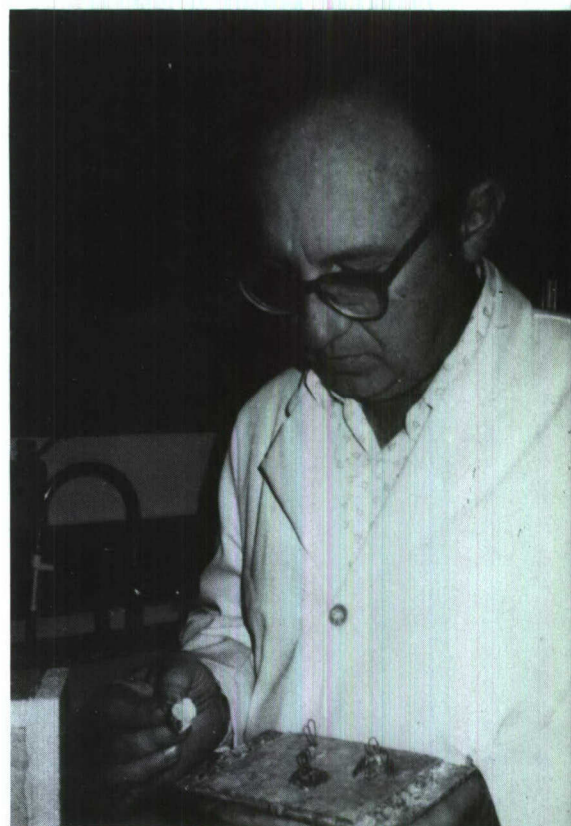
W. Webster (left) and D. Evenson check out the Poseidon electron beam generator as J. Sethian inspects from the rear platform.

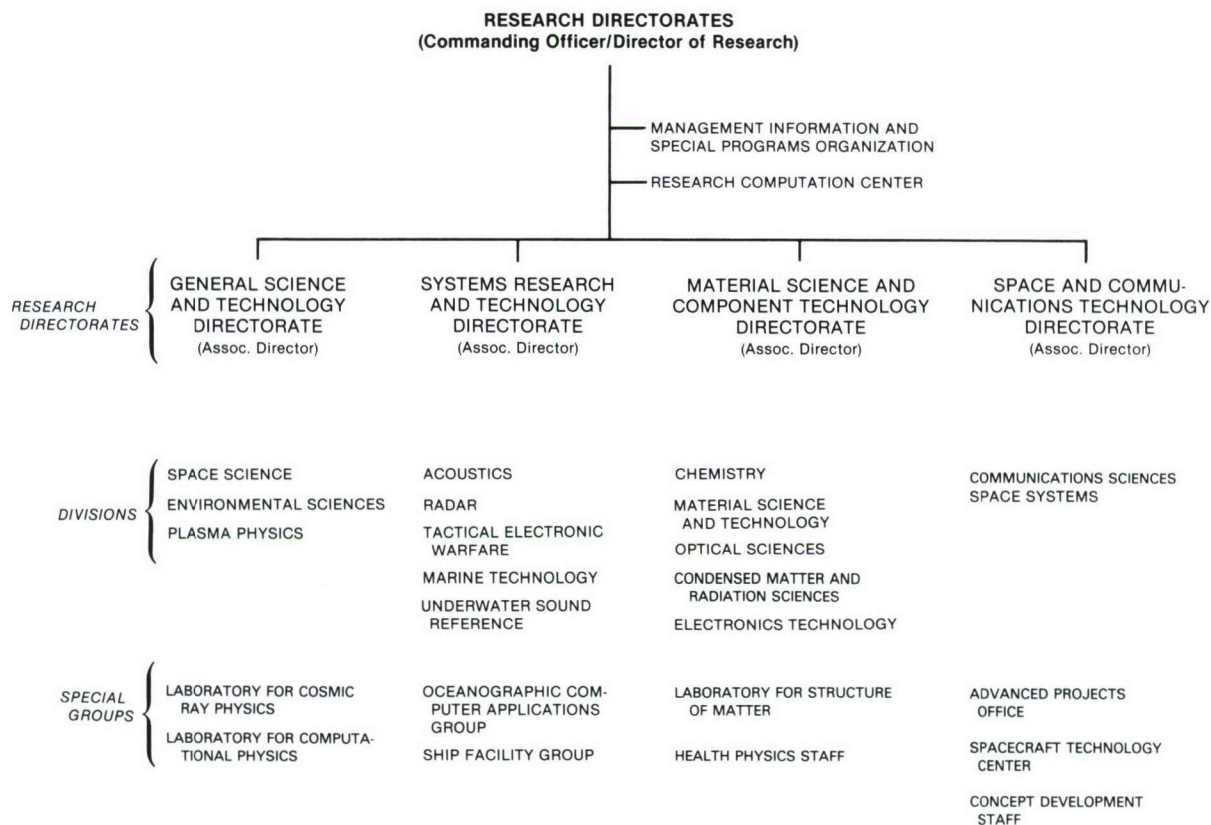
D. Tran experimenting with drawing a fiber vertically from a heated glass sample.

Under manual control of J. Dixon, NRL's experimental robot arm retrieves a geological sample from a simulated seabed.

R. Colton conducting a surface-enhanced Raman experiment by pyridine physisorbed on silver and gold in ultrahigh vacuum.

L. Luker (left) with A. Van Buren making a final adjustment on a transducer suspended on the in-line framework used for NRL hydrophone calibration. See page 84.





Organization of the Research Directorate, December 1980

THE NRL PROGRAM—RESEARCH AND PROGRESS

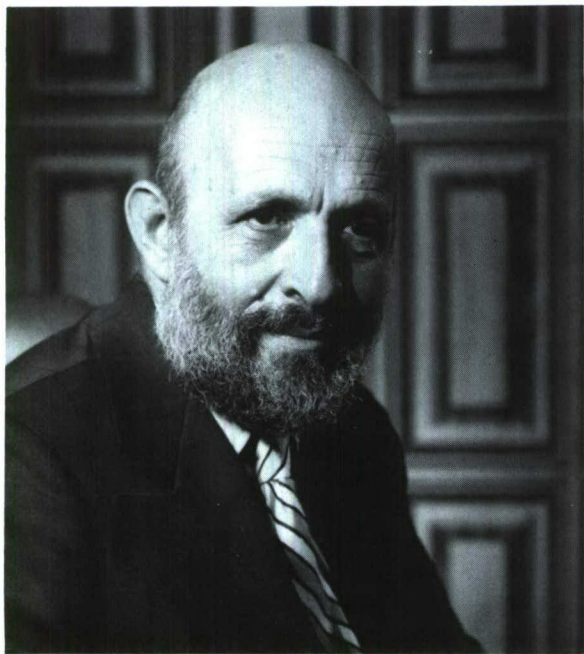
Annual reports are designed to summarize an organization's performance during the past year. In a publicly owned corporation, performance is generally measured in terms of the bottom line and in terms of the corporation's posture for successful future activities. By definition, in a government laboratory there should be no fiscal gain or loss from operations. Thus it is necessary for us to speak of the value of our work and the implications of this work to the Navy and to other sponsors. NRL's efforts can be measured in many ways. We are judged by the success of programs we managed, by our success in transferring research concepts into operational Navy and DoD systems, and by our ability to develop and discover new concepts that will provide the Navy with new capabilities. The conventional measures of scientific performance must also be applied to our efforts. These involve the quality of papers published and

presented to peer groups, the recognition accorded our staff in the form of honorific awards, professional society recognition, and the number of distinguished U.S. and foreign scientists who visit us to seek advice, exchange ideas, and engage in collaborative efforts. A final measure of our performance is the support our staff provides to our sponsors and to the nation as a whole by service and consultation on high-level national and international committees. Such activities provide a major means of impacting many important technical and scientific decisions.

To the degree that such activities can be reported in a document of this type, we believe there is a persuasive argument that NRL's performance during the past year was outstanding. Despite many complex problems related to facilities, equipment, personnel, and funding, we believe that the prognosis is excellent for continued high levels of performance in the years ahead.

As a corporate laboratory, NRL must conduct basic research, translate the results of this research into technology, and assist in transferring this technology to other Navy and industrial laboratories so that it can be incorporated into useful military systems. This *Review* presents an account of some of our scientific and technological activities. Its objective is to furnish some insight into the comprehensive coverage provided by NRL in its endeavor to ensure a broad base in science and technology for the Navy. Our efforts cover the multidisciplinary fields needed to increase the combat effectiveness of the fleet. In the future, as in the past, the motivations outlined in this overview will continue to guide the scientific activities of NRL.

The past year witnessed a changed national perception of the need for a strong and technologically superior defense establishment. Worldwide political turbulence and our national difficulties in reaction to it served to demonstrate that marginal technological advantages and marginal changes in the availability of key resources and technology can mean the difference between the life and death of a nation.



Dr. Alan Berman
Director of Research
Naval Research Laboratory

This year our R&D program was conducted with an increasing awareness that the problems revealed in international relationships and in our growing resource dependence must be translated into technological solutions that will ensure the defense and economic survival of our nation. We adjusted some of our programs to concentrate on those elements that offered a rapid and well-defined increase in our nation's and our Navy's technological base. However, we still continued to engage in many programs whose payoff can be measured only over a period of many years. The objective of these long-term programs is to ensure that our military posture will not be rendered unstable by possible future changes in the technology of other nations and that, to some degree, our economy will not be subject to perturbations caused by sudden changes in the availability of basic materials such as petroleum or special materials for electronics or critical structural applications. Our efforts in this respect continue to demand an orderly prosecution of a sound basic research program supplemented by a rapid response to perceived Navy needs.

Adhering to the precedent established during the last several years, we have subdivided this review of our efforts into eleven general categories. Each area reflects impressive and significant advances.

Traditionally, NRL has invested considerable effort in the important areas of information processing, transmission, and analysis. We believe that our work on adaptive processing and system architecture includes some major advances that may change currently accepted approaches to problems in these areas. Continuation of NRL work in high-frequency (HF) RF architecture has resulted in significant progress, and many of the concepts have matured to experimental equipments that are being tested in the laboratory. As an outgrowth of the HF technology activity, NRL has been named by the Naval Electronic Systems Command to serve as the System Designer for the High Frequency Improvement Program (HFIP). We are extending our HF wideband architecture technology base to include consideration of the technological implications of integrating HF, ECM, ESM, and communications capabilities. Analysis performed by NRL personnel has the potential of providing significant improvement in HF broadcast communications with concurrent reduction in manpower requirements for the HF stations and equipment.

The NRL lead development of the Advanced Narrow Band Voice Terminal (ANBVT) HF voice modem is being considered for use as the NATO standard HF voice modem over narrowband skywave communication channels. A voice processing technique operating at 800 bits/s was implemented on a signal processor operating in real time, and its performance permits communication at this very low data rate.

In line with current DoD emphasis on C³CM, NRL achieved a major milestone in its role as lead laboratory for airborne communication jamming by completion and laboratory evaluation of the advanced development model of the AN/ALQ-149 airborne jammer. This jammer is also being analyzed as an AJ/LPI communication set, and commonality of communication and communication jamming assets is being studied in all frequency ranges.

It is axiomatic that in order to be effective, a fleet must be able to acquire, assess, and efficiently manage data on all platforms within its sphere of interest, including those potentially within weapon ranges that exceed the horizon of its indigenous sensors. Although much of NRL's activities in these areas cannot be addressed here, we can report some significant advances in capabilities for RF environment simulations and studies and in real-time image analysis architecture. A stand-alone target tracking technique for shipboard radar indicators was developed that utilizes the internal microcomputers currently available in modern displays. The system, called MCAT, is intended for use on non-NTDS ships to reduce operator track overload in multiple-target scenarios. The operator detects targets and initiates tracking, after which MCAT remains locked onto the radar video signals, thereby eliminating operations now done by grease pencil on a reflection plotter. In the current system design, up to 32 targets can be tracked automatically, and graphics such as NTDS identifier symbols, velocity vectors, and scan history can be attached to each track.

In the area of marine geoscience, we can report good progress in our ability to measure the behavior of surface waves and large ocean current systems as well as crustal geophysical characteristics. In recent years, NRL has pioneered techniques for mapping ocean currents by use of HF over-the-horizon and dual-frequency radars. As these techniques have achieved maturity, they have provided the Navy and the oceanographic

community with new methods for broad area studies of the dynamics of the ocean surface.

The section that presents some of our work related to acoustics also reports impressive progress. Major field expeditions were undertaken and successfully completed. Low-frequency acoustic experiments in the arctic regions have shown that smooth ice cannot be treated as totally reflective and may be a significant factor in transmission losses between 0.2 and 1 kHz. Exciting results also are reported in acoustic applications to microparticle detection and non-destructive evaluation and in our studies of new sensors and sensor calibration techniques.

A number of striking advances in the development of optical and electro-optical technologies were achieved. New advances are reported in phase measurements for fiber-optic interferometers, in fiber-optic gyroscopes, and in blurred-image restoration. Exploitation of these capabilities will have many important applications. Also reported is an exciting development that can, in effect, provide an infrared microscopy capability with a resolution of less than $1\text{ }\mu\text{m}$.

The several topics discussed in the section on atmospheric behavior provide interesting illustrations of the value of broad multidisciplinary capabilities that permit coordinated theoretical, modeling, and experimental problem-solving efforts. Our studies of hot, reduced-density channels produced by electric discharge and laser radiation have provided new insights, with important implications ranging from nitrogen fixation to fusion reactors. Also presented are exciting advances in our understanding of ionospheric behavior that can contribute to a predictive capability with important C^3 and navigation applications.

As in past years, NRL's recent involvement in space-related activities was quite significant. On a purely scientific basis, many results have been achieved. NRL scientists have developed the capability to monitor ozone, water vapor, and carbon monoxide in the mesosphere by passive microwave observation from the ground utilizing advanced techniques of radio interferometric imaging. In addition, they have succeeded in revealing the character of the highly unusual galactic variable object SS433, which displays a radiation pattern due to a precessing beam. Our work has resulted in a highly refined interpretation of airglow emissions, including the first self-consistent analyses of the far-ultraviolet emissions of atomic oxygen. From both a military

and a scientific standpoint, our staff takes justifiable pride in the development of a new imaging x-ray sensor that demonstrates a factor of five increase in sensitivity without sacrifice of spatial resolution.

NRL has long recognized the importance of improved materials to the performance of U.S. Navy platforms and systems. Our scientists have developed unique methods of surface modification by ion implantation and laser processing. Tantalum implantation has provided greatly improved corrosion- and wear-resistance properties to engine bearings. In addition, polyacetalene has been implanted for the first time, yielding a highly stable surface with good retention of optical reflectivity. Greatly improved wear and corrosion properties also have been achieved by new laser processing techniques. Injection of carbide particles into laser-melted metal surfaces has shown improvements in wear resistance as much as two orders of magnitude. A remarkably efficient technique has been developed for cleaning metal surfaces. It employs a mixture of a water-soluble polymer and a chelating agent that is applied as a thick paste, gradually hardens into an encapsulating film, and can be easily peeled from the surface when cleaning is complete. Also, NRL scientists have obtained a significant advance in partially stabilized zirconia (PSZ), a new type of tough ceramic. Having demonstrated the strength-limiting effects of grain boundaries and defects in conventional powder processed PSZ, they then collaborated successfully with a major commercial supplier of fully stabilized zirconia crystals to obtain practical size PSZ crystals that are two to three times stronger than typical polycrystalline PSZ. Such materials can have a variety of important applications, including IR windows and domes.

The effects of stress and radiation on materials are areas of long-standing interest and productive activity at NRL. During the past year, our studies of fatigue crack growth in metals have shown significant progress. Among these are improved understanding of strain hardening rates in titanium alloys and of the influence of grain boundary properties on crack propagation in stainless steel. Another important advance has elucidated the high-temperature chemistry and critical role of sulfur trioxide in turbine blade corrosion. Studies of radiation-induced damage and soft upset of semiconductor memories were continued. As semiconductor technology has evolved, the spacing between components has

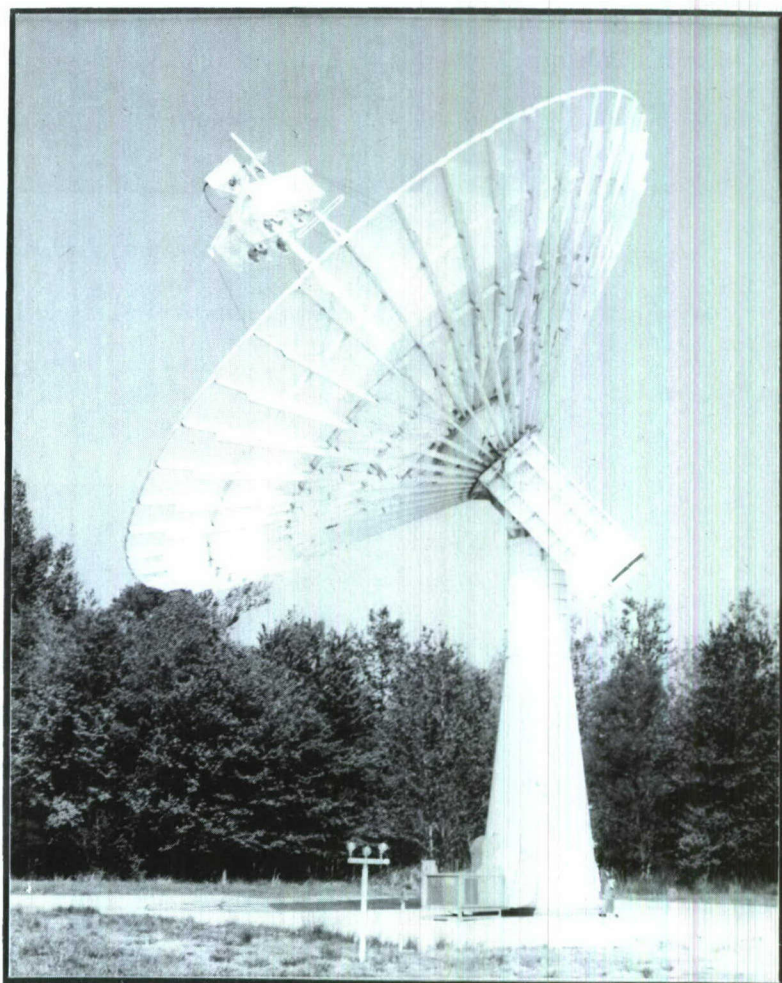
THE NRL PROGRAM—RESEARCH AND PROGRESS

decreased steadily, making them more sensitive to soft upsets. Understanding the nature of such effects may remove one of the technological barriers to the ultimate development of electronic devices at the $0.1\text{-}\mu\text{m}$ level.

Of necessity, this *Review* gives a somewhat incomplete picture of the Laboratory's operations and accomplishments. Only a limited presenta-

tion of our research results is included. Our classified contributions are omitted entirely, leading to somewhat unavoidable imbalance in the character of work reported here. Beyond such obvious omission, the *Review* does not convey the immense contribution of our staff in the form of advice, consultations, and emergency services provided to many U.S. Navy and other defense organizations.

INFORMATION PROCESSING, TRANSMISSION, AND ANALYSIS



INFORMATION PROCESSING, TRANSMISSION, AND ANALYSIS

The Navy is faced with a broad range of mission requirements and responsibilities. Its forces must be prepared to take prompt, appropriate, and effective action in a myriad of possible situations. To meet these responsibilities, the Navy must be able to coordinate and utilize its limited resources—it must be able to obtain, understand, select, and communicate the necessary information quickly and reliably. NRL has many research efforts that are contributing to the realization of these important requirements.

Adaptive Processing	23
Microwave Optical Lenses	26
Microwave GaAs Field-effect Transistor Oscillators	28
Surface Acoustic Wave (SAW) Convolvers	29
Survivable Intra-Task-Force Communications	31
Automation of Military Message Handling	33
Conversational Tests for Evaluating Voice Systems	34
Inverse Scattering Method for Measurements of Sinusoidal Surfaces	36

Adaptive Processing, by B.L. Lewis, F.M. Staudaher, and W.F. Gabriel, *Radar Division*

Adaptive array antenna systems are currently a subject of intense interest for radar and communications applications. The principal reasons are their abilities to automatically steer nulls onto jammers (ECCM), to minimize clutter in airborne MTI systems, and to resolve multiple sources or targets within a beamwidth (superresolution). The impact for future Navy radar systems will be dramatic improvements in target detection, location, and tracking in the presence of jamming and ground clutter. A three-pronged effort on adaptive techniques has been pursued at NRL for several years, consisting of a sidelobe-canceler program, an airborne adaptive MTI program, and a theoretical analysis program on adaptive algorithm processing.

A typical generic sidelobe-canceler configuration is illustrated in Figure 1. The mainbeam antenna is usually large and of high gain, whereas the associated auxiliary antennas are small and omnidirectional. A simplified explanation of its operation is that the auxiliary antennas, together with the mainbeam antenna, collectively determine the exact positions of the interference sources, and the array weights are then automatically adjusted to precisely cancel those sources in

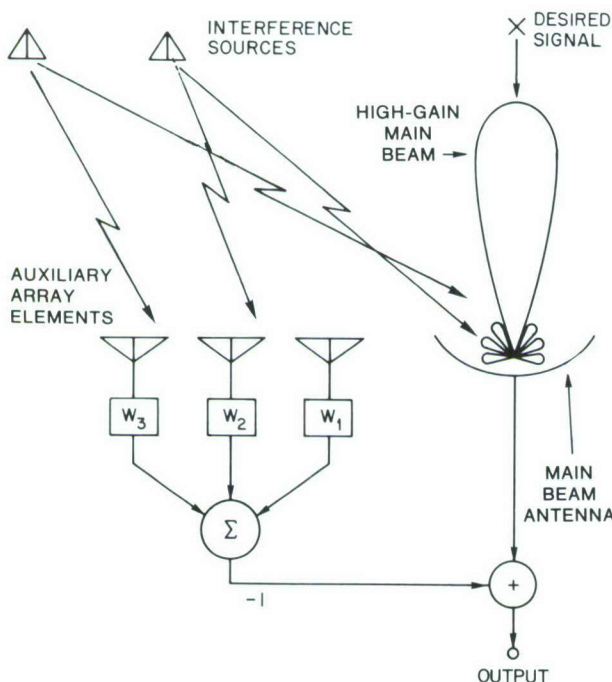


Figure 1. Typical sidelobe-canceler system. The complete adaptive array senses the locations of the interfering sources and automatically steers nulls in those directions.

the sidelobes of the mainbeam antenna; i.e., the system automatically steers nulls onto the jammers.

For a single auxiliary antenna corresponding to a single degree of freedom, the weight was traditionally obtained by performing a correlation between the auxiliary antenna input signal and the canceled interference residue signal. This was achieved using analog components and feedback circuitry to compensate for component drift. For multiple degrees of freedom, the loops were connected in parallel so that the weights were derived from a correlation between the resultant residue signal and each auxiliary channel signal. This approach resulted in slow settling times and poor cancellation in many situations.

A new approach, originated at NRL, uses an orthogonalization procedure known as the Gram-Schmidt procedure. This approach overcomes the difficulties inherent in conventional sidelobe-canceler systems. Next, open-loop digital sidelobe cancelers were developed at NRL and incorporated in the Gram-Schmidt configuration. This had a significant impact on the adaptive processing field, since the algorithm has very fast convergence and is amenable to implementations using single building blocks.

Adaptive array processing can be used in an airborne radar system to suppress jamming signals received via the antenna sidelobes. However, when the system adapts to jamming, the antenna pattern in the main-beam region may be perturbed and the sidelobe response may be raised in certain areas. This creates problems in an airborne system searching for low-flying targets. Any main-beam perturbations cause a pulse-to-pulse jitter to appear in the strong clutter region. The radar signal processor would sense this as a moving target response, thereby causing false alarms. Also, the higher sidelobe levels effectively raise the background clutter residue level in the Doppler filters, which would decrease the system's detection sensitivity.

These effects can be overcome by increased smoothing of the adaptive weights, by constraining the adaptive processor response, or by adding adaptive channels to process the Doppler signal response simultaneously with the antenna spatial signal response.

A system was implemented to record the radar returns digitally in real time from targets, clutter, and jamming. These recordings are used to investigate the effectiveness of various processors in handling these dynamic problems. They

can also be used as inputs to different adaptive processors implemented on NRL's general purpose computers. This data base can also be used to study the statistics of these real-time signals for other purposes such as the development of adaptive algorithms or testing of proposed adaptive mechanizations.

An adaptive-array flight-test system was used to collect the data base. The system includes a high-power radar transmitter, an antenna (Figure 2) having receivers for each antenna element, analog-to-digital converters, a high-speed buffer, and a recording system. The experiment is controlled by an operator using a CRT terminal.

The system was installed in an NRL EP-3 flying laboratory (Figure 3) and was used to gather data in flight during the fall and winter of 1979–1980 and the fall of 1980. This data base will be used in a continuing series of adaptive processing investigations.

Nonlinear superresolution techniques are now of considerable interest because of their capabilities for resolving closely spaced target spectra beyond the conventional windowed Fourier transform methods. The best known of these techniques are the maximum-entropy spectral analysis (MESA) method and the maximum-likelihood method (MLM). Since these tech-



Figure 3. William H. Hopkins manning the operator control station in the EP-3A flying laboratory, showing instrumentation, computer, and magnetic tape recorder

niques are most significant when processing short data sets, it is natural to consider their use for radar applications.

Studies conducted at NRL have shown that the MESA and MLM techniques are closely related to certain nonlinear-processing adaptive-array antenna techniques that consist of a generic

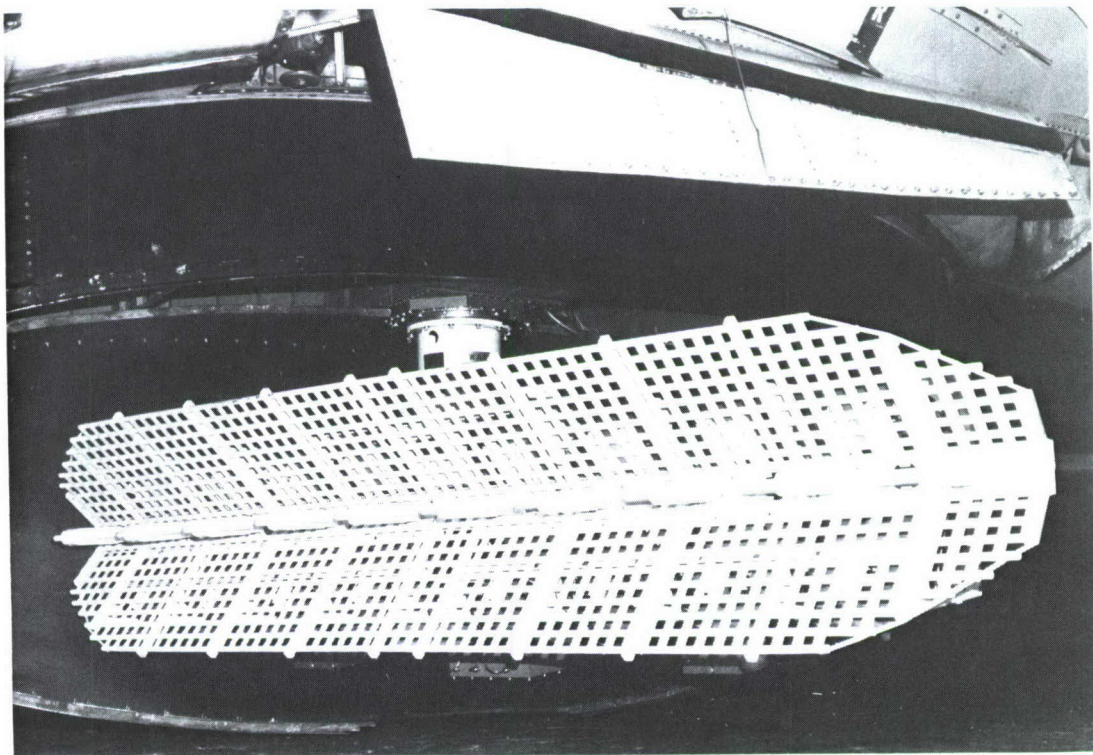
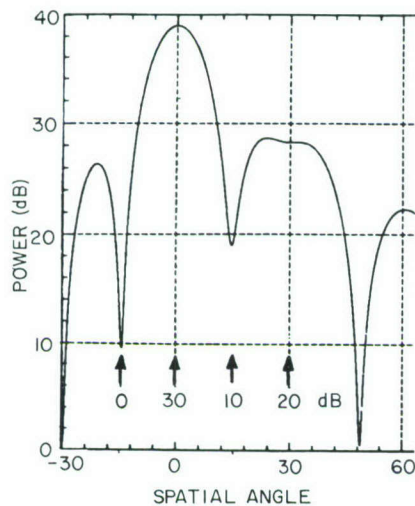


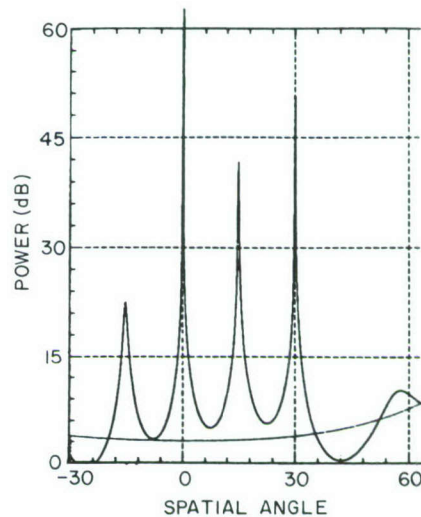
Figure 2. An eight-channel UHF antenna-receiver array installed in the belly radome of an EP-3A flying laboratory

sidelobe-canceler configuration and directional gain-constraint methods. This similarity increases the number of superresolution techniques available and brings to bear the real-time processing algorithms commonly associated with adaptive array operation. Computer simulations have demonstrated the superresolution of incoherent spatial sources via several of these algorithms, which may be classified as Toeplitz covariance matrix nulling techniques [1]. One highly significant dividend obtained to date is the easy resolution of unequal-strength sources. This has

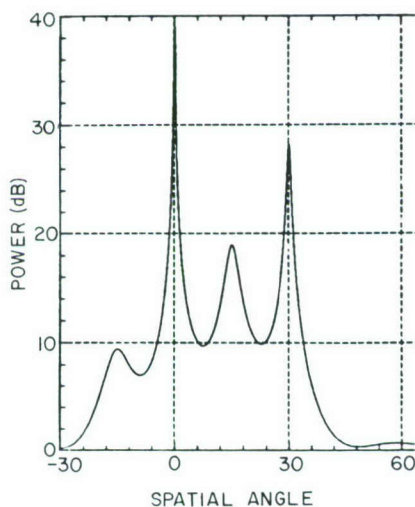
always been a difficult problem area for conventional linear beam processing because of sidelobes. An example of this is shown in Figure 4, where spatial spectrum estimates are shown for four noncoherent sources, each separated by 15° . The nonlinear processing leads to easy adaptive resolution of all four sources by an eight-element array with a uniform-illumination beamwidth equal to their separations. Notice in Figure 4a that, even though the sources are separated by a full beamwidth, a conventional beam scan cannot resolve them because of its sidelobes. Tapering



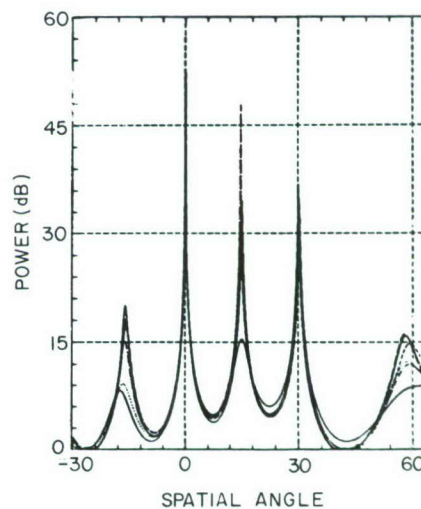
(a) Conventional beam scan



(b) Adapted pattern inverse



(c) Constrained-optimized beam scan



(d) Orthogonal lattice filter solutions, snapshot nos. 25, 40, 55, 70, 85, 100

Figure 4. Spatial spectrum estimates for four noncoherent sources of 0-, 30-, 10- and 20-dB strength located at -15° , 0° , $+15^\circ$, and $+30^\circ$; eight-element linear-array sampling aperture. Figures 4a, b, and c were computed from sample covariance matrix of 1024 snapshots.

the conventional beam illumination to reduce its sidelobes would only make matters worse because the new beamwidth would then become greater than the source separations. Figure 4b is obtained via the Weiner matrix inverse algorithm. It exhibits excellent resolution but inaccurate relative source strengths. Figure 4c is equivalent to MLM and both resolves the sources and accurately indicates their relative strengths. Figure 4d illustrates several time-sequence patterns obtained via the orthogonal lattice filter algorithm, wherein the solution firms up after about 50 snapshots, i.e., a demonstration of very rapid convergence.

[Sponsored by NAVSEASYSOM, NAV-AIRSYSOM, and ONR]

Reference

1. W.F. Gabriel, "Spectral Analysis and Adaptive Array Superresolution Techniques," *Proc. IEEE* **68** (6), 654–666 (June 1980).

Microwave Optical Lenses, by J.P. Shelton, Radar Division

There are many applications for microwave antenna arrays in radar, communications, navigation, and electronic warfare for which new techniques of forming multiple, directive beams have been developed at NRL.

Recent work on multiple-beam antennas has involved the study of microwave optical lenses. Microwave optics was an extremely active field of research 25 years ago, but it was eclipsed by the surge of activity in phased-array techniques. The field is now enjoying a revival with the advent of new system requirements and greatly expanded signal processing capabilities. Three aspects of NRL's multiple-beam antenna work are described

here—innovations in the design of microwave optical lenses, new concepts in geometrical optics, and the application of a three-dimensional microwave optical lens to a linear array.

The basic configuration under study is sketched in Figure 5. It consists of three antenna arrays—a feed array, a lens array, and an aperture (or radiating) array. The feed and lens arrays are separated by an unconstrained transmission region. The lens and aperture arrays are connected by transmission lines. Because of the interlacing of the transmission lines when the system is wired, this configuration has come to be known as a *bootlace* lens. Any element on the feed array drives (feeds) all the elements on the lens array. Because of path-length differences, the transmission volume serves as a beamformer, one beam being associated with each element on the feed array. The two-dimensional (2D) realization of this lens was studied initially, and it was shown that optimum performance is obtained by imposing symmetry on the shape of the curves forming the feed and lens arrays. It was also shown that, although lens operation is based on geometrical path-length differences, the performance of a properly designed multiple-beam *lens*-fed array is essentially equivalent to that of a Butler-matrix (i.e., FFT) *network*-fed array, so that lenses and networks can be regarded as interchangeable.

Whereas the 2D bootlace lens generates multiple beams for a linear radiating array, a three-dimensional (3D) lens is required for use with a *planar* radiating array. The design and performance of air-filled 3D lenses was investigated. In an air-filled lens, the transmission region consists of material with a uniform, homogeneous index of refraction, so that all rays travel in straight lines. It was found that the air-filled lens can be made quadrifocal; that is, the beams

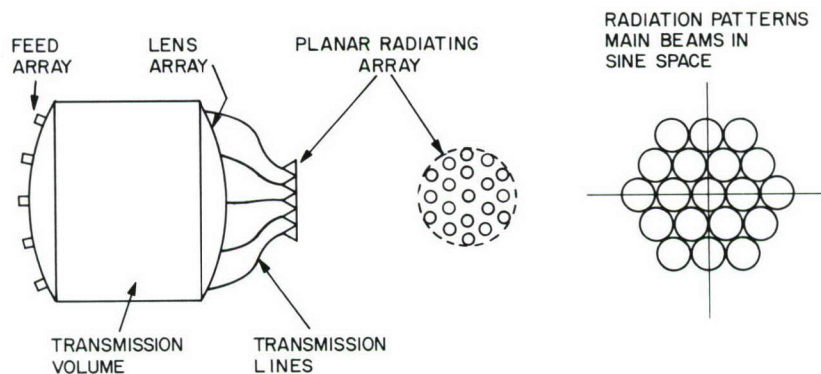


Figure 5. Microwave optical lens

formed by four of the elements (the four foci) on the feed array are perfectly collimated. The beams formed by the off-focus elements are less than perfectly collimated. One focus is on the lens axis and the other three are uniformly spaced. The location of the other foci can be selected to optimize the lens performance, that is, to minimize the wavefront aberrations produced by off-focus feed locations in the feed array.

The optimum location of the other foci was found, unexpectedly, to be on the lens axis. This element thus becomes a fourfold focal point. This result has led to the conjecture that, for any multifocal 3D optical system, optimum performance is obtained by collocating all the foci on the axis of the system.

Even though the 3D air-filled lens is quadri-focal, it exhibits astigmatism, and the collimation of the off-focus beams is rather poor. NRL scientists have found that the collimation performance of 3D bootlace lenses can be improved significantly by using an inhomogeneously loaded dielectric transmission region in which the index of refraction n is given by $n = 2/(1 + r^2)$, where r is the normalized distance from the center of the region. In this type of optical medium, known as a fisheye and originally analyzed by Maxwell, all ray paths are circular. The resulting lens is free of astigmatism, and coma is the limiting aberration.

A basic feature of bootlace lenses is that, when they are used to generate multiple beams over a large angular sector, the transmission region separating the feed and lens arrays is invariably larger than the aperture array. In many applications, this structural size would be a deterrent to the use of the lens. The lens—network equivalence concept mentioned above has been extended by NRL scientists to include 3D lenses as well as 2D lenses. Furthermore, it is possible to make 2D and 3D lenses equivalent to the same network, and therefore equivalent to each other. The practical result of this application of the lens—network equivalence principle is to enable the use of space-saving 3D lenses with linear arrays. As shown in Figure 6, a linear array can be fed by a large 2D bootlace lens, or equivalently by a smaller air-filled 3D lens, or finally by a still smaller dielectrically loaded fisheye-based 3D lens. The size reduction factor between the 2D and the 3D fisheye lenses feeding an N -element array is approximately $1/\sqrt{N}$.

The practical feasibility of these concepts and design techniques has been demonstrated experi-

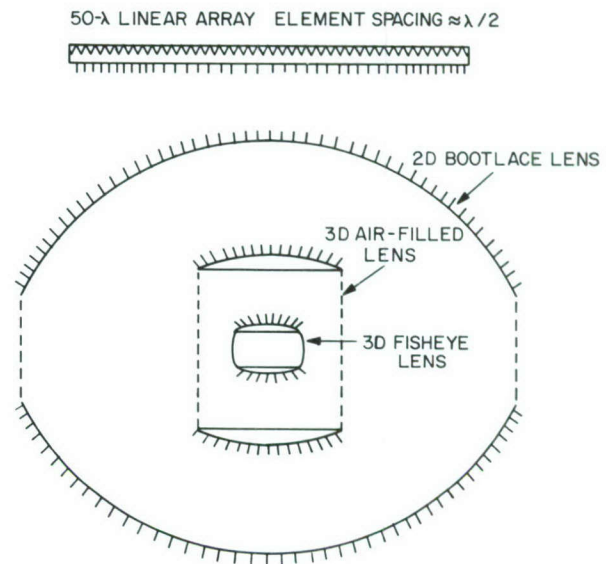


Figure 6. Size comparisons of 2D and 3D lenses feeding a linear array

mentally. A 3D air-filled lens with a 37-element feed array has been fabricated and connected to a 37-element linear array operating at a frequency of 5 GHz. This multiple-beam system is shown in Figure 7 being tested on NRL's radiation pattern measurement range. The 37 inputs to the

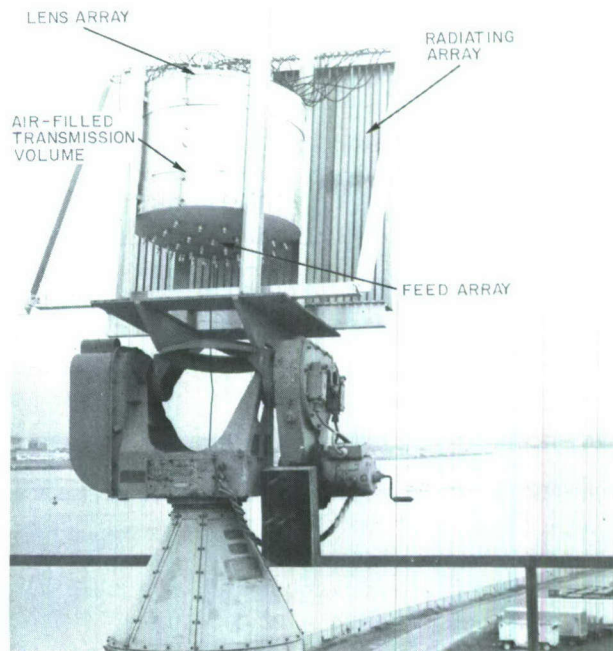


Figure 7. Air-filled 3D lens and linear array being tested at NRL

feed array, seen on the lower convex surface of the lens, generate 37 directive beams covering $\pm 56^\circ$ from the normal to the linear array. All antenna parameters, such as beam angles, beam widths, sidelobe levels, etc. were found to be as predicted.

These new concepts and design techniques represent significant advances in the theory of microwave optical multiple-beam antenna systems. However, many questions remain unanswered, such as: Can the conjecture on the optimum location of multiple foci be proved? Is the fisheye-based 3D lens the best that can be devised? Work on these topics is continuing.

[Sponsored by ONR]

Microwave GaAs Field-effect Transistor Oscillators, by C. Rauscher, *Electronics Technology Division*

Oscillators are among the basic building blocks required in the design of radar and EW systems. In the microwave range, GaAs field-effect transistors (GaAs FETs) are emerging as attractive contenders for use as oscillating devices up into the 30-GHz region. In comparison with competing GUNN-effect and IMPATT oscillators, the GaAs FET offers considerably higher DC-to-RF conversion efficiency. Furthermore, its superior bandwidth capabilities are particularly valuable when broadband tunability of the oscillating frequency is called for.

In the past, the full exploitation of GaAs FET performance capabilities in oscillator circuits has been impeded by the lack of an accurate and systematic large-signal design theory. In response to the need for such a theory, research at the Naval Research Laboratory has been focused on developing a generalized oscillator design technique. The basic design task is that of synthesizing a lossless three-port network (Figure 8), which provides optimum feedback and impedance matching conditions for the device, thereby maximizing the RF power delivered to the external 50-ohm load of the overall circuit.

The approach pursued is to represent the transistor by an equivalent circuit composed of linear and nonlinear elements and to subsequently identify the dominant nonlinearities. This leads to a remarkably simple formulation of the optimum conditions for oscillation. According to these conditions, the coupling network must possess a minimum of four real-variable degrees of freedom. This translates into a circuit

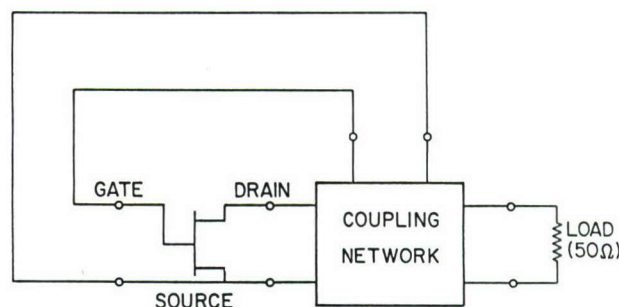


Figure 8. A microwave GaAs FET oscillator that incorporates the NRL-developed coupling network

comprising two reactances and one complex-valued impedance element physically implemented with a lossless two-port matching circuit terminated in the external 50-ohm load resistor. In the case of a voltage-tuned oscillator (in contrast to fixed-frequency), the conditions for optimum performance require that both reactances be tunable in voltage. This is accomplished through the use of either yttrium-iron-garnet (YIG) devices or variable-capacitance diodes (varactors).

The overall design procedure is characterized by its conceptual simplicity, derived from the fact that it essentially involves only linear circuit transformations in the frequency domain without the need for employing numerical optimization techniques. Moreover, the efficiency of the method is critically dependent on the scheme used for determining reliable approximations to the properties of the nonlinear transistor model elements. These approximations are needed to avoid tedious large-signal RF measurements on the transistor.

Two test circuits were designed with this method to verify the validity of the approach experimentally. In both cases, the measurements agreed very well with predictions. The first circuit involves a 17-GHz fixed-frequency oscillator, in the form of a distributed microstrip circuit. The oscillator provides 45 mW of output power at a DC-to-RF efficiency of 25%, using a transistor with a 0.5- by 375- μ m gate geometry. The second test circuit is a broadband, varactor-tuned oscillator, implemented as a lumped-distributed network (Figures 9 and 10). Both of the basic circuit reactances mentioned above, which must exhibit voltage tunability, are realized as series connections of two individual hyperabrupt varactor chips, with the interconnecting bond wires serving as lumped inductors. (Hyperabrupt varactors provide improved tuning linearity and

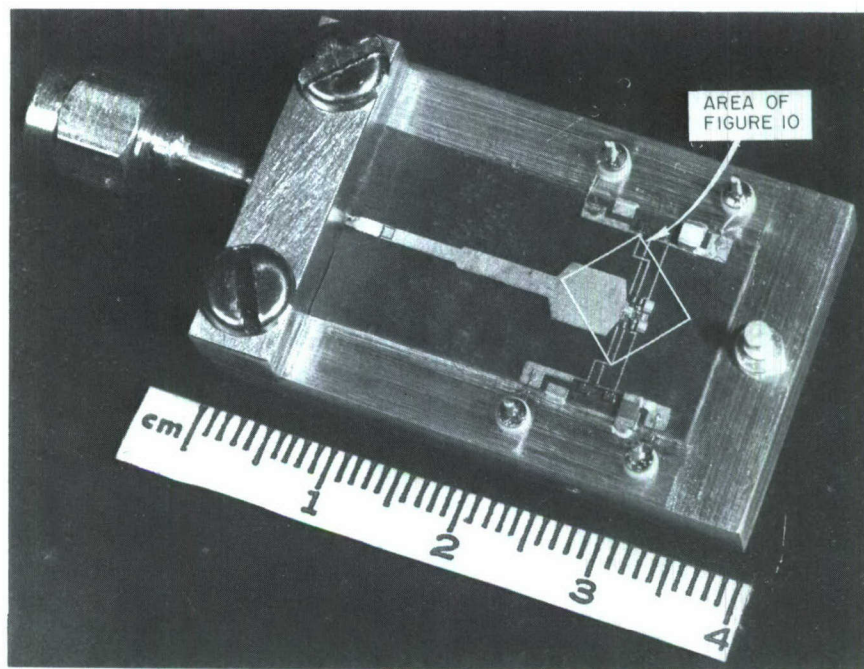


Figure 9. Varactor-tuned, 7.4- to 13.1-GHz GaAs FET oscillator. Details of the coupling network (middle of rectangular frame) are shown in Figure 10.

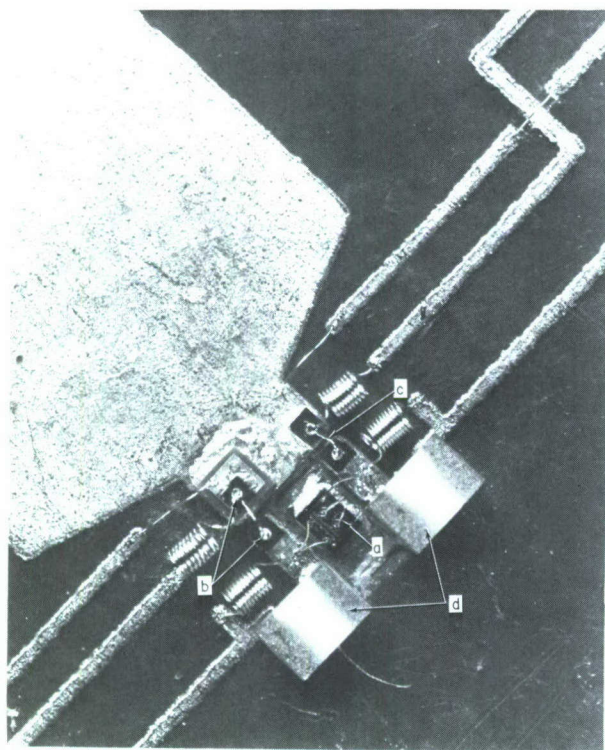


Figure 10. Close-up view of transistor and tuning arrangement: (a) GaAs FET, (b) two gate varactors (in series), (c) two source varactors (in series), (d) stabilizing resistors

larger tuning bandwidth than conventional varactors with abrupt doping profiles.) With use of a transistor having a 0.5- by 750- μ m gate geometry, an RF output power level of 30 mW was achieved across the entire frequency tuning interval of 7.4 to 13.1 GHz. It is interesting to note that an increase in bandwidth of 30% was achieved by employing *two* independently tunable varactor elements, as opposed to the conventional use of only one.

The NRL studies on microwave GaAs FET oscillators have provided a thorough understanding of nonlinear device-circuit interaction. At the same time, a systematic procedure for developing oscillators with large-signal-optimized RF performance has been established in support of current and future Navy needs.

[Sponsored by NAVELEXSYSCOM and ONR]

Surface Acoustic Wave (SAW) Convolver, by K.L. Davis, *Electronics Technology Division*; and J.F. Weller, *Optical Sciences Division*

The Naval Research Laboratory (NRL) is developing surface acoustic wave (SAW) convolvers as programmable matched filters to decode spread-spectrum communications and

identification, friend or foe (IFF) signals. A convolver is a device that operates on two separate input signals and gives a large output when the inputs are identical, and a small output when they are not. The SAW approach offers compact, low-power-consuming, matched-filter implementations for very wide-bandwidth signals. A critical feature of the device is the method for compressing wide acoustic beams from SAW transducers into a narrow waveguide for optimum nonlinear mixing efficiency. NRL scientists have developed a planar prism coupler that provides a unique method for efficiently coupling acoustic beams into narrow metal-film guides.

The convolver offers several advantages over alternate approaches. These advantages include: (a) selective excitation of a single waveguide mode, thus avoiding spurious signals resulting from mode interference; (b) relatively simple fabrication (no tiny geometries to resolve) even at high frequencies; and (c) freedom from bulk wave interference, since spurious bulk waves excited from the transducers do not couple into the waveguide or propagate parallel to it.

The coupler concept, first suggested by workers at the Brooklyn Polytechnic Institute, is based on evanescent coupling of energy from the prism into the waveguide across a very narrow gap ($< 10 \mu\text{m}$) in the metal film.

The NRL convolver configuration is illustrated in Figure 11. The convolver consists of two couplers and a waveguide, all formed by a single planar metal-film pattern on the surface of a piezoelectric crystal. Wave propagation in the guide is pictured as a ray bouncing along the guide at angle θ , which is associated with a specific waveguide mode and signal frequency. A surface wave launched from the transducer at

angle θ couples efficiently from the prism across the gap into the waveguide. The input signal is excited by an interdigital transducer at one end of the device. The signal radian frequency is ω and the wave vector is \mathbf{k} . A reference signal with frequency ω is excited at the opposite end of the substrate and propagates in the opposite direction from the signal with wave vector $-\mathbf{k}$. In the region where the two waves overlap, they mix according to the nonlinear properties of the medium, forming a new signal with frequency equal to the sum of the input frequencies (2ω) and a wave vector equal to the sum of the input wave vectors (0 since the input wave vectors cancel in this case). This signal, which is detected between the grounded bottom of the substrate and an output convolution electrode covering the interaction region, represents the mathematical convolution of the input and reference signals (hence the name *convolver*). If the reference signal is time reversed before being inserted into the device (so that the leading edge goes in last and the trailing edge first), the output is the *correlation* of the input and reference signals. Thus, the convolver acts as a correlator or matched filter that is completely programmable, since the reference is supplied by the user.

The mixing process in the convolver takes place because of small nonlinearities in the elastic and piezoelectric properties of the crystal. For better efficiencies, the surface waves are compressed into a narrow convolution output electrode shown in Figure 11, which also acts as an acoustic waveguide to confine the beam and thereby produce a higher acoustic intensity for a stronger nonlinear interaction.

Figure 12 shows a sequence of 290-MHz SAW beam cross-section profiles for a device

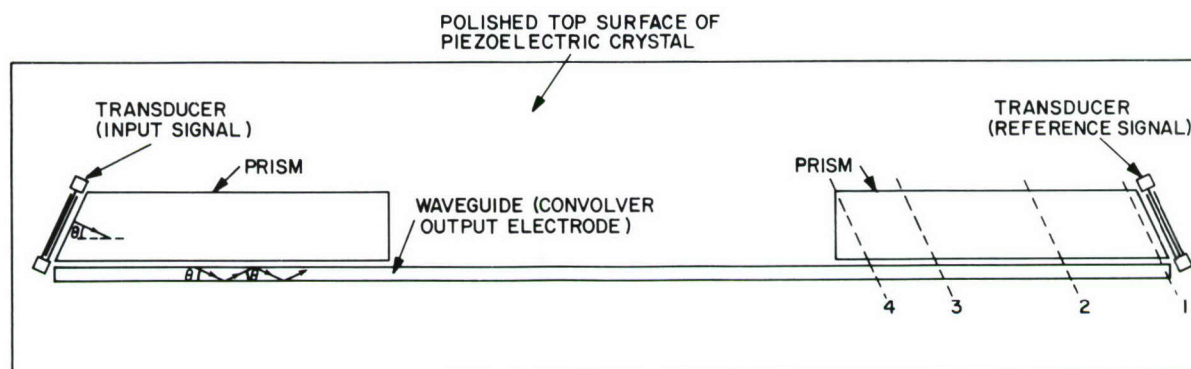


Figure 11. SAW convolver with a crystal 50.8 mm long. Metal pattern is not drawn to scale. (Dashed lines on right-hand prism refer to Figure 12.)

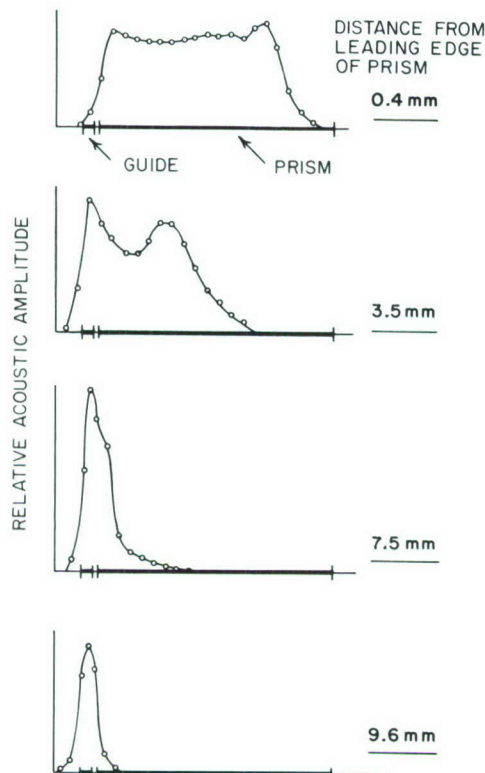


Figure 12. Beam profiles for a 290-MHz SAW beam in the prism region. These are four plots of measured acoustic amplitude vs position that show the beam cross-section along the four cuts represented by dashed lines in Figure 11.

designed and fabricated at NRL, representing the first prism coupler demonstrated on a single-crystal substrate. The measurements of acoustic amplitude are obtained by scanning a laser beam across the prism at the four positions labeled in Figure 11. The scans show that the acoustic energy does actually couple from a wide input beam into the narrow waveguide. Furthermore, the measured coupling efficiency is within 1 dB of the theoretical maximum of 80%.

In SAW convolvers, efficient coupling over a wide frequency range (i.e., a wide fractional bandwidth) is essential for achieving wide operating bandwidth for the device at the lowest possible operating frequency. The low frequency is desired because both acoustic propagation loss and device fabrication difficulty increase significantly with frequency. In the configuration of Figure 11, the angle θ for a given waveguide mode changes with frequency. Thus, to couple efficiently over a wide frequency range, the transducer should be oriented at a different angle θ for

each frequency. The fractional bandwidth of the present design is limited to about 15% of the center frequency.

Work is under way at NRL to develop a special transducer structure that excites each signal frequency at the optimum angle. That design is expected to result in fractional bandwidths that exceed 50% while retaining the inherent advantages of the prism coupler structure. Convolver with a bandwidth greater than 100 MHz are needed for spread-spectrum applications such as packet radio or planned IFF systems.

[Sponsored by NAVAIRSYSCOM]

Survivable Intra-Task-Force Communications, by D.J. Baker, *Communications Sciences Division*

The trend toward computerized naval platforms is generating new requirements for communications within a task force that cannot be met by existing communication systems. New systems are needed to provide responsive, efficient, and survivable communications among naval units at ranges between 50 and 1000 km. Radio links at these ranges are usually in the high-frequency (HF) spectrum (2 to 30 MHz), where the ability to communicate from one unit to another varies with frequency and time. Because of this variable connectivity and the need to provide network survivability, the new systems will require techniques that adaptively organize the mobile units into efficient network structures and maintain these structures in spite of node and link losses.

As part of a broad development effort in HF systems, NRL has developed the organizational architecture for an intra-task-force (ITF) network that provides a structure and a set of procedures to deal with the variable-connectivity problem, regardless of its source. The problem can arise from changes in factors such as ranges between platforms, relative orientations and antenna pattern effects, noise levels at the receivers (possibly due to jamming), propagation conditions, and operating frequency. The change in connectivity might also result from platform destruction or equipment failure.

A typical link in an HF network is a *broadcast channel*: transmissions from one platform, or communication *node*, are heard by many nodes, and simultaneous transmissions from two or more nodes may interfere with each other at several nodes. In a broadcast channel in which

all nodes can hear each other, mutual interference can be minimized by having nodes that are about to transmit first check the channel to determine whether it is in use. Algorithms are available to deal efficiently with those occasions when two transmitters begin transmitting at the same time.

However, inefficiencies arise when all nodes cannot hear all other nodes, as in an HF network. This is the so-called *hidden terminal* problem. The ITF Network deals with the hidden terminal problem by organizing itself into node clusters, each with a central controller or *cluster head*, which can hear and be heard by all other nodes in the cluster. Within a cluster, schemes for random channel access can be used, with the cluster head broadcasting a busy signal whenever the channel is in use. Alternatively, controlled access schemes can be employed with the cluster head exercising control. To provide for intercluster communications, the ITF Network has gateway nodes that link the cluster heads together into a *backbone* network as in Figure 13. The *linked-cluster algorithm* has been developed to allow the network to organize itself and maintain the structure.

In the linked-cluster algorithm, each node performs its role on the basis of local information and information obtained from its neighboring nodes on the control channel. A *neighboring* node is defined as one to which the node is connected bidirectionally. The schedule of events on the control channel is shown in Figure 14. The total frequency band available is partitioned into a number of subbands (say M) within which a single interconnectivity map is expected to exist. The control channel is divided into the same number (M) of *epochs*, each of which represents the time required to complete the algorithm in one subband. During each epoch, one subband is used to transmit control messages while normal message traffic exchanges are conducted in the other subbands. Each epoch of the control channel is divided into two frames of N time slots each, where N is the number of nodes. Each node transmits a control message during its assigned time slot in each frame of an epoch. During the first frame, a node broadcasts the identities of the nodes it has heard from during previous slots in the frame. By the time it is ready to transmit in Frame 2, each node knows all its neighbors.

The linked-cluster algorithm provides a deterministic rule by which each node can deter-

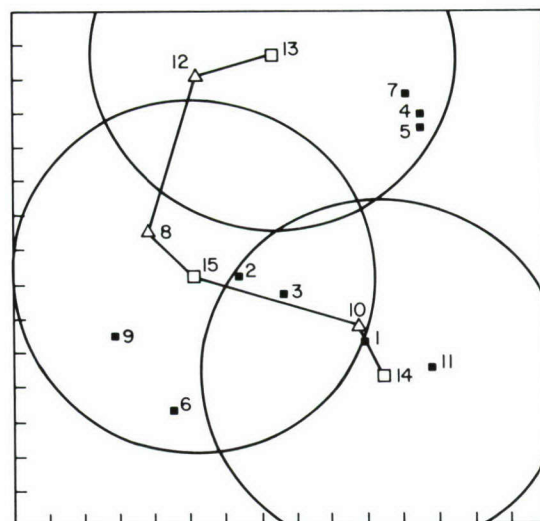


Figure 13. Example of linked-cluster organization of an intra-task-force network. Nodes 13, 14, and 15 are cluster heads. They are linked together by gateway nodes 8, 10, and 12 to form the "backbone" network. In this example, nodes are within communication range of a cluster head if they lie within the circle drawn around it.

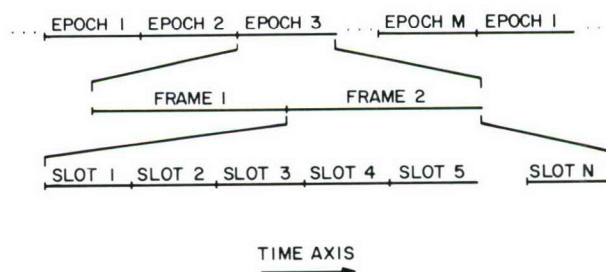


Figure 14. Control channel schedule for the linked-cluster algorithm

mine, just prior to its Frame 2 transmission, whether it should become a cluster head. The node then broadcasts this determination in its assigned Frame 2 slot along with its list of neighbors. Thus, by the end of Frame 2, each node also knows its neighbors' neighbors: information that is needed to establish the backbone network for linking the clusters. After the M epochs have occurred, the network has been organized into a distinct structure for each of the M subbands. The algorithm is then repeated, recognizing that connectivity is time varying. To optimize the revisit time in each subband, the algorithm can be generalized either to provide intervals between any successive epochs during which no control

information is passed on any subband, or to provide for control information passing on more than one subband in a given epoch.

The linked-cluster algorithm provides the ITF Network with a survivable architecture that adapts the network structure to connectivity changes arising for any reason. Path redundancies resulting from distinct structure within each subband provide a robustness to the ITF Network. The architecture provides the framework for investigating remaining networking issues, including routing, flow control, and protocol design.

[Sponsored by NAVELEXSYSCOM]

Automation of Military Message Handling, by C.L. Heitmeyer and S.H. Wilson, *Communication Sciences Division*

During the late 1960s, two American military crises, involving the U.S.S. *Liberty* and the U.S.S. *Pueblo*, were exacerbated by unacceptably long delays in the delivery of critical messages. Members of Congress investigating the quality of U.S. military communications identified several causes for the communications delays, including two problems in military message processing: lengthy processing times and opportunities for human error. A likely means for reducing processing times and decreasing human errors is to apply computer technology to message processing. In 1975, the Navy, the Defense Advanced Research Projects Agency, and the Commander-in-Chief, Pacific (CINCPAC), initiated a project called the Military Message Experiment (MME) to demonstrate and evaluate the utility of an interactive, computer-based message handling system for operational military users.

The MME was completed in 1978 and the report of findings was issued in 1980. NRL was involved in all phases of the MME. In particular, NRL led the team that evaluated the utility of an interactive message system in a military environment.

For conducting the MME, a PDP-10-based system running the TENEX operating system was installed at CINCPAC Headquarters and was used by approximately 100 members of the CINCPAC Operations Directorate. SIGMA, a program written by the Information Sciences Institute of the University of Southern California, provided the message handling functions. These functions included most of those needed by a military user: message creation and release; the construction of electronic "readboards"; message filing and

retrieval; replies to messages; and message "chopping," commenting, and distribution. The MME was designed so that the user could handle all of his message traffic (incoming and outgoing, formal and informal) on the automated system. The multilevel security rules that SIGMA enforced were based on the security kernel model developed by Case Western Reserve and MITRE. While not rigorous enough for certification, the rule enforcement was sufficiently rigorous to determine the effects of security constraints on the users' interactions with the automated system.

Information regarding the military utility of systems like SIGMA was collected from several sources—computer-generated statistics, questionnaires, interviews, observations of users, and controlled exercises. The evaluation team reached several conclusions, including the following:

1. An automated message handling system can be highly useful in a military environment, especially during a crisis. The system must be both highly reliable and routinely available. Any message system that will be used in a crisis must also be available during routine operations. This is so that users will become skillful enough to use the system effectively during a crisis, and also so they can collect and organize messages in preparation for a crisis.

2. An automated message system must provide services to everyone involved with message handling. Each user may not have a terminal; thus the system must have well-thought-out procedures for including these individuals in procedures that have been automated (e.g., message distribution).

3. For certain message handling tasks, some users will find it more convenient to use manual rather than automated procedures. For example, in the MME, many users preferred paper copies for reviewing messages and manual rather than automated coordination.

4. An automated message system must be an integral part of the user's information handling system. Users who draft messages need to refer to many documents, including other messages, reports, and letters. Many of these may be stored on other automated systems, such as word processors and command and control systems. Future message systems should allow a user to integrate information from other systems into his messages. Conversely, a user should be able to transfer information from his message system to other automated systems.

5. A user-oriented message system (e.g., SIGMA) and the telecommunications center with which it is associated (e.g., the Local Digital Message Exchange) must be integrated. Otherwise, some functions, such as message storage and error checking, are duplicated, and serious incompatibilities arise.

NRL has written a final report that describes the MME and summarizes its findings. Currently, the Department of Defense is planning the development of a new generation of interactive, computer-based military message systems. The lessons learned in the MME should be helpful in developing this new family of systems.

[Sponsored by NAVELEXSYSCOM]

Reference

1. C.L. Heitmeyer and S.H. Wilson, "Military Message Systems: Current Status and Future Directions," *IEEE Trans. Commun. COM-281*(9), 1645 (1980).

Conversational Tests for Evaluating Voice Systems, by A. Schmidt-Nielsen and S.S. Everett, *Communications Sciences Division*

Considerable effort is being directed toward the development of techniques and systems for digital transmission of voice signals in both military and commercial applications. In support of these efforts, extensive standardized testing is needed to assess and compare the performances of the various schemes. An accurate assessment requires the use of several types of tests that measure different aspects of the voice signal. Three general types of voice tests can be specified:

1. Intelligibility tests provide a measure of the ability to distinguish individual speech sounds (phonemes).
2. Quality tests measure acceptability on the basis of characteristics such as voice naturalness or pleasantness.
3. Conversational tests measure the actual usability of a working two-way communication link and require active participation rather than passive listening.

In commercial applications where high data rates are employed (16 to 64 kbit s⁻¹), intelligibility is usually high, and quality measures such as voice naturalness are an important factor. In military applications, where it may be necessary to accept lower quality in order to operate on links limited to 2.4 to 9.6 kbit s⁻¹ (*NRL Review*,

issued July 1980, pp. 31–34), intelligibility becomes a dominant factor but does not fully measure the usability or communication quality of a system. Conversational tests provide feedback about the success of the communication and give users the opportunity to adapt to the constraints of a given system.

Reliable tests of intelligibility, the Diagnostic Rhyme Test (DRT), and of quality, the Diagnostic Acceptability Measure (DAM), are widely used for military operations. The area of conversational testing is considerably less well developed. NRL has been using conversational tests to evaluate digital voice processors and has developed a short, versatile test called the Mini Communicability Test (Mini-CT) that is easy to administer and use. The Mini-CT is based on the Diagnostic Communicability Test (DCT), which was developed by Dynastat, Inc. under sponsorship of the Naval Electronic Systems Command and further refined in collaboration with NRL.

In a conversational test, participants perform a task that requires them to exchange information over the communication system being tested. After completing the task, the participants rate the quality of the communications. The DCT employs a stock-trading game as the task and requires five trained participants. It has been designed with an understanding that a good test should use the same participants repeatedly, should avoid changes in task difficulty, should maintain interest and motivation, and should generally keep test variations at a minimum.

To test the sensitivity of the DCT to small differences in voice quality, we trained a test crew at NRL and conducted tests during 1980 with several voice processing systems. The tests included two versions of a 2.4-kbit s⁻¹ linear predictive coding (LPC) algorithm, a 2.4-kbit s⁻¹ digital vocoder, the NRL 9.6-kbit s⁻¹ multirate processor (MRP) algorithm (*NRL Review*, issued July 1980, pp. 31–34), and a clear, unprocessed voice channel. The participants used and rated each system five times, and the results were averaged. The ratings clearly differentiated among the systems, with even the two highly similar 2.4-kbit s⁻¹ LPC systems showing a small but consistent difference. The digital vocoder was rated markedly poorer than these two, the 9.6-kbit s⁻¹ MRP was rated considerably better, and the unprocessed speech, as expected, received the highest rating.

These tests indicate that the DCT has sufficient sensitivity to be used to assess the usa-

bility of voice processors. However, it is cumbersome to administer: the use of five participants requires a conferencing capability, and the stock-trading game used as the communication task requires considerable training of the test crew. To provide a more versatile test that can be readily used in a variety of contexts, we developed the Mini-CT. This test uses only two participants and an abbreviated version of the game Battleship with a smaller grid and only one ship. Those who have participated in both tests find the Mini-CT more interesting to perform, and good motivation is essential in repetitive testing.

Preliminary tests comparing the Mini-CT and the DCT suggest that the Mini-CT may also yield more stable scores and greater differentiation among systems than does the DCT. The Mini-CT has four rating scales for participants to rate the success of communication over a given link: effort required, unnaturalness, need to speak carefully, and acceptability. The DCT has a larger number of scales, including the four used on the Mini-CT. Average scores on each rating scale are computed to evaluate each processor. In addition, a proportion of the total variability in individual scores can be ascribed to each experi-

mental factor (processor differences, participant differences, experimental error, etc.). These variance proportions serve as a measure for evaluating the degree to which test score fluctuations reflect differences in processor usability as opposed to differences among participants or other factors. As can be seen from Table 1, the variability attributable to processor differences alone is greater for test scores of the Mini-CT than for those of the DCT.

A large-scale test program to further evaluate the usefulness and sensitivity of the Mini-CT and the DCT is in progress. The Free Conversation Test (FCT), which is used extensively by the British, will also be included in this program. Although the FCT provides reasonable discrimination among systems, the communication task (comparing two photographs to determine which one was taken earlier) is less suited to repeated testing and may lead to more uncontrolled variability.

The tests at NRL have confirmed that conversational tests can provide good usability information to supplement intelligibility and quality scores provided by more conventional tests, and the newly developed Mini-CT shows promise of comparing well with other tests. As a result,

Table 1. Proportion of the Total Variance in Each Test Scale Accounted for by Each Experimental Factor

Factor Test Scale	Variance Proportion	
	Mini-CT	DCT
Processors		
Effort required	0.744	0.666
Unnaturalness	0.779	0.729
Need to speak carefully	0.805	0.513
Acceptability	<u>0.725</u>	<u>0.694</u>
Average	0.763	0.651
Participants		
Effort required	0.054	0.135
Unnaturalness	0.087	0.119
Need to speak carefully	0.011	0.070
Acceptability	<u>0.066</u>	<u>0.086</u>
Average	0.055	0.103
Participant-Processor Interaction		
Effort required	0.027	0.080
Unnaturalness	0.000	0.071
Need to speak carefully	0.017	0.226
Acceptability	<u>0.003</u>	<u>0.094</u>
Average	0.012	0.118

the Mini-CT, the DCT, and the FCT (in addition to the DRT and the DAM) will be used by the DoD Digital Voice Processor Consortium in their tests of secure voice processors.

[Sponsored by ONR]

Inverse Scattering Method for Measurements of Sinusoidal Surfaces, by A.K. Jordan, *Space Systems Division*

Inverse scattering theory provides the mathematical tools with which information about unknown surfaces can be derived from data obtained by remote sensing. In contrast, *direct* scattering theory predicts the inputs to a remote sensor on the basis of geometry, incident radiation pattern, and reflecting surface. For example, the direct theory predicts sensor input when radar signals are scattered off the ocean surface. The inverse theory estimates the parameters of the ocean surface from the received radar scattering off the ocean. These theories apply to scattering of optical, acoustic, and other forms of radiation as well as that of radar. Clearly, both aspects of scattering theory are important in a variety of Navy applications.

A new computer algorithm has been developed at NRL to obtain surface parameters with use of the methods of inverse scattering theory. The algorithm employs the *regula falsi* method, which is an iterative procedure related to the well-known Newton—Raphson numerical technique, and a direct scattering theory for sinusoidal surfaces developed earlier at NRL [1]. This direct theory avoids the use of linear (slightly rough surface) approximations and has been shown to be consistent with scattering data obtained from periodic rough surfaces in laboratory experiments. The new algorithm has been

found to converge rapidly to accurate estimates for periodic rough surfaces that can be represented by the sum of a fundamental sinusoid and its harmonics.

To illustrate the algorithm, consider the sinusoidal surface shown in Figure 15, which is an idealization of a periodic rough surface. The problem in this case is to determine the surface period l and amplitude d of the sinusoidal surface from a plot of scattered energy density $S(\theta)$ as a function of observation angle θ . Figure 16 is a typical scattering pattern that results when a finite beam illuminates a surface with periodic roughness. Specular forward scatter occurs at an angle $\theta = \theta_0$ that is equal to the angle of incidence Φ_i but on the opposite side of the vertical. Additional major lobes occur at angles θ_n determined by the wavelength λ of the incident radiation and the surface roughness period l according to the grating equation

$$\sin \theta_n = \sin \theta_0 + n(\lambda/l)$$

$$(n = 0, \pm 1, \pm 2, \dots).$$

The minor peaks, or sidelobes between the major peaks in Figure 16 result from the finite beam size of the incident radiation. With λ known, the roughness period l is readily obtainable from the scattering pattern by use of the grating equation. The roughness amplitude d , however, is not so easily obtained, and therein lies the contribution of the new algorithm. In general, the problem is to find the value of Δ , called Δ^* , that minimizes (in some sense) the quantities f_n given by the nonlinear functional

$$f_n(\Delta) = \sqrt{S(\theta_n)} - \Gamma_n(\Delta)$$

$$(n = 0, \pm 1, \pm 2, \dots),$$

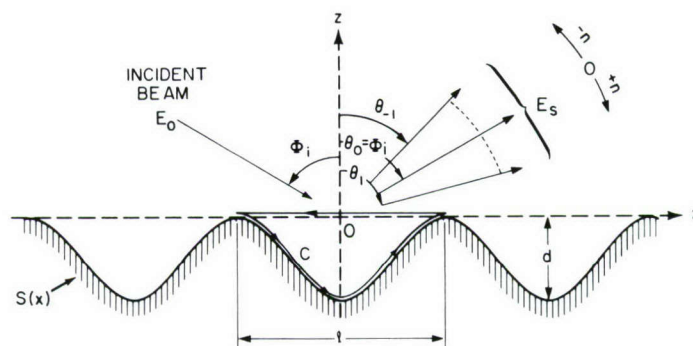


Figure 15. Electromagnetic wave scattering by a sinusoidal surface:
 E_0 = incident wave; E_s = scattered waves.

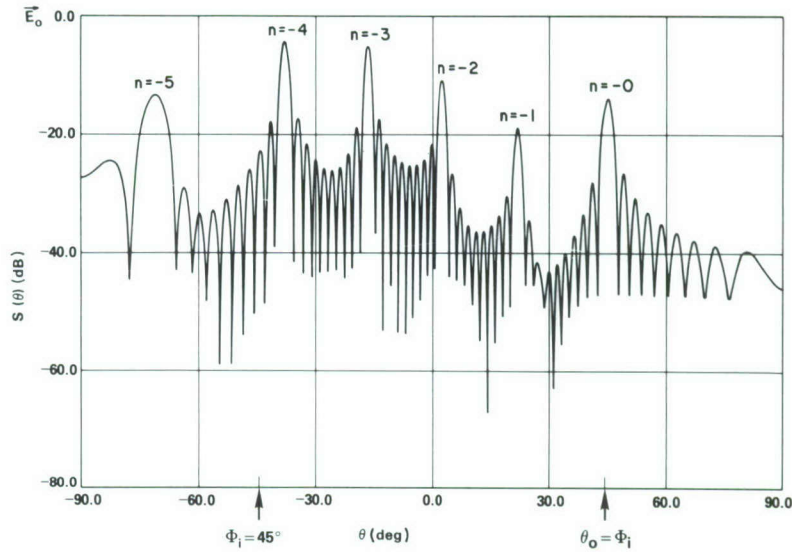


Figure 16. Scattering pattern from a sinusoidal surface for beam incidence angle $\Phi_i = 45^\circ$. The specular peak ($n = 0$) occurs at $\theta_o = \Phi_i = 45^\circ$.

where $\Delta = \pi d/\lambda$ is the normalized roughness amplitude, $S(\theta_n)$ is the scattering pattern measured at the main peaks θ_n , and $\Gamma_n(\Delta)$ is the nonlinear functional dependence of $S(\theta_n)$ on Δ .

The problem is complicated by the fact that in general there are multiple roots of each f_n . The Γ_n for $n = -1$ and $n = -2$ in this example (obtained from application of the algorithm) are plotted in Figure 17. Note that, in this example, there are two values of Δ that make $f_{-2} = 0$ and also two values that make $f_{-1} = 0$. However, only one value, Δ^* , makes both $f_{-1} = 0$ and $f_{-2} = 0$. In general, there will be multiple solutions to $f_n = 0$ for each n , but only one value $\Delta = \Delta^*$ for which $f_n = 0$ for all n . An efficient search for multiple roots requires a systematic

means for setting the limits of the search. Use of the maxima and minima of the Bessel function $J_n(\Delta)$ has been found convenient for this application, since no more than one root of f_n can occur between a maximum and minimum of $J_n(\Delta)$.

After the value of l has been determined from the grating equation, the algorithm proceeds as follows. A particular peak, $n = -2$ in this example, is chosen for primary attention. By using $\Delta = 0$ for one initial starting point required in the *regula falsi* method, and the first maximum of $J_{-2}(\Delta)$ for the other initial point, one is assured that Δ' , the first zero found, will be the smallest value of Δ for which $f_{-2} = 0$. Having found Δ' , the next step is to determine whether $f_n(\Delta') \approx 0$ for all n . If so, Δ' is Δ^* . Otherwise,

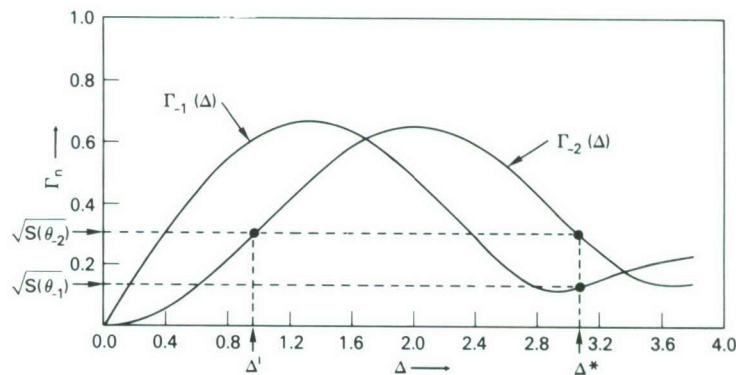


Figure 17. Nonlinear dependence of normalized scattered energy density Γ_n vs normalized surface roughness Δ , for $n = -1, -2$.

successively larger zeros of f_{-2} are located and examined until Δ^* is found. In this example, Δ^* is the second root of f_{-2} .

The algorithm has been found to converge rapidly for sinusoidal surfaces. Work is in progress to extend the theory to three-dimensional targets (volume scattering), to composite surfaces (roughness represented by the sum of sinusoids), and to lossy surfaces. This research has been

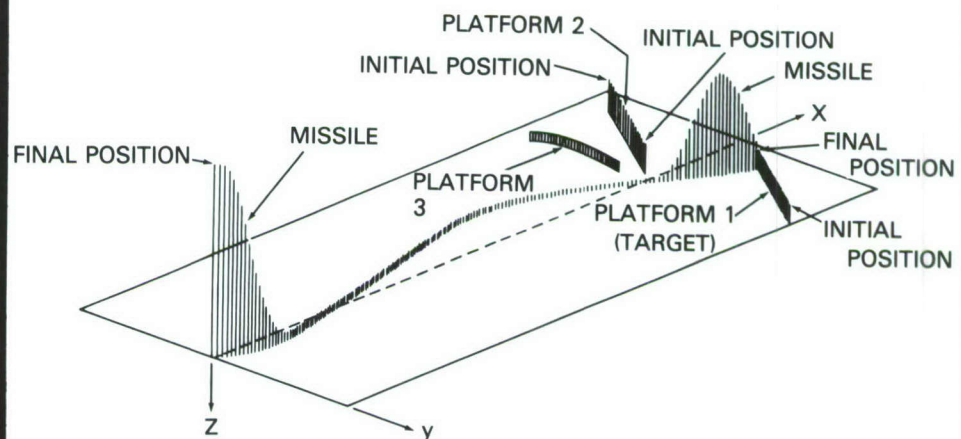
performed with the assistance of Prof. R. H. Lang, George Washington University.

[Sponsored by ONR]

Reference

1. A.K. Jordan and R.H. Lang, "Electromagnetic Scattering Patterns from Sinusoid Surfaces," *Radio Sci.* **14**, 1077–1088 (1979).

DETECTION AND DEFENSE



DETECTION AND DEFENSE

The importance of a fleet's capability to detect, identify, and counter potential threats can hardly be overstressed. At stake are operating effectiveness, mission accomplishment, and even survival. Since its beginning more than 50 years ago, NRL has made many important contributions to these capabilities, and that productive tradition continued in 1980.

A Microcomputer Aided Tracking System	41
Scenario Generator for Radar Environment Simulations	43
RF Environment Simulation via Matrix Array	45
Real-time Image Analysis Architecture	47
Granular, Niobium Nitride Weak Link SQUIDs	49

A Microcomputer Aided Tracking System, by D.C. Cross, A.B. Mays, and P.M. Thiebaud, *Radar Division*

Manning a radar scope at sea is very demanding. Operators often stand long watches (2 to 4 h) during which there may be little activity. Studies have shown that they cannot maintain a high degree of alertness for such extended time periods and that good performance is achieved for intervals of only 20 to 30 min. Therefore, detection of radar targets that may represent serious threats to the ship or task force can be missed or dangerously delayed simply because the operator is tired or inattentive. The job also requires that operators, after a long period of low activity, be able to change quickly to a high level of activity in which they must rapidly detect new targets while maintaining several tracks on previously detected targets. Good operators can track only four or five targets before they become overloaded. The tracking function is time-consuming and therefore interferes substantially with the detection function. Thus a busy operator may miss targets just because there is no time to notice them. An obvious approach to mitigate these difficulties is to automate some of the detection and tracking functions.

As a result of these considerations, NRL has developed a Microcomputer Aided Tracking (MCAT) system. This system employs several microprocessors and a microcomputer-driven plan-position indicator (PPI), with graphics capa-

bility, to provide automatic tracking of up to 32 targets. The tracks are initiated by the operator and are then maintained by the display processors. When operators detect a target, they roll a marker to its position on the PPI with a ball control. They then push a track-initiate button and the display processor tracks the target automatically. The operators are then free to look for new targets. Figure 1 shows the feasibility demonstration model of MCAT designed and built at NRL. The current version has been tested successfully with use of recorded data from a radar located at NRL's Chesapeake Bay Detachment.

The system presents the operator with a normal radar PPI display. The same signal seen on the PPI is also processed by the MCAT system when the operator requests that a specific target be placed in automatic track. The signal is processed using standard automatic detection and tracking (ADT) signal processing. The MCAT differs from fully automated systems in that the operator performs the initial detection function. The hardware is required only to detect targets that are "known" to exist. This additional information, normally not available in ADT systems, simplifies the logic needed to establish a track. The target is known to exist in a relatively small range and azimuth sector; therefore, only the detections occurring in that region need be considered as candidates for the target of interest. Because of this fact, MCAT requires only a small amount of memory and computing capacity compared to fully automated systems.

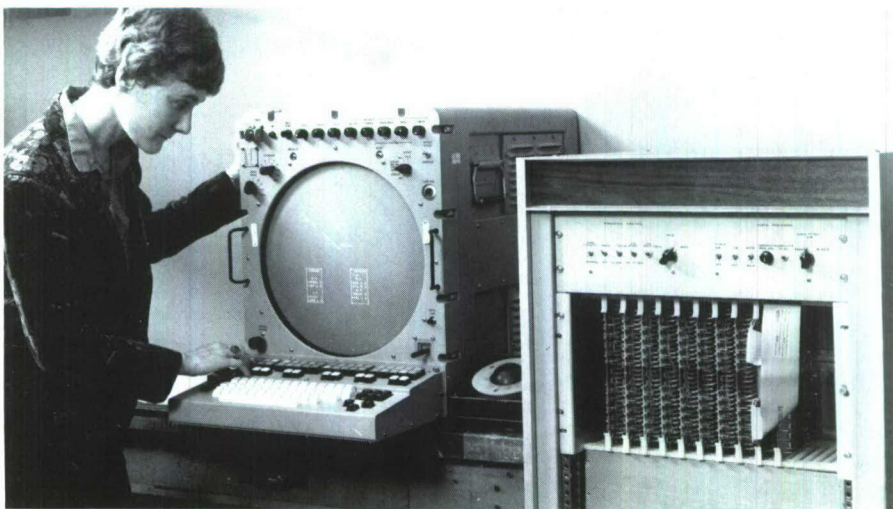


Figure 1. Ms. A. B. Mays operating the AN/UYQ-23 scope used in the feasibility demonstration model of MCAT. The equipment rack on the right contains video signal processors for detection and track association.

New detection data in the region of each tracked target are collected in small random access memories (RAMs) individually dedicated to each target track. Low-cost 8-bit microprocessors then scan each memory, sorting and testing the detections to determine which is most likely to be the target selected initially by the operator. The range and azimuth of each new detection, together with an estimate of the quality of the data, are then transmitted to the main-display processor. This processor is the heart of the MCAT system. It performs the needed track updates and smoothing, resolves any track anomalies or conflicts, and simply extrapolates tracks when these conflicts cannot be resolved or

when the target fades. Using standard Navy Tactical Data System (NTDS) symbols, the processor continuously plots each target's position in real time and notifies the operator by flashing symbols when targets can no longer be tracked automatically.

Additional aids are also available, such as operator-composed labels that move with the target symbols, and a visual display of target history and velocity for any number of operator-selected tracks. Figure 2 is an example of the MCAT display, showing its graphics capability.

In addition to the potential for increased operator effectiveness, MCAT shows promise as a key element in an improved command-and-

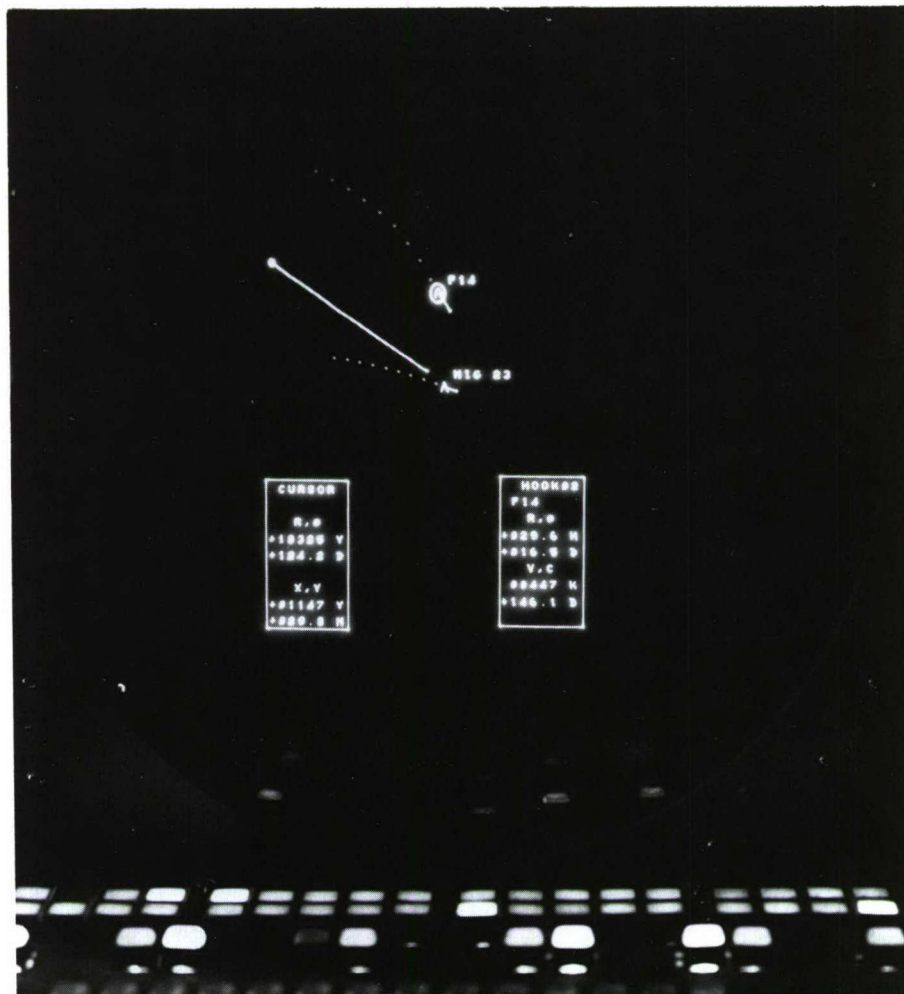


Figure 2. A typical MCAT PPI presentation showing two simulated target tracks. The targets' positions are marked with standard NTDS symbols and operator-generated labels. The target labeled *F-14* is "hooked." Current estimates of the range, bearing, course, and speed of that target are shown in the box labeled *hooked*. The dots trailing behind the target symbols are track histories, and the small vectors emanating from the center of the target symbol are graphic indications of target speed. The vector pointing toward the *MIG 23* is a cursor. The length, direction, and origin of the cursor are shown in the "cursor" box.

control system for non-NTDS ships. The graphics capability provides a powerful situation display directly on the radar indicator. With built-in computers, interfaces can easily be implemented to provide a flexible weapon-designation capability. Further, the computers can be used to solve many of the routine Combat Information Center problems, such as the maneuvering-board calculations needed to determine courses for ship movements in formation or calculations of intercept vectors for friendly aircraft. NRL is currently investigating the feasibility of these concepts and, together with the Naval Sea Systems Command, is working to develop a specification for a new radar display that will have the capability of implementing an MCAT system. At the same time, work is in progress for testing the feasibility of employing MCAT techniques with the standard-product-line Navy indicators.

[Sponsored by NAVSEASYS COM]

Scenario Generator for Radar Environment Simulations, by B. McGhee and W. Morris, *Tactical Electronic Warfare Division*

A major use of the NRL Central Target Simulator (CTS) is to test and evaluate the effectiveness of electronic warfare systems and

techniques to counter the tactical missile threat to the Navy. In the simulator, the actual hardware to be tested is subjected to a controlled radio-frequency (RF) environment capable of simulating tactical air and sea engagements in real time. The scenario generator software allows the CTS user to specify the RF environment as a function of space and time by defining position, motion, and the radar cross section (RCS) of multiple platforms and chaff, and by specifying electronic countermeasures (ECM) techniques and their activation.

The major elements of the CTS are diagrammed in Figure 3. The antenna array and its control hardware are described in the following article. Three Digital Equipment Corporation PDP-11/55 computers and their linkage through a shared memory constitute the CTS data processing network (DPN). Software of the DPN processors provides the user with a flexible tool for specifying elements of the RF scenario, missile control parameters, and target signature components. In addition, the software updates the scenario in real time, driving the three-axis gimbaled flight table and commanding the ECM signals and computed target returns to the antenna array.

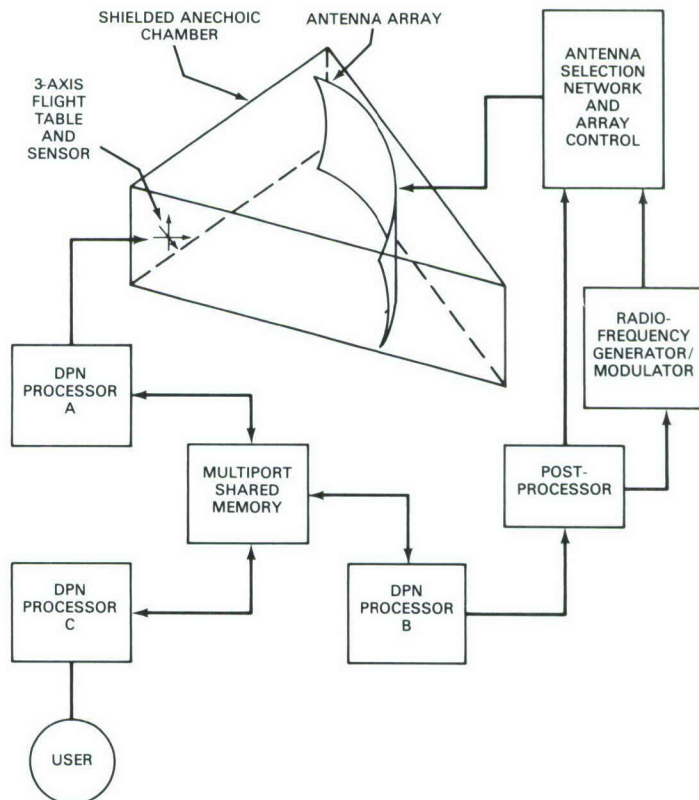


Figure 3. Central Target Simulator

The scenario generator software includes models to handle platforms, chaff, and ECM techniques. The platform model enables definition of each platform's initial position and velocity in a fixed coordinate system, as well as the allocation of CTS resources according to the platform's priority and a linkage to its associated RCS. The platform RCS may be specified as a function of aspect angle by either of two sub-models, both of which include elevation effect and scintillation and glint parameters. The chaff model provides for the specification of the orientation, burst geometry, and firing timing and sequencing of up to eight launching systems. In addition, the chaff RCS is modeled as a function of time and provides for the specification of scintillation and glint parameters. During a simulation run, the components specified by the scenario model are activated by scenario events. These event capabilities include changing a platform's speed, heading, and position; performance of selected maneuvers; and single or sequential chaff release.

The scenario generator's ECM model enables the investigator to select and combine FM and AM waveforms to be radiated by antennas at the simulated platform's position. Up to five ECM techniques may be specified for activation during each simulation run by defining a set of parameters, host platforms, and activation times or ranges for each technique. The parameters needed to specify a technique include center frequency, FM noise bandwidth, sawtooth RF deviation and sweep rate, AM noise amplitude and bandwidth, asymmetry pulse period, pulse width, AM attenuation, and range-gate pull-off parameters. These parameters are used to control

the radio-frequency generator/modulator subsystem as each specified ECM technique is activated and deactivated according to the scenario.

It is necessary to perturb the computed ideal signals representing radar returns in order to simulate real-world radar phenomena realistically. The major contributors to signal degradation are target RCS amplitude scintillation and target angular glint. In the DPN processors, the perturbations are simulated by first generating a normal random process with a realistic temporal correlation. This process is then transformed into a more specific stochastic process that models the perturbation. For azimuth or elevation glint, the angular extent of the platform in the appropriate coordinate is used to transform the normal random process. RCS amplitude scintillation observed and reported for most classes of aircraft and ships falls into either Rayleigh power, chi-squared four-degree-of-freedom, Rice power, or log-normal distributions. Four parameters supplied by the RCS model control the transformation into the appropriate distribution.

With the capabilities of the scenario generator and the CTS facility, the investigator can specify a realistic engagement. An example of such an engagement is a specific enemy missile attacking a formation of Navy ships. In the CTS, the missile seeker is mounted on the flight table and is subjected to realistic pitch and yaw accelerations as the relative geometry between the seeker and the individual ships is accurately simulated. Those ships with simulated ECM systems are programmed to detect the threat and respond with chosen ECM techniques, chaff rounds, and combinations thereof. The response of the seeker to this complex environment deter-

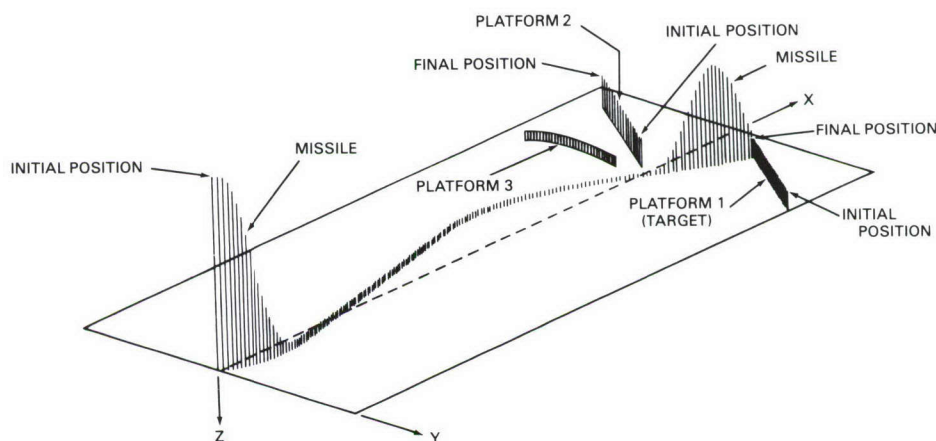


Figure 4. Sample trajectories, illustrating a simulated successful missile attack

mines whether the missile hits its intended target, as depicted in Figure 4, or falls harmlessly into the sea. Simulations such as this in a controlled laboratory environment can help to optimize systems' effectiveness and to minimize critical at-sea testing time and cost.

[Sponsored by ONR]

RF Environment Simulation via Matrix Array,
by B.W. Edwards, *Tactical Electronic Warfare Division*

The Naval Research Laboratory has developed a state-of-the-art Electronic Warfare (EW) simulation facility, referred to as the Central Target Simulator (CTS), to enable the testing and evaluation of EW systems and techniques for countering the missile threat to the Navy. The CTS is a laboratory facility that includes a centrally located modern computer complex and a radio-frequency (RF) physical effects simulator. The CTS uses actual system hardware (e.g., missile seekers, countermeasures equipments) and mathematically derived computer models to perform a realistic simulation of the various elements of naval tactical engagements.

A major subsystem of this new facility, called the RF Programmable Array (PA), utilizes a large microwave antenna array and a computer-controlled RF-distribution network to provide the rapid and accurate positioning of signals needed

to represent complex RF environments. The array itself is mounted on a spherical surface at one end of a large shielded anechoic chamber and is focused to a point 23 m distant at the other end of the chamber, where the RF sensor system (e.g., missile seeker) is mounted on a three-axis flight table. The PA provides both electronic movement to simulate target angular motion and trajectory and amplitude change to simulate variations in engagement geometry and target characteristics in a continuous manner and in real time.

As shown in Figure 5, the PA consists of three major parts: array feeds, antenna selection networks, and antenna assemblies. The array feed (AF) accepts RF signals from an RF generator/modulator and adjusts their amplitude according to the scenario geometry. The AF then divides the RF inputs into four RF steering lines, each of which is connected through an antenna selector (i.e., RF switching tree) to an antenna assembly to form a four-element "quad" array. As shown in the figure, each steering line has provisions for independently adjusting its relative amplitude and phase, thereby varying the RF signal fed to the associated quad antenna. The PA is configured with 2 array feeds, 8 antenna selectors, and 128 antenna assemblies. The major performance characteristics for the PA are given in Table 1. Figure 6 shows a view of the PA hardware from behind the antenna array, and Figure 7 from the chamber focus.

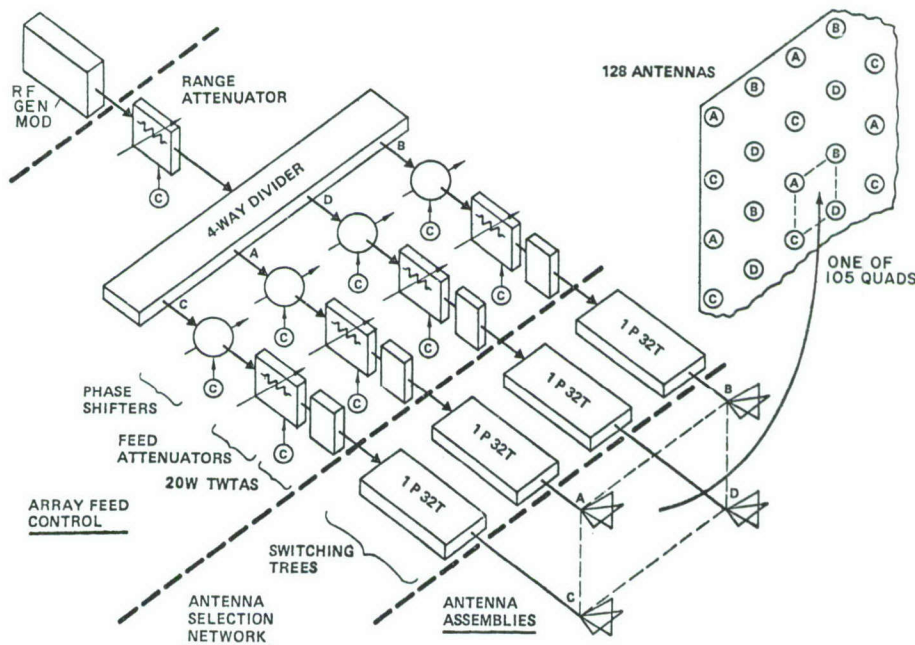


Figure 5. RF programmable array

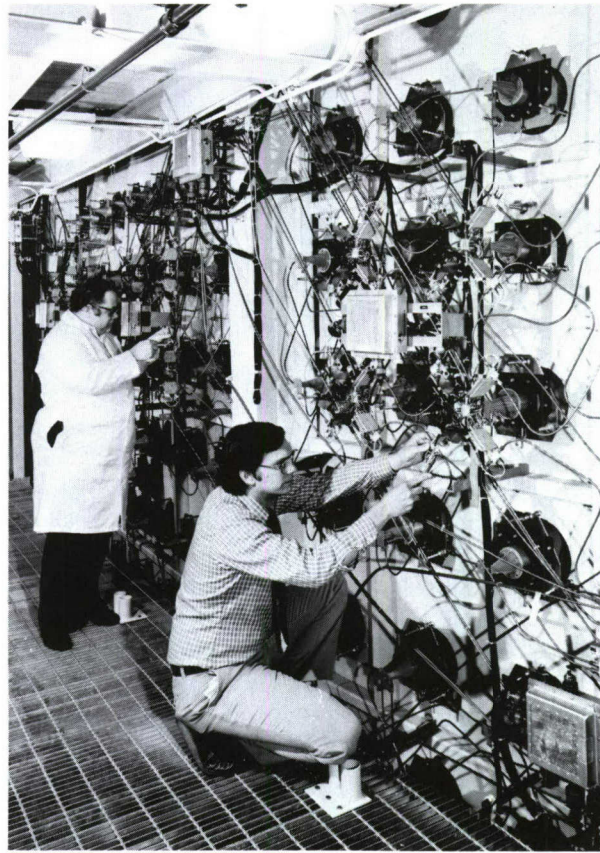


Figure 6. Charles Schoppet and Robert Surratt making adjustments to the programmable array

Table 1. Key Characteristics

Frequency coverage	8 to 18 GHz
Field-of-view	20° azimuth × 10° elevation
Array size	128 elements
Position accuracy	1 mrad
Effective radiated power	+30-dBm array +75-dBm high-power branch
Calibration	Via table look-up every 100 MHz
Polarizations	Horizontal and vertical
Number of targets	14 (7 per feed)
Timing (command to steady state)	2.0 μ s

Platform motion across the face of the array is an important feature. The PA utilizes a four-element, amplitude-only balance point technique for simulating target or source motion across the face of the array. The basic unit is an antenna quad consisting of four adjacent antennas (located at the corners of a square) whose relative phases are equalized and whose relative amplitudes are varied to provide an apparent source of radiation at any position within the physical limits defined

by the quad. The equations that govern this motion are similar in formulation to those developed for tracking radars. Coarse positioning is achieved by selecting the appropriate quad from the array of antennas. Attenuators and phase shifters are then employed to achieve the phase and amplitude control necessary to simulate target motion.

The balance point technique requires a system that is substantially free of phase and amplitude mistrack. Thus, to be effective, the system must be precalibrated. For the PA, this precalibration takes the form of stored tables containing the proper digital control words for correcting the PA system phase and amplitude commands.

The PA also has several special features that include a high-power branch, several auxiliary channels, and a receive mode capability. The high-power branch provides a higher effective radiated power than the normal array outputs, permitting the simulation of very small missile-to-target ranges (e.g., <0.25 nmi for an aircraft

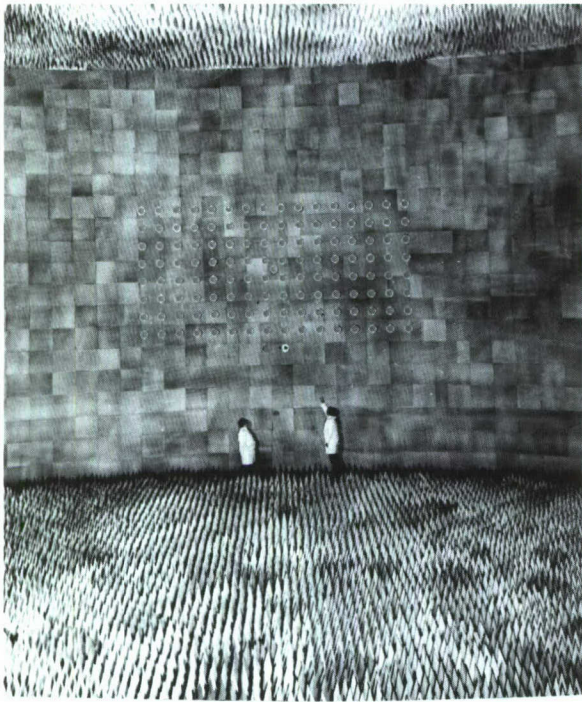


Figure 7. Charles Schoppet and George Farmer with the CTS RF programmable array as viewed from chamber focus

carrier). The auxiliary channels permit the simulation of a dense signal background by allowing noncritical emitters to bypass the quad and be connected to individual array antennas. The receive mode permits the PA to perform real-time seeker antenna pattern measurements as part of the simulation run. These features serve to enhance the PA's performance and overall utility.

The performance goals set for the PA have all been achieved, and the CTS facility is now operational. Future PA developments will include an increase in azimuth coverage to 80° (i.e., 224 elements) in 1981, with additional feed networks and augmented polarization capability planned for later years.

[Sponsored by ONR]

Real-time Image Analysis Architecture, by R.H. Evans, T.R. Husson, and E.F. Williams, *Tactical Electronic Warfare Division*

Countermeasures designed to keep a guidance system from tracking a target are an integral part of modern defense systems. Typically, such countermeasures include spoofing maneuvers and false targets generated either by the target or by potential alternate targets. To evaluate the effectiveness of various countermeasure systems

and techniques, NRL has developed a programmable guidance-system simulator. It is designed to implement many types of guidance logic and thus to provide a versatile threat simulator as well as a good baseline reference for the study and analysis of countermeasures effectiveness.

The simulator is an imaging type of guidance system, i.e., one in which data from sensors appear on a video screen as a two-dimensional image. In the NRL simulator, the sensor is an electronic camera mounted on a servo-controlled mechanical gimbal. A key element in the simulator is the image processing logic, which operates on the image data to provide steering commands to the gimbal in real time. Programmable logic is required so that the simulator can represent several types of guidance systems and incorporate future intelligence updates. An architecture consisting of an array of microprocessors was designed for use as the logic control function, thereby providing both substantial computing power and programmability. The individual processors were designed, fabricated, and tested at NRL using standard commercial integrated circuits (Figure 8). These processors were assembled into a parallel-pipeline array. This system constitutes a significant advance in guidance system simulation in that it is programmable and can provide a wide variety of search, acquisition, and tracking algorithms.

The basic operation of the system is shown in Figure 9. The first operation performed in the image analysis is conversion of the analog image from the camera into an array of digital values. Successive images are averaged (added) in the first pipeline stage to improve the quality of the digitized image. Two parallel arrays of six microprocessors each are used in the next two pipeline stages. These parallel processors search the data from the digitization stage for potential targets. A potential target is identified as a connected cluster of points whose intensity is greater than both the global and local backgrounds. The potential targets are passed to the next two pipeline stages, where target selection and track/no-track decisions are made and status commands are transmitted to the final two stages of the pipeline. These last two stages control the steering of the gimbal to keep the target within the camera's field of view, and they also interface with the system video displays.

Real-time operation is required of the digital logic to hold the camera on the target. Each new image array of 128×192 8-bit words is processed by a parallel pipeline array of 16 microprocessors

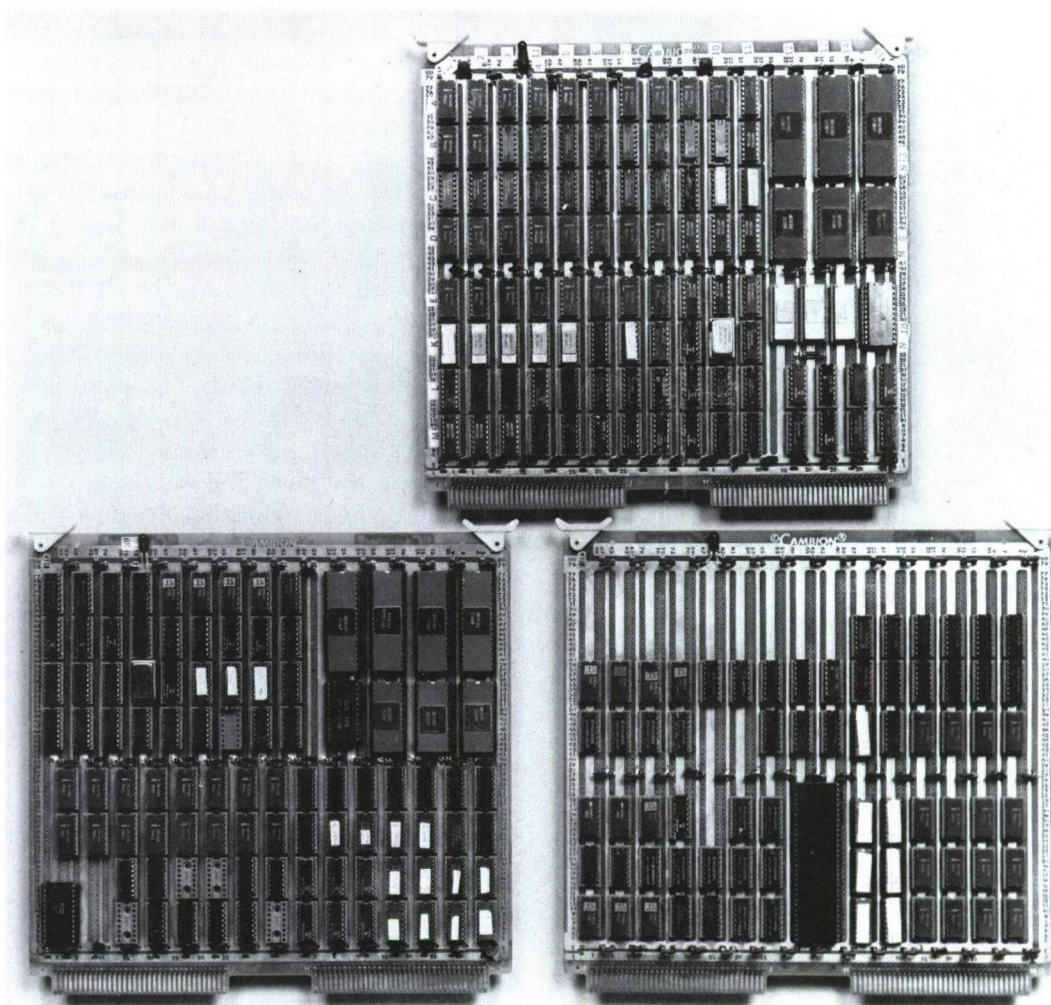


Figure 8. Image analysis processors designed and built at NRL. The top processor is 12-bit, the two bottom ones are 16-bit.

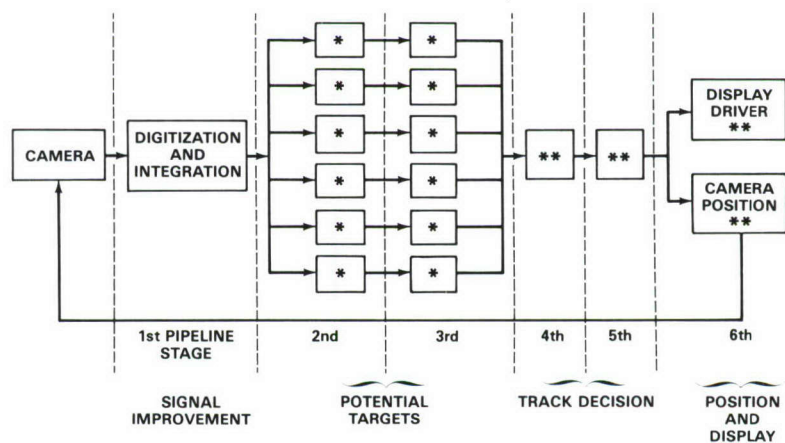


Figure 9. Pipeline array of microprocessors for real-time analysis of image data. The single and double asterisks denote 12-bit and 16-bit microprocessors, respectively.

to keep up with the data rate. The total image processing algorithm is separated into small sub-tasks assigned to various stages of the pipeline. Each pipeline stage receives data from the previous stage, performs its assigned calculations, and passes the results on to the next stage. For operation in real time, some pipeline stages (potential target calculation) require a parallel array of processors. Each processor in the second and third stages operates on its own subarray of one-sixth of the camera screen. This parallel pipeline architecture offers a processing speed at least an order of magnitude faster than a single computer.

However, efficient operation of the image analysis system required even more speed than was available in commercially available software-programmable processors. Consequently, individualized processors were designed and built at NRL from standard integrated circuits. The processor instructions for the image analysis processing were defined, and the processors were custom built around them. This tailor-made approach produced substantial improvements over general purpose processors. In its present configuration, the system updates its steering commands in a 33-ms cycle.

Many tests have been conducted with this system, both in the laboratory and in the field. Static tests were made against passive targets to develop the tracking algorithms and to validate the operation of the equipment. With the system installed in an NRL P-3 Orion research aircraft, measurements have been made with dynamic targets performing evasive maneuvers. Analyses of countermeasure effectiveness, made using this simulator, have led to the development of superior countermeasures techniques.

With the flexibility inherent in this research tool, new processing algorithms representing a wider variety of guidance systems will be developed in the future. Evaluation of countermeasures techniques against many classes of seekers may be simulated with the expanded algorithm sets, thereby permitting a more thorough test and evaluation of existing and new countermeasures techniques.

[Sponsored by NAVELEXSYSCOM]

Granular, Niobium Nitride Weak Link SQUIDS, by E.J. Cukauskas, J.H. Claassen, and M. Nisenoff, *Electronics Technology Division*

Until recently, most refractory RF SQUIDS (superconducting quantum interference devices)

were fabricated from bulk niobium (Nb). They incorporated an adjustable point contact as the Josephson junction. The point-contact SQUID possessed good noise properties when properly adjusted but was mechanically unstable and therefore of limited usefulness. However, with state-of-the-art microfabrication techniques, we have undertaken the development of an all-refractory, thin-film, radio-frequency (RF) SQUID with stability as well as good noise properties. These SQUIDS are fabricated from thin-film niobium nitride (NbN) and incorporate a granular weak link as the Josephson junction element.

We have studied the noise characteristics of these devices at frequencies of 23 MHz and 10 GHz, and several have operated at temperatures as high as 14 K [1]. Unlike thin-film SQUIDS with metallic weak links, these devices typically have low noise and operate over a wide temperature range. The magnetic flux noise inferred from our measurements was found to be intrinsic and in agreement with theoretical predictions. The best energy sensitivity we have measured at 10 GHz for one device yielded a value of $1 \times 10^{-30} \text{ J Hz}^{-1}$ and is believed to be limited by the preamplifier noise. Improvements in preamplifier design using cooled GaAs field effect transistors (FET) promise increased sensitivity by at least two orders of magnitude.

Conceptually, an RF SQUID consists of a superconducting, cylindrical, thin-film ring that is interrupted by a Josephson junction and is inductively coupled to an RF tank circuit or microwave cavity. The Josephson effect, together with the fluxoid quantization, relates the superconducting current circulating around the ring to the magnetic flux threading the ring. This results in a modulation of the circuit impedance by the magnetic flux with a period of ϕ_0 , where ϕ_0 is the magnetic flux quantum. These changes in impedance are typically measured at 20 MHz by coupling the SQUID to a resonant tank circuit and measuring the changes in the induced voltage as a function of magnetic flux. The SQUIDS being studied at NRL are fabricated from high T_c ($\sim 16 \text{ K}$) refractory superconducting films of NbN and incorporate a granular weak link as the Josephson element. Figure 10 illustrates the device geometry and dimensions. The cylindrical film is slotted to leave a central bridge 50 by 600 μm as shown. A segment of this bridge, $\sim 1 \mu\text{m}$ long, is thinned by anodization and becomes granular or inhomogeneous, because the anodization process progresses along the grain boundaries

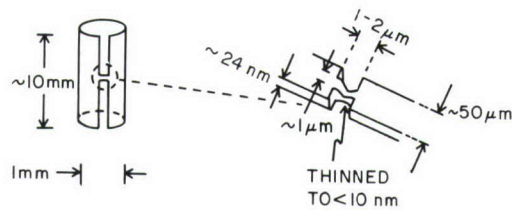


Figure 10. The geometry used in fabricating a thin-film NbN SQUID. The granular weak link is thinned to 10 nm or less by the anodization process.

of the film and leaves the grains electrically isolated by the oxides of niobium. After the thinning process was completed, this region was narrowed in some SQUIDs by using photolithographic masking and ion milling. Weak-link SQUIDs fabricated in this manner have shown nearly ideal Josephson properties when operated at 23 MHz and 10 GHz.

The critical current density (i_c , above which the weak link becomes nonsuperconducting) can be controlled by the degree of anodization of the granular region. If the film is thinned to $\sim 10 \mu\text{m}$, the grains are electrically isolated by the thin oxides of Nb and are strongly coupled by Josephson tunnel currents with $i_c \sim 10^6 \text{ A cm}^{-2}$. Further thinning weakens the coupling and reduces i_c by at least two orders of magnitude. SQUIDs fabricated with critical current densities of 10^4 A cm^{-2} or less typically operate over a very wide temperature range and have intrinsic noise that is limited by the external measurement electronics.

Figure 11 illustrates a series of 20-MHz RF current-voltage characteristics of a granular, weak-link SQUID with a $T_c \sim 8 \text{ K}$ and a maximum i_c of $\sim 10^4 \text{ A cm}^{-2}$. Each trace is the voltage response of the SQUID coupled to the resonant tank circuit as a function of the RF drive current to the tank circuit for a particular applied magnetic flux. Two traces were taken for each temperature, one with applied magnetic flux of $n\phi_0$ and the other with $(n + 1/2)\phi_0$, and were then superimposed (ϕ_0 is the magnetic flux quantum $2.07 \times 10^{-15} \text{ Wb}$). At a particular drive current, the voltage across the tank circuit is a periodic function of the applied magnetic flux, with a period of ϕ_0 . The loop pattern formed by the superimposition of the two traces gives the modulation envelope of the SQUID. The noise characteristics of the device can be inferred by measuring the step rise parameter α , the ratio of

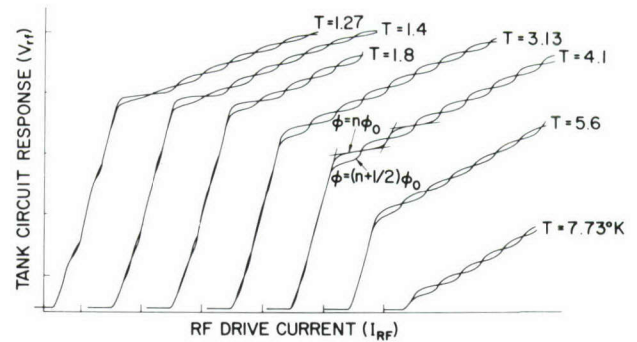


Figure 11. The RF current-voltage (arbitrary units) characteristics of a granular weak-link SQUID taken at various temperatures (T) for two values of applied magnetic flux. The first step (at the top of the riser) is at maximum for a flux of $n\phi_0$ and at minimum for a flux of $(n + 1/2)\phi_0$. The two traces produce the loop pattern when superimposed. Tangents drawn to the 4.1-K trace indicate the steplike structure.

the voltage rise along the first step to the voltage difference between the first two steps. The tangents drawn to the $n\phi_0$ trace for a temperature of 4.1 K illustrate the steplike structure from which α is measured.

The tilting of the steps is due to thermal fluctuations within the weak link. The parameter α has been shown to be independent of the tank circuit and preamplifier noise. The device has $\alpha = 0.18$ at 4.1 K and 23 MHz, which corresponds to a noise sensitivity of $4 \times 10^{-30} \text{ J Hz}^{-1}$. The noise inferred from these measurements is in agreement with the theoretical predictions of Kurkijarvi [2]. In practice, this noise sensitivity is not achieved due to additional noise associated with the room-temperature preamplifier.

Further development of the granular NbN weak-link RF SQUIDs will be focused on lower critical current densities and a wider operating range for the higher- T_c devices. A cooled low-noise preamplifier is being designed and constructed that will allow the direct examination and analysis of the noise spectrum of these devices. SQUIDs using a high- T_c material such as NbCN and Nb₃Sn will be investigated in the future. With the use of these high- T_c materials, it may be practical to use a closed-cycle refrigeration system to provide the necessary cooling. These systems become reasonably efficient at temperatures above 10 K, and we are preparing to operate some of these SQUIDs in such a system.

Superconducting magnetometers or SQUIDs are potentially the most sensitive detectors of

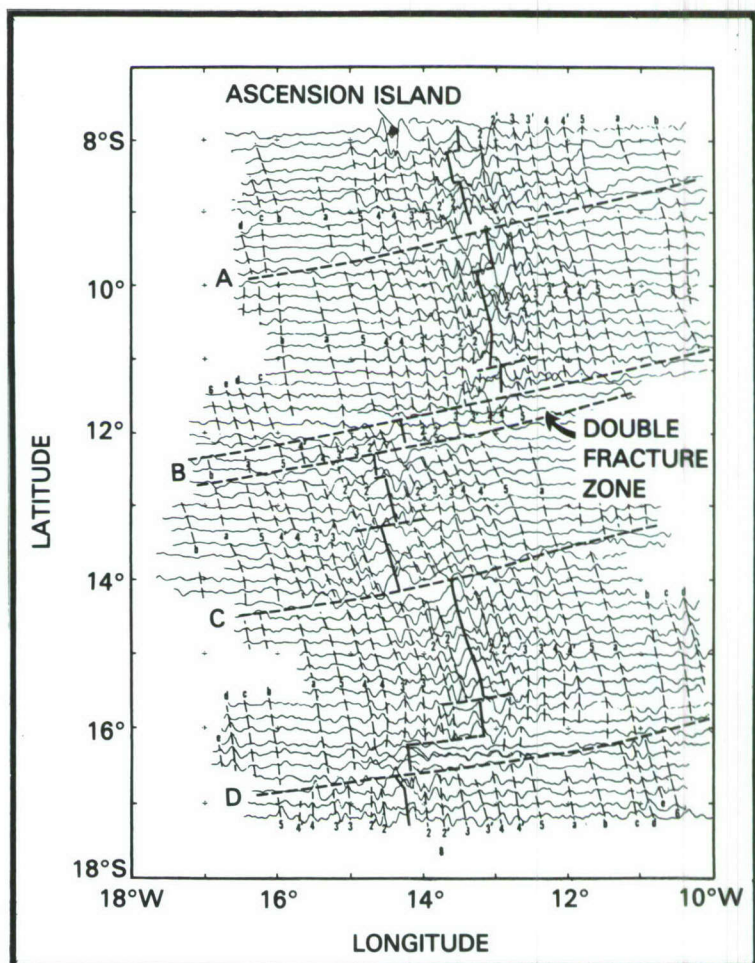
magnetic fields and magnetic field gradients. The further development of these devices, improvements in preamplifier noise, and higher operating frequencies should result in SQUIDs with energy sensitivities approaching the quantum limit, $\sim \hbar$. These devices have potential naval applications in systems for submarine antenna receivers and for magnetic anomaly detection.

[Sponsored by NAVELEXSYSCOM and ONR]

References

1. E.J. Cukauskas and M. Nisenoff, *J. Appl. Phys.* **52**, 1555 (Mar. 1981).
2. J. Kurkijarvi, *J. Appl. Phys.* **44**, 3729 (1973).

MARINE GEOSCIENCE



MARINE GEOSCIENCE

The properties and behavior of the marine environment rank high among the many complex and interrelated factors that affect mission success at sea. NRL scientists are working in many areas to measure and understand these properties and to provide the knowledge and means to predict, mitigate, or exploit them in order to improve the Navy's ability to function effectively in, on, and over the world's oceans.

Lagrangian Oceanographic Measurements	55
Mapping Ocean Currents with Over-the-horizon Radar	57
Modeling of Isothermal, Upper-ocean Water Masses	61
Coherent Radar Observations of Breaking Shoaling Waves	63
Crustal Geophysics Studies in the South Atlantic Ocean	65
Portable Systems for Oceanographic Data Acquisition	67
Automated Aerosol Sampling System	68
Bioluminescence in the World's Oceans	70

Lagrangian Oceanographic Measurements, by C.M. Gordon and D. Greenewalt, *Environmental Sciences Division*

The persistence of submarine-generated, hydrodynamic signals as recognizable patterns in the open sea is an important factor in assessing potential ASW systems. Of the oceanographic variables contributing to the dispersal of such patterns, vertical and horizontal current shear are among the most significant. Measurement of current shear in the upper ocean using moored current meters (Eulerian methods) is both difficult and expensive. However, since the first use of drift bottles, Lagrangian methods (following the fluid motion) have provided valuable information on ocean current trajectories and the evolution of differential motions in the sea. In

the past, a major limitation of the Lagrangian method has been uncertainty in the location of drifters or drogues with the available navigational instrumentation. The introduction of the NAVSTAR continuous satellite navigation coverage, scheduled for the 1980s, and recent developments in satellite-tracked drogue techniques should greatly improve positioning accuracy in future measurements. We have initiated a program of Lagrangian oceanographic measurements to collect data on upper-ocean shear and kinematic properties on the scale of 1 to 40 km.

In our deep-ocean experiment, a group of 10 drogues was deployed over several miles horizontally at a site near Bermuda (Figure 1). Six drogues were placed in the ocean mixed layer at a depth of 5 m, and four were below the layer at 45

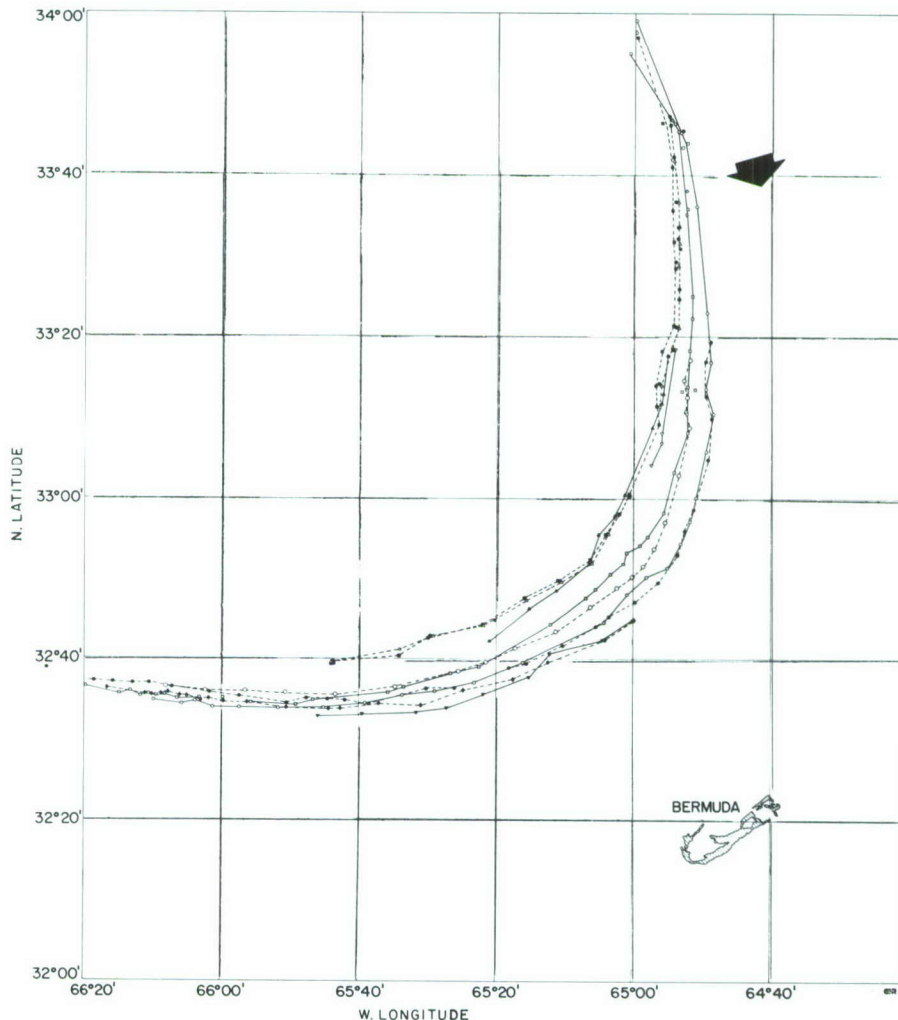


Figure 1. Drogue sightings during a Lagrangian current-following experiment, September 17–23, 1979, showing trajectories of drogues in the mixed layer (at 5 m depth, dashed lines) and below the layer (at 50 m, solid lines). The drogues were deployed at 34°N, 65°W, and the general trajectory direction is indicated by the large arrow.

or 60 m depth. The drogues were followed for about 220 km over six days, and positions of the drifters were recorded at intervals of about 4.5 h using the LORAN-C navigation system (± 350 m). Hourly positions of the drogues were derived by interpolation, using several computer fitting procedures.

The initial data treatment was based on the simplest possible assumption, namely: if two drogues are deployed at different depths, their rate of separation is a measure of the difference in current velocity at the two depths, that is, of the vertical current shear. This assumption is reasonably good for short-term measurements when the drogues are close to each other horizontally. However, for longer time-series measurements of shear in which the drogues at different depths may be separated by kilometers, the validity of this assumption has not been tested.

Figure 2 shows the measured separations of selected drogue pairs (one shallow, one deep) as a function of time. Assuming that no other forces contribute to the separation of a given drogue pair, the slopes of the curves at a given time, divided by the vertical separation of the drogues, are a measure of the vertical shear.

It is clear from Figure 2 that the measured separation rates of the shallow and deep pairs are highly variable. Some pairs drift apart at a relatively constant rate for 40 to 100 h, others actually move closer during equivalent time intervals, and some show separation rates that change con-

siderably with time. The average vertical current shear calculated from the data is $1.3 \pm 0.6 \times 10^{-3} \text{ s}^{-1}$, but the variability leads to a probable error of approximately 50% in this value.

The source of much of this variability was found to be horizontal shearing deformation. This horizontal shear apparently originates from the turning of the current as seen in Figure 1. Since the turning water mass has a finite "radial" extent, one would expect a systematic, tangential shear as the outer edges of the mass are approached. Because the tangential shear at the outside is greater than that at the inside, one would expect that drogues closer to the outside edge of the turn would move more slowly than those toward the "center" in relation to solid body rotation. The data shown in Figure 3 are consistent with this interpretation. The figure shows the locations of the drogues in the mixed layer (5 m depth) at 6-h intervals over a period of about four days. If the water mass turned as a solid body, we would expect the "outer" drogues (squares) to move at speeds approximately 10% faster than the "inner" ones (circles). In fact, they move at approximately the same speeds. The average tangential shear calculated from the drogues in the figure is about $5 \times 10^{-6} \text{ s}^{-1}$.

Since this horizontal deformation contributes appreciably to the separation rate of inner and outer drogues, taking it into account in the computation of vertical current shear considerably reduces the uncertainty in that value, that is, $1.1 \pm 0.2 \times 10^{-3} \text{ s}^{-1}$.

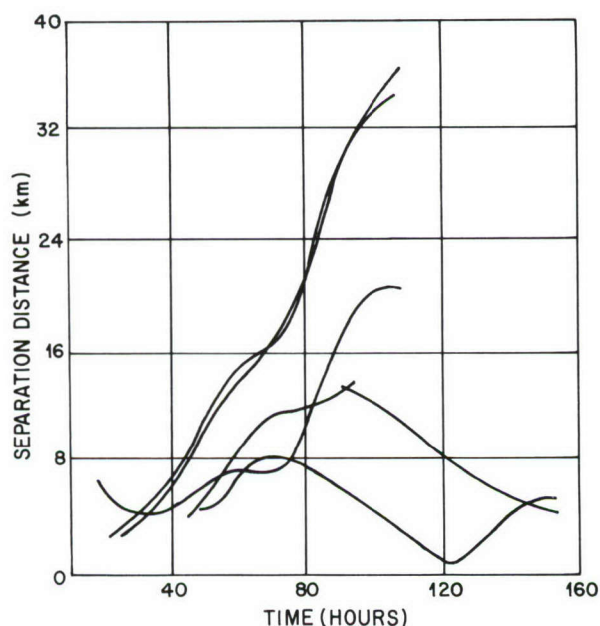


Figure 2. Horizontal separation of selected pairs of shallow and deep drogues as a function of time. Each curve represents a single drogue pair, and the instantaneous slope is indicative of the vertical shear (velocity gradient).

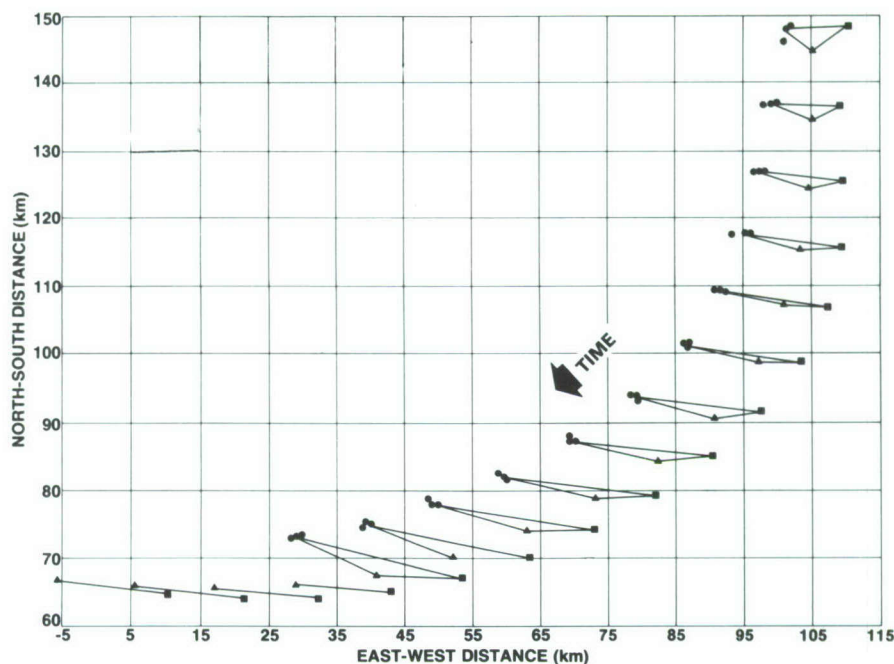


Figure 3. Locations of drogues in the mixed layer (5 m depth) at 6-h intervals. The arrow indicates the advancement of time. These data are used to calculate the horizontal shearing deformation to correct the vertical shear measurements.

Although considerably more study is needed to understand and model the interaction of vertical and horizontal current shear in the upper ocean, these initial results show that at-sea measurements with arrays of Lagrangian drifters can provide significant insight into this problem.

[Sponsored by ONR and NORDA]

Mapping Ocean Currents with Over-the-horizon Radar, by D.B. Trizna, *Radar Division*

The Navy has a vital interest in understanding the movements of the Gulf Stream and the warm and cold water rings or eddies that it sheds. These rings are "weather systems" of the ocean, and their anomalous thermal structure affects underwater acoustic propagation and the accuracy of passive detection. Hence, accurate and timely location of these systems is of importance to naval strategies. Present location techniques rely on infrared (IR) imagery of the ocean surface obtained from satellites. However, clouds and atmospheric haze can severely limit their coverage so that several days may be required to build up the complete image. During this time, the current structure can change markedly, introducing some uncertainty in the accuracy of location. For example, comparisons of the operational out-

puts of two satellites, each taken over a seven-day period but with five days common to both, have revealed differences up to 80 km.

In the past year, high-frequency (HF), over-the-horizon (OTH) radar has been used successfully to locate the Gulf Stream and associated eddies. Although propagation conditions may not always allow mapping on a daily basis, the radar is insensitive to clouds and therefore can observe areas that are under cloud cover for long periods of time. In addition, the radar map represents conditions on the day of measurement, rather than an average of several days. Mapping ocean currents using OTH radar may provide a complementary capability to the Navy's operational monitoring of the ocean surface.

The principle of locating ocean eddies and the Gulf Stream with HF OTH radar is based on a measurement of current structure rather than thermal features. The radar sends out pulses that are coherent in phase relative to one another, thus enabling Doppler processing of the backscattered signals returned from the ocean surface. The sea surface motion imparts a Doppler shift in frequency to the scattered radar waves. Two types of motion need to be considered. The first is that of the wind-driven surface waves. These include all wavelengths from a few centimeters to tens of meters. Each component travels at a

unique velocity determined by its wavelength, the longer wavelengths traveling faster than the shorter ones. (This is exemplified by a pebble dropped into a pond: a bigger pebble produces longer, faster waves than does a smaller one.) However, the only wave that returns a significant amount of backscattered radar energy is the one whose wavelength is one-half the radar wavelength. This phenomenon, known as Bragg scattering, produces two Doppler-shifted lines in the spectrum of the received radar signal, one associated with an approaching surface wave and one with a receding wave.

The second motion is surface current, which imparts an additional Doppler shift to the echo signal by an amount proportional to the current speed. This additional shift either adds to or subtracts from the shift produced by the surface wave motion, depending on whether the surface current has a spatial component toward or away from the radar bearing.

As an example, for a 10-MHz radar, the Bragg lines would be Doppler-shifted 322 mHz. A slow surface current of 15 cm s^{-1} (approximately 0.3 knot) would produce an additional shift of 10 mHz, which is the Doppler resolution

of the radar used in this study. Currents in the Gulf Stream and eddies can range up to 5 knots (approximately 250 cm s^{-1}), producing Doppler shifts up to 170 mHz. Since the Doppler shift of the Bragg lines is fixed by the radar frequency, Doppler analysis of the radar return enables a measurement of current speed.

An OTH radar operates typically at frequencies between 2 and 30 MHz, the same range used for shortwave radio broadcasts. These radio waves propagate to very long distances by being reflected back to earth from the cloud of electrons in the ionosphere. For HF applications, this cloud extends from roughly 80 km altitude upward to several hundred kilometers. Radar ranges between 650 and 2000 km can be achieved if the radar signal is reflected off the *E*-layer, a very stable layer in the lower ionosphere with little motion and low turbulence. *E*-layer propagation can be achieved by transmitting at low elevation angles on frequencies less than 15 MHz between sunrise and local noon for an eastern bearing.

For each pulse transmitted on a given bearing, the radar echo signal is sampled at time delays that correspond to the two-way signal tran-

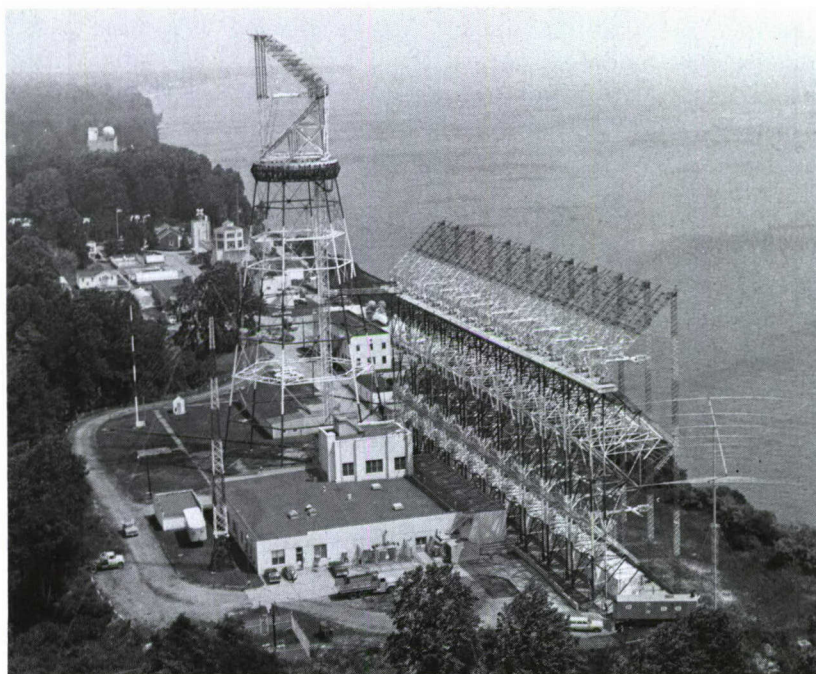


Figure 4. NRL's MADRE HF radar, on the western shore of the Chesapeake Bay, is continuously steerable from 47° to 107° true bearing, with a beamwidth of about 13° at 13.5 MHz. The two rows of horizontally polarized dipoles, one above the other, can be fed in phase or anti-phase for moderate elevation angle control. It was used as the transmitter for the surface-current measurement program.

sit times to a series of range cells. Each cell covers a small patch on the ocean surface, with the range extent determined by the radar pulse duration and the azimuthal extent by the radar antenna beamwidth. A series of such echo samples is processed to yield an average power spectrum of received energy vs Doppler frequency. The Doppler shifts due to ocean currents are then determined, and a radial current estimate is made for each range cell. The procedure is repeated over several azimuthal bearings, and a range-azimuth map of current measurements is established.

Mapping of ocean currents by NRL was accomplished using existing Navy radar facilities in a proof-of-concept experiment. The NRL MADRE HF radar (Figure 4) was used as the radar transmitter, and the wide-aperture (1100 m) ONR array at Whitehouse, Virginia, was used as the receiver. The large ONR array was needed to form narrow beams for high azimuthal resolution. Coverage of the two systems is shown in Figure 5, which shows the radar beams as straight lines, although their actual great-circle paths should show some curvature at the longer ranges in this projection.

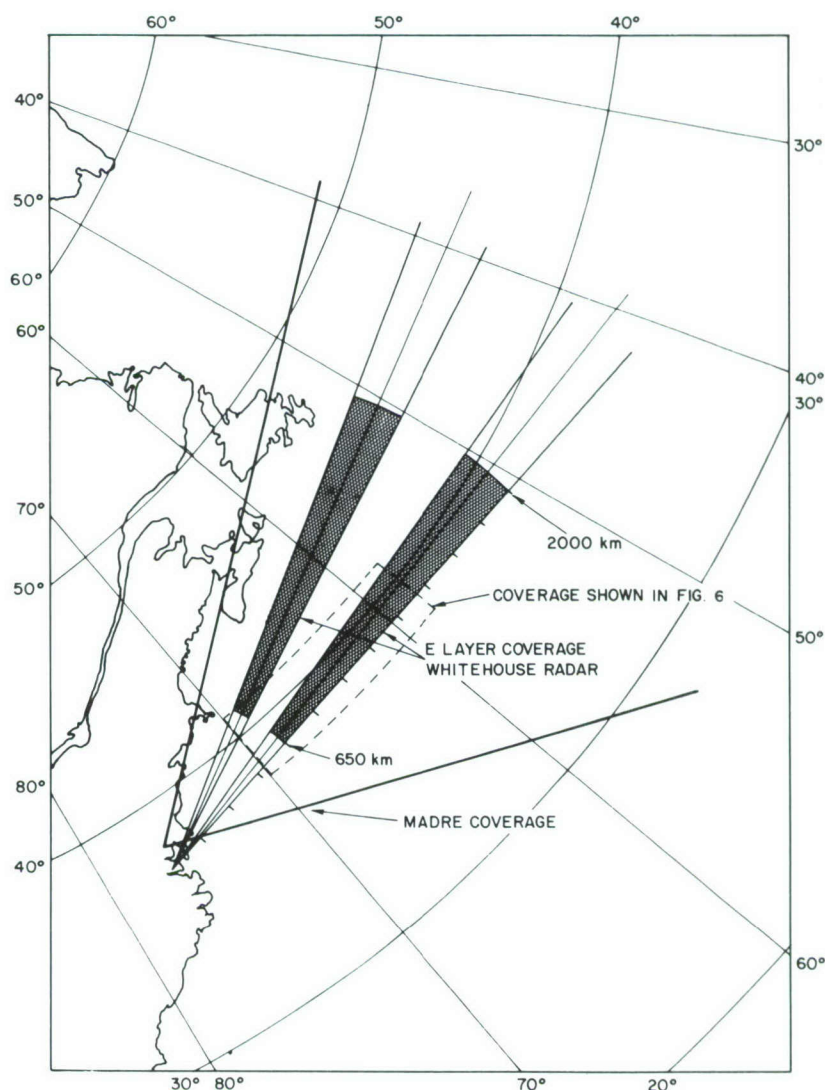


Figure 5. Antenna coverage for the transmit and receive systems used in the experiment. While MADRE is continuously steerable, the Whitehouse Chapel Bell 1100-m-aperture array is steerable in fifteen 0.5° steps, 3.5° to either side of three bearings: 45° , 60° , and 75° , the latter two of which are shown shaded in the figure. High-quality *E*-layer ionospheric coverage, as shaded, is typically used for surface-current experiments.

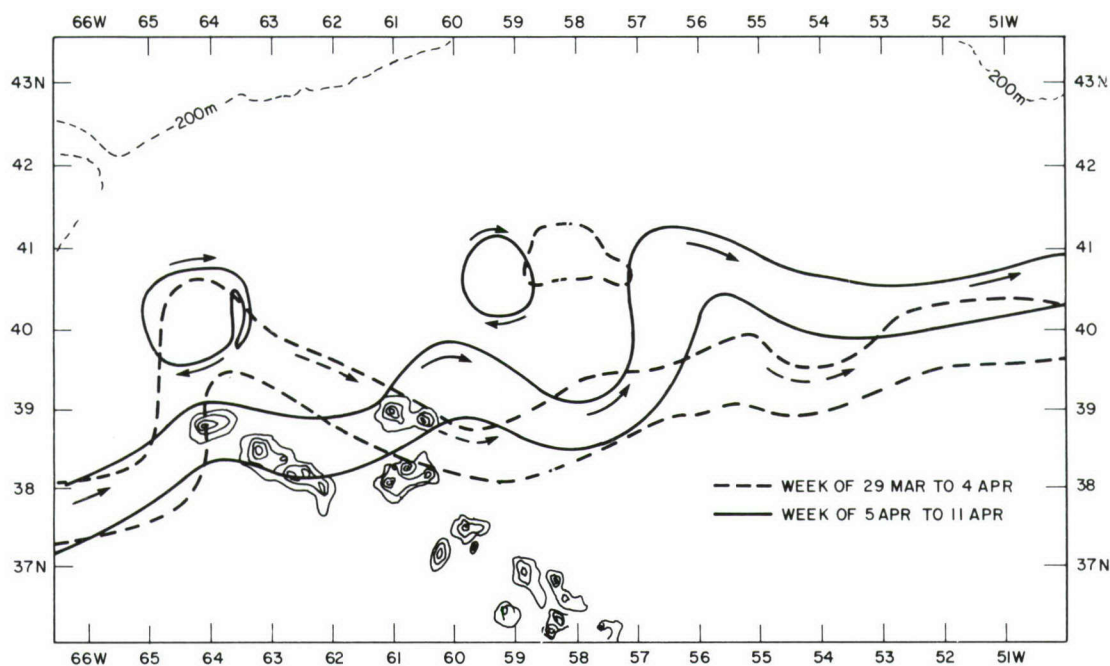


Figure 6a. Two different Naval Ocean Center ocean current maps show the result of a week's worth of satellite infrared imagery. The sharp bend of the Gulf Stream in the earlier map (-----) near 41°N, 64°W has evolved into an eddy in the subsequent map (—). Surface-current directions are indicated by the arrows, although no current magnitudes are available with this technique.

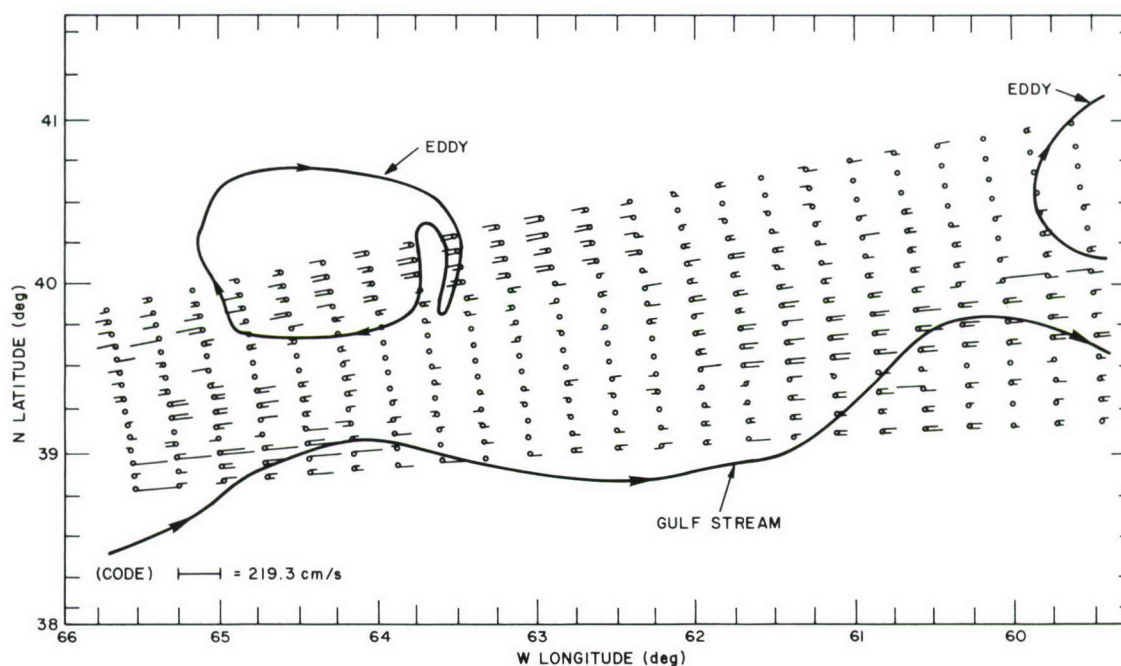


Figure 6b. Components of ocean surface-currents radial to the radar bearing are indicated by pairs of lines, each an independent estimate determined from radar data as described in the text. Although the radar data were collected over a 2-h period, vs the 1-wk montage of satellite imagery used to compile the map, there is generally good agreement between the two different techniques in locating edges of the Gulf Stream and part of an ocean eddy.

An example of Gulf Stream data is shown in Figure 6. Figure 6a shows contours developed from satellite IR imagery by Navy Eastern Oceanography Center, Norfolk, for two successive one-week periods. The contours show the boundaries of major thermal features, and these are interpreted as the Gulf Stream and associated eddies. The sharp Gulf Stream bend shown in the first map (dotted line) is believed to have broken off to form the eddy shown in the same area in the second map (solid line). Significant movement of the Gulf Stream also occurred from one week to the next.

Radar data were collected on a day at the beginning of the second week. The IR and radar data are superimposed in Figure 6b. In the radar data, each range cell is plotted as a small circle at its true coordinates. Two radial line segments are drawn from each cell, representing the two estimates of radial current derived from the approach and recede Bragg lines. The figure shows 15 azimuthal beams, all that are available from the receive array as it is presently configured. This suffices for the present demonstration, since the array covers an area of relatively high eddy activity. In other operational locations, additional beams would probably be required for adequate coverage.

The current reversal in the northwest portion of the radar map is well correlated with the portion of the newly evolved thermal eddy that falls within the radar map. The older eddy to the east has no clear counterpart in the current map. This may be because the current surface-structure of this eddy has been diffused, possibly by wind action upon the surface at some time in the past. The northern edge of the Gulf Stream is also seen to have a strong surface-current signature. In terms of Gulf Stream and eddy location, the comparison shows the potential of the OTH radar technique.

A program is proposed for building a transportable HF radar that could be set up anywhere around the world. It could be used to measure currents in regions where constant cloud cover or surface haze inhibit satellite coverage; to compare thermal imagery with current maps to resolve differences that have appeared in some recent experiments; and to provide surface truth data for future satellite systems. Such a system would pay benefits many times its construction and operational costs.

[Sponsored by ONR]

Modeling of Isothermal, Upper-ocean Water Masses, by R.P. Mied, J.P. Dugan, and A.F. Schuetz, *Environmental Sciences Division*

It is well known that the ocean is density stratified with respect to depth. Less well known but equally important is the fact that there are density variations in the horizontal plane as well. The Navy is interested in this horizontal variability because knowledge of the phenomenon—both its behavior and origin—is of value in understanding acoustic propagation and nonacoustic phenomena. Toward this end, through a joint NRL- and ONR-sponsored program, data were collected from multiship traverses of the Atlantic and Pacific Oceans using expendable bathythermograph (XBT) probes. Participants in this Ocean Eddy Surveying Program include NRL, Scripps Institution of Oceanography, and the University of British Columbia.

The relative temperature variation within a vertical cut through the ocean is shown in Figure 7a and 7b. We have chosen these traces because they exhibit an interesting phenomenon. In Figure 7a, the central trace has a region of constant temperature (hence constant density, assuming constant salinity) in the permanent thermocline, although contiguous XBT casts reveal no evidence of an isothermal region. In Figure 7b, three sequential XBT traces indicate an isothermal region that is not present in the remaining temperature plots. Moreover, no evidence of this phenomenon was observed by adjacent ships that deployed XBTs.

Considering the spacing of the ships (≈ 25 km) and the distance between successive XBTs from a given ship (Figure 7a, 7b), we infer that these isothermal regions in the upper ocean have horizontal dimensions of 25 to 50 km and vertical extents of ~ 100 m. Although their occurrence is widespread in the Sargasso Sea, we don't know the precise mechanism that accounts for their generation. Nevertheless, we may say a great deal about their dynamics by invoking the simple conservation laws of fluid mechanics.

We would expect that a homogeneous region would tend to collapse to a thin lamina and seek its own depth according to the density-stratified ocean in which it exists. As fluid starts to flow horizontally, the Coriolis force directs the flow to the right in the Northern hemisphere. The collapse continues until the Coriolis, pressure gradient, and centrifugal forces are balanced and a fully collapsed equilibrium state is achieved. This isothermal mass (called a *thermostad*) is thus a

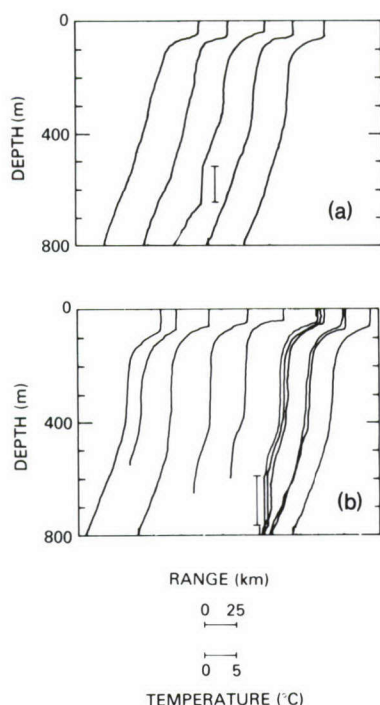


Figure 7. Traces of ocean temperature as a function of depth showing the isothermal regions of interest at 600 to 700 m. Each trace shows the relative temperature variation measured by an XBT whose relative spatial position is given by the upper end at 0 depth.

rotating body whose precise shape and internal velocity structure are unknown. We model the thermostad as an azimuthally symmetric oblate mass of homogeneous fluid in a density-stratified environment (Figure 8). The assumption of azimuthal symmetry permits description in terms

of the radius r , so that the shape $h(r)$ and velocity field $v(r)$ are not known a priori.

We know that the local vertical component of the earth's angular velocity F varies with latitude θ . It has a value Ω at the North Pole and zero at the equator: $F = \Omega \sin \theta$. The sum of F and the local fluid rotation rate ($\omega/2$), divided by the local thermostad height, is conserved for the fluid motion: $[F + \omega(r)/2]/2h(r) = \text{constant}$. This conservation law (conservation of potential vorticity) and the radial force balance described above constitute two nonlinear equations. These equations, together with the appropriate boundary conditions, are solved for the collapsed equilibrium state.

As the initially motionless thermostad starts to collapse, local fluid elements must rotate clockwise ($\omega < 0$) because $F > 0$. The accompanying velocity profile must then be clockwise, or negative also: $v(r) < 0$. The computer solution (performed by P. C. Mignerey of the University of Maryland) (Figure 9a, 9b) indicates that, indeed, $v(r) \leq 0$, or the flow is clockwise, and that closed oval shapes exist. Moreover, the results indicate that horizontal extents are typically ~ 20 to 40 km, which is consistent with observations, and fluid velocities at the rim are ~ 10 to 20 cm/s. These velocities are comparable with those of other upper-ocean mesoscale currents, and it is therefore not surprising that their existence has only recently been documented.

It should be emphasized that the stability of the thermostad solutions has not been verified. A treatment of their stability properties has not been attempted, but is essential in establishing the parameter ranges for which these thermostads are possible. Moreover, the inclusion of the variation of the Coriolis force with latitude (the so-

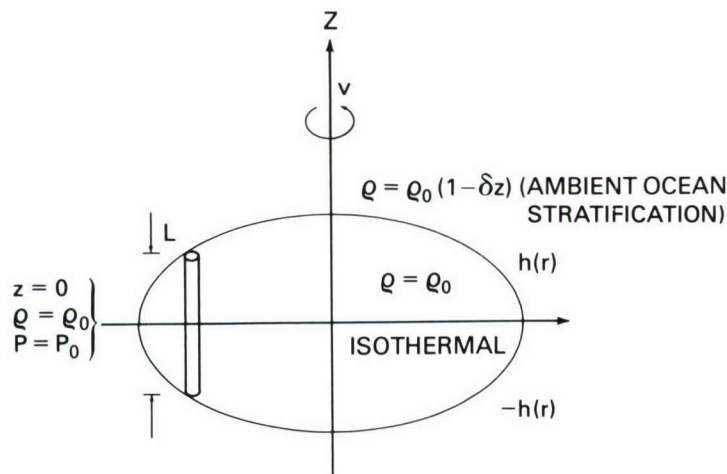


Figure 8. Geometry of thermostad model

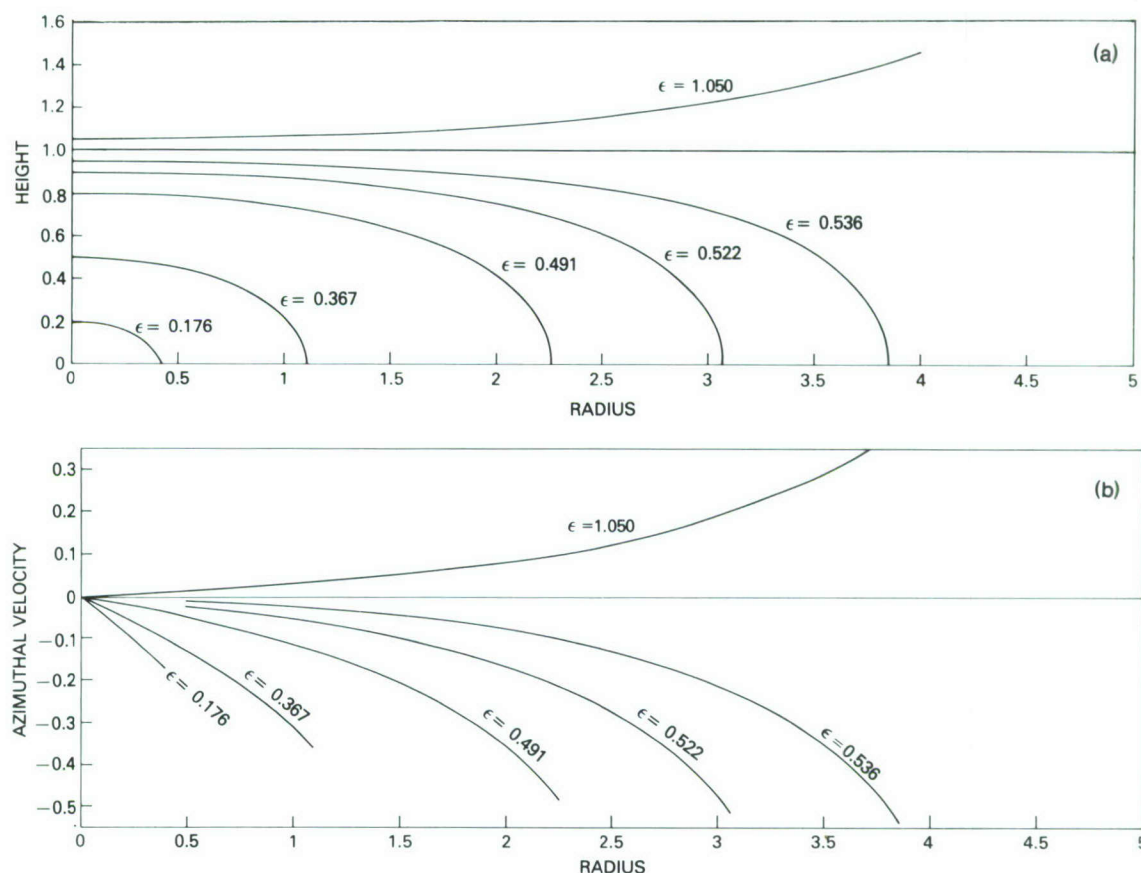


Figure 9. The fully collapsed thermostad equilibrium shape h and azimuthal velocity v . Each is non-dimensionalized with environmental parameters and is plotted as a function of nondimensional radial distance r . The absolute value of the maximum nondimensional velocity is ϵ , so that the thermostads are grouped according to ϵ .

called beta effect) would probably cause a propagation of these thermostads to the southwest, in the same fashion as warm-core Gulf Stream rings. [Sponsored by ONR]

Coherent Radar Observations of Breaking Shoaling Waves, by W.C. Keller, W.J. Plant, and G.R. Valenzuela, *Environmental Sciences Division*

For several years, the Naval Research Laboratory has been engaged in basic research on the dynamics of wind-waves and their interactions with electromagnetic (EM) radiation and other ocean waves. This work is important to Navy programs in ocean wave prediction, remote sensing of the ocean, and antisubmarine warfare (ASW). The NRL program is well balanced in ocean experiments, controlled-wave tank studies, and theoretical work aimed at providing a quantitative explanation of the experimental results. The primary experimental approach employs microwave Doppler spectrometry with coherent

radar (1.5 to 35 GHz), and optical and photometric techniques. The NRL program has consistently been in the forefront of the field with important contributions on the growth and straining of gravity-capillary waves, and in the energy transfer from the wind to ocean waves (1973, 1974, 1977 Review, and NRL Review, issued July 1980).

Wave breaking is an oceanographic process that has been difficult to elucidate either theoretically or by conventional oceanographic measurements. It is a strong nonlinear process of the upper ocean that transfers horizontal momentum from waves to surface currents and plays an important role in the equilibrium of the ocean-wave spectrum. Breaking waves are also important to remote sensing, contributing very strong backscatter to microwave sensors. There are two basic classes of breaking waves: *spilling breakers* and *plunging breakers*. Spilling breakers occur mostly in deep water and are caused by instability of the free surface near the wave crest, forming a

quasi-steady whitecap on the forward face of the wave. Plunging breakers are characterized by wave crests toppling forward and falling violently on themselves. The plunging type of breaking occurs mostly in coastal waters where the speed of the fluid increases with wave height and the speed of the shoaling waves decreases with decreasing depth.

Coherent radar may be the ideal instrument to obtain new insight into the process of wave breaking. A coherent radar is a remote probe that simultaneously records the amplitude and phase (velocity) variations of the short gravity waves of the ocean. The principal (Bragg) backscatterers of the EM radiation are short gravity waves of length $\lambda \sec \theta/2$ traveling in the line of sight (λ is the EM wavelength in free space and θ is the local grazing angle). The short gravity waves (Bragg scatterers) are strained (modulated in amplitude) and advected (their frequency is modified) by the fluid (orbital) velocity of the long waves and drift currents. The intensity of the backscattered power is proportional to the amplitude squared (energy) of the short gravity waves, and the resulting phase (frequency) of the return is a measure of the net speed of the Bragg waves including advection.

A few years ago [1], an experiment conducted by NRL used coherent radar to determine the modulation transfer function of gravity-capillary waves by shoaling waves. During the past year, it was decided that the data could also be used to provide insight into the complicated process of wave breaking and they have therefore been recently analyzed to extract this information.

A dramatic demonstration of information that coherent radars can provide regarding wave breaking is given in Figure 10. The figure shows short-time-averaged (0.5 s) Doppler spectra of radar return obtained with a continuous wave (CW), 9.375-GHz, vertically polarized radar from a 200-m pier at the Outer Banks of North Carolina [1].

In Figure 10a, the shoaling waves are not breaking; however, the advection of the Bragg scattering waves (1.95 cm in length) by the orbital velocity of shoaling waves is clear. The maximum Doppler frequencies on the wave crests are about 100 Hz, corresponding to a fluid velocity of 1.95 m s^{-1} . On the other hand, in Figure 10b, the shoaling waves are longer and are breaking on the crests. The spectra are much broader, and the maximum Doppler frequencies approach 300

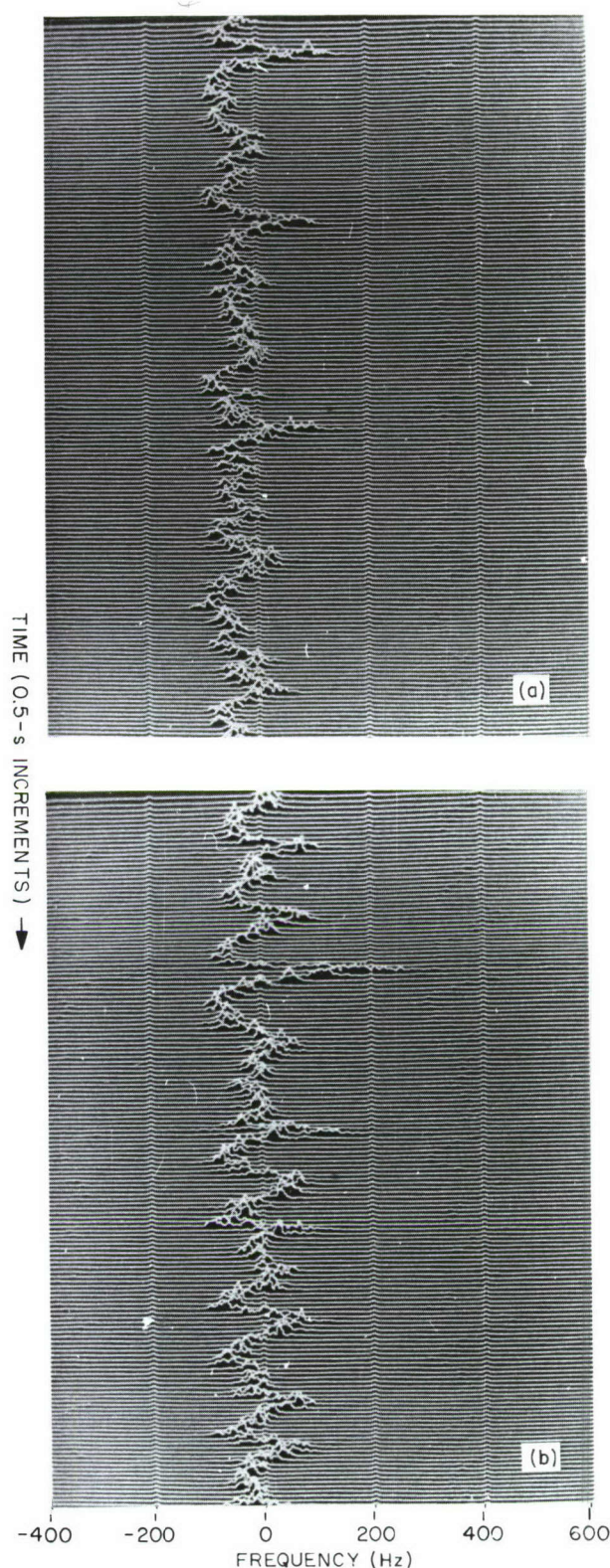


Figure 10. Doppler spectra of radar return (0.5-s averages) at 9.375 GHz from (a) nonbreaking and (b) breaking shoaling waves. Third axis shows power backscattered in linear scale. g is the acceleration of gravity and H is the mean water depth.

Hz, equivalent to $(gH)^{1/2} = 5.9 \text{ m s}^{-1}$ since $H = 3.5 \text{ m}$ in this case. It is common knowledge that for plunging breaking waves, the maximum speed of water parcels approaches the phase speed of the waves. However, for breaking waves, air is entrained by the turbulent fluid, and the EM scattering mechanism is no longer pure surface scattering (the intensity of the backscattered power is not proportional to the energy of the Bragg waves). However, the Doppler frequency of the return still corresponds to the speed of the scatterers on the breaking wave. Further insight into the breaking and EM scattering processes may be obtained with radar observations at a number of microwave frequencies and with various illuminated spot sizes on the surface.

The Laboratory's capabilities for wave dynamics research are being enhanced by the construction of a new 8-ft-wide by 100-ft-long wave tank. In addition, test trials are under way in the development of a remote orbital wave sensor (ROWS) to obtain the directional wave spectrum of the ocean from aircraft and spacecraft. NRL is organizing and acting as lead laboratory for a remote sensing experiment in the Nantucket Shoals (SEBEX) for September–November 1983 that will involve a number of academic institutions and industrial and governmental agencies. The major objectives are to delineate the processes responsible for surface expressions of bathymetry in radar imagery from shallow water and to investigate the dynamics of thermal fronts.

[Sponsored by ONR]

Reference

1. W.J. Plant, W.C. Keller, and J.W. Wright, *J. Geophys. Res.* **83**, 1347–1352 (Mar. 1978).

Crustal Geophysics Studies in the South Atlantic Ocean, by R.K. Perry, *Acoustics Division*

During 1980, a joint U.S./Brazilian Navy marine crustal geophysics program, Project Bode Verde I, was undertaken in the South Atlantic Ocean by NRL and the Brazilian Naval Research Institute. The long-term goals of the joint studies are to determine the tectonic nature and sea-floor spreading history of the South Atlantic Ocean between 7°S and 20°S latitudes; to establish the geologic relationship of South America to Africa; to determine the location, distribution, and trends of major topographic features of the Mid-Atlantic

Ridge; to determine the sediment distribution in the Brazilian abyssal plain; to map residual magnetic and gravity anomaly fields of the study area; and to develop a sound-speed data base for acoustic transmission experiments.

Field experiments during 1980 included airborne and shipboard geophysical measurements of the Mid-Atlantic Ridge south of Ascension Island between 8°S and 18°S latitudes. The results of the aeromagnetic investigation are shown in Figure 11. The profiles represent flight lines flown by an NRL P-3A Orion research aircraft equipped with a proton precession magnetometer. Flight altitude and speed were nominally 300 m and 450 km/h, respectively. During the flights, the magnetic field total intensity and the aircraft position and altitude were sampled every 3 s. An onboard minicomputer was used to reduce the total magnetic-field-intensity data to residual magnetic-field data, and to plot the residual value along the track while in flight. A brief deviation in the trace is associated with a magnetic anomaly at that point along the flight line.

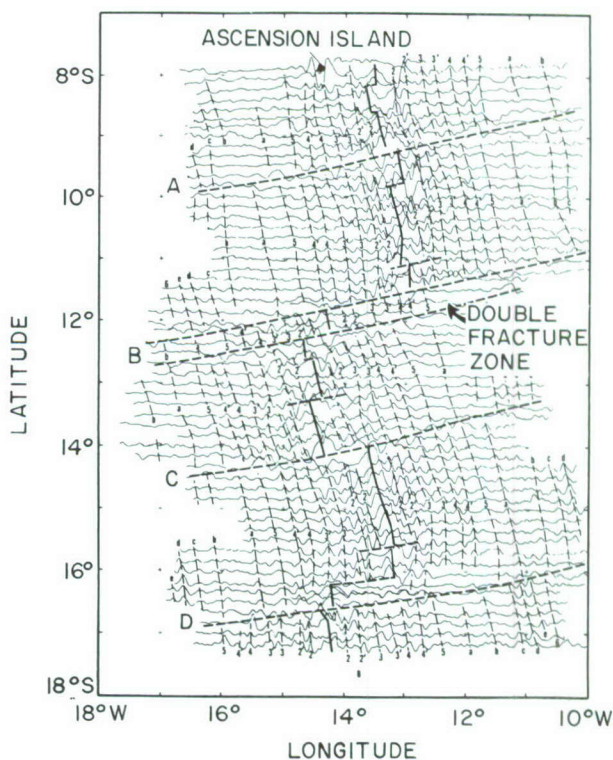


Figure 11. Aeromagnetic profiles of the Mid-Atlantic Ridge. Features illustrated include earth field reversals (vertical dashed lines), the ridge crest (vertical solid lines), deep axial troughs (horizontal dashed lines), and a double fracture zone that is only the second of its kind to be discovered.

The anomalies are seen to fall along nearly parallel tracks, as indicated by the north-south dashed lines in Figure 11, and are the result of reversals of the earth's magnetic poles over the past 15 million years. Disruptions within the anomaly pattern, represented by east-west dashed lines, reveal the presence of deep axial troughs cutting across the ridge (transform faults). Heavy north-south black lines over the large-amplitude anomalies mark the location of the ridge crest.

The aeromagnetic profiles shown in Figure 11 also indicate that the ridge contains an uncharted seamount with an unusually shallow peak at $9^{\circ}44'S$, $12^{\circ}49'W$. Shallow-peaked seamounts are of interest because they pose a hazard to submarine navigation. The airborne data also indicate the presence of a double fracture zone; that is, two continuous troughs in close proximity with a ridge between them. This feature is only the second of its kind to be discovered, the other

being the Gibbs Fracture Zone at $52^{\circ}N$ in the Mid-Atlantic Ridge. Three single-trough fracture zones were also indicated by the data at $10^{\circ}S$, $14^{\circ}S$, and $16^{\circ}40'S$ latitudes. Joint NRL/Brazilian geophysical experiments aboard USNS *Hayes* confirmed the indications of the aeromagnetic data. A seamount of 70-m depth was found at the indicated coordinates and was carefully charted (see Figure 12). It has been named the Hayes seamount, after the discovering ship. The double fracture zone was found to consist of a pair of deep troughs (over 4000 m) striking $N78^{\circ}E$, with the ridge segments displaced more than 233 km across the two troughs.

The origin and development of fracture zones in midocean ridges are still a subject of debate. In the North and South Atlantic Oceans, they are generally characterized by a continuous V-shaped trough 20 to 30 km wide and spaced hundreds of kilometers apart along the length of

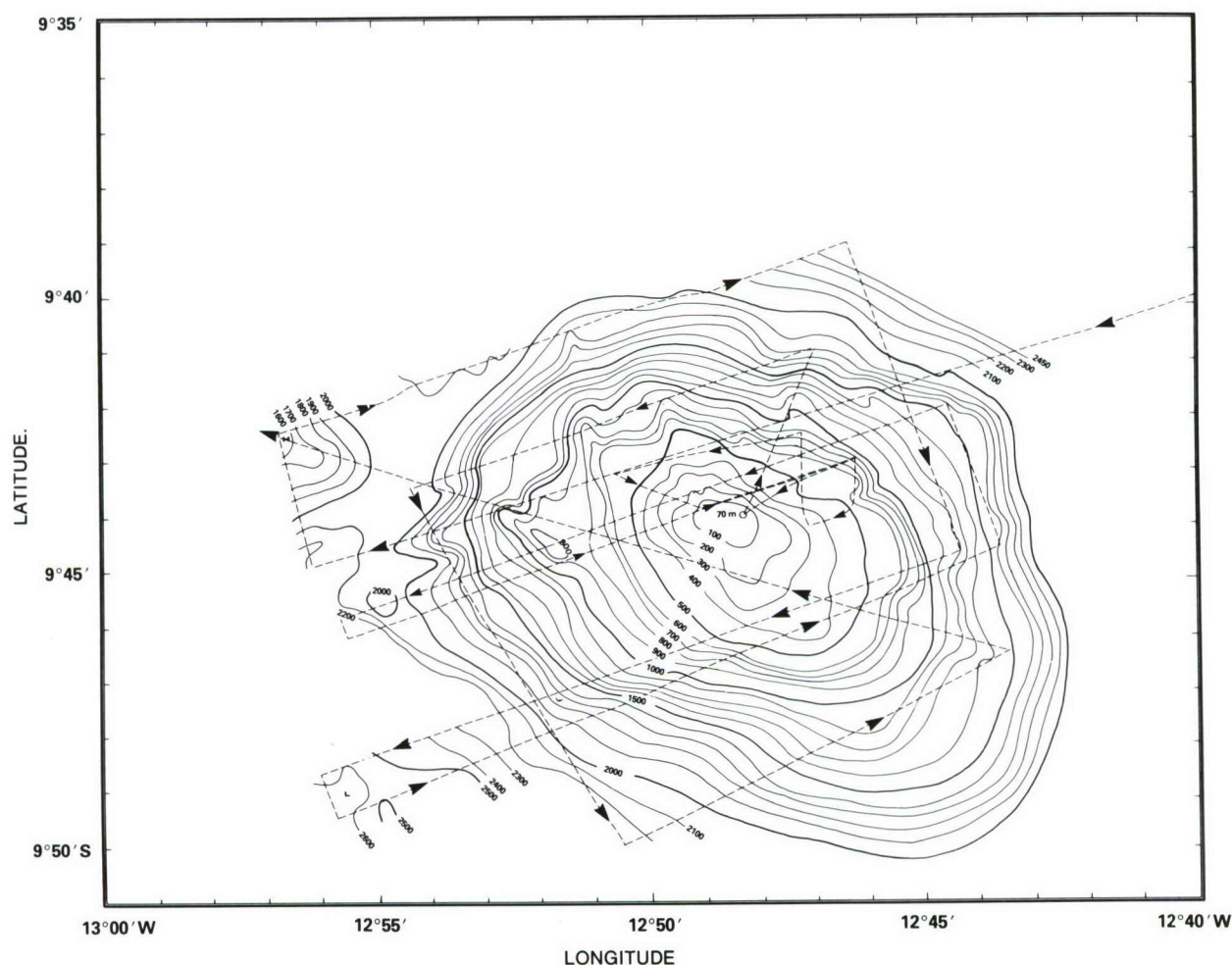


Figure 12. Survey of the Hayes seamount discovered in the NRL/Brazilian joint project. Bode Verde I. Dashed lines show the ship's track.

the Mid-Atlantic Ridge. In terms of sea-floor spreading, fracture zones form small circles around a pole of rotation and thus are used to infer the direction of crustal movement on opposite sides of a spreading ridge. What tectonic conditions lead to the development of two deep axial fracture zones in such close proximity (double fracture zone) is not known. The double-trough Gibbs Fracture Zone at 52°N is known to mark the southern extent of the Iceland "hot spot" (a zone of intense ridge buildup). Therefore the double fracture zone at 12°S may represent the southern extent of an Ascension "hot spot."

The success of this work has led to a continuation of the joint U.S./Brazilian program. In 1981, another survey will be made using the USNS *Hayes*, the Brazilian research ship *Admiral Câmara*, and an NRL P-3 Orion research aircraft. This new work will extend the ridge study into the Brazilian basin and will also attempt to map the double fracture zone over to the continental margin. These studies will help establish the history of sea-floor spreading in the South Atlantic.

[Sponsored by NAVELEXSYSCOM, DMA, and ONR]

Portable Systems for Oceanographic Data Acquisition, by D. Steiger, *Oceanographic Computer Applications Group*

NRL has developed highly portable data acquisition and processing systems for use aboard oceanographic platforms when larger minicomputer systems are impractical or unavailable. For example, during experiments aboard aircraft it is often not feasible to install a minicomputer system because of size and weight limitations or because of personnel needed to install, maintain, and operate the system. Also, when "piggybacking" on other operations, a researcher may have to minimize the equipment and personnel he can bring along.

The portable data acquisition systems have been developed by adapting existing computer terminals, thus obviating additional purchases. These terminals are compact (1 cu ft), lightweight (45 lb), reliable, and easy to operate. They usually serve as a standard peripheral to a computer system, such as the Oceanographic Mini-Computer System developed at NRL (see 1976 Review). However, they can also be used independently as a microcomputer system, since they contain a programmable processor, internal storage of data and program, external storage,

capability for parallel or serial interface to peripherals, and software development tools; i.e., all the salient features of a computer. Terminals having all these features have been dubbed "intelligent."

To date, three intelligent terminal data acquisition systems have been developed that use Hewlett Packard HP2645 terminals, and these have been used aboard aircraft and ships. These systems were developed for acquisition and processing of (a) earth's magnetic-field data, (b) airborne expendable bathythermograph (AXBT) data, and (c) ocean and atmospheric environmental data collected during ocean acoustics experiments.

Figure 13 is a diagram of the AXBT system. A standard aircraft AXBT recorder RO-308/SSQ-36 is digitally interfaced to the terminal. This recorder receives ocean temperature data transmitted by radio link from a sinking probe in the ocean and records temperature vs depth on paper for use by the tactical team on maritime surveillance aircraft. A digital clock and a switch panel are also interfaced to the terminal through parallel terminal boards.

When the bathymetric recorder receives a temperature reading, it sends an interrupt to the terminal. The terminal then accepts the temperature information and also records clock time and switch panel setting. The panel setting provides an AXBT identification number set by the operator at the time of deployment. Because the probe sinks at a known rate, the clock times can be converted to probe depths during the processing phase. During data acquisition, each temperature, time, and AXBT number set is displayed on

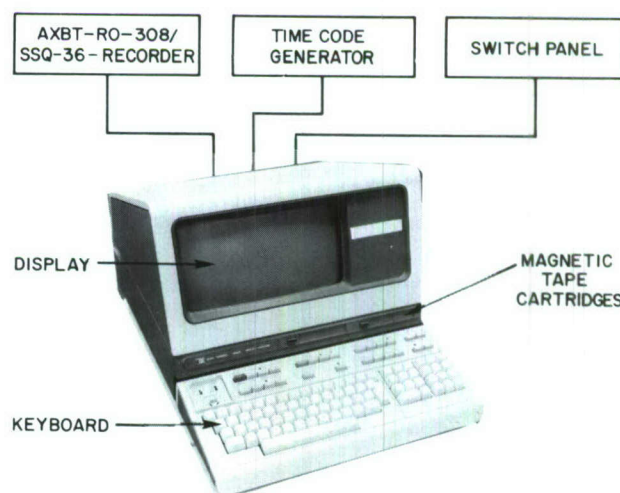


Figure 13. Functional diagram of AXBT recording system

the terminal's cathode ray tube (CRT) and is recorded on a digital cassette tape.

The AXBT data recorded on cassette tape can be processed by several systems. For field work, it was convenient to use an HP2647 intelligent graphics terminal. This terminal is similar to the HP2645, but includes a hardware graphics capability and a BASIC language interpreter stored in read-only memory. A program was written in BASIC to read the AXBT data from the cassette, process the time data, and produce a plot of temperature vs depth on the terminal CRT display. A hard copy of the plot can be obtained from the display by a HP2631G graphics printer.

The advantage of this system is that it provides a computer-compatible tape record of the temperature data for subsequent use, in comparison with the RO-308/SSQ-36, which produces only a paper chart record. This compact recording capability has considerable value in airborne oceanographic studies. In coming generations of aircraft that include onboard digital systems, it could also help to improve the Navy's compilation of large-area synoptics of ocean temperature.



Figure 14. Daniel Steiger at the console of AXBT data acquisition and processing system aboard an NRL aircraft

When collection and limited real-time processing during the experiment will suffice, only the HP2645 terminal is required, resulting in a truly small package. Figure 14 shows an AXBT system installed aboard an NRL P-3 Orion aircraft with both the HP2645 (at top) and the HP2647 graphics terminals.

Many features of these systems are noteworthy. When the terminal is not in its real-time data acquisition/processing mode, it can revert to its role as a standard terminal for an onboard computer system. The terminal's processing capability can be used in real time or in deferred playback in the field, or after the experiment back in the laboratory. Field experience has shown the data collection accuracy of the terminal-based system to be the same as that of a larger minicomputer system. The intelligent terminal records data on a computer-compatible tape format for subsequent compilation or analysis. With these features and their high degree of portability, it is anticipated that intelligent-terminal-based data acquisition and processing systems will find increasing applications in oceanographic experiments and surveys.

[Sponsored by ONR]

Automated Aerosol Sampling System, by F.K. Lepple, D.J. Bressan, and R.E. Larson, *Environmental Sciences Division*

A substantial portion of the Navy's new ships are powered by gas turbine engines. Compared to diesel propulsion units, gas turbines are simpler to operate, occupy less space, and require fewer crew members for maintenance and repair. However, since gas turbine engines consume very large quantities of air (approximately 60 kg/s or 50 m³/s at full power for each of the four engines on a DD 963-class destroyer), they are subject to loss of performance or even catastrophic damage from the ingestion of marine aerosols such as sea salt or continental dust. Some reduction of aerosol particles entering the turbine by impaction or filtration methods is required, but this is often limited by space constraints, pressure drop limitations, or economic considerations.

Over the past four years, we have conducted extensive surveys on diverse types of gas-turbine-propelled vessels such as freighters, destroyers, frigates, patrol boats, and experimental hovercraft. Primary objectives were to determine changes in the particle size distribution, composition, and mass concentration of marine aerosols upstream and downstream of different types of

filtration systems in various applications. A major goal is the production of a Navy gas turbine inlet design handbook that can be used to evaluate existing systems and guide future engineering designs and test specifications.

Results of past field trips have shown that ship-generated sea spray, debris, and/or stack emissions often overshadow the naturally derived aerosol components. In addition, the aerosol concentrations near the turbine inlet were found to be a complex function of inlet location and local turbulence induced by a particular wind direction and speed. Thus, literature values of ambient sea-salt concentrations as a function of windspeed alone are of minimal value in predicting the amount of salt that will reach the external turbine inlet and pass through to the engine itself. Accurate monitoring or modeling of conditions at either location would allow timely decisions on filter maintenance or engine washes that

would extend the time between major turbine overhauls, as well as guide the selection of future shipboard configurations.

At present, there are no commercially available salt monitors that are seaworthy and can operate reliably and unattended for a long time. Such a device is needed because our present data base is sparse for ship-generated aerosols at windspeeds in excess of 18 m/s (35 knots). The alternative of further manned surveys would be too costly, and the collection of data could be limited by safety considerations during rough sea conditions.

To improve this situation, we have developed the automated radon counter and aerosol sampler (ARCAS), a more sophisticated version of an atmospheric radon monitor (described in the *NRL 1976 Review*) patented by NRL scientists. This new device, shown in Figures 15 and 16, consists of a portable aerosol-sampling unit

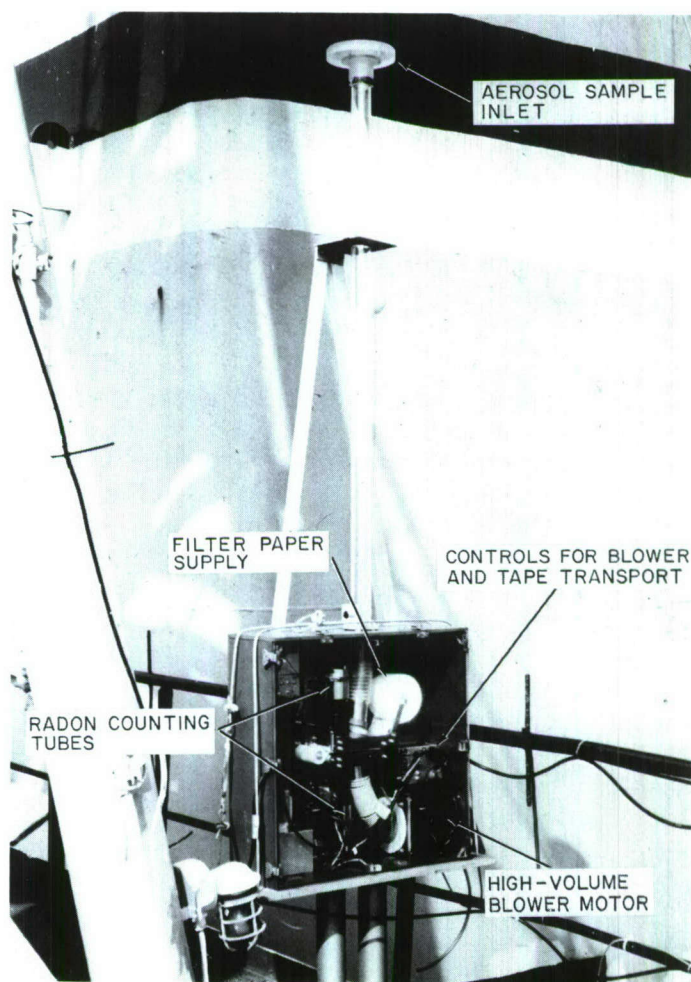


Figure 15. ARCAS deck unit mounted on the flying bridge of GTS Callaghan

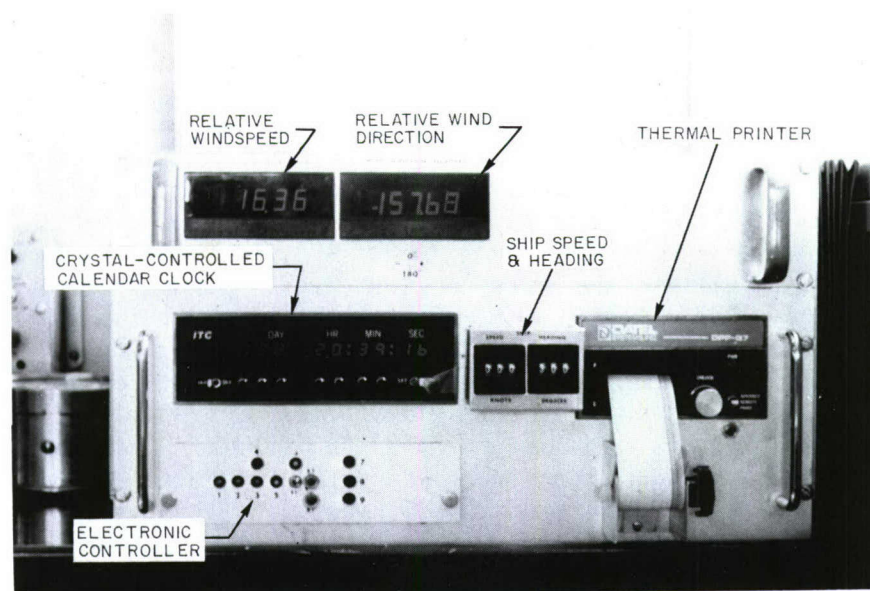


Figure 16. ARCAS control and readout unit in the wheelhouse of GTS *Callaghan*

mounted on deck and an indoor rack panel unit that contains the system controls, sensor displays, and data printer. The ARCAS can be programmed to collect aerosol samples automatically on a filter paper roll for a variety of durations and predetermined intervals. The usual scheme is a 20-min sample every 90 min. Concurrently, radon concentration is measured automatically in nearly real time for each sample and is recorded, together with date, time, ship speed and heading, average relative windspeed, and relative wind direction. These accessory data yield information on the age and source of the air being sampled and permit correlations between aerosol concentration and true windspeed. Selected samples are then analyzed chemically at NRL for sea-salt and/or continental aerosol components.

The ARCAS was successfully tested for a five-month period aboard the GTS *Callaghan*, a gas-turbine-powered ship that regularly traverses the North Atlantic. The only servicing required was to change filter paper and data paper approximately every four weeks. Severe winter weather, dense fog, and hurricane-force winds did not adversely affect the system's performance. During this period, more than 1000 discrete aerosol samples were collected. Preliminary analysis on representative samples has shown that the *local* aerosol concentration can be as much as 70% lower than the ambient and/or ship-generated salt load. These local zones of reduced salt concentration are thought to be due to combinations of

particle sedimentation, upstream impaction, and/or mixing with cleaner air from aloft. These results particularly stress the importance of selecting the optimum turbine air-inlet placement, because such significant reductions in salt aerosol loadings to the filtration system and engine would allow less frequent preventive maintenance and would extend engine life.

The present ARCAS has proven to be a very useful prototype that can provide the required long-term statistical data on aerosol concentration under varying conditions at sea. Recently, an improved version of the control unit has been constructed that contains additional environmental sensors (relative humidity, air temperature, and barometric pressure) and has magnetic tape data storage for computerized data reduction at NRL. Early in 1981 this new unit will be deployed on the *Callaghan* to establish more reliable short-term relationships between marine aerosol properties and meteorological conditions.

[Sponsored by ONR and NAVSEASYSOM]

Bioluminescence in the World's Oceans, by R.V. Lynch, *Environmental Sciences Division*

Bioluminescence, or the emission of light by living organisms, is a common marine phenomenon. It has been estimated that, in the depths of the oceans where light never penetrates, some 90% of the individuals and 70% of the species are

luminous. Even near the surface many luminous species occur, particularly among the plankton. Also, at night many luminous species normally found very deep migrate vertically to near the surface. Several of these organisms are among those comprising the deep scattering layers.

Organisms normally luminesce to fulfill biological needs, but they can also be stimulated to luminesce by a variety of means, including mechanically induced turbulence. Thus, objects moving at night through waters containing organisms can stimulate luminescence. If the concentration of luminous organisms is sufficiently high, the light emitted can be detected by the human eye. Fishermen in certain areas of the world, such as the coastal waters of Baja California, have long used this phenomenon to locate fish schools at night. During both world wars, combatants on both sides occasionally used stimulated bioluminescence to locate enemy shipping at night.

As long as the human eye was the best available detecting instrument, bioluminescence was not considered important to the Navy. However, in the late 1960s the National Marine Fisheries Service (NMFS) developed a low-light-level image intensifier (LLLII) TV camera in the hope of improving catches by locating fish schools more easily and efficiently. This LLLII was deployed in the Gulf of Mexico from both ships and aircraft and located fish schools outlined in bioluminescence too dim to be seen by eye. Experienced observers even learned to identify the kind of fish by the shape of the light patch. This technique has been used successfully along the Pacific coast of North, Central, and South America, the Atlantic coast of North America, around the British Isles, and along the coast of Namibia. Furthermore, current LLLIIs are approximately 20 times more sensitive than the original NMFS instrument.

This new technology obviously extends the possibilities for night detection of moving objects. However, the question remains, Where and at what times of year will bioluminescence be detectable even with a LLLII? More broadly stated, what is the geographical and seasonal distribution of marine bioluminescence? NRL began to investigate this question in 1973.

NRL's approach is three-pronged. First, existing literature on bioluminescence is being reviewed and analyzed. An example is the analysis of the data on taxonomic distributions obtained during the International Indian Ocean

Expedition; although the published results did not mention bioluminescence, its presence could be inferred from the known luminous organisms found.

Second, NRL has conducted a series of cruises and flights that included measurements of bioluminescence, as well as other physical, chemical, and biological properties of the oceans. Of approximately 200 locations where data were gathered, bioluminescence was observed in all but one. Luminous euphausiids, dinoflagellates, and copepods, in that order, have been the most frequently encountered organisms, although the luminescing species have varied greatly from station to station. Since these field trips have taken place in widely scattered locations and at different times of year, it may be inferred that marine bioluminescence occurs worldwide at all seasons. This suggestion is corroborated by the literature analysis. This apparent ubiquity of bioluminescence, however, is characterized by great variations in the number and intensity of flashes recorded and the population counts of luminous organisms collected. These variations have not yet been correlated with any other parameter. Also, because of their varying missions and investigative areas, these cruises have provided little information on seasonal or daily variations of bioluminescence in a given location. However, the recent acquisition of an advanced airborne LLLII has provided a tool for making rapid surveys of broad areas and for periodic revisits to chosen areas on both short and long time scales. Such repetitious coverage can be achieved more cheaply and easily with an airplane than with a ship.

Third, Navy ships have recently been instructed to report visual observations of bioluminescence along with certain ancillary data. These reports are being collected by ONR West, Pasadena, and forwarded to NRL for analysis. It is hoped that over a period of several years, enough reports will be received to permit a statistically meaningful analysis of temporal variations in some well-traveled patrol areas. So far, most of the reports have been received from the Arabian Sea area, which is considered to be the brightest in the world. Although the causative organisms and triggering mechanisms are unknown, there is an established seasonal variation in that area. A maximum occurs in late summer, corresponding to the time of maximum upwelling and mixing caused by the Southwest Monsoon, and there is a secondary maximum in midwinter.

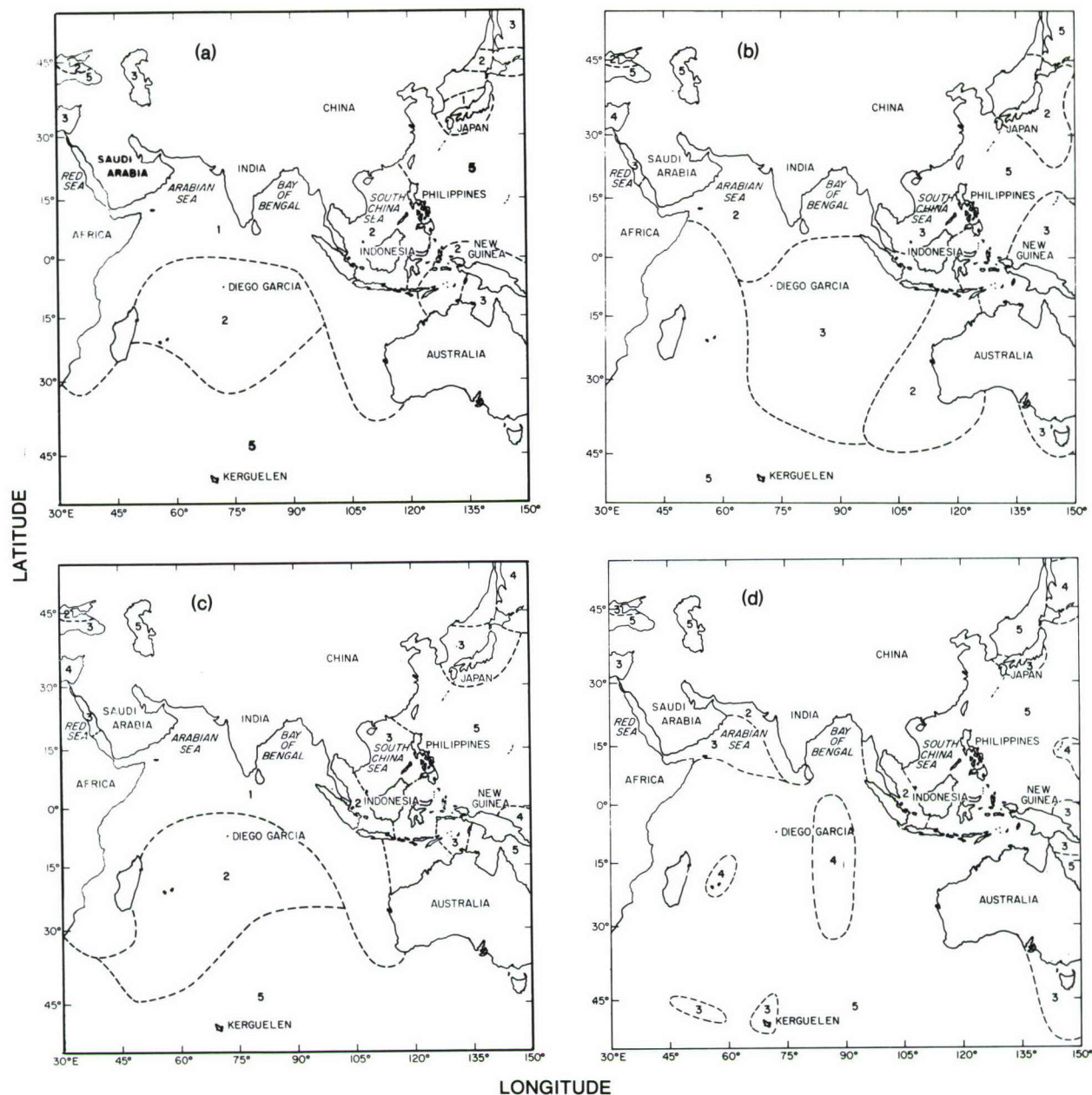


Figure 17. Frequency of bioluminescence encounters in the Indian and Western Pacific Oceans for (a) January–March, (b) April–June, (c) July–September, and (d) October–December. Frequencies are indicated by number as follows: (1) very high, (2) high, (3) moderate, (4) low, and (5) unknown.

Figure 17 provides a rough summary of the seasonal distribution of bioluminescence in that part of the world as derived at NRL from available literature data and fleet reports.

Studies of bioluminescence distribution are in their infancy, and the results presented here are only a beginning. Data gathering at random, as has been done so far, is useful in identifying areas of interest, but cannot provide the information needed to understand variations and to con-

struct predictive models. The chief problems are the vast size of the oceans and the large amount of observational time required to establish statistically reliable seasonal variations at any given location. Area and seasonal coverage can be improved by the development of simple towable instruments for fleet use in measuring bioluminescence. NRL is providing information about the biology of luminous organisms and the chemistry and optical properties of flashes to

engineers at other laboratories interested in designing such instruments. The reliability of remote sensing of bioluminescence by airborne LLLIs can be increased by the development of remote means of stimulating luminous organisms to flash. NRL is collaborating in the pioneering use of tunable dye and CO₂ lasers to provide such stimulation. Initial experiments on dinoflagellate cultures have been highly promising. Long-term localized measurements of bioluminescence in a

natural environment can be made by floating radio-controlled bathyphotometers designed to eliminate instrumentally induced disturbances. NRL is cooperating in the testing of such an instrument under development at Scripps Institution of Oceanography. New tools such as these should begin to overcome the problems of time and space in distributional studies of bioluminescence.

[Sponsored by ONR]

ACOUSTIC PROPERTIES AND APPLICATIONS



ACOUSTIC PROPERTIES AND APPLICATIONS

The ability to transmit and acquire information with sound waves is an important and sometimes unique aspect of naval activities. Ever since the formation of the underwater acoustics unit that was a part of NRL's beginnings in 1923, the Laboratory has maintained a continuing and productive interest in acoustic transmission, properties, and applications.

Microparticle Detection Using Focused Ultrasound	77
Low-frequency Sonic Reflectivity of Ice	78
Sound Propagation Through Fluids in Piping Systems	80
Applications of Acoustic Holography in Nondestructive Evaluation	82
Phase Calibration of Hydrophones	84
New Omnidirectional Standard Transducers	85
A New Underwater Shock-wave Sensor	87

Microparticle Detection Using Focused Ultrasound, by J. Jarzynski, *Acoustics Division*

The detection and identification of microparticles in fluids is a problem in several areas of interest to the Navy. These include the detection of traces of oil (microdroplets) in filtered effluent water and of metallic particles in hydraulic and fuel fluids. In recent work at Brown University, it has been demonstrated that scattering of ultrasound in the frequency range of 1 to 10 MHz is a promising approach to this problem, and NRL scientists (in collaboration with the University of West Florida) are continuing to develop this technique.

The experimental setup is shown schematically in Figure 1. A transducer is used to generate periodic bursts of ultrasound, and the waves scattered by the microparticles are received by a second transducer. Spherical lenses (1.27-cm diameter, 3.1-cm focal length) are attached to both transducers and are mounted so that their focal regions overlap. This arrangement ensures that echoes are received mainly from microparticles in the fluid volume defined by the overlap of the two focal regions. At ultrasonic frequencies, this volume is quite small ($\sim 3.7 \times 10^{-4}$ cc for the system in Figure 1) and the probability of multiple-particle occupancy is negligible at the low microparticle concentrations usually encountered in practice. Thus, the echo received is usually from a single microparticle, which greatly facilitates monitoring and identification.

A novel and simple signal processing technique that discriminates among echoes from different types of microparticles has been successfully developed at NRL. This technique is based on the fact that the amplitude of ultrasound scattered by a microparticle depends on the frequency of the incident wave. This frequency dependence is characteristic of the size and elastic properties of the scatterer and forms a "signature" useful for identification. Therefore, the probe employed in the NRL system is a frequency-modulated (FM) chirp signal in which the frequency increases linearly with time during the signal. Use of the FM chirp signal allows the frequency dependence of the scattered pressure amplitude to be determined directly from the shape of the echo envelope. Two echo waveforms are shown in Figure 1. Previously, the approach had been to estimate the concentration of particles from the number of repetitive probing signals that returned an echo. This approach could not discriminate between different types of particles and was prone

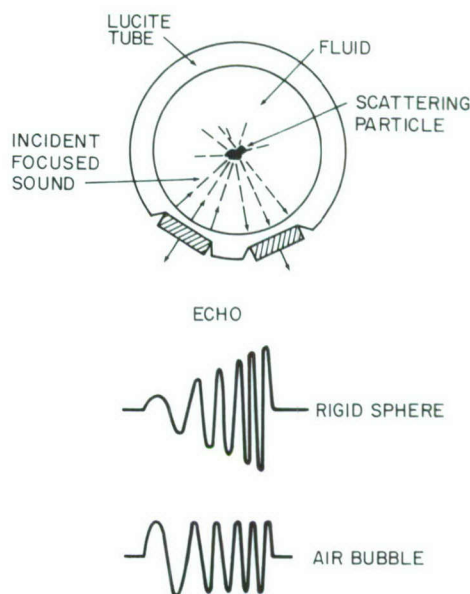


Figure 1. Schematic of the experimental setup for focused ultrasound microparticle studies (top) and typical echoes (bottom)

to error because of echoes from ubiquitous air microbubbles. Other approaches for obtaining the signature are also under consideration, but they generally require the complexity of a costly minicomputer system to produce the signature spectrum via Fast Fourier Transform processing. The NRL system is relatively simple and inexpensive.

Measurements of echo amplitude and shape have been made for various types of spherical microparticle scatterers by using FM chirp pulses of 30 μ s duration with a linear frequency sweep from 3.5 to 6.5 MHz. The microparticle sizes varied from 25 to 60 μ m in diameter. The NRL measurements have so far been limited to spherical scatterers of known dimensions and elastic properties, so that the experimental data could be compared with theoretical predictions. The theory for scattering of focused sound from spherical elastic particles was developed concurrently with the experimental work, and the agreement between experimental data and the theory is good.

Typical results are shown in Figure 2, where the measured relative scattered pressure amplitude (normalized to unity at 5.5 MHz) is plotted as a function of frequency for two scatterers: a spherical glass shell 55 μ m in diameter, and an air bubble ~ 50 μ m in diameter. The frequency

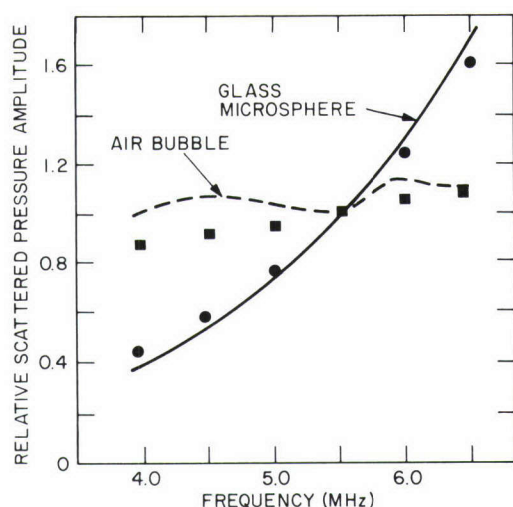


Figure 2. The measured relative scattered pressure amplitude as a function of frequency for a glass shell 55 μm in diameter (solid line) and an air bubble approximately 50 μm diameter (dashed line). The circles and squares are the corresponding calculated values.

dependence of the scattered pressure amplitude clearly is quite different for the two scatterers.

The accomplishment of the NRL work has been to demonstrate the feasibility of using focused ultrasound both to detect and to discriminate between different microparticles in fluids by measuring the amplitude and frequency content of ultrasonic echoes from the microparticles. The ability to discriminate against echoes from air microbubbles is particularly significant because the presence of air bubbles in fluids is often unavoidable. Current investigations include a study of ultrasound scattering from various microparticles of practical interest, such as oil microdroplets in water. Potential applications, in addition to those described above, include the detection of asbestos fibers in air and the monitoring of particulates in boiler water.

[Sponsored by ONR]

Low-frequency Sonic Reflectivity of Ice, by T.C. Yang and C.W. Votaw, *Acoustics Division*

Much of the Arctic Ocean is inaccessible to surface ships because of low temperatures and thick ice cover. But, for modern nuclear submarines with the capability of cruising submerged for weeks at a time, the Arctic is not much more forbidding than other oceans. The Navy thus has an interest in underwater acoustic propagation in these waters, and especially in features that could

produce changes in sonar and surveillance system performance in this unique environment.

Acoustic propagation in the Arctic Ocean has distinctive characteristics owing to temperature and the prevailing ice cover. In low latitude waters, the sound speed initially decreases with depth in a sun-warmed surface layer until the ever-increasing hydrostatic pressure compels it to increase with depth. The decreasing sound speed in the surface layer refracts acoustic ray paths downward, and there are some paths that do not encounter the surface. In the Arctic, however, the surface is cold, and the pressure-induced increase of sound speed with depth becomes dominant near the surface; thus all acoustic ray paths are refracted upward to the surface. The distinctive characteristics of the Arctic are, therefore, that all paths interact with the surface and that, for the most part, the surface is ice covered. Ice has different sonic reflectivity than air, and knowledge of the reflection and scattering process at the interface between ice and water is the key to understanding propagation in Arctic waters.

Typically, large areas of ice consist of relatively shallow, smooth-bottomed plates separated by rough ridges that penetrate to greater depths. The smooth plates cover about 80% of the area. It has usually been assumed in the literature that a smooth ice plate is totally reflective at low grazing angles. Thus losses at the water-ice interface have been considered the result of scattering at the rough ridges. This assumption, which has been nearly universal in propagation loss modeling in the Arctic, has been cast in doubt by the experiment reported here.

In April 1980, NRL made ice reflectivity measurements in the Arctic Ocean north of Ellesmere Island as part of the East Arctic 80 Experiments. These experiments were sponsored by the Office of Naval Research and covered such diverse topics as seismic refraction and reflection, long-range acoustic transmission, reverberation, and ambient noise measurement. The NRL work discussed here involved measurements of the sonic reflectivity of smooth ice plates at low frequencies (below 1 Hz) and shallow grazing angles (18° to 26°), values representative of underwater surveillance conditions. These data are noteworthy in that little is known of low-frequency reflectivity, since most previous data have been taken at higher frequencies.

Conducting the experiment in the harsh Arctic environment meant that men and supplies had to be air lifted to the site and an ice camp (see Figure 3) set up to support the scientists during

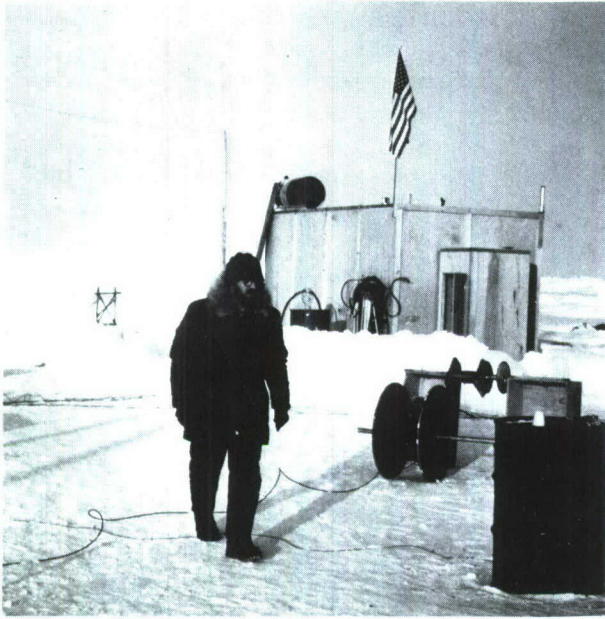


Figure 3. Charles Votaw at the NRL ice camp in the Arctic Ocean north of Ellesmere Island

the 30-day experiment. Holes were made through the 2-m-thick ice cover with specially adapted drills and chain saws. The drilling sites were chosen after the surface of the ice was surveyed for smoothness, as the smoothness of the underside of ice plates is known to match closely that of the upper surface.

A receiving hydrophone was lowered through one hole to a depth of about 100 m. Through the other hole, some 500 m distant, was lowered a novel sound source—an ordinary 60-W electric light bulb. Each bulb was weighted and slowly lowered until hydrostatic pressure caused it to implode. Implosion depth was then determined by retrieving the lowering line and measuring the length paid out. Implosion depths varied from 50 to 125 m, thereby producing grazing angles between 18° and 26° .

The imploding light bulb is not only economical and handy to use, but it also has two features that are essential for this type of measurement: a very short pulse and a smooth, low-frequency spectrum. A short pulse is required to resolve the direct arrival from the closely following ice-reflected arrival. The three pairs of received signals shown in Figure 4 demonstrate that the direct and reflected signals are clearly resolved. Previous attempts at these measurements using a pulsed acoustic oscillator were not as successful in resolving the two arrivals.

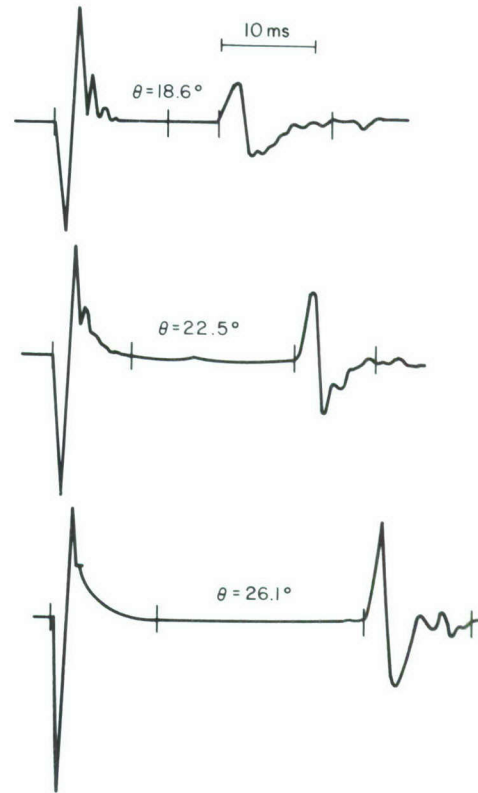


Figure 4. Pressure vs time series of direct and ice-reflected arrivals. The pulses used for FFT are between the vertical bars.

Although bulbs larger than 60 W would have been more desirable because they produce more acoustic energy, they contain an inert gas to increase filament life, and oscillations of this gas bubble after implosion were found to lengthen the signal and to distort the otherwise smooth spectrum. Use of the lower power 60-W bulbs, which are evacuated, was found to be best for these measurements. This method reduced the lowest frequency at which the reflectivity of the ice could be measured by a factor of five.

The first step in obtaining the reflectivity of the ice was to spectrum-analyze the two arrivals into their component frequencies. Since the two paths were nearly the same in length, the attenuation and geometric spreading losses accumulated along each path differed by a negligible amount (less than 0.4 dB). Thus, any significant difference in the two spectrum levels is attributed to reflection loss. The decibel difference of the two spectra is termed the reflectivity of the ice plate. If the ice were totally reflective, as so often assumed, the two spectra would show no significant difference in level and the reflectivity

would be 0 dB. This was not the case, as typical data in Figure 5 show. There are losses at all frequencies above about 200 Hz, and losses in excess of 10 dB are seen above 500 Hz. These results indicate that a smooth, flat ice plate cannot be treated as totally reflective in the low-frequency range.

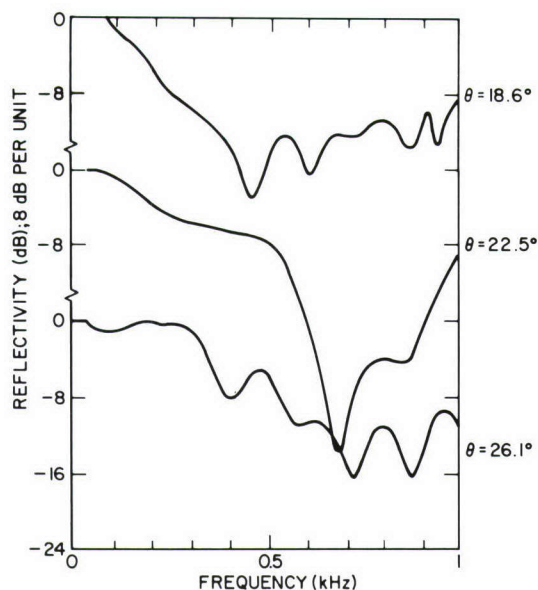


Figure 5. Coefficients of reflection for frequencies up to 1 kHz for various incident (grazing) angles. The data are from a hydrophone at a range of 474 m.

What happened to the acoustic energy lost from the ice-reflected arrivals? Although the complete theoretical analysis of low-frequency reflectivity from a point source has not yet been developed, a likely answer is that much of the lost energy went into generating stress waves, such as Lamb waves, within the ice. Analysis of the grazing angle and the frequency dependence of the major nulls in the reflectivity data suggests that these nulls occur at absorption resonances associated with the excitation of the lowest order, antisymmetric mode of Lamb waves. However, a definite conclusion is not possible from these data, as they also contain fades caused by interference between specular and nonspecular reflections from the ice. Additional experimentation is required to answer the question and is already being planned.

One improvement planned for the next experiment is to use a trigger to implode the light bulbs at preselected depths rather than relying on the inherently random variation of crush depth.

This will permit systematic control over the variation of grazing angle, which is necessary to pursue the question of generation of Lamb waves within the ice during low-frequency reflection.

The results of the work already completed are being fully reported to the acoustical community. These results should help point the way to a new generation of improved modeling and understanding of acoustic propagation in Arctic waters.

[Sponsored by ONR]

Sound Propagation Through Fluids in Piping Systems, by R.A. Skop and M.P. Horne, *Marine Technology Division*

The propagation of low-frequency sound waves through fluids in piping systems results in the concomitant radiation of sound away from the piping system. This radiated sound is a source of internal environmental and external detectable noise on Navy combatant vessels. One approach to reducing the level of the radiated sound is to reduce the level of the sound in the piping system through use of sound-absorbing viscoelastic materials as pipe walls or pipe-wall liners. Because of the diversity and complexity of these materials and of piping system geometries and uses, the identification and selection of candidate materials in the past has been on a more or less ad hoc basis.

Investigators at NRL have recently undertaken an effort aimed at the development and experimental verification of analytical models for predicting low-frequency sound-wave propagation through fluids in piping systems containing viscoelastic walls or wall liners. The goal of this effort is to establish approximately correct models from which the influences of viscoelastic parameters and piping system geometries on sound-wave propagation can be readily ascertained.

As a first step in this effort, sound propagation through fluids contained in thin-walled, viscoelastic, circular cylinders was examined. The approximate analytical model is based on two assumptions that greatly simplify the problem: (a) the sound wave can be treated as a plane wave with constant properties over a cross-section transverse to the cylinder axis, and (b) the cylinder wall can be treated as "locally reacting." The latter assumption decouples the transverse and longitudinal motions of the wall and allows the inclusion in the model of a general viscoelastic constitutive relation for the wall material.

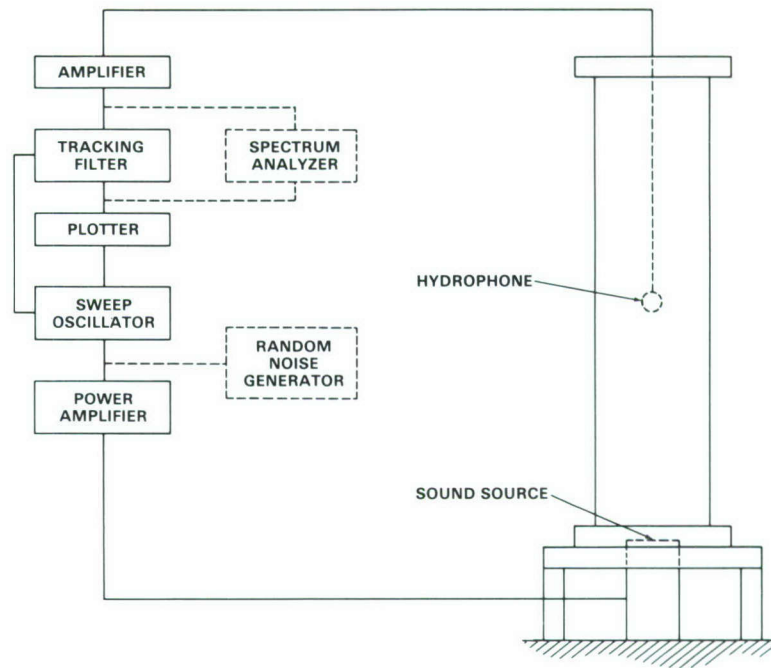


Figure 6. The experimental system used to produce and record the sound pressure levels in the water column contained within the open-ended pipe (183 cm long, 19.05 cm in diam)

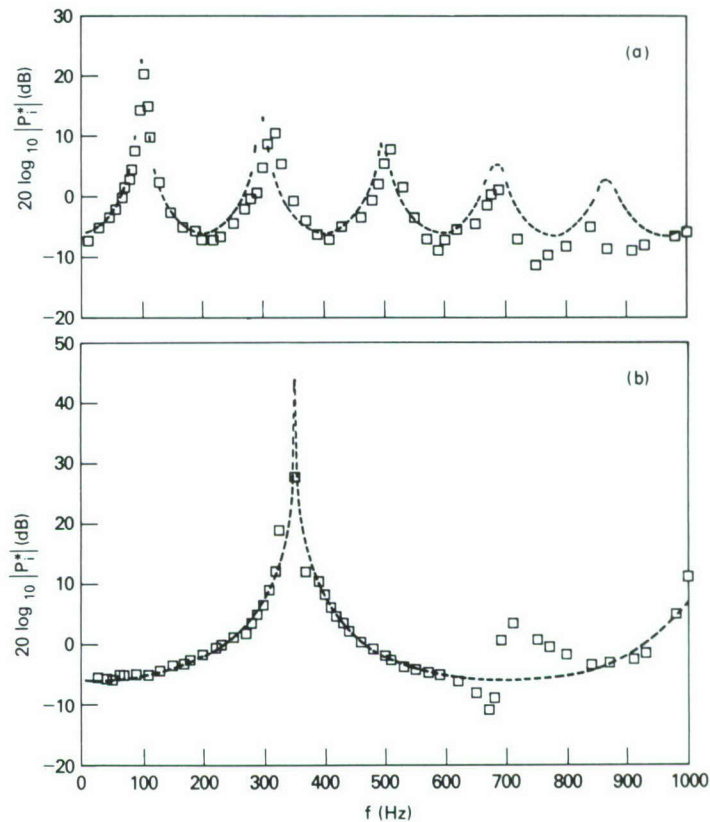


Figure 7. Predicted (dashed line) and measured (squares) sound-pressure levels at a point halfway up the water column in (a) acrylic pipe and (b) steel pipe

Details of the model and of its predictions of sound pressure levels along the cylinder axis as a function of the viscoelastic parameters of the wall material can be found in Ref. 1.

The validity of this simplified sound-propagation model has been tested experimentally in the system shown in Figure 6. The water column in the open-ended pipe was ensonified by a transducer at its base, and the resulting pressure levels along the cylinder axis were measured by a small, traversing hydrophone. Comparisons between experimental results and model predictions are shown for a 0.635-cm viscoelastic acrylic wall and a 0.953-cm elastic steel wall in Figures 7a and 7b, respectively. The viscoelastic properties of the acrylic wall material were measured by the NRL Chemistry Division. The measured values of the wall material were used in making the model predictions. Standard handbook values were used for the steel, as its material properties are well known. In both figures, the sound pressure level at a point halfway up (91.5 cm) the fluid column, relative to the sound pressure level at the ensonifying transducer, is plotted vs the driving frequency. The generally good agreement between the predicted and measured results has encouraged us to extend the simplified sound-propagation model to more complex piping systems and to viscoelastic wall-liner materials.

[Sponsored by ONR]

Reference

1. R.A. Skop, "Sound Propagation Through Liquids in Viscoelastic Circular Cylinders," *Shock Vibr. Bull.* **51** to be published (1981).

Applications of Acoustic Holography in Nondestructive Evaluation, by A.V. Clark, Jr., *Marine Technology Division*

Scientists at NRL are investigating new ultrasonic methods to determine the size, shape, and orientation of materials' defects, as well as types of defects. Such methods are a significant advance over conventional ultrasonic nondestructive evaluation (NDE) methods, which reveal the presence (or absence) of a flaw but provide little additional information. Coupled with a knowledge of fracture mechanics theory, determination of the type of flaw and its geometry allows an assessment of the remaining service life of an object. The ability to estimate the service lifetime reliably can result in substantial savings,

since a part will not necessarily be rejected because it contains a flaw. Safety will also be enhanced.

One promising method of obtaining the acoustic image of the interior of an object is liquid surface levitation holography (LSLH). A typical system is shown in Figure 8. Ultrasonic waves (approximately 3 MHz) passing through a submerged object are imaged onto the surface of a thin film of imaging liquid. The imaging liquid, contained in a small tank (minitank), is separated from the water tank by a thin membrane (see Figure 9). A reference transducer of the same frequency emits a wave that forms an interference pattern with the acoustic image. This interference pattern creates a ripple on the surface, and the ripple is an acoustic phase hologram. Laser light reflected from the surface is phase modulated by the ripple and optically processed to reconstruct the acoustic image.

The potential of LSLH was assessed by calculating the transfer function for each subsystem. This served to determine the maximum image quality of the system under ideal conditions and to delineate the constraints required to achieve or approach this quality under real conditions. With this analysis as a guide, tests of the system were made at NRL. In these tests, the system was found to give good images of the interior of

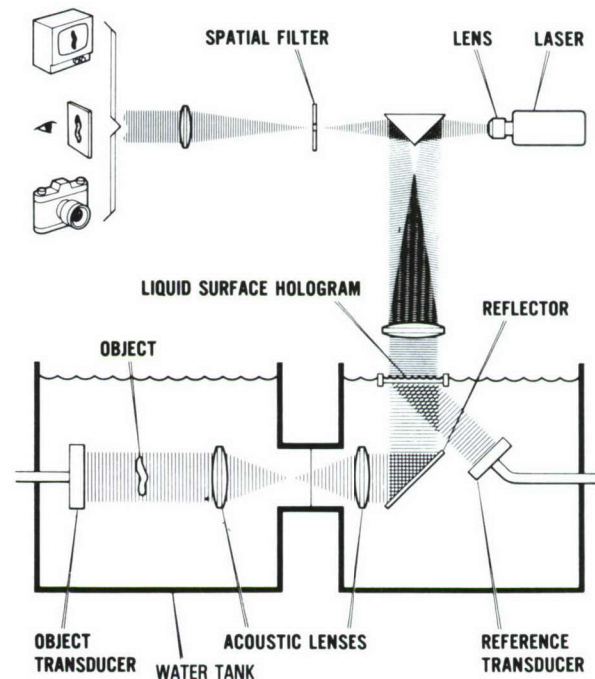


Figure 8. A typical liquid surface levitation holography system

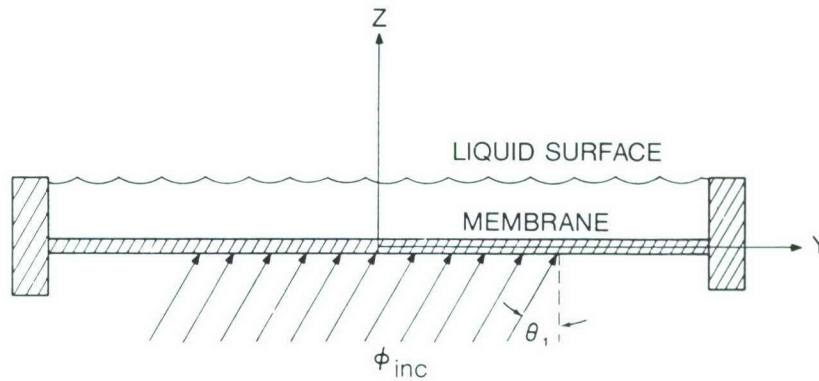


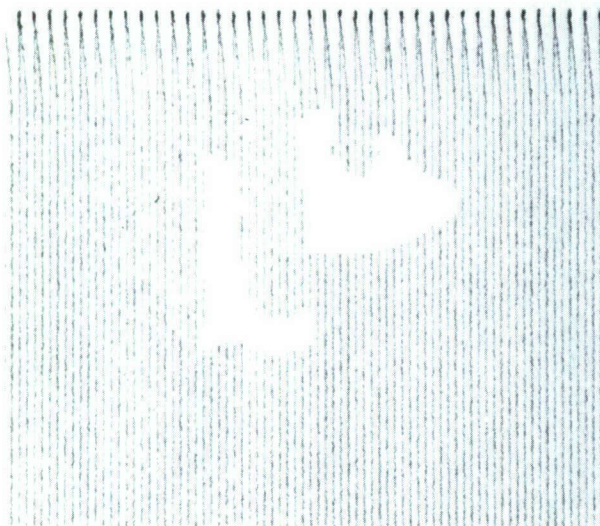
Figure 9. Acoustic wave ϕ_{inc} incident on the minitank membrane. The membrane is the bottom of the minitank and separates imaging liquid from the water in the water tank. The acoustic hologram is formed at the liquid surface.

objects that are good sound transmitters. Experiments to detect artificially produced flaws have shown that the system can give better images than conventional ultrasonic scanning techniques; an example is shown in Figure 10. Under ideal conditions, the system has a lateral resolution of about 1 mm. Also, the system produces real-time images, which is an asset should inspection of a large number of items be necessary.

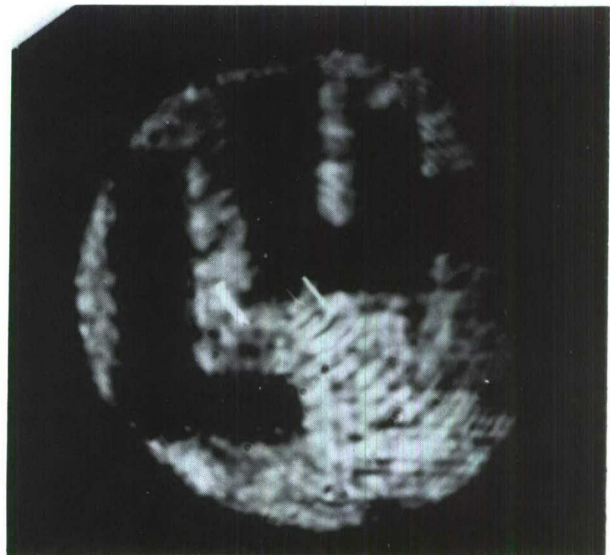
As a result of system use, some limitations on its performance were discovered. Since the image is composed of sound waves traveling at different angles of incidence to the liquid surface,

the most faithful reconstruction of the image would be obtained if the particle velocity of the imaging liquid surface were the same for every angle of incidence. However, multiple internal reflections within the thin film of the imaging liquid set up an angle-dependent interference pattern at the surface, thereby producing angle-dependent particle velocities. This effect can be reduced by suitable choice of the mechanical properties of the membrane, but it cannot be eliminated entirely.

Distortion of the membrane also degrades image fidelity. For instance, if the membrane has



C-SCAN IMAGE
5 MHz



ACOUSTIC HOLOGRAPHIC IMAGE
5 MHz

Figure 10. Comparison of acoustic images made with a conventional ultrasonic system (C-scan) and the LSLH System. Three Ls are imbedded at different depths in a graphite-epoxy composite panel. The image area is approximately 7 cm in diameter.

a sinusoidal deformation, then a wave passing through it emerges as several waves traveling in different directions in the minitank. Limits must be placed on the magnitude of the acoustic intensity of the object and reference beams to avoid distorting the membrane.

The ripple pattern is caused by the intensity of the interference between the reference beam and the acoustic image. There is also a slowly varying bulge of the liquid surface owing to "self-interference" of the reference beam and of the acoustic image, i.e., the intensity of each beam alone without interaction with the other. This bulge causes multiplicative noise in the optical reconstruction. Since the noise has the same spatial frequency content as the reconstructed acoustic image, it cannot be removed by optical filtering. However, if the bulge is flat over the illuminated portion of the surface, it will not degrade the optical playback; specifically, if the bulge distortion is a small fraction of an optical wavelength, it can be ignored. To achieve this requires that the acoustic intensities again be kept below a certain level.

Because of the constraints on acoustic intensity, the system cannot be used to image objects that have regions of high and low sound transmission (high-contrast objects). If the intensity is increased to form a reasonable image of the low-transmission region, the intensity in the high-transmission region may well exceed the allowable intensity levels. In fact, the system's dynamic range is rather limited because of constraints on intensity; it is much less than that of many other acoustic imaging systems.

The capabilities and limitations of the system have now been fully explored. Some improvement is possible, particularly regarding the minitank membrane, but the system's limited dynamic range restricts its utility at present to objects whose contrast between high and low sound transmission regions is not too high. For such objects, the system can be a useful NDE tool. For other objects, it will be necessary to develop different methods to meet the Navy's NDE needs.

[Sponsored by ONR]

Phase Calibration of Hydrophones, by L.D. Luker and A.L. Van Buren, *Underwater Sound Reference Detachment*

The Navy's use of sound in the ocean depends critically on its ability to detect incoming

sound signals. A key element in the detection process is the hydrophone, a device that transforms the sound signal into a corresponding electrical signal that can be analyzed to classify the incoming sound signal. In order to do this, however, we must know the receiving sensitivity of the hydrophone as a function of frequency.

Although the hydrophone sensitivity is often treated as an amplitude only, it also includes a phase angle. Except at low frequencies, the phase angle of the sensitivity varies considerably with frequency. Because of this variable phase angle, the frequency components of the signal combine differently at the output of the hydrophone than at the input, thereby changing the shape of the waveform. The original signal shape or waveform can be accurately reconstructed only if both the amplitude and phase angle of the hydrophone sensitivity are known.

The conventional calibration of hydrophones rarely involves the phase angle, possibly because of experimental difficulties encountered in its determination. One such difficulty is the accurate determination of measurement distances used in the calibration. At high frequencies, a very small distance error can produce a relatively large phase error. Another difficulty encountered is the accurate determination of sound speed in the measurement medium. Small errors in sound speed can also lead to large phase errors.

NRL scientists have developed a new hydrophone calibration procedure to eliminate these measurement problems. This procedure is an extension of a conventional three-transducer calibration to include phase, together with a special experimental configuration. The calibration requires the following three transducers: a sound source P, the hydrophone H to be calibrated, and a sound source T that can also be used as a hydrophone. A series of three sound source—hydrophone measurements are made using either P or T as the sound source and H or T as a hydrophone.

The hydrophone sensitivity is calculated from the results of these measurements. The phase angle calculation includes a factor that is ordinarily very sensitive to small changes in either the sound speed or the measurement distances. In the NRL procedure, however, the three transducers are mounted in a special in-line configuration in which this factor becomes a constant, independent of the sound speed and distances. The accuracy of the resulting phase angle determination is then limited only by the accu-

racy of the phase angles obtained in the series of three sound source—hydrophone measurements. Digital processing can be used to achieve high accuracy in these phase angle measurements.

A framework constructed to provide the required straight-line configuration for P, H, and T is shown in Figure 11, with the hydrophone H located between P and T. The results obtained with this framework and the new procedure are illustrated in Figure 12, which shows the phase angle of the sensitivity of a USRD type F42C hydrophone. The sensitive element in this hydrophone is a hollow ceramic sphere with a diameter of 2.54 cm. Two sets of measurements (indicated by triangles and circles) are shown to indicate the typical consistency of values between measurement sets. The experimental calibration results were systematically repeatable to within $\pm 2^\circ$.

The theoretical phase angle for a rigid sphere is shown in Figure 12 as the solid curve, showing the accuracy of the calibration procedure. Rigid-sphere theory is appropriate for lower frequencies, but at higher frequencies the sphere will deform under the influence of the oscillating sound field and a substantially more complex theory is required. Though not shown here, this theory calls for a null in the phase angle, as seen in the data here at 100 kHz. This null occurs as the hollow sphere transitions through a resonance from a stiffness-controlled mode on the low-frequency side to a mass-controlled mode on the

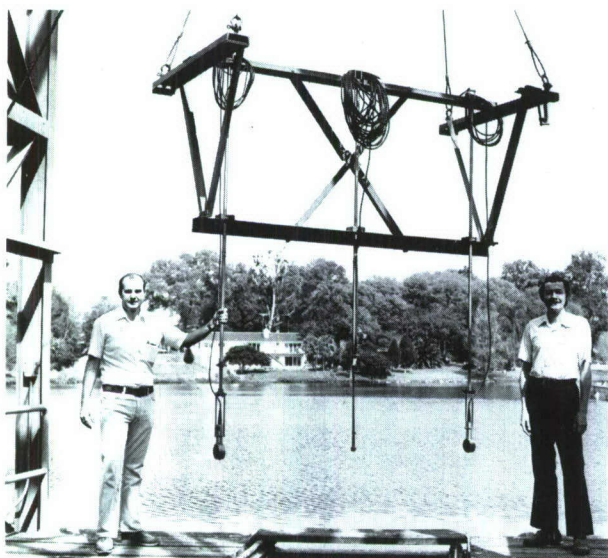


Figure 11. L. Dwight Luker (left) and A. Lee Van Buren with the framework for in-line support of the three transducers for NRL hydrophone calibration

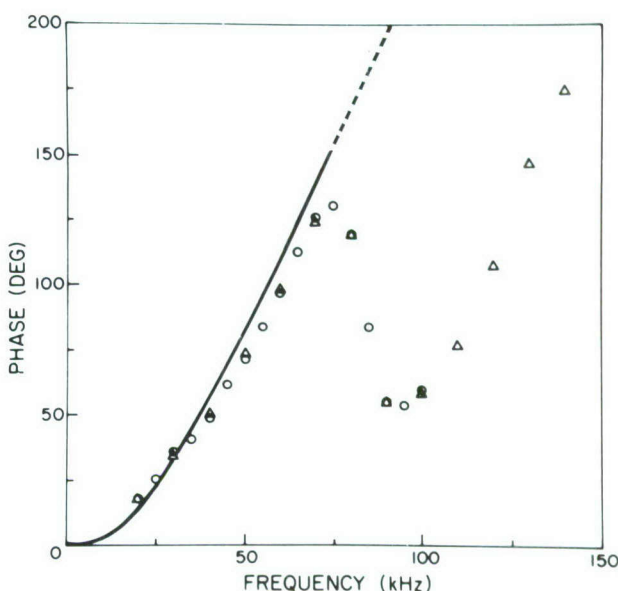


Figure 12. Phase angle of the receiving voltage sensitivity of the F42C hydrophone plotted as a function of frequency. Measured results are shown by circles and triangles, theoretical values by the solid curve.

high-frequency side. The good agreement between the measurements and the rigid-sphere theory up to about 75 kHz validates the calibration procedure.

This new calibration procedure allows the Navy to determine accurately both the phase angle and the amplitude of the sensitivity of a hydrophone, even at high frequencies. With this combined information, an incoming sound signal can be completely reconstructed from the hydrophone signal. This calibration procedure has been incorporated into NRL's underwater measurement system in Orlando, Florida.

[Sponsored by ONR]

New Omnidirectional Standard Transducers, by L.E. Ivey, *Underwater Sound Reference Detachment*

Since 1945, one of our missions has been to provide and maintain reliable, calibrated, wide-frequency-range hydrophones, reciprocal transducers, and projectors to meet the needs of the Navy and its contractors for standard measurement transducers in support of sonar, oceanography, and other underwater sound research and development. The transducers are calibrated and stocked in sufficient quantities to meet the Navy's current need for underwater electroacoustic standards covering the frequency range of 1 Hz to 3

MHz. They are calibrated at static pressures to 10 000 psi and at temperatures from 0 to 35°C. Calibration curves are prepared and furnished with each standard.

Also, transducers with special characteristics are provided as requested to meet urgent or unique Navy requirements. This service ensures quick response to calibration requirements and provides uniformity, accuracy, and reliability in underwater acoustic measurements throughout industry and the Navy. The USRD's underwater acoustic calibration center and standard transducer stock avoid duplication of effort and reduce the cost of the test and evaluation programs. In 1980, six new types of broadband, omnidirectional, underwater transducer standards were developed and added to the stock, bringing the inventory to 1500 standards of 35 different types.

The Navy's need for broadband transducers (projectors and receivers) with omnidirectional patterns to 150 kHz led to the development of the six new types of standards shown in Figure 13. For each of the six new standards, a hollow sphere was chosen as the sensitive element to obtain omnidirectional response characteristics in both the horizontal and vertical planes, and to provide simplicity of design coupled with good sensitivity. Each piezoelectric, lead zirconate-lead titanate (PZT) hollow sphere was designed to

give the highest sensitivity and drive level possible, consistent with omnidirectional characteristics for its particular frequency range. The spheres range from 1.27 to 15.0 cm in diameter and from 1.0 to 7.9 mm in wall thickness.

Each sphere is entirely encapsulated in a protective coating of black polyurethane that has good acoustic characteristics and provides excellent coupling to the water. The finished transducers (Figure 13) range from 2.6 to 19.0 cm in diameter and weigh from 0.5 to 13.6 kg (with cable).

Figure 14 shows the typical measured free-field voltage sensitivity of all six standards, each at the end of its individual cable length. The free-field voltage sensitivity is the ratio of the output open-circuit voltage to the free-field sound pressure in the undisturbed plane progressive wave. The responses indicate the usable frequency range and sensitivity level. Below 1 kHz, all are flat to 1 Hz.

Figure 15 shows the typical measured transmitting voltage responses of the six omnidirectional transducers. The transmitting response is the ratio of the sound pressure apparent at a distance of 1 m from the transducer's effective acoustic center to the signal voltage applied across the electrical input terminals. In their useful frequency ranges an undistorted

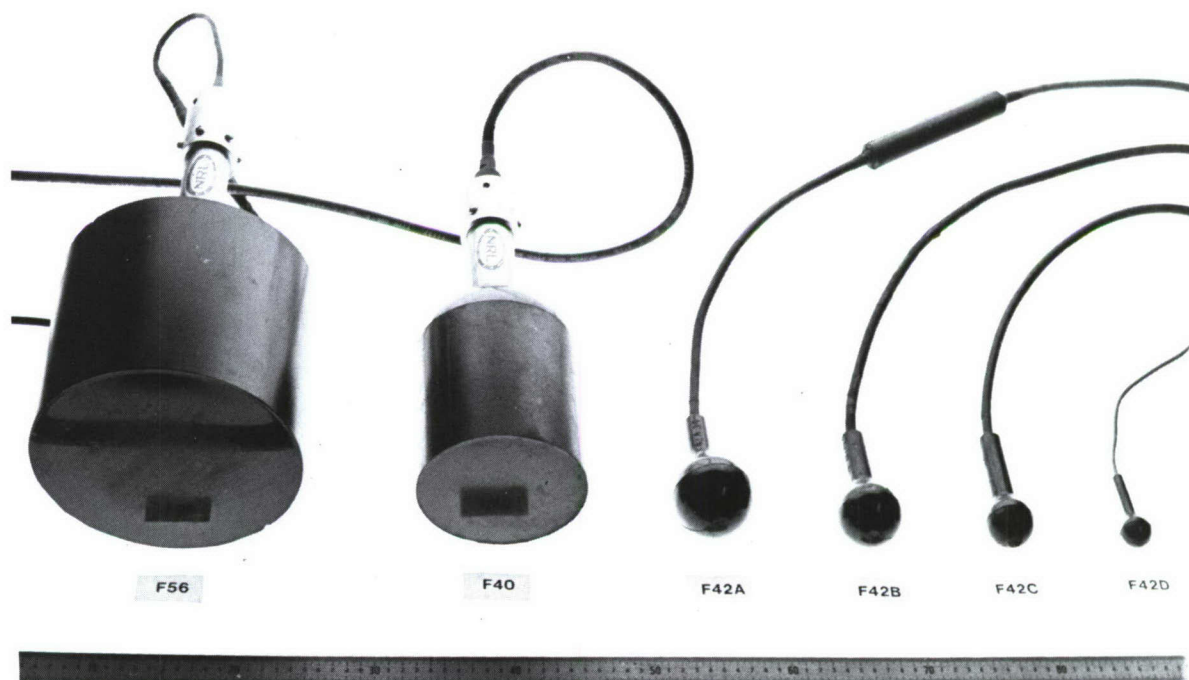


Figure 13. The six USRD type omnidirectional transducer standards

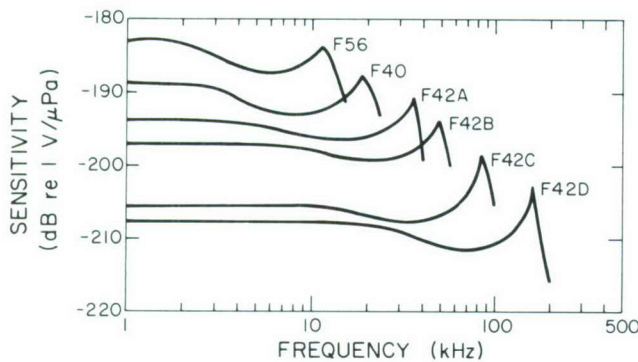


Figure 14. Typical free-field voltage sensitivity curves

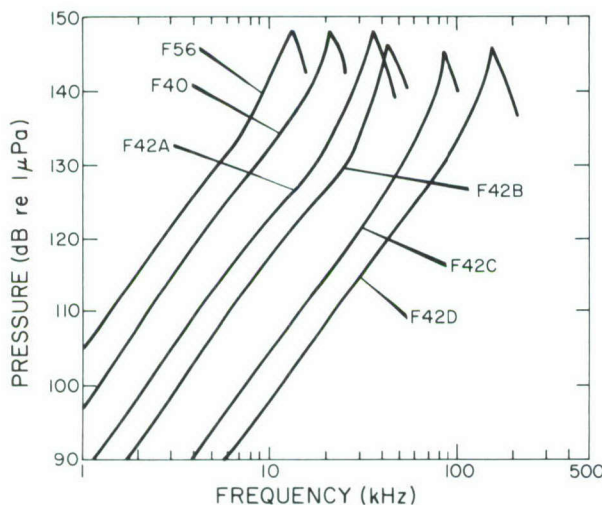


Figure 15. Transmitting voltage response curves for the six USRD omnidirectional transducer standards

source level can be produced that is linear with driving voltages up to 1000 V rms for the F56 and F40, 500 V rms for the F42A, 400 V rms for the F42B and F42C, and 100 V rms for the F42D. Below 1 kHz, the response has a slope of 12 dB/octave.

The broadband omnidirectional underwater transducers are now a part of the USRD transducer standards loan services program and can be requested by interested Navy activities and contractors.

At present, we are working to develop several additional underwater transducer standards to meet perceived needs. Three of these are as follows:

1. A pressure gradient hydrophone standard whose output is stable at temperatures ranging from 3°C to 40°C and at static pressures to 69

MPa. A working model has been developed and successfully evaluated at USRD. The basic design consists of a 6.35-cm aluminum sphere with two end-poled piezoelectric cylinders acting as accelerometers mounted 180° apart inside the sphere.

2. A towable at-sea, low-frequency sound-source monitor phone. This standard will eliminate cross-talk interference with the calibration signal normally encountered when monitoring a sound source output through long towing cables. The basic design consists of an FM communication system (modulator and demodulator) used to shift the frequency of its return signal to eliminate the effects of crosstalk. The FM signal is then amplified and transmitted by a line driver over the electromechanical towing cable.

3. A high-frequency probe hydrophone standard with a relatively flat receiving response and a nominal receiving sensitivity of -200 dBV/ μ Pa in the frequency range from 50 kHz to 1 MHz. A prototype model with an active element of thick film PVF₂ polymer has been successfully constructed and tested. This work is discussed in more detail in the following article.

A New Underwater Shock-wave Sensor, by S.W. Meeks, *Underwater Sound Reference Detachment*

The ability to measure the amplitude of large underwater shock waves is important to the Navy. For example, shock waves are used to test sonar transducers for resistance to underwater explosions, and their amplitude must be measured during the test.

The piezoelectric polymer polyvinylidene fluoride (PVF₂) shows promise for use as the active element of shock sensors. It is superior to piezoelectric ceramics frequently employed in this application because it is flexible and hence is less susceptible to deterioration or failure when subjected to the large stresses involved in a shock wave. Other advantages over piezoelectric ceramics are its acoustic impedance (near that of water) and its low mechanical Q factor. The good impedance match to water keeps the shock wave from making internal reflections in the PVF₂. The low value of the mechanical Q factor signifies damped mechanical resonance, which reduces ringing of the shock sensor. These material properties make PVF₂ an attractive candidate for an underwater shock-wave sensor. However, it was not known whether the material could provide sufficient bandwidth and linearity of response to

make it comparable to conventional sensor materials. Development and test of a prototype PVF₂ shock-wave sensor at USRD has answered the question in the affirmative.

The new PVF₂ shock sensor, designed and constructed at NRL, is shown in Figure 16. A thick-film (0.05-cm thick) PVF₂ element is embedded in the circular portion of the sensor nearest the viewer. The tripod-like frame is used to align the sensor with the axis of a shock tube during testing.

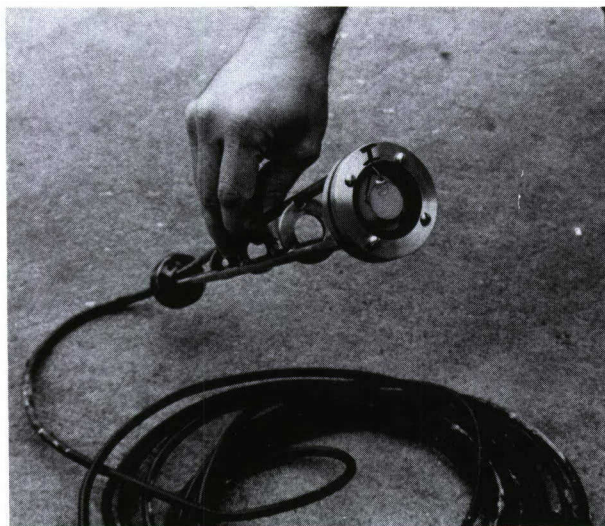


Figure 16. The new NRL shock sensor. A 0.05-cm-thick PVF₂ element is held by a steel retaining ring. Tripod is only for mounting during test and is not part of the sensor.

The frequency-domain calibration of the sensor is shown in Figure 17. This calibration provides the frequency response of the sensor by giving the output voltage for a unit incident pressure as a function of incident frequency. The calibration shows that the sensor's response is essentially flat and has a bandwidth of 2 MHz. The fundamental resonance of the PVF₂ film at this thickness occurs at 1.5 MHz, as seen by the slight rise in sensitivity at this frequency. The two deep fades in the frequency response at 100 and 200 kHz have been traced to the steel retaining ring seen in Figure 16, and could be eliminated by better design. The flatness of the frequency response is desirable in that no frequency correction is required to obtain the shock-wave characteristics. The 2-MHz bandwidth is comparable to conventional sensors and is required for the sensor to respond to the very high frequency components that are present in a shock wave.

A second area of importance in a shock sensor is the linearity of the device. Figure 18 shows the charge output in picocoulombs of a piece of thick-film PVF₂ vs the peak pressure of a 1-ms pressure pulse, as measured in a high-pressure test chamber. The dashed line indicates a perfectly linear response, and the solid line shows the measured output of the PVF₂. Figure 18 indicates that the PVF₂ is linear to within 0.6 dB to a peak pressure of 69 MPa (10 000 psi). This linearity is comparable to the conventional shock sensor materials tourmaline or PZT (lead zirconate-lead titanate).

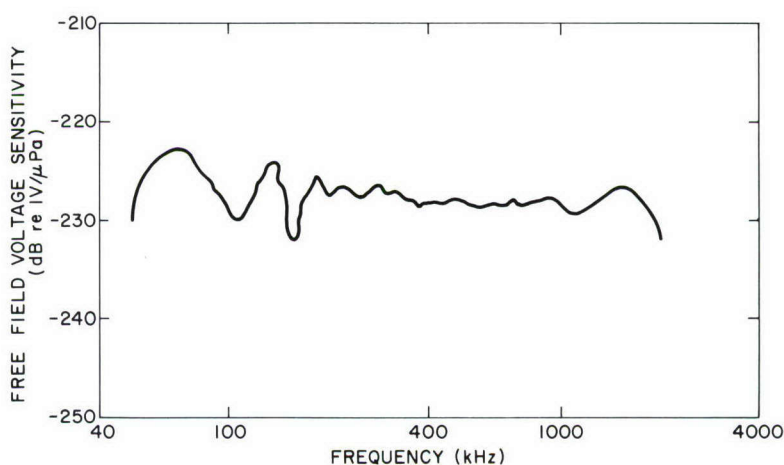


Figure 17. Frequency response of the PVF₂ shock sensor is flat from 300 to 1000 kHz. Deep fades at 100 and 200 kHz are caused by the steel retaining ring and could be removed by improved design. The slight resonance at 1500 kHz is associated with the 0.05-cm thickness of the PVF₂ element.

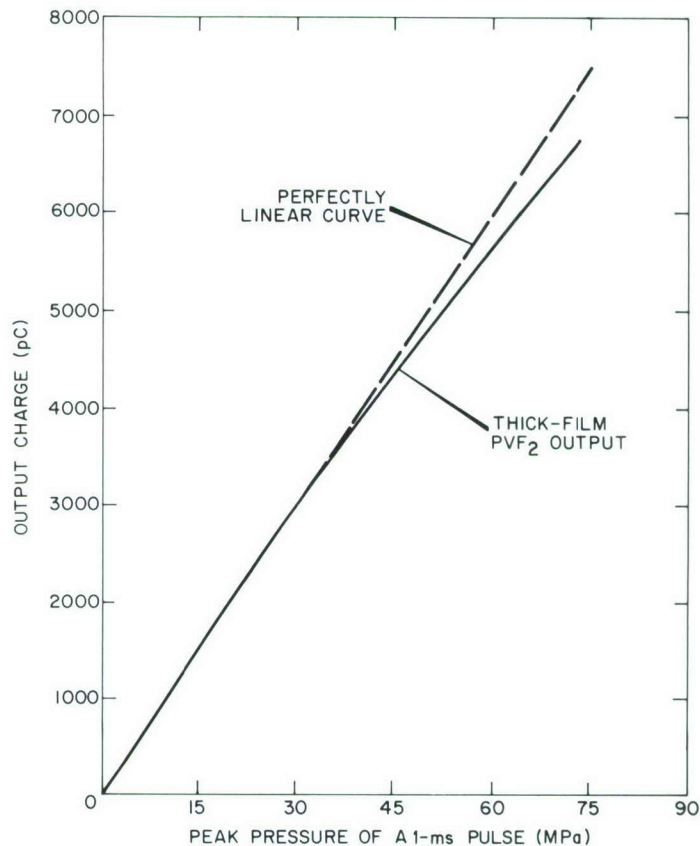


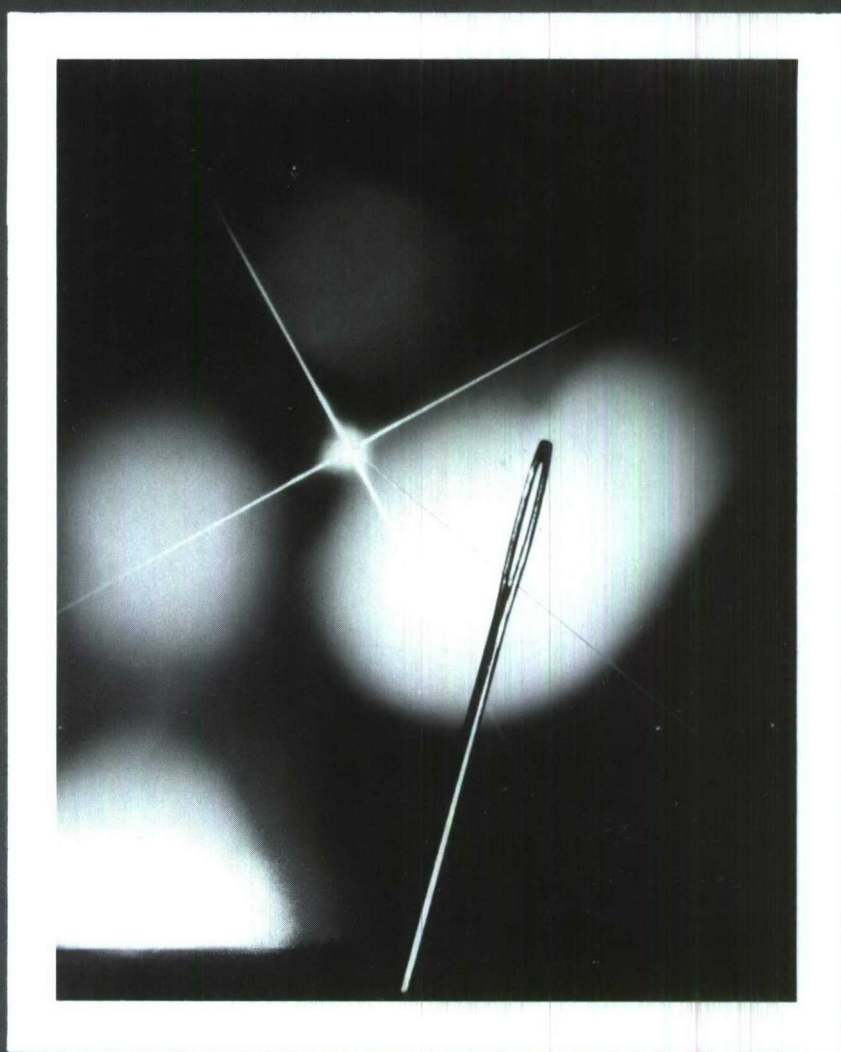
Figure 18. Pressure amplitude response of PVF₂ shock sensor. Response is linear to within 0.6 dB for a peak pressure of 69 MPa (10 000 psi).

The PVF₂ shock sensor has shown itself to be comparable in performance to shock sensors with active elements of conventional materials. No shortcomings or drawbacks have been found in its use in this application. Because of its supe-

rior resistance to failure under high stresses, this material is expected to provide improved sensors for shock-wave testing.

[Sponsored by NAVSEASYSKOM]

OPTICAL RESEARCH AND APPLICATIONS



OPTICAL RESEARCH AND APPLICATIONS

Traveling three hundred million meters a second with properties of both waves and particles, light provides unparalleled opportunities for the transmission, management, and collection of information and energy. NRL has made many important contributions to these areas, and Laboratory scientists and engineers are continuing the search for new understanding and innovative applications of optical phenomena.

Accurate Phase Measurement for Fiber-optic Interferometers	93
Fiber-optic Gyroscopes	94
Circumventing the Spatial-Resolution—Wavelength Barrier in Microscopy	96
Local Instances of Good Seeing	99

Accurate Phase Measurement for Fiber-optic Interferometers, by I.J. Bush, *Underwater Sound Reference Detachment*

In the past year, a system has been developed at NRL that produces accurate phase measurements in an optical fiber interferometer. This measurement system has demonstrated unique abilities in extracting signal information from interferometric sensors and promises to have significant applications in fiber sensor systems and their calibration. The measurement system is called a phase-feedback fiber-optic interferometer (PFFOI). It has the ability to operate accurately in the presence of thermal fluctuations, laser intensity fluctuations, and acute polarization rotation of the guided light.

Fiber-optic interferometric sensors produce phase-modulated (PM) signals, and thus require a PM detection system. The PFFOI detects PM signals, and its operation is similar to that of an electronic phase-locked loop (PLL) commonly used for detecting frequency-modulated (FM) signals. The fundamental difference between them is that the PLL feeds back to a voltage-controlled oscillator, and the PFFOI feeds back to a voltage-controlled phase shifter.

Figure 1 shows the block diagram of the NRL PFFOI set up for acoustic detection. Light from a single-frequency laser is split and launched into both arms of a single-mode fiber interferometer. The sensor arm is phase modulated by the acoustic signal, and the reference arm is phase modulated by modulators Mod 1 and Mod 2. The beams are then recombined to produce an interference pattern on the detector. Both Mod 1 and Mod 2 consist of lengths of fiber tightly wrapped around thin-walled piezoelectric cylinders. These modulators induce optical phase shifts resulting from an electromechanical radial

displacement of the cylinders. Mod 2 produces an optical phase that oscillates at frequency f_m and serves as a carrier for the acoustic information. Mod 1 is the voltage-controlled phase shifter. It produces the feedback from the system output that keeps the interferometer locked in phase, and also tracks thermally induced phase fluctuations. In the present laboratory configuration, Mod 1 is able to track phase shifts up to 1000 rad without loss of lock. If the system does lose lock, it resets itself to zero in approximately 1 ms and resumes its tracking of thermal and acoustic phases.

In addition to working in the presence of thermally induced phase fluctuations, it is also desirable that the system be robust to laser intensity fluctuations and acute polarization rotation within the interferometer. These effects produce amplitude fluctuations at the output of the optical detector. Since the signal information is at a carrier frequency f_m , these amplitude fluctuations are practically eliminated over a range of about 40 dB by use of an AC-coupled automatic gain control (AGC) following the detector.

The system was analyzed theoretically in order to assess the measurement potential of the PFFOI. The analysis showed that the system has nonlinear and nonconstant coefficient terms. However, when the system is operating in phase lock and system parameters are within specified bounds, approximations may be incorporated to model the system as linear and time invariant. This approximation presumes that the cutoff frequency for the low-pass filter is much lower than f_m (this effectively eliminates the nonconstant coefficient terms) and that the input signals to the multiplier are very close to quadrature (this implies that the system is in lock and is operating linearly). Then the model shows that the optical

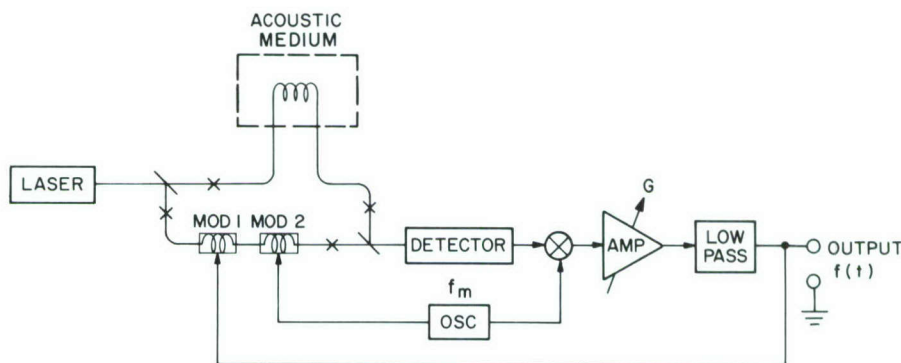


Figure 1. Phase-feedback fiber-optic interferometer (PFFOI)

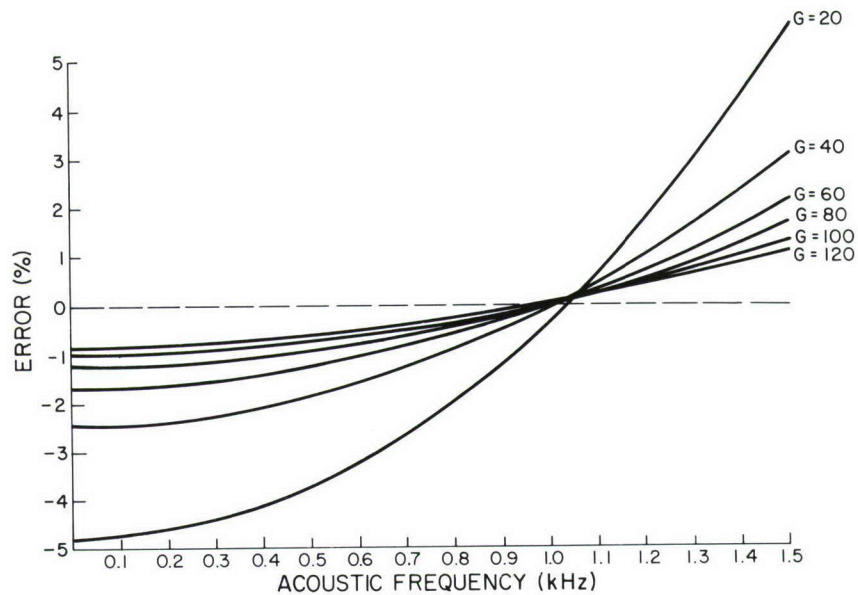


Figure 2. Detection system error vs acoustic frequency for various feedback gains G . Error is the difference between the acoustically induced phase in the sensor arm and the phase associated with the output voltage $f(t)$.

phase shift induced in the fiber coil by a sinusoidal acoustic driving function is also sinusoidal, and the steady state voltage output $f(t)$ depends only on the modulator constant, the feedback gain, and the low-pass filter time constant. Figure 2 shows the calculated measurement error of the system as a function of acoustic frequency for various feedback gains G . Note that the error decreases as G is increased. Typical measurement systems in the laboratory operate with G between 100 and 1000. The performance of the PFFOI has also been tested experimentally. A simulated acoustic signal was injected into the system, and the output was compared to the theoretical prediction. This test was performed over various ranges of feedback gain and acoustic frequencies; in each case, the theoretical predictions and experimental results were synonymous.

Devices that produce phase measurements with the accuracy seen in Figure 2 are very useful in the calibration of interferometric fiber-optic sensors. The first application of this system will be in the calibration and utilization of optical fiber hydrophones.

[Sponsored by ONR]

Fiber-optic Gyroscopes, by W.K. Burns, *Optical Sciences Division*

The optical fiber rate-of-rotation sensor or gyroscope concept is extremely attractive for

numerous Navy applications, especially for use in navigational systems. The components are inexpensive, compact, and without moving parts. The miniature solid state couplers are rugged, with minimal environmental sensitivity. Power requirements should be very low and component reliability should be very high. The inherent sensitivity of the fiber rate sensor is limited by detector noise, but is one to two orders of magnitude better than the corresponding quantum limit for ring laser rate sensors currently in use. These factors indicate that fiber rate sensors are potentially useful for very high precision applications.

The application of fiber optics to rotation sensing via the Sagnac effect (responsible for the phase difference between counterrotating beams in an optical fiber) was first demonstrated in 1976 [1]. Since then, progress has been made with fiber-optic sensors that detect rotation near the earth's rate ($15^\circ/\text{h}$). However, detectable rates are still far from the theoretical minimum rates of four to five orders of magnitude below the earth's rate. Barriers to progress generally are caused by environmental (i.e., temperature, barometric pressure, humidity) effects on unsophisticated optical components and by inherent limitations in design.

The traditional layout of an optical fiber rate sensor is shown in Figure 3. The output of a laser is divided by a beam splitter into two beams that are focused into opposite ends of an optical

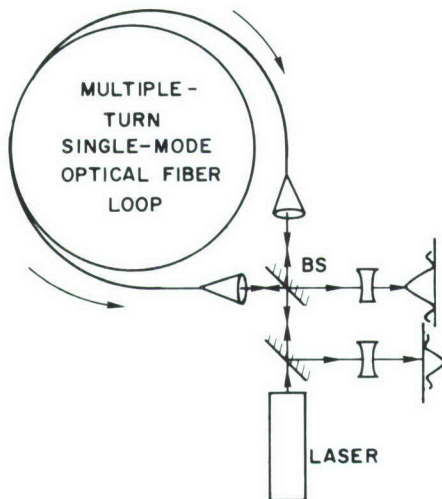


Figure 3. Standard fiber-optic rotation sensor. A beam splitter (BS) divides the laser output into two beams, each focused into opposite ends of an optical fiber loop. After the beams traverse the loop, they are recombined by the beam splitter into an interference pattern. The magnitude of the phase shift is a measure of the rotation rate. One weakness of this system is its zero sensitivity at a zero rotation rate.

fiber loop. After traversing the loop, the beams are recombined by the beam splitter to form an interference pattern. Rotation of the coil in its plane causes a relative phase shift between the counterpropagating beams that is detected by motion of the fringes in the interference pattern. The magnitude of the phase shift depends on the fiber length and coil radius, as well as the rotation rate.

One problem with the arrangement shown in Figure 3 is that it will have zero sensitivity at zero rotation rate. Sensitivity increases to a maximum when a nonreciprocal phase shift of $\pi/2$ is inserted in the fiber loop. This phase shift can be achieved by use of the Faraday effect, Bragg deflectors, or, less desirably, by misaligned or absorbing beam splitters. Alternatively, new input coupler schemes may be used to achieve maximum sensitivity.

NRL scientists have recently invented and demonstrated two novel input coupler configurations with which rate sensors displayed maximum sensitivity at zero rotation rate, without any additional component in the rate sensor loop. The first coupler concept, shown in Figure 4a, simply provides two inputs, with an adjustable phase difference between them, to the rate sensor's input beam splitter. When the

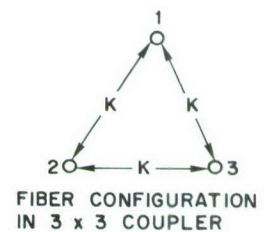
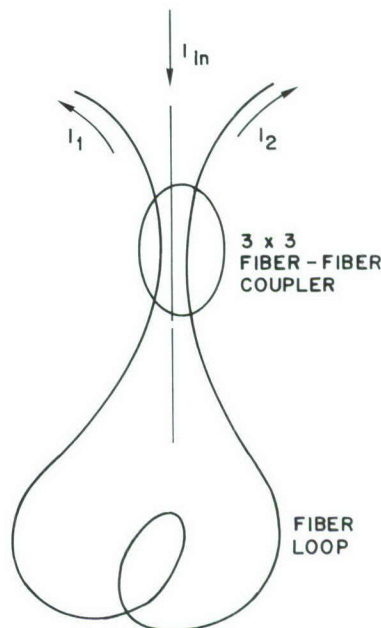
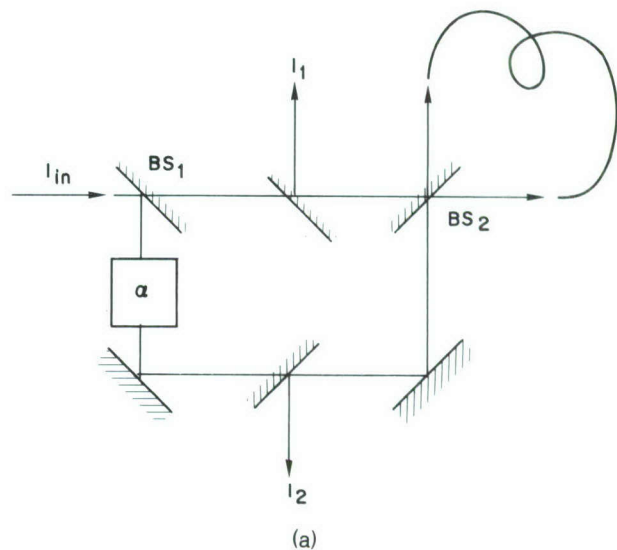


Figure 4. NRL's novel coupler concepts that provide inputs to the beam splitter. (a) Dual-input fiber gyroscope provides two inputs of equal amplitude but different phase to the beam splitter in Figure 3 (BS). The gyroscope (rate sensor) operates at the maximum sensitivity point, even at zero rotation, by appropriate adjustment of the input phase difference. Beam splitters can be any type, i.e., bulk, fiber, or integrated optics. (b) Fiber gyroscope with 3 input \times 3 output ports. Input is on one fiber I_{in} , which yields two evenly excited outputs and a maximum sensitivity point at zero rotation.

input phase difference is adjusted by a relative change in the optical path length to the appropriate value, the rate sensor automatically operates at maximum sensitivity. The beam splitter was first demonstrated in bulk form, but we envision improved performance with an integrated optics version. This rate sensor has considerable potential for a highly precise device.

The second NRL coupler concept (Figure 4b) is radically different because it is a 3×3 (3 input and 3 output ports) rather than the conventional 2×2 coupler. This device was implemented with three fibers in a fiber-fiber coupler. The input is on one fiber, with outputs from the other two. Because of the symmetry of the excitation of the outputs, maximum sensitivity is automatically achieved. This approach also provides a continuous fiber-optic path from source to detector, eliminating component motion and reflection effects for the first time in a fiber rate sensor. This concept was also demonstrated experimentally, and the resulting device represents the first rate sensor built without bulk optic components.

These experiments deal with one aspect of the fiber gyroscope problem. Further work will seek to isolate and reduce noise sources in the fiber-optic gyroscope.

[Sponsored by NAVAIRSYSCOM]

Reference

1. V. Vali and R.W. Shorthill, "Fiber Ring Interferometer," *Appl. Opt.* **15**, 1099 (May 1976).

Circumventing the Spatial-Resolution—Wavelength Barrier in Microscopy, J. Reintjes, T.J. Manuccia, and R. Waynant, *Optical Sciences Division*

The middle of the infrared spectrum (mid-IR) would be ideal to use in microscopic studies in biology and chemistry. Every biomolecule absorbs strongly somewhere in the mid-IR and has narrow, well-separated absorption bands at frequencies that are characteristic of the molecular species. Illumination with radiation in this wavelength range would provide the capability for microscopic studies in which the spatial distribution of naturally occurring molecular types could be determined. The spatial resolution of a microscope, however, is limited by the available aperture and the wavelength of the illumination light. For typical imaging systems it ranges

from one to a few times the illumination wavelength. This limitation is referred to as the wavelength—resolution barrier. For radiation in the mid-IR, spatial resolution is typically limited to values between 3 and 20 μm and is therefore insufficient to resolve many structures of biological interest.

Better resolution can be obtained by using visible light with wavelengths of the order of 0.5 μm . However, most naturally occurring molecules are transparent in the visible and therefore cannot be distinguished from one another. Some contrast can be achieved in the visible by using elaborate sample preparation techniques such as dyes, immunofluorescent agents, or metal-based stains to show the location of substances of interest, such as nucleic acids or fats. However, these techniques often do not have the capability for molecular discrimination and can introduce confusing artifacts, problems that are not present with the IR technique.

In the past year, scientists at NRL have devised a technique for circumventing the wavelength—resolution barrier. The technique allows them to perform microscopic studies that use molecular selectivity based on the vibrational infrared energy levels of naturally occurring molecules with the spatial resolution that is characteristic of visible light. The NRL technique makes use of coherent anti-Stokes Raman scattering (CARS). In this technique, the sample is illuminated with two laser beams with different wavelengths. The wavelengths are adjusted so that their frequency difference coincides with the vibrational frequency of the molecule of interest, driving the molecular vibration at resonance and exciting the vibrational mode. Simultaneously, the interaction of the laser light with the excited molecule produces a third light beam at a shorter, visible wavelength. This shorter, visible radiation, termed anti-Stokes radiation, is then imaged in any system with sufficient resolution, such as a conventional microscope. The anti-Stokes radiation is emitted only from those regions of the sample that contain the selected type of molecule. The image of the sample is the same as if it were taken in a dark field using the appropriate infrared radiation for illumination, but with improved spatial resolution.

The use of visible light allows access to specimens that may be opaque at the IR wavelengths of interest but which are transparent to visible light. Extremely short pulses, of the order of a few picoseconds in duration, are used

to obtain the high peak powers required for this technique without excessive average power requirements or excessive sample heating.

Preliminary experiments have been performed to demonstrate various methods for molecular discrimination. In these experiments, laser beams from an argon laser ($\lambda = 514.5$ nm, green light) and from a dye laser ($\lambda = 580\text{--}610$ nm, orange light) were used as pump sources to illuminate various samples. The anti-Stokes radiation for these interactions is typically in the blue region of the visible spectrum near 450 nm. Photographs of the anti-Stokes radiation from different types of samples are shown in the figures.

Figures 5a and 5b illustrate a technique for molecular discrimination based on the shift of the vibrational frequency depending on the type of molecule to which a molecular group is bonded.

The sample cell contained an immiscible combination of octane (top) and acetonitrile (bottom). For each picture, the top and bottom regions of the cell were illuminated with the pair of laser beams. In Figure 5a, the frequency difference of the pump lasers was adjusted to match the C—H vibrational frequency in octane, and the anti-Stokes radiation, which appears as a bright spot in these pictures, is visible only in the top of the cell. In Figure 5b, the frequency difference was changed to match the C—H vibrational frequency of the acetonitrile, and the anti-Stokes radiation is visible now only in the bottom of the cell.

A second technique for molecular discrimination is illustrated in Figure 6, which is based on using a different type of molecular group. In this figure, the difference frequency was adjusted to match the frequency of the $\text{C}\equiv\text{N}$ vibration of acetonitrile, and anti-Stokes radiation is visible

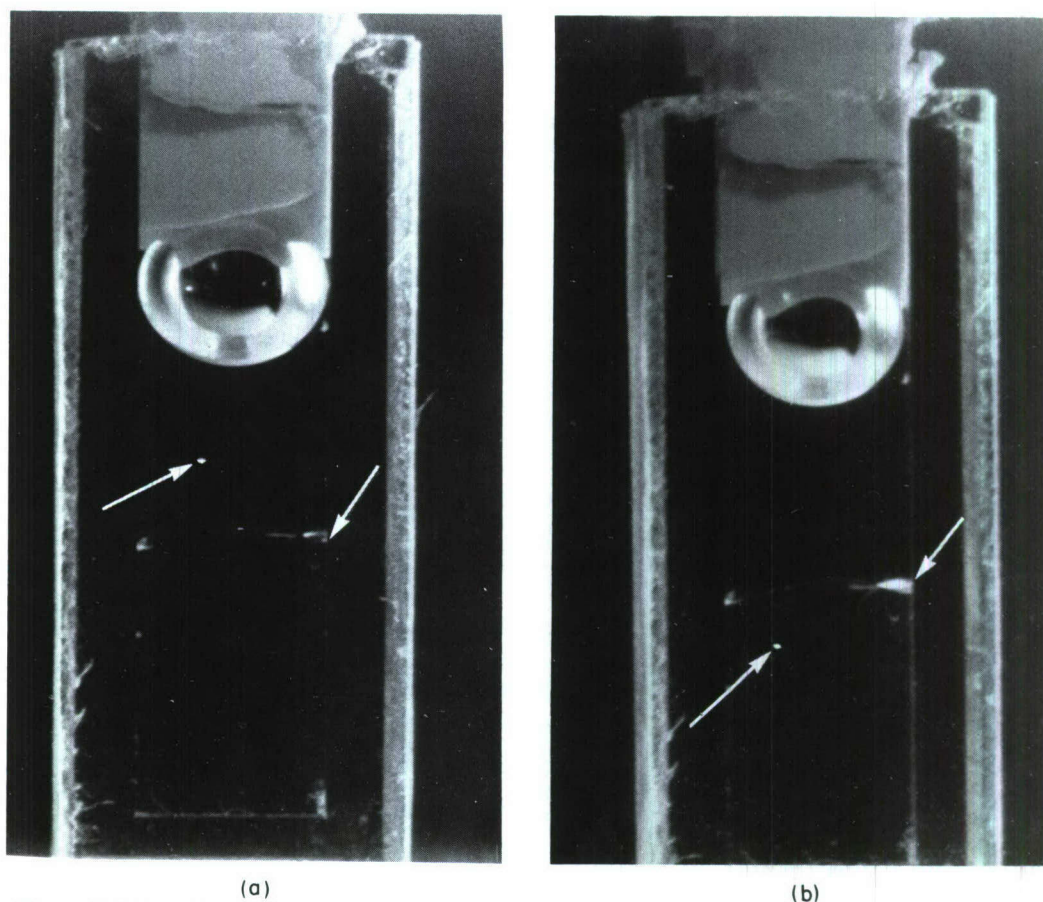


Figure 5. Intermolecular contrast using a shift in the frequency of a given type of Raman resonance (in this case C—H) in different molecular species. The cell contains an immiscible combination of octane at top and acetonitrile at bottom. Both regions are illuminated with two laser beams as described in text. The frequency difference of the two laser beams is adjusted to match the C—H Raman resonance of octane in (a) and of acetonitrile in (b), and CARS beams (left-hand arrows) are observed only from the corresponding regions of the cell. The horizontal outer dimension of the cell is 5 mm, and the anti-Stokes Raman spot is $50\text{ }\mu\text{m}$ in diameter. The meniscus dividing the two liquids is indicated by the right-hand arrows, and an air bubble is evident at the top in each picture.

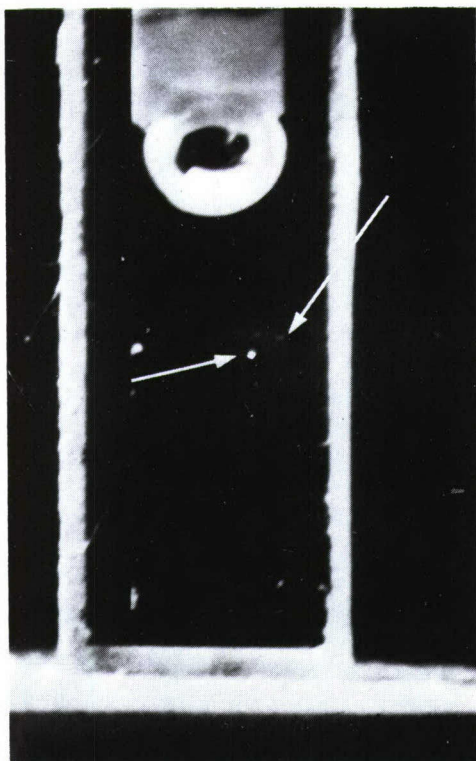


Figure 6. Intermolecular contrast resulting from functional group substitution. Same arrangement as in Figure 5. The frequency difference is adjusted to match the $\text{C}\equiv\text{N}$ Raman resonance in acetonitrile. The CARS beam (left arrow) is observed only from the bottom region of the cell.

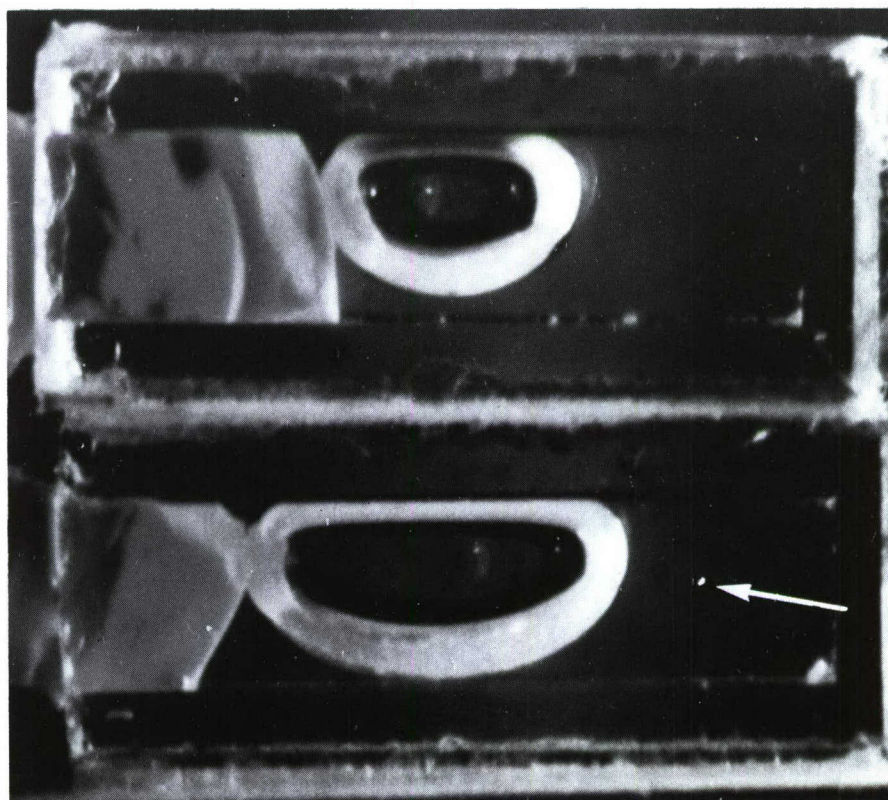


Figure 7. Intermolecular contrast resulting from isotopic substitution. The two cells contain normal octane (top) and deuterated octane (bottom). Frequency difference is adjusted to match the $\text{C}-\text{D}$ Raman resonance of the deuterated material. The CARS beam is observed only from the deuterated octane cell. The vertical outer dimension of each cell is 5 mm, and the diameter of the anti-Stokes spot (arrow) is $50\ \mu\text{m}$.

only from the acetonitrile at the bottom of the cell.

In Figure 7, a third method is used, based on a shift in frequency due to an isotopic substitution. In this case, deuterium was substituted for hydrogen. Two sample cells were used, one containing normal octane (top) and the other deuterated octane (bottom). When the difference frequency is adjusted to match the frequency of the C—D vibration, anti-Stokes radiation is visible only from the lower cell. The spatial resolution of these pictures was limited by the available laser power to the size of the laser spot, about 50 μ m.

With reasonable increases in laser power, spatial resolution of the CARS technique should improve. We anticipate that this technique, in combination with the use of deuterated materials, would allow one to observe the uptake, metabolism, and final disposition of nutrients, drugs, toxins, and other environmental agents within biological cells. Purely physical processes such as membrane translocation, cytoplasmic transport, and storage could be viewed, leading to unique information in biochemical/structure issues such as the spatial organization of metabolic pathways in micron-sized organisms. We believe that this technique will prove to be considerably more convenient than techniques such as immunofluorescence and autoradiography now being used to obtain similar information. Certainly, the NRL technique can serve as a valuable complement to them.

[Sponsored by ONR]

Local Instances of Good Seeing, by H.H. Szu and J.A. Blodgett, *Optical Sciences Division*

Imaging through a medium that is varying randomly with time, such as the atmosphere or a disturbed liquid—air interface, produces distorted and blurred images. The development of automatic pattern-recognition systems, however, requires good imagery in order to use such standard techniques as template matching. Although only limited restoration toward a true picture is possible with the information contained in a single image, improvements should be possible when a time sequence of the available distorted and blurred images is used. Image degradations do not distort or blur all parts of an image equally, and occasionally there are entire image frames or parts of frames that are not degraded at all. This accounts for the fact that seeing through

a telescope frequently seems to be better than photography indicates. In this case, the eye and brain perform a selection of those instances of good seeing and a rejection of the degraded images.

In an earlier work, Gregory [1] developed an analog scheme that mimics this selection process and applied it to the stellar imaging problem. This technique selects only those instances when the entire image is good, and hence is very inefficient if applied to imagery with a spatially varying distortion, such as is obtained with a wide field-of-view imaging system looking through a turbulent atmospheric path. Because disturbances do not always degrade all portions of an image and because many distortions are really local relative movements of parts of an image, a technique that operates locally on each portion of an image to perform a limited correction and selection process would be considerably more efficient and would provide significantly improved imagery.

The theoretical basis for an approach to image restoration based on these ideas has been published [2]. Basically, we have the image equation

$$i_l(\bar{x}) = \int s_l(\bar{x}, \bar{x}') O(\bar{x}') d\bar{x}' + n_l(\bar{x}),$$

where $i(\bar{x})$ is the image, $s(\bar{x}, \bar{x}')$ is the point spread function, $O(\bar{x}')$ is the object, and $n(\bar{x})$ the noise. In general we wish to find a filter $m(\bar{x}, \bar{x}')$ that restores the object $q(x)$ from the available image data

$$q(x) = \sum_{l=1}^L \int m_l(\bar{x}, \bar{x}') i_l(\bar{x}') d\bar{x}'.$$

For nonselective image summation,

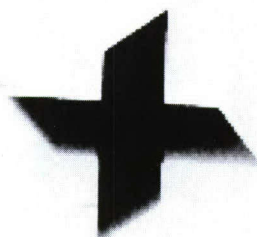
$$m_l(\bar{x}, \bar{x}') = \frac{1}{L} \delta(\bar{x} - \bar{x}').$$

This would produce a long-time-average image. In this approach, we wish to find a new filter m_l that selects and corrects individual images in the sequences based on image measures of the individual images and the long-time-average image.

An algorithm to implement these ideas has been developed and tested on simulated laboratory imagery. The actual steps in the process are as follows: (1) perform a global centroid registration for each image frame of the sequence, i.e.,

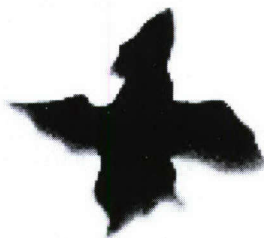
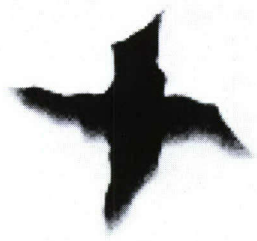
$$\langle \bar{x}_l \rangle = \int \bar{x} i_l(\bar{x}) d\bar{x}$$

is determined for each image and superimposed; (2) sum all of the centroid registered frames to get a motion-corrected master frame; (3) divide



(a)

Figure 8. (a) Undistorted object (no surface waves or object motion) used for testing; (b) Three typical images from a sequence of 30 used for processing. Distortion was the result of imaging the moving object (Figure 8a) through a wavy water surface.

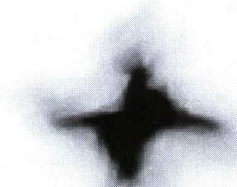


(b)

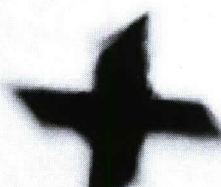
the master frame and each frame of the sequence into small square regions the approximate size of an isoplanatic patch (the region over which the blur or distortion is the same); (4) perform a local centroid correction on each square of each frame so each square agrees with the corresponding square of the master frame; (5) compute the integrated intensity of each square and compare with that of the master frame; (6) select or reject the individual parts of the image on the basis of predetermined threshold differences; (7) and, finally, perform a properly weighted average of all

of the corrected and selected elements to form the restored image.

A video image of a simple pattern was obtained by looking through a wavy water surface at a moving object; this image was used to test the restoration scheme. Typical images from the sequence as well as the undisturbed image are shown in Figure 8. Thirty frames in a 1-s sequence were used to obtain a restored image. The frames were processed using our hybrid image processing system and the NRL advanced scientific computer system. Each frame required



(a) LONG-TERM
AVERAGE



(b) CENTROID
CORRECTION



(c) LOCAL CORRECTION

Figure 9. (a) Long-term-average image obtained by directly adding the 30 distorted images in the sequence; (b) Long-term-average image obtained by adding the 30 distorted images after each was shifted so as to have a common centroid; (c) Restored image obtained by adding the acceptable corrected portions of each of the 30 images of the sequence. Note that the sharp and soft edges of the object are more faithfully reproduced in (c) than in (b).

about 1 s of central processor time, but the code was not optimized with parallel processing.

Results of the restoration are shown in Figure 9. Figure 9a shows the simple sum of all 30 images, Figure 9b shows the sum of the 30 frames after each was registered to a common global centroid, and Figure 9c shows the result of the local restoration scheme. The restored image is considerably closer to the undisturbed one than the centroid registered sum. The "hard" edges are much sharper (a factor of 3 compared to Figure 9a), while the "soft" edges maintain their gray scales faithfully (compare with Figure 9a). The overall integrated difference from the true image has been reduced by about 35%.

The use of image sequences to obtain restored images has the potential of making a significant impact on automatic image-processing and pattern-recognition systems. The improvements offer the promise of increased stand-off ranges for target recognition and/or improved target distinction.

[Sponsored by ONR]

References

1. R.L. Gregory, *Nature* **203**, 274 (1964).
2. H.H. Szu, J.A. Blodgett, and L. Sica, *Opt. Commun.* **35**, 317 (1980).

ATMOSPHERIC BEHAVIOR AND PROPERTIES



ATMOSPHERIC BEHAVIOR AND PROPERTIES

The ocean of air that surrounds our planet is an ever-present and sometimes critical factor in naval activities. Many of these functions involve the transmission of electromagnetic energy and the manner in which it affects, and is affected by, the atmosphere. From molecular composition to global structure and dynamic behavior, the atmosphere has been a long-standing area of productive research activity at NRL.

Reduced-density Channels in Gases at Atmospheric Pressure	105
Convective Cooling of Lightning Channels	106
Starlight and the Nighttime Ionosphere	108
Modeling the Equatorial Spread-F Scintillation Environment	109
Finite-element Modeling of Convection-diffusion Problems	111

Reduced-density Channels in Gases at Atmospheric Pressure, by R.E. Pechacek, M. Raleigh, and K.A. Gerber, *Plasma Physics Division*

The Navy has always needed to understand both natural and man-made atmospheric phenomena, but with the rising possibility of directed-energy weapons, the need to understand effects caused by the interaction of such potential weapons with the atmosphere has been heightened. To satisfy this need, NRL scientists have designed and developed an experiment to study the formation and relaxation of hot, reduced-density channels in the atmosphere.

Channels are created by the absorption of pulsed CO_2 laser radiation in nitrogen and by ohmic heating from laser-guided (and unguided) electric discharges in the atmosphere. The channels produced by the CO_2 laser are used to study the influence of channel shape on the hydrodynamics of cooling, whereas those formed by laser-guided electric discharges are used to study prebreakdown phenomena and the decay of ionization in the atmosphere. Thus the two types of channels are used to simulate particular characteristics of channels that might be formed by the passage of a charged-particle beam through the atmosphere as well as those formed by lightning (see the following article). Of course, for the former application, it would be more direct to study channels produced by the passage of suitable charged-particle beams through the atmosphere, but such beams do not yet exist. In the meantime, these simulated channels provide real data for comparison with theoretical models and allow us to develop diagnostic techniques.

A long cylindrical chamber has been constructed (Figure 1) to produce reduced-density channels in nitrogen by the absorption of pulsed CO_2 laser radiation. The chamber is divided into two main sections: a nonabsorbing, convergence section filled with dry nitrogen and an absorbing target section filled with nitrogen doped with 1% sulfur hexafluoride. The CO_2 laser beam is focused through a windowless transition region to small diameter and high intensity in the target section. The pressure inside the chamber is maintained at slightly above atmospheric pressure by causing the gases to flow continuously as indicated. The CO_2 laser pulse duration is $\leq 3 \mu\text{s}$, and the laser can deposit 50 to 200 J in the channel at energy densities of $\sim 0.4 \text{ J cm}^{-3}$. Between shots, the chamber must be evacuated and filled with dry nitrogen before the system flow can be reestablished.

The generation of hot channels in the atmosphere by laser-guided electric discharge involves a preliminary designation of the desired path by laser-induced, aerosol-initiated air breakdown. Radiation from the Q-switched Nd:glass laser (60 J in 40 ns) is focused with a 5-m focal-length lens (Figure 2), and air breakdown is enhanced by the presence of a light smoke ($\sim 10^{-7} \text{ g cm}^{-3}$). Air breakdown occurs over a length of at least 2 m near the focus of the lens, and the atmosphere is sufficiently perturbed to guide an electric discharge along the laser path, provided that the voltage is applied within 10 to 100 μs . The electric discharge is driven by a small Marx generator that is normally charged to $\sim 240 \text{ kV}$ and fired $\sim 30 \mu\text{s}$ after the Nd:glass laser. The peak

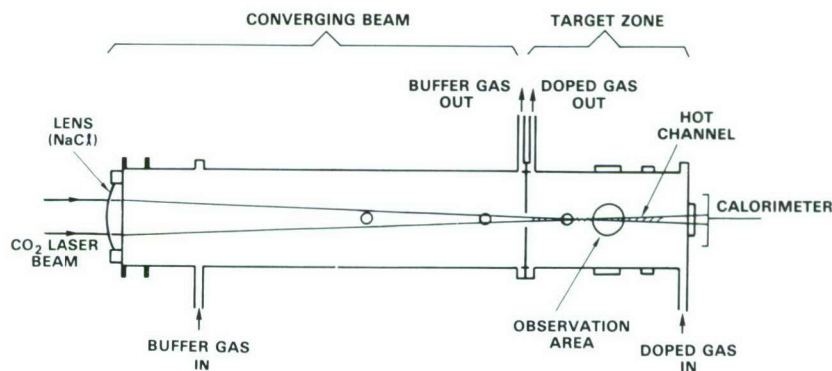


Figure 1. The chamber used to produce reduced-density channels by the absorption of pulsed CO_2 laser radiation in an absorbing atmosphere. The overall length of the chamber is 3.5 m, the length of the target section is 1 m, and the focal length of the salt lens is 3 m.

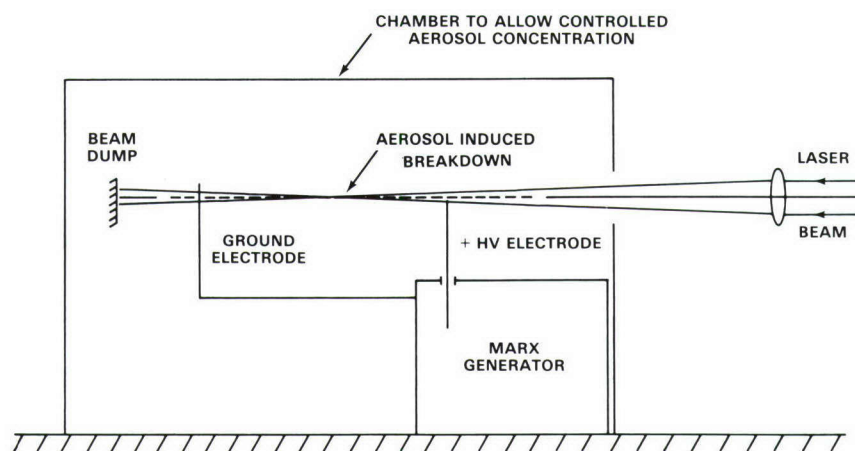


Figure 2. The arrangement used to produce laser-guided electric discharges in the atmosphere

discharge current is typically ~ 10 kA, which dies away in $\sim 6 \mu\text{s}$. For channels ~ 100 cm long, the Nd:glass laser deposits ~ 15 J per meter of channel length and the electric discharge deposits 350 J m^{-1} .

After the deposition of energy, both types of channels expand and reach pressure equilibrium with the surrounding cold gas at radii between 1 and 2 cm. Then they become turbulent and expand again as they are cooled by entrainment of cold outside gas into the hot channel. The channels that are most nearly cylindrically symmetric (i.e., some of those produced by absorption of CO_2 laser radiation) cool from an initial equilibrium temperature of ~ 1500 to ~ 350 K within ~ 10 ms. Channels produced by laser-guided electric discharges cool from equilibrium temperatures of ~ 5000 to ~ 400 K in only ~ 1 ms. If these centimeter-size channels were to cool by thermal conduction (i.e. with no turbulence), the time scale for cooling would be ~ 100 ms. Clearly, the observed cooling rates are orders of magnitude faster and show the significance of turbulence in this situation.

[Sponsored by ONR and DARPA]

Convective Cooling of Lightning Channels, by J.M. Picone and J.P. Boris, *Laboratory for Computational Physics*; and J.R. Greig and M. Raleigh, *Plasma Physics Division*

Lightning exerts a profound influence on both the atmosphere and the biosphere of the earth through the production of nitrogen oxides (NO_x). Nitrogen oxides participate in many

important photochemical reactions and may be a major factor in determining the atmospheric ozone content. In addition, NO_x deposited on the earth's surface by precipitation represents a significant input to the fixed nitrogen reserve of the biosphere and is important in photosynthesis.

A lightning stroke produces NO_x by intense heating of the air along the path of the stroke. After the lightning current ceases, a channel filled with hot gas, including nitrogen oxides, remains. The volume of hot gas and the rate at which the channel cools determine the net amount of NO_x produced. These two factors have been quite controversial for the past twenty years. Recently, NRL scientists have been involved in experimental and theoretical studies of similar hot gaseous channels produced by electric discharges in the laboratory. Application of the NRL results to lightning has resulted in a clearer picture of the behavior of lightning channels, a physical mechanism for the cooling of such channels, and a much-needed estimate for the cooling rate.

Scientists at NRL produced the schlieren photographs of separate, identical electric discharges shown in Figure 3. The photographs were taken at different times after the discharges were initiated, thus providing a unique study of the time development of the hot channels. The discharges, each 15 cm in length, were produced by a Marx generator with an erected voltage of ~ 250 kV. The current had a peak value of ~ 10 kA, a period of $\sim 3 \mu\text{s}$, and a duration of $\sim 6 \mu\text{s}$. The ambient pressure and temperature were ~ 1 atm and 300 K, respectively, and the initial radius of each discharge was ~ 3 mm. Figure 3 shows

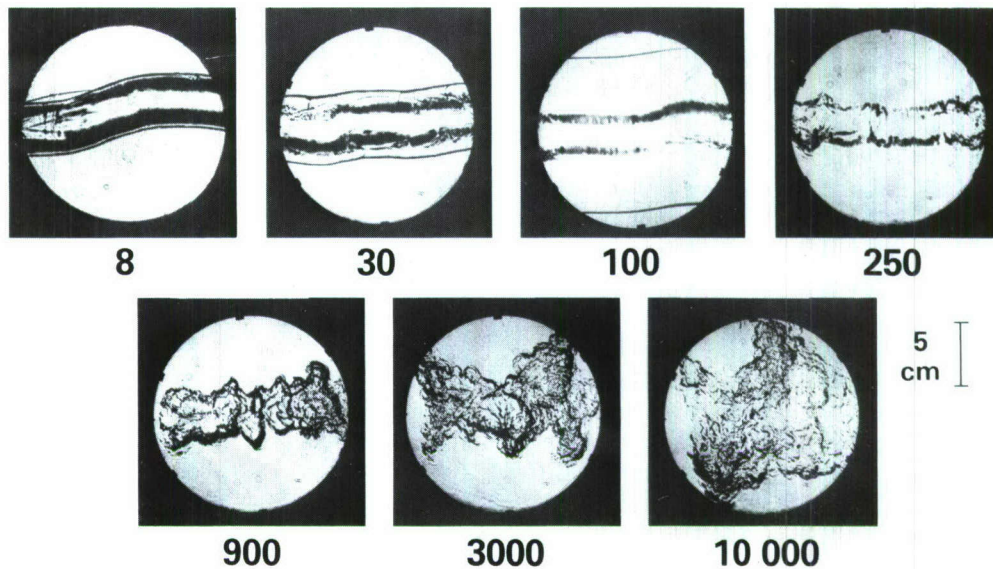


Figure 3. Schlieren photographs of separate, nominally identical, unguided electric discharges in the atmosphere. The discharge length and voltage were 15 cm and 250 kV, respectively. The numbers beneath the photographs are the times, in microseconds, at which they were taken. The exposure time was 25 ns.

that a hot, smooth, curved channel with a diameter of ~ 3 cm forms within $8 \mu\text{s}$ of the initiation of the discharge. The rapid expansion of the hot gas has compressed the cooler air just outside the channel boundary, producing a shock wave, which appears as a sharp line at the edges of the channel. By $100 \mu\text{s}$, the shock has decoupled from the channel and has propagated toward the limits of the camera's field of view. The channel is now at pressure equilibrium with the surrounding air. The interior gases have a temperature of around 5000 K and a density that is approximately $1/20$ the density of ambient air. Notice that the channel boundary is smooth and appears to be undisturbed. By $900 \mu\text{s}$, however, the boundaries have begun to distort violently and the channel has started to expand due to entrainment of the cooler ambient air. The photograph at $3000 \mu\text{s}$ shows evidence of further expansion and of small-scale density variations, indicated by the chaotic structure inside the channel. We interpret this as evidence of turbulence. By $10^4 \mu\text{s}$, the channel contains ~ 20 times the original volume and density variations are less pronounced, indicating that the channel has cooled considerably. Although lightning discharges have a higher peak current and last longer, their behavior should follow the pattern shown in Figure 3. This will be especially true for the cooling process, since both lightning and laboratory

discharges are quite short relative to the respective cooling times.

From our experiments, therefore, we see strong evidence that a hot channel produced by lightning cools by the entrainment of cool surrounding air. Although others have proposed this mechanism, NRL scientists are the first to explain how such convective mixing can occur. Our theoretical analysis and computer simulations have revealed that asymmetries in the discharge channel during the expansion to pressure equilibrium will generate long-term rotational motion (vorticity) in the vicinity of the hot channel. Examples of possible asymmetries in the case of lightning include the following: two-dimensional distortion from a circular cross section, displacement of the axis of the lightning stroke from the axis of a preceding lightning stroke, and three-dimensional distortions, as in Figure 3. Theoretical calculations at NRL have provided analytic formulas for the strength of the rotational motion, the time scale of the cooling process, and the relationship between the cooling rates of the laboratory channels and actual lightning channels.

By using these formulas in conjunction with detailed numerical simulations and the experimental data, we have reached two major conclusions. First, the proposed mechanism of vorticity generation by asymmetries in the electric discharge channels provides excellent agreement

with the laboratory data and applies to lightning discharges as well. Second, an average of 400 cm³/s of cool air mixes convectively into the hot lightning channel for each 1 cm³ of hot gas present in the channel after expansion to pressure equilibrium. This mixing rate is ~ 1000 times faster than that due to thermal conduction. Thus, lightning channels cool quickly, leaving behind a large percentage of the nitrogen oxides present after expansion to pressure equilibrium.

Through the above work, NRL scientists have provided considerable insight into the process by which lightning discharges produce nitrogen oxides. We have described the formation and cooling of lightning discharge channels in detail and have calculated the cooling rate, a key parameter in NO_x production. This work should thus be instrumental in resolving the long-standing controversy regarding the dynamics and cooling of lightning discharge channels.

[Sponsored by ONR and DARPA]

Starlight and the Nighttime Ionosphere, by R.R. Meier, *Space Science Division*; D.F. Strobel, *Plasma Physics Division*; and C.B. Opal, *Space Science Division*

To understand and ultimately predict the effects of changing ionospheric conditions on communications requires that the sources and sinks of ionization be identified and understood. Early theoretical models of the ionosphere could account for the observed ion abundances during the day, but at night the predicted decay rate of ionization through recombination in the lower ionosphere was too rapid. Observations showed that additional ionization in the *E*-region (95–150 km) occurs throughout the night.

A variety of potentially important sources had been suggested, but a quantitative evaluation was not performed until 1974 when a study was conducted jointly by the Plasma Physics and Space Science Divisions at NRL [1]. This work showed that high-altitude atomic hydrogen in the earth's outer atmosphere (extending halfway to the moon) remained sunlit and therefore was capable of scattering solar far-ultraviolet (FUV) ionizing radiation into the night sector. This radiation consists primarily of the H-resonance line at 102.6 nm (the Lyman- β line), which can ionize only O₂. These calculations, based on early observations of this airglow, showed that it was of sufficient magnitude to account for the missing source. At that time, it was also recognized that

starlight (stellar continuum between 91.1 and 102.6 nm) could contribute to nighttime ionization, but quantitative models of FUV star fields were not available.

In the intervening years, several developments occurred that led to the reevaluation of these conclusions, and a new study was undertaken to assess the relative importance of ionization sources at night. First, new observations of the terrestrial Lyman- β (and its by-product at 656.3 nm, the H Balmer- α line) required a downward revision by a factor of 4 of the ionization rate as deduced from earlier measurements. Thus, whereas Lyman- β remained an important source just after sunset, it was insufficient by midnight and an additional ion production mechanism was needed. Second, a computerized UV star catalog was developed at the Smithsonian Astrophysical Observatory; this could be used for a quantitative study of the ionizing effects of starlight.

Again in 1979 a joint modeling effort by the Plasma Physics and Space Science Divisions was performed to reevaluate the problem [2]. The resulting computations showed that starlight (along with Lyman- β) can indeed account for routinely observed ionization levels at midnight through ionization of O₂.

An interesting conclusion of this work is that a strong seasonal modulation of the ion production rate is expected as the positions of the Milky Way and Orion in the sky change. In Figure 4, the calculated starlight production rate of O₂⁺ at 120 km (in the *E*-region) is plotted as a function of time of year at three latitudes. Since the brightest stars occur in the southern hemisphere sky, it is not surprising that 30°S latitude has the largest ionization rate, almost a factor of 4 larger than 18°N during the northern spring. The time variation of the O₂⁺ production rate is consistent with the positions of the southern Milky Way and Orion in the night sky.

In summary, it now seems that we can satisfactorily account for the major sources of ionization at night. However, a detailed comparison of theory with any specific observations of ion abundances in the *E*-region is difficult because dynamic effects of winds and gravity waves can substantially redistribute the ions. Nonetheless, it may be possible to detect the seasonal variations shown in the figure by incoherent backscatter radar measurements. Such an observational test to verify the theoretical expectations would be highly desirable. Ultimately, all photo-

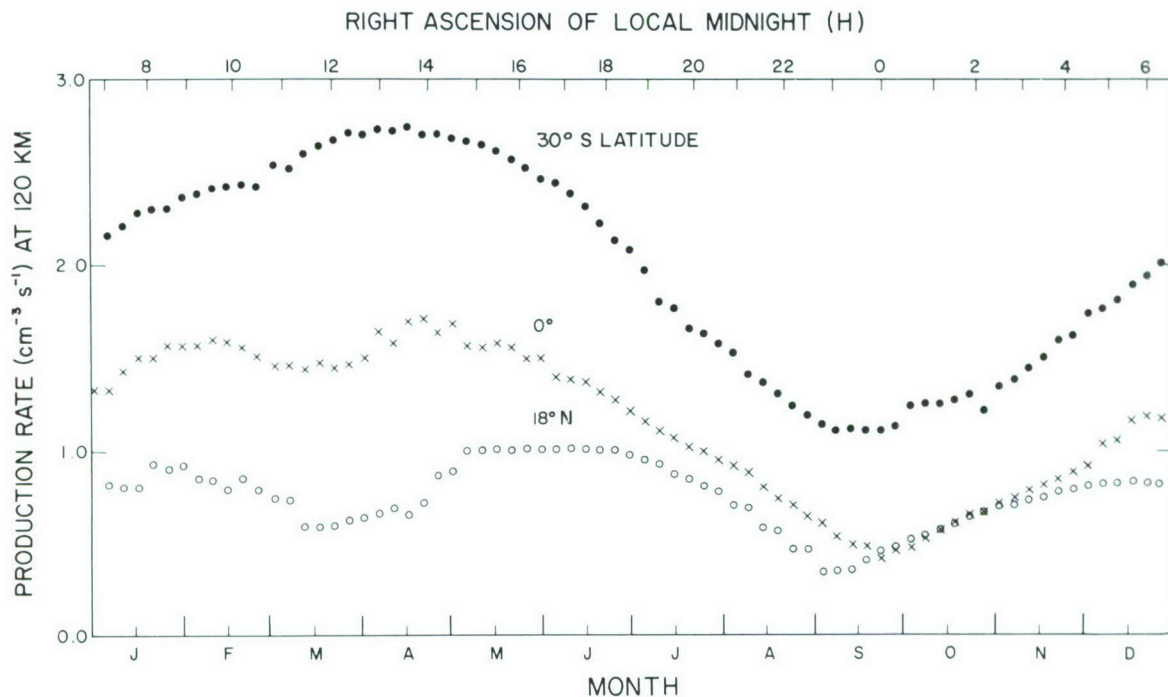


Figure 4. Calculated seasonal variation of midnight O_2^+ ionization rate at 120 km at various latitudes. Point-to-point structure is due to discrete placement of individual stars in the sky map.

chemical models of the ionosphere should routinely incorporate these sources of radiation.

[Sponsored by ONR]

References

1. D.F. Strobel, T.R. Young, R. R. Meier, T.P. Coffey, and A.W. Ali, *J. Geophys. Res.* **79**, 3171 (1974).
2. D.F. Strobel, C.B. Opal, and R.R. Meier, *Planet Space Sci.* **28**, 1027 (1980).

Modeling the Equatorial Spread-F/Scintillation Environment, by S.L. Ossakow and S.T. Zalesak, *Plasma Physics Division*

Ionospheric *F*-region irregularities can seriously perturb radiowave signals sent from Navy satellite systems, i.e., Command, Control, Communication, and Intelligence (C^3I) systems. The effect of irregularities in the refractive index or electron density is to superpose random fluctuations of signal amplitude, phase, and polarization (known as scintillation effects) that may cause an intolerable number of errors in the received signal and result in unusable information. *Ionospheric spread-F* is the term used for the diffuse echoes shown in the virtual height vs frequency

diagrams (ionograms) obtained from ionosonde (pulse-sounder) observations. The cause of spread-*F* is the irregular structure in the electron density of the ionospheric region. Spread-*F* occurs at all geomagnetic latitudes, mainly at nighttime, but also at high latitudes in the daytime. However, it is most intense at the geomagnetic equator. Spread-*F* has a high correlation with the occurrence of *F*-region irregularities that cause satellite radio-wave signal scintillation.

An understanding of the basic physical processes governing the formation of these irregularities must be obtained if they are to be predicted. To that end, NRL scientists are conducting theoretical and numerical simulation studies of equatorial *F*-region irregularities to provide a better understanding of the basic mechanisms involved and of the relationships among these irregularities, spread-*F*, and scintillation phenomena. An important element of this research has been the development of the non-linear two-dimensional (perpendicular to the geomagnetic field) model discussed in this article.

Although equatorial spread-*F* (ESF) was discovered over four decades ago as diffuse echoes on ionograms, it is only in the past five years that significant headway has been made in understanding the phenomenon. Much of this

progress comes from a combined theoretical and experimental approach to the problem. Advances in radar backscatter measurements, satellite and rocket in situ measurements, and theoretical and numerical simulation techniques have provided a clearer picture of the fundamental mechanisms causing ESF.

Figure 5 depicts the basic equatorial night-time ionospheric F -region geometry under which ESF occurs. Gravity, g , pointing down, causes a horizontal current in the x -direction. Coupled with the electron density $N(y)$ gradient on the bottom side (below the F -region peak, which is defined by the maximum in $N(y)$), this drives the instability (collisional Rayleigh-Taylor instability) on the bottom side. The geometry for our model is two-dimensional (x, y in Figure 5), because the physical quantities have been averaged over the geomagnetic field direction. Also, F -region irregularities are seen to propagate mainly perpendicular to the geomagnetic field.

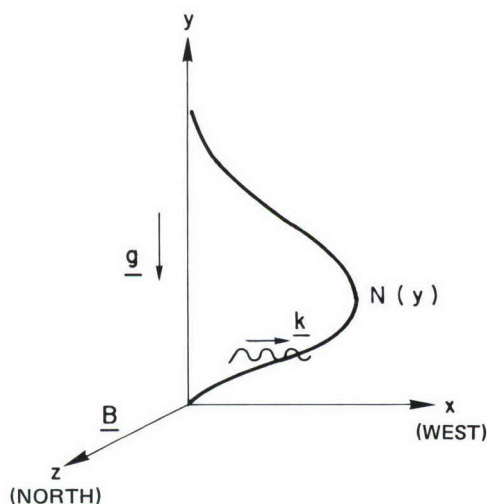


Figure 5. Basic equatorial spread- F geometry. $N(y)$ represents the ambient background electron density as a function of altitude y . Gravity g points down, the geomagnetic field B is horizontal and points north (z), and k represents a horizontal perturbation in the electron density and points westward (x).

The geometry is similar to fluid situations in which a heavy fluid is supported by a light fluid (increasing electron density on the bottom side), which we know to be unstable. The bottom side of the profile steepens and rises at night due to chemical recombination and upward electrodynamic forces. Irregularities are then observed

on both the bottom and top sides of the F peak. Large plasma depletions (bubbles of low electron density) are observed on the bottom and top sides. Linear theories had been able to explain irregularity formation (instability) on the bottom but not on the top. It is the nonlinear evolution included in our models that allows us to explain how irregularities, which initially form on the bottom, appear on the top, and also how large plasma bubbles are formed.

The appropriate system of coupled, nonlinear, two-dimensional differential equations, which are derived theoretically and are thought to represent the essential physics of the processes under study, includes (a) a continuity equation for the electron density and (b) a Poisson-like equation for the electrostatic potential that results from setting the divergence of the current equal to zero. A two-dimensional (x, y) numerical simulation corresponding to the geometry depicted in Figure 5 has been carried out.

Figure 6 shows the time evolution of the electron isodensity contours at 300, 700, 1000 and 3000 s after initialization (at zero s an east-west perturbation, representing a long-wavelength, neutral, atmospheric gravity wave or noise in the physical situation, is impressed on the entire simulation plane). The first frame (300 s) shows ripples in the density contours on both the top and bottom sides, with the bottom-side ripple growing and the top-side ripple damping (decaying) according to the linear theory of the collisional Rayleigh-Taylor instability. This instability mechanism, driven by gravity and the bottom-side electron density gradient in the regime where collisions between ions and neutrals are important, initiates bottom-side ESF. The succeeding frames show the nonlinear evolution of the irregularities by the collisional Rayleigh-Taylor mechanism. Note that at 700 s the top-side ripple has decayed appreciably while the bottom-side irregularities are still growing (increasing in amplitude). At 1200 s, we see a single bubble (depletion) of ionization extending from the bottom to the top side. The bubble has a vertical rise velocity of 200 m s^{-1} , and its central portion is depleted by over two orders of magnitude. Thus, low-density plasma is convected from the bottom to the top side of the F -region along with the irregularities. Further irregularities would develop from the steep electron-density gradients surrounding the bubble and could be seen with higher resolution simulations.

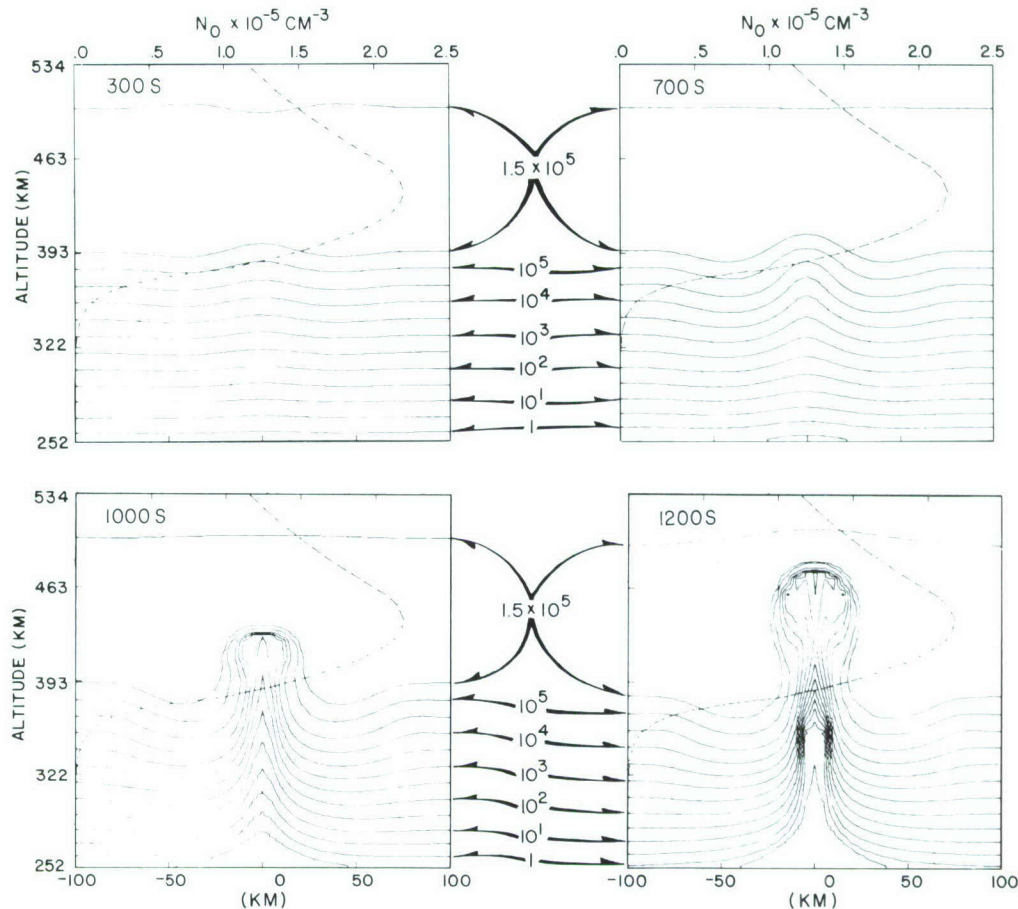


Figure 6. Sequence of plots showing electron isodensity contours of numerical simulation at 300, 700, 1000, and 1200 s. Superimposed on each plot is a dashed curve showing $N(y)$, the ambient background electron density, at any point in the east-west (x) direction, and labeled at the top. The isodensity contour levels indicated are in units of cm^{-3} .

These results show that the collisional Rayleigh-Taylor instability generates ionospheric irregularities and plasma bubbles on the bottom side of the nighttime equatorial F -region, which then rise beyond the F peak by nonlinear induced electric-field motion. These types of results were the first to explain the appearance of long-wavelength irregularities on both the bottom and the top side of the equatorial F -region. In addition, the bubble phenomenon produced is in accord with many observations. The tools developed constitute a major advance in our understanding of ESF phenomena and provide a basis for further study.

Although a coherent picture of ESF is emerging, there are still problems worthy of investigation. We have included only gravity as a driver in order to pursue a simple model. For explanation of other ESF phenomena, the effects

of horizontal neutral winds, electric fields, etc. should be incorporated into the model. The conditions needed to produce ESF irregularities and the properties of these irregularities, derived from the numerical simulations, are vital in obtaining a true understanding of and the ability to predict these irregularities. The predictive ability, in terms of onset and duration times of the irregular structures and their properties, is important for useful satellite systems' design, as well as for prediction in areas where data are sparse or nonexistent.

[Sponsored by ONR and DNA]

Finite-element Modeling of Convection-diffusion Problems, by G.A. Keramidas, *Marine Technology Division*

Various physical phenomena are described by the same governing equation, known as the

generalized transport equation. One of its forms is the convection-diffusion equation which may describe the propagation of thermally induced waves or the transport of pollutants in the atmosphere or in the ocean. The study of these physical phenomena requires the solution of this equation in physically realistic domains. Because of the complexity of these problems in realistic settings, analytic solutions are not feasible and numerical solutions must be obtained directly from the governing equation.

Many classical numerical approaches exist in the literature for limiting cases in which the process is dominated by either convection or diffusion. These existing numerical approaches are derived from either a finite-difference or a finite-element approximation. Most of the schemes produce results of acceptable accuracy for either convection- or diffusion-dominated flows, but they lack uniformity of performance over the intermediate range that is frequently encountered in physically realistic problems.

A program of research has been undertaken at NRL to develop a uniformly valid approach for solving convection-diffusion problems. The principal objective is to establish a capability for the numerical solution of this equation under realistic conditions. One result of this effort has been the formulation of a strong variational principle for the convection-diffusion equation through the introduction of a variable termed the *transport displacement* [1]. The formulation of this principle immediately brings to bear on the problem some of the most powerful techniques of numerical approximation theory. In particular, the finite-element method in its strong form can be applied to this variational formulation for the solution of the convection-diffusion equation. An example

of this application is the simulation of the dispersion of a pollutant in the atmosphere or of dissolved impurities in the ocean.

For a wide class of initial distributions of the pollutant, the numerical model will predict accurately not only the position of the concentration in time and space but also the change of the form of the distribution caused by different physical conditions. For instance, if the initial distribution propagates through a medium with very small diffusion, the form of the wave should remain almost the same. But if the medium has diffusive properties, then the pollutant should also disperse as it propagates.

The accuracy of the new method can be illustrated by a simple one-dimensional example for which the exact analytic solutions are known. Figure 7 shows the propagation of a pollutant concentration past a fixed observation point for four combinations of physical diffusion (K_0) and medium velocity (V_0). In each case, the discrete numerical results are in good agreement with the analytic solution (solid curve). The uniform accuracy of this method throughout the range of parameter values is demonstrated by the comparison. Other numerical methods do not achieve such accuracy over the whole parameter range. With this new method, calculations can be made in realistic two- and three-dimensional geometries to study how different parameter combinations affect the redistribution of an initial concentration of pollutant.

[Sponsored by ONR]

Reference

1. G.A. Keramidas, "Finite Element Modeling for Convection-Diffusion Problems," NRL Memorandum Report 4225 (May 1980).

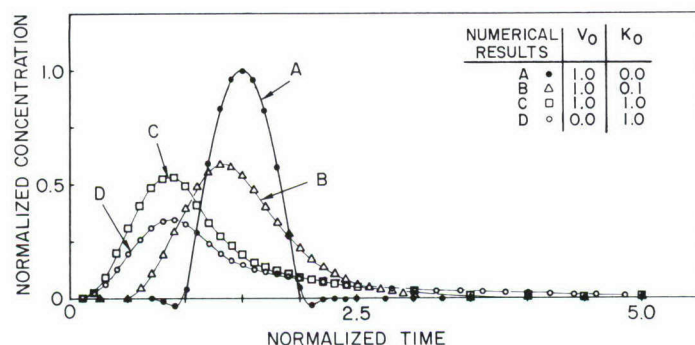
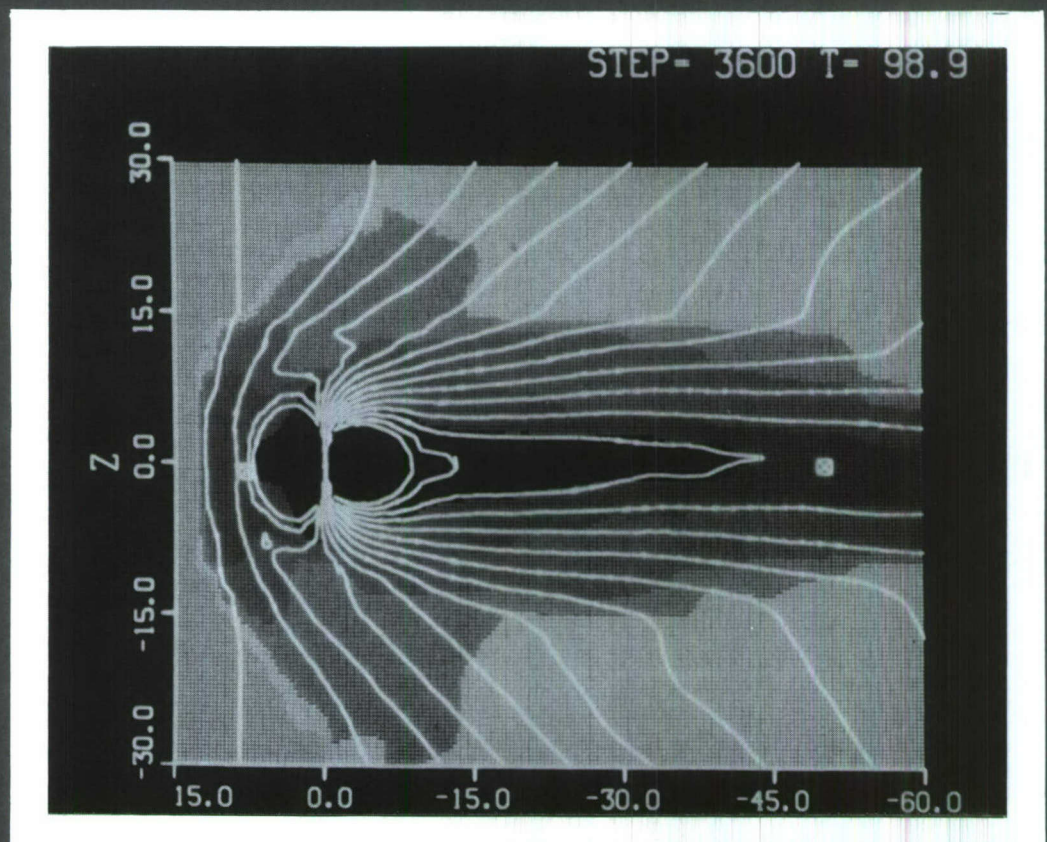


Figure 7. Concentration as a function of time at a fixed observation point. The numerical results agree with the exact analytic solutions (solid curves) for all four combinations of physical diffusion (K_0) and medium velocity (V_0).

SOLAR SCIENCE AND SATELLITES



SOLAR SCIENCE AND SATELLITES

NRL was twenty-three years old when its scientists conducted the first rocketborne astrophysical experiments in 1946. Eleven years later, the earth's first artificial satellite heralded new opportunities for important capabilities in communications, navigation, and data collection. Today, *satellite* is a household word, and there are many sophisticated systems providing those new capabilities. NRL has been a significant contributor to these developments and is continuing to seek both improved capabilities and the new understanding of our planet and universe that they make possible.

The Sun as a Variable Star	115
Solar Ultraviolet Spectral Irradiance Monitoring Program	116
High-resolution X-ray Spectra of Solar Flares	119
Modeling of Solar Wind Interaction with the Earth's Magnetosphere	121
Semianalytic Method for Satellite Orbit Determination	122
Parametric Wave-spectra Measurements from Aerospace	124

The Sun as a Variable Star, by J.W. Cook, G.E. Brueckner, and M.E. VanHoosier, *Space Science Division*

Astronomers have long thought of the sun as a typical, quiet, well-behaved star producing a steady output of radiation. Other stars *do* show quite large changes in their emitted radiation, some periodically and others irregularly. Some examples are δ Cephei variables, RR Lyrae variables, novae and supernovae, and a host of other variable types that astronomers have classified. These variables represent a small fraction of all stars, are typically more massive than the sun, and have evolved to later stages of their life cycle. But we know that the sun is, in some sense, a variable star because it does go through a solar activity cycle. This is most obviously characterized by a growth and decay in the number of sunspots present on the solar surface and also by a similar growth and decay, in about 11 years, of the amount of bright active regions surrounding sunspots.

With the beginning of space observations of wavelengths below 300 nm (the far ultraviolet), pioneered by NRL, astronomers began to suspect that the solar radiative output at these shorter wavelengths might vary by quite noticeable amounts. This is plausible, because the shorter wavelengths are emitted from regions of the solar atmosphere that are higher and hotter than those emitting the visible light. While the far-UV (FUV) wavelengths represent a small fraction ($<2\%$) of the total solar energy received at earth per second (the solar constant, $1.37 \times 10^3 \text{ W m}^{-2}$), they show greater variation in intensity than the visible wavelengths on the solar surface.

The problem with these space observations was the lack of agreement between measurements from different experiments. It is difficult to calibrate detectors to measure the absolute intensity of solar UV radiation. Nearly all of the potentially most useful experiments, on long-duration satellites, suffered degradations in instrument sensitivity due to space environmental conditions.

The inherent interest in this possible FUV variability derives, in part, from the belief that the sun is a typical star, and thus offers the chance to study, at close hand, phenomena that probably occur on many other stars. In fact, the observed solar activity cycle led to a long-term observational program by O.C. Wilson of Mt. Wilson Observatory to monitor a number of solar-type stars. He found that some other stars go through a cycle of activity that seems analo-

gous to the solar cycle. The solar FUV radiation is also important because it greatly influences processes in the heliosphere, the local solar interplanetary neighborhood. Finally, changes in the FUV can affect processes, such as ozone production, in our atmosphere, and possibly our climate as well.

Why might the sun's output vary with time? Perhaps the entire sun brightens and fades uniformly. However, space observations have shown that the sun is increasingly structured into quiet and active areas (Figure 1) at greater heights and temperatures. We have pursued this idea and developed an estimate of solar variability over the 117.5- to 210-nm region [1]. Our model assumes that variability arises from the changing amount of solar surface covered by active regions, which are brighter than the background (quiet) surface, during the solar activity cycle. Using the wealth of solar observations from NRL experiments

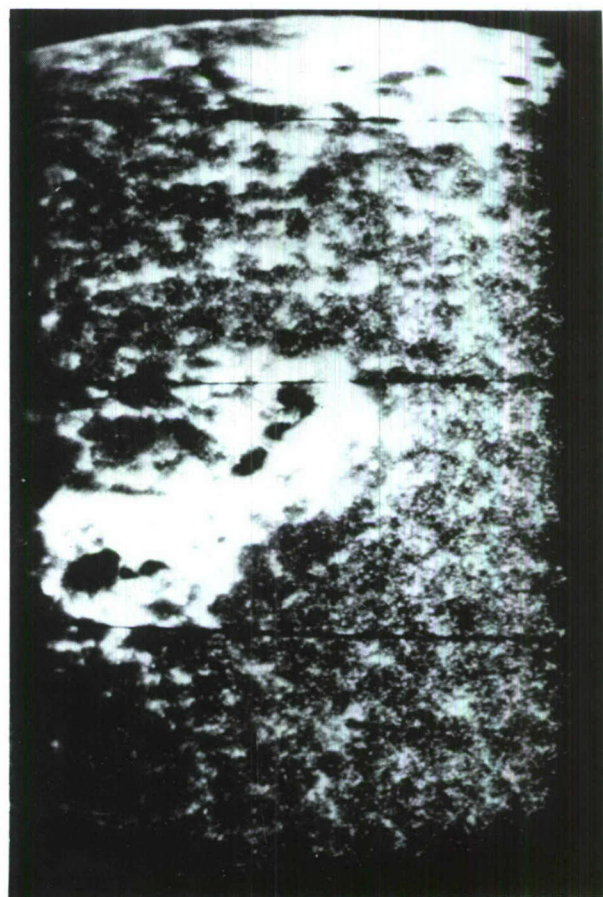


Figure 1. The solar surface as seen in the FUV (near 160 nm) from the NRL High Resolution Telescope and Spectrograph sounding rocket payload launched February 13, 1978. Active regions are seen near the center and near the solar limb at upper right.

aboard Skylab and from sounding rockets, we measured the intensity contrast between quiet and active areas. We also estimated the fraction of the solar disk covered by active regions as a function of the number of sunspots present, which is monitored daily by a number of ground solar observatories. The fractional increase in emission at a particular wavelength over the emission from a completely quiet sun (sunspot cycle minimum) would be given as $Cf + (1-f)$, where f is the fraction of the solar disk covered by sunspots and C is the active-to-quiet region contrast. For example, we measured $C = 3.6$ for the continuum at 160 nm. For sunspot number equal to 200 (a relatively high level of activity, although numbers in excess of 300 have been observed), our work showed that f is approximately 13%. Thus the fractional increase on such a day would be approximately $(3.6)(0.13) + (1-0.13) = 1.34$, or 34% brighter in the 160-nm continuum than it was at solar minimum. In Figure 2 we show a comparison of our estimates with recent observations from the Atmospheric Explorer satellite. Allowing for estimated errors in C , f , and the basic quiet sun emission, the agreement is good.

We have developed a model of FUV variability that can be tested against available observa-

tions, and can also be used to provide a plausible estimate of the potential variability any future experiment might encounter. The greatest current need is for more accurate measurements of the actual solar FUV variability. Two requirements for an instrument that will give reliable, high-precision measurements are a high degree of sensitivity to detect even small (1%) changes, and a reliable calibration system so that changes in solar radiation measured at different times can be convincingly attributed to actual solar variation, not instrumental change. Such a system is now being developed at NRL and will be described in the following article.

[Sponsored by NASA]

Reference

1. J.W. Cook, G.E. Brueckner, and M.E. VanHoosier, "Variability of the Solar Flux in the Far Ultraviolet 1175-2100 Å," *J. Geophys. Res.* **85** (A5), 2257-2268 (1980).

Solar Ultraviolet Spectral Irradiance Monitoring Program, by M. VanHoosier, J.-D.F. Bartoe, and D.K. Prinz, *Space Science Division*

There is a growing interest in measurements of the solar flux and its variability in the 120- to

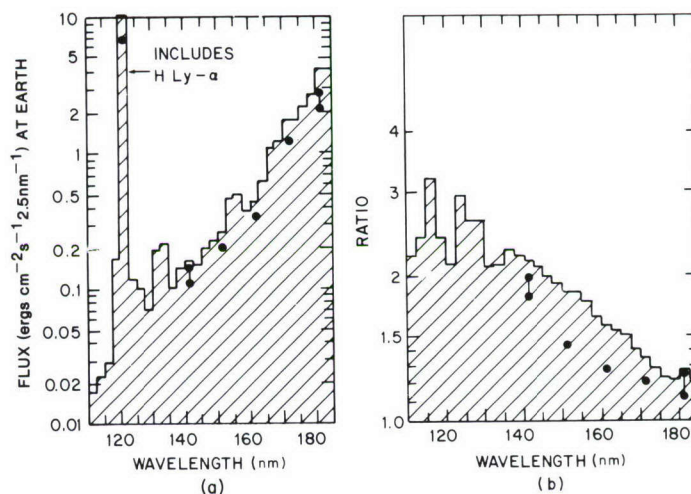


Figure 2. Comparison of NRL model predictions (●) with observations from the Atmospheric Explorer satellite (provided by H. Hinteregger). (a) Fluxes from January 22, 1979 when sunspot number was 178, and (b) the ratio of January 22 fluxes to observations from July 1976 when sunspot number was 0 (completely quiet sun). At 140 and 180 nm, model predictions are shown for the continuum alone (two lower values) and for continuum plus emission lines, giving improved agreement.

400-nm wavelength region. Much of the increasing interest is due to the important role this solar radiative output plays in many processes in the heliosphere, such as interaction with the local interstellar medium streaming through the solar system, the physics of planetary atmospheres, and comet chemistry and evolution. However, the importance of accurate solar flux measurements for use in modeling the terrestrial atmosphere has caused the greatest current interest. As mentioned in the preceding article, the 120- to 400-nm region presents a difficult regime for achieving precise measurements. A program has been developed by NRL, using the solar ultraviolet spectral irradiance monitor (SUSIM) instrument, which will meet the need for improved measurement accuracy, together with long-term monitoring of the variability of solar ultraviolet radiation.

The main scientific objective of the SUSIM experiment is to measure precisely full-disk solar fluxes and their changes over a solar activity cycle in the 120- to 400-nm wavelength region. This task can be broken down into two subtasks: (1) Improve the absolute accuracy of solar continuum and emission line irradiance measurements in the 120- to 400-nm region to ± 6 to 10%. (2) Measure the wavelength-dependent degree of correlation of the solar fluxes in the 120- to 400-nm region with the following ground observables: the Zürich sunspot number, the solar 10.7-cm radio

flux, the Ca II plage index, and full-disk Ca II H and K indices.

The SUSIM instrument consists of two identical double-dispersion scanning spectrometers, seven detectors, a UV calibration light source, a sun sensor, a microprocessor system, and associated electronics. Figure 3 shows the instrument configuration. The spectrometers and detectors are sealed in a canister filled with 1.1 atm of argon gas to minimize the effects of contamination of the optics that occur from irradiation under high vacuum outgassing conditions (the absorption cross section of argon is insignificant in the 120- to 400-nm region). Opening the shutter for a selected spectrometer allows incident radiation to enter through a MgF_2 window that provides the necessary pressure seal for the canister. Each spectrometer has interchangeable entrance and exit slits to provide either 0.15- or 5-nm spectral resolution over the entire spectral range. Wavelength scanning is achieved by synchronously rotating the first and second gratings, keeping the entrance and exit slits fixed. Pivoting the first grating off-center compensates for the changing focal distance as the spectrum is scanned. One spectrometer is used almost continuously during the daylight portion of each solar-pointed orbit; the second is used only infrequently to track any change in the sensitivity of the first.

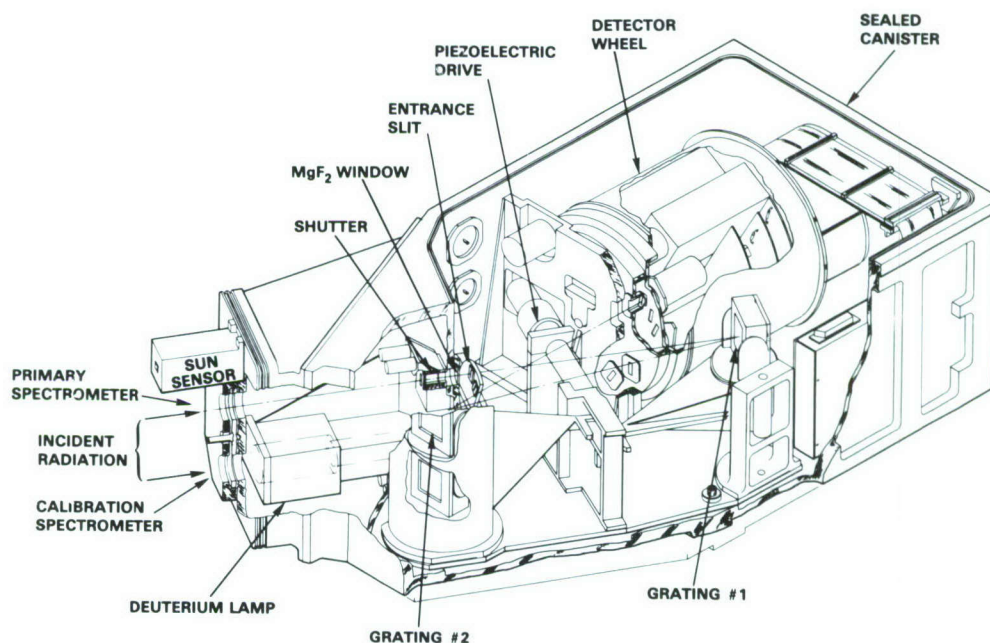


Figure 3. SUSIM instrument design showing component placement; the light path for primary spectrometer is also shown.

A deuterium lamp that is used for periodic inflight calibration is located outside of the MgF_2 window. This lamp is being developed by the National Physical Laboratory (NPL) of the United Kingdom and is being calibrated and tested at the National Bureau of Standards (NBS) and NRL. Through an extensive program of development and calibration, significant progress has already been made in absolute calibration accuracies and in resolving a long-standing difference in absolute calibration between NBS and Britain's NPL. The lamp is specifically developed to provide highly stable and predictable aging characteristics and to cover the entire wavelength range of 120 to 400 nm. The calibration lamp can be moved in front of either spectrometer and will be used periodically to allow tracking of the instrument's efficiency while not causing undue aging of the lamp. Similarly, the detectors are mounted on a wheel and are arranged so that any of the seven can be moved behind either spectrometer.

Extremely accurate absolute calibration of this instrument is critical for its success. For this reason, an extensive calibration program has been developed in close cooperation with the National Bureau of Standards. The calibration methods are based on the extensive experience and knowledge of NBS, NPL, and NRL.

Pre- and postflight absolute calibration of the instrument will be based on three independent absolute spectral irradiance source standards that have been developed by NBS. The fact that the calibration procedure and theory used for each of these standards are different provides a powerful method of uncovering systematic errors in any one of the calibrations. A full error analysis shows that the RMS uncertainty of absolute spectral irradiance measurements by the SUSIM experiment in its absolute mode should be ± 6 to 9% over the entire wavelength range. However, the solar output at wavelengths longer than 300 nm is constant to within $\pm 1\%$; therefore, one can measure the solar radiation below 208 nm relative

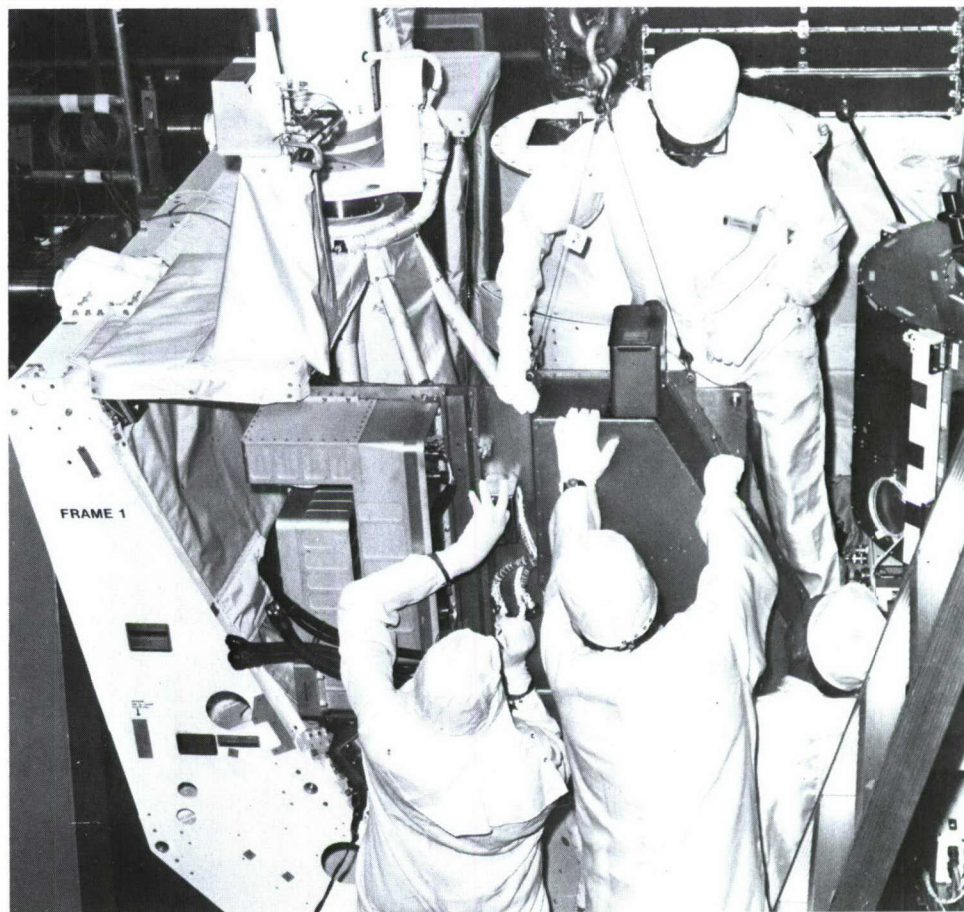


Figure 4. David Blizzard (left) and Kenneth Carlson (second from left) assist NASA technicians in installing the SUSIM instrument on the NASA OSS-1 pallet, which will fly on the fourth Space Shuttle flight in early 1982. (NASA photograph G-80-4346)

to the 300-nm-wavelength regime, providing that the instrument sensitivity degradation can be measured with precision.

The dual approach used in developing the SUSIM instrument was (1) to minimize degradation of the optical elements by techniques such as filling the instrument with argon, and (2) to provide inflight tracking of stability through the use of an inflight calibration standard and redundant optical systems. With this approach, the total expected RMS uncertainty in solar absolute spectral irradiance relative to the 400-nm continuum should be $\pm 1\%$.

Before the solar UV flux change can be determined, it is absolutely necessary to improve upon existing observations, to extend them over longer time periods, and to measure a variety of solar emission lines and continua that originate from different layers of the solar atmosphere. The instrument design must include the ability to monitor long-term calibration changes that would otherwise be interpreted as solar changes, and must allow for a thorough assessment of errors.

The SUSIM program has been carefully designed to fulfill these requirements. The SUSIM instrument has now been installed on the Office of Space Science Mission 1 (OSS-1) experiment pallet for the Space Shuttle cargo bay as shown in Figure 4. With the flight of OSS-1 in early 1982, we will enter a decade of solar ultraviolet spectral irradiance monitoring. Flight aboard Spacelab 2 (1984) and follow-on flights at least annually are now being planned. The development of two additional SUSIM instruments has just begun for the Upper Atmospheric Research Satellite (UARS) mission, which will allow longer duration observations (approximately one and a half years) from each of two satellites to be launched in the late 1980s.

[Sponsored by NASA]

High-resolution X-ray Spectra of Solar Flares, by R.W. Kreplin, G.A. Doschek, and U. Feldman, *Space Science Division*

Solar flares emit copious quantities of x-rays that can result in major disruptions of Department of Defense (DoD) communication networks. These x-rays are generated by very hot multimillion-degree gases (plasmas) confined by magnetic fields in curved tubelike structures that permeate the solar atmosphere (Figure 5). A typical magnetic flux tube may have a length of 10 000 km and a diameter of about 1500 km.

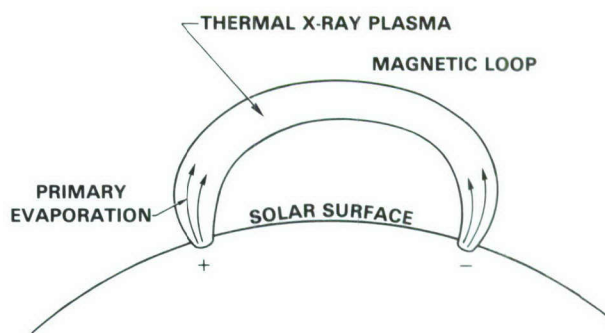


Figure 5. Schematic representation of a solar magnetic flux tube. Such tubes contain dense, x-ray emitting, multimillion-kelvin flare plasmas. This plasma may be injected into the flux tube from the solar surface at the time of flare onset by a process called primary evaporation, or cold plasma may exist in the tube prior to the flare.

The ends of the tubes appear to be anchored deep in the lower solar atmosphere known as the chromosphere. The mechanism by which the gases are heated to temperatures exceeding ten million kelvins is not yet known and represents one of the outstanding unsolved problems of solar physics.

Scientists at NRL have recently studied hot flare plasmas by obtaining very-high-resolution x-ray spectra from an NRL experiment launched by the Air Force on February 24, 1979 under the Space Test Program. Atoms such as iron in the flare plasma are stripped of many of their electrons by interatomic collisions to form different ionic species. (Atoms not possessing their full complements of electrons are called ions.) These ions are further induced by collisions with electrons to emit radiation at discrete wavelengths (emission lines) in the x-ray region. The emission lines are detected in the NRL instrument illustrated in Figure 6, through diffraction of the x-rays by crystals of germanium. The number of diffracted photons is then counted by a proportional counter, a device quite similar to an ordinary Geiger counter.

Two examples of x-ray iron-line spectra of a solar flare that occurred on August 20, 1979 are shown in Figure 7. The Roman numerals following the chemical symbol for iron (Fe) specify how many electrons (N) the ion possesses according to the scheme, $N = 27 - \text{Roman numeral}$. Thus Fe XXV refers to an iron ion with only two electrons; Fe XXIV refers to an ion with only three electrons, and so forth. The atoms most ionized, i.e., with the smallest number of electrons, are formed in the hottest portions of the

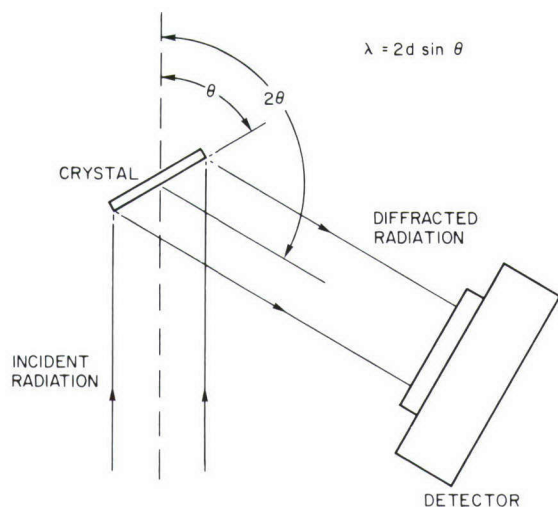


Figure 6. Schematic of a Bragg crystal spectrometer. Different wavelengths are observed by varying the angle by use of a stepping motor.

flare plasma. As the flare cools, the interatomic collisions become less severe and the ions capture more electrons, becoming less ionized. The effect of this on the spectra is that the lines of less ionized iron such as Fe XXI become stronger relative to those of highly ionized species such as Fe XXV as the flare plasma cools. Conversely, the reverse trend occurs when the plasma heats up. Thus in Figure 7 the lines of ions such as Fe XXI and Fe XXII are stronger relative to lines of Fe XXV and Fe XXIV in the lower spectrum than in the upper one, indicating that the flare was cooler at the time the lower spectrum was recorded than it was 67 min earlier when the upper spectrum was recorded.

So far, many different types of flares have been studied, and several exciting results have emerged. For one, the maximum temperature achieved by most flares is very rarely in excess of twenty million kelvins. There seems to be a limit on the degree of plasma heating that is usually possible in flares, and this result is clearly important to physicists interested in flare heating mechanisms. In Figure 7, the temperatures indicated by the upper and lower spectra are 23 million and 16 million kelvins, respectively. Another interesting result is that there is evidently continuous energy input into the flare plasma, which can last well into the decay phases of flares, i.e., the phase in which the x-ray flux of radiation is declining. This result has also been indicated by previous experiments such as the NRL experiment on Skylab. For some flares, the

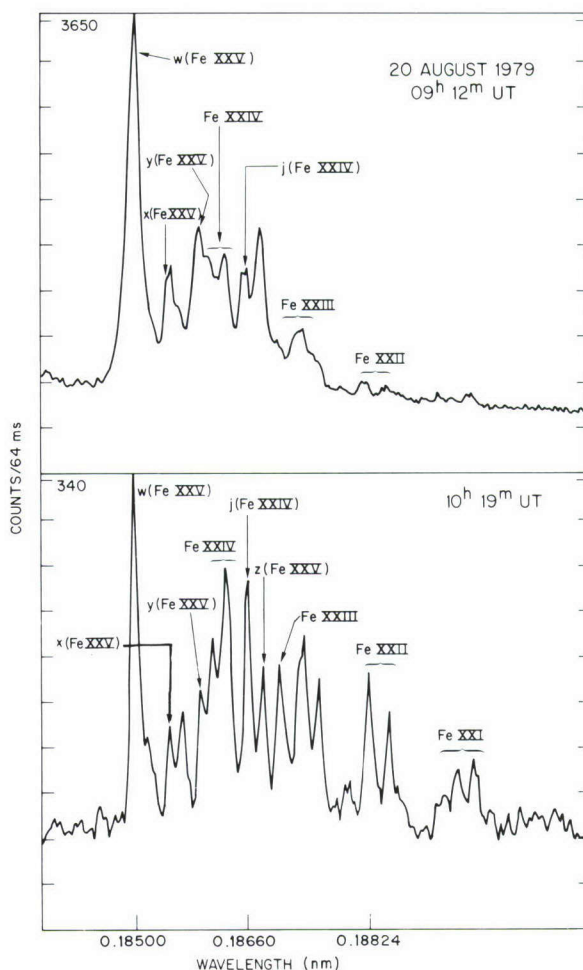


Figure 7. Iron-line spectra of a solar flare. The number in the top left-hand corner of each figure is the peak scale value. The letters w, x, y, z, and j denote particular transitions in Fe XXV and Fe XXIV. The intensity of line j to line w is used to derive the electron temperature.

temperature was observed to remain constant for times as long as 40 min. In these cases, the decline in x-ray flux may be associated with a reduction of the gas density in the flux tubes.

Perhaps the most surprising result obtained so far concerns the gas motions within the flux tubes, and possibly adjacent and external to the tubes. The gas motions can be determined from the *widths* of the spectral lines of iron, by use of the Doppler effect. We find that during the onset time of flares there is considerable turbulent motion, with speeds on the order of 160 km s^{-1} . As the flare progresses, the motions subside to values on the order of 60 km s^{-1} . For two events, plasma at temperatures of about 15 million kelvins was observed moving outward from the flare site at speeds equal to or greater than

about 400 km s^{-1} . The precise site of origin of the ejected plasma is presently unknown, but the violent motions are most likely closely linked to the elusive flare heating mechanism. These observations, coupled with theoretical studies, promise to greatly increase our understanding of solar flares.

[Sponsored by ONR]

Modeling of Solar Wind Interaction with the Earth's Magnetosphere, by J.A. Fedder and P.J. Palmadesso, *Plasma Physics Division*

The sun creates a supersonic, outflowing plasma imbedded with solar magnetic field, called the solar wind, that flows throughout interplanetary space. Disturbances in the solar wind that strike the outer regions of the earth's magnetosphere can often lead to disruptions of Navy command, control, and communications systems. These disruptions of ground-based and satellite systems are caused by the effects of magnetospheric substorms and magnetic storms. The effects include: energization of plasma particles in the earth's magnetosphere that degrade satellite systems via spacecraft charging, radiation damage, and increased atmospheric drag; precipitation of energetic particles into the atmosphere and generation of ionospheric irregularities that interfere with short-wave radio propagation, VLF signal propagation, and satellite-ground communication links; and large geomagnetic field disturbances caused by substorm current systems which, on occasion, interrupt land-line communications and power grid systems.

To gain a better understanding of the processes involved, NRL is developing and studying numerical magnetohydrodynamic (MHD) models of the earth's magnetosphere. Currently, we have in operation both 2- and 3-dimensional computer models of the solar wind-earth's magnetosphere system. The models have been used to simulate a solar wind shock interacting with the magnetosphere, as well as the southward interplanetary magnetic field (IMF) interaction with the magnetosphere, which we present here.

Statistical studies of satellite and earth-based data have shown that a period of southward IMF in the solar wind often leads to the occurrence of magnetospheric substorms. This correlation of southward IMF and substorm occurrence has been qualitatively understood in the following empirical model [1,2]. It is known that, in the presence of plasma resistivity, the southward IMF will merge with the northward geomagnetic field

on the front of the magnetosphere. In this merging process, earth's magnetic field lines and IMF lines are connected and are subsequently carried along by the solar wind across the polar regions, into the geomagnetic tail. This process continues to increase the tail field magnitude and magnetic stress until very rapid merging of oppositely directed field lines begins in the geomagnetic tail. The explosive merging in the midplane of the tail causes heating and acceleration of plasma and is thought to be responsible for many of the substorm phenomena. Although this model of the substorm mechanism is physically appealing and appears to be in general agreement with many satellite measurements, it had not been verified in a comprehensive way until we performed the 2-dimensional magnetospheric simulations.

The computer code that constitutes the magnetospheric model solves the usual MHD equations over a large region in two or three dimensions. The equations include: continuity, momentum, and energy equations; Maxwell's equations; and Ohm's law. The solution is obtained by a new, minimally diffusive, flux-corrected transport method developed at NRL. Only recently have sophisticated numerical algorithms, sufficient computer memory, and computational speed been available to undertake such a large and complex simulation effort. After a number of years of developmental effort, we have recently done full-scale simulations.

A 2-dimensional simulation of the southward IMF-magnetosphere interaction has been completed. Figure 8a shows the geomagnetic field and the southward IMF. Magnetic merging is taking place on the nose (at point marked X) with the merged magnetic flux being carried along by the solar wind over the poles and into the magnetospheric tail. The tail field strength is being enhanced, and the field becomes stretched in the antisolar direction (to right in figure). Twenty real-time minutes later (Figure 8b), strong magnetic merging has begun in the midplane of the tail. Plasma acceleration away from the \times -point is occurring along with plasma heating, and flow velocities in the geomagnetic tail become greater than 400 km s^{-1} . After an additional 20 min has elapsed (Figure 8c), the merging point is rapidly moving tailward and is leaving the near-earth tail region. If the southward IMF is continued, the whole merging substorm process repeats itself. If the southward IMF is reversed to northward, the substorm processes quickly end.

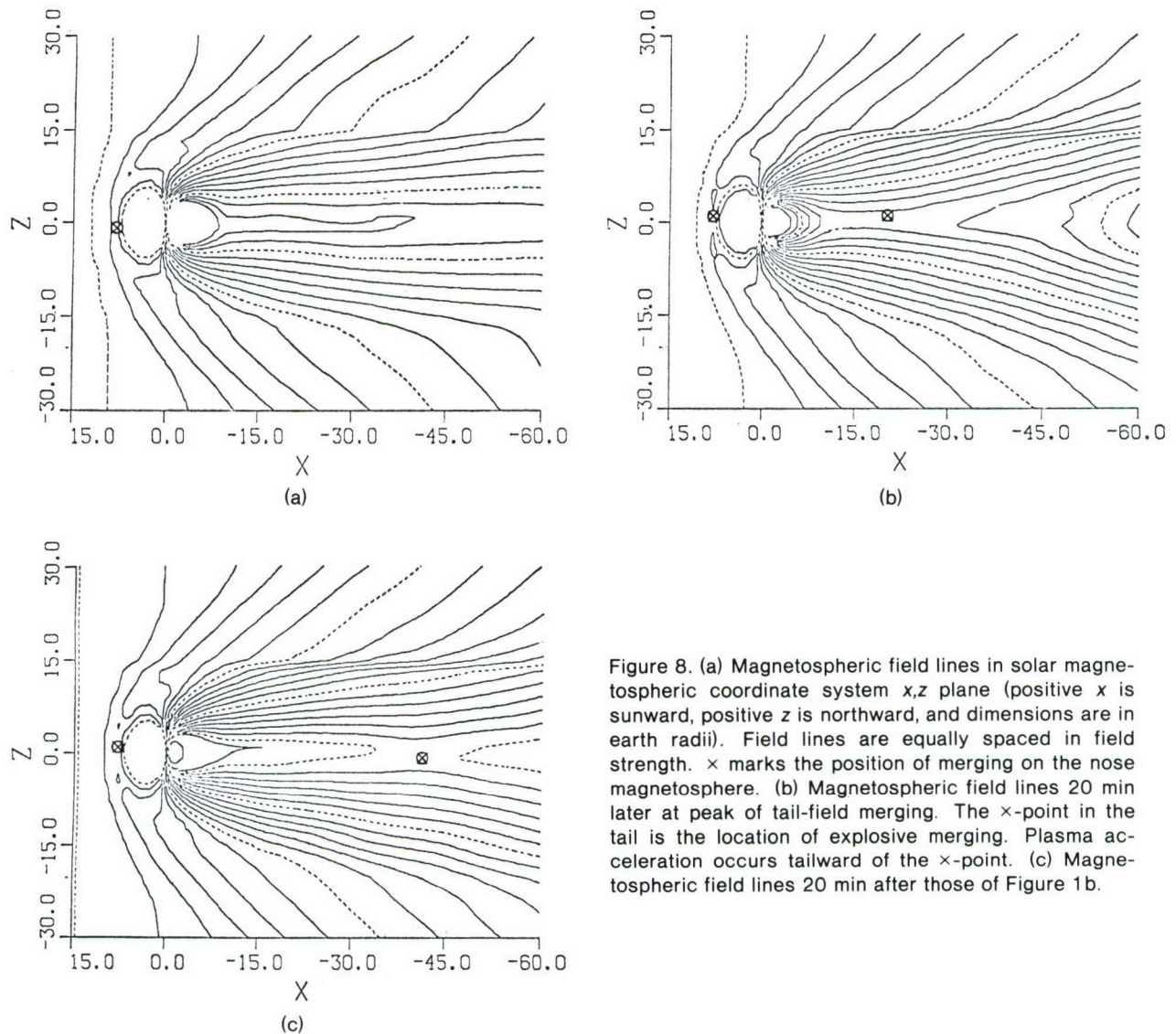


Figure 8. (a) Magnetospheric field lines in solar magnetospheric coordinate system x, z plane (positive x is sunward, positive z is northward, and dimensions are in earth radii). Field lines are equally spaced in field strength. \times marks the position of merging on the nose magnetosphere. (b) Magnetospheric field lines 20 min later at peak of tail-field merging. The \times -point in the tail is the location of explosive merging. Plasma acceleration occurs tailward of the \times -point. (c) Magnetospheric field lines 20 min after those of Figure 1b.

The simulation discussed above provides strong support for the empirical model [1,2] of substorms. It provides the means to understand plasma processes in different parts of the magnetosphere simultaneously, and also provides a tool for understanding substorm processes in detail. Such simulations constitute a major advance in the study of magnetospheric physics and substorm processes.

Clearly, we have just begun. We have completed simulations of the simplest types of solar wind disturbances and their effects on the magnetosphere. The results are encouraging but must be studied in more detail. More simulations of varied solar wind-magnetospheric interactions will be needed to understand the natural processes in detail. After completing and under-

standing these studies, we expect that it will be possible to predict solar wind disturbance effects on Navy systems.

[Sponsored by ONR]

References

1. E.W. Hones, *Radio Sci.* **8**, 979 (1973).
2. R.L. McPherson, C.T. Russell, and M.P. Aubry, *J. Geophys. Res.* **78**, 3131 (1973).

Semianalytic Method for Satellite Orbit Determination, by B. Kaufman, *Space Systems Division*

The purely numerical methods now used for accurate orbit determination require the calculation of many points on a spacecraft trajectory. Most of these points are of no direct interest but

are necessary to the numerical integration procedure. As a result, accurate orbit determination requires large amounts of computer time. On the other hand, semianalytic (seminumerical) methods require complex algebraic manipulation to develop the final equations of motion, but once these are developed, substantial savings in computer time can result.

Until recently, the software available for this large-scale algebraic manipulation has been limited, and the semianalytic methods could be used only to obtain the long-term behavior of a satellite. For that purpose, analytical methods can be used to average out short-term effects (those with periods on the order of the orbital period or less) to simplify the problem. The simplified equations are then integrated numerically using very large time steps. The process is fast but does not provide the accurate positional information that is often required.

In the past year, significant progress has been made at NRL in developing a semianalytic method that can be used to obtain accurate estimates of satellite position and velocity at specific times of interest. This is accomplished by numerically integrating the *averaged* equations as discussed above using large time steps, and then analytically applying the short-period contributions only at times of direct interest. This eliminates the calculation of intermediate points and can result in large savings in computer time.

Obtaining the accurate state vector (position and velocity) of a satellite with semianalytic techniques requires a great deal of algebra to develop the final equations of motion. The averaged equations may require the manipulation of hundreds of terms, and the recovery of the short-period contributions may require manipulation of literally thousands of terms before the final equations are obtained. The proper choice of intermediate coordinates during the development may reduce these thousands of terms to a few hundred in the final form of the equations of motion. Performing this algebra has had to wait for the development of useful machine-automated algebraic-manipulation programs, and it is only within the past few years that a rigorous development could be undertaken.

Averaged equations were developed in detail in an earlier study [1]. That work includes a high-order development for perturbations caused by the moon and sun, and includes contributions from the zonal terms J_2 , J_3 , and J_4 of the shape of the earth. The contributions due to the longi-

tudinal asymmetry (tesseral harmonics) are included by numerically averaging them over one orbit and using the result in the final equations. This numerical averaging does increase the computer time considerably.

Recovery of the short-period terms in the perturbative function is done in a purely analytic fashion. The Hamiltonian for the third body (moon and sun) and for the zonal J_2 is developed in a standard fashion frequently used in orbital mechanics. Since short-period perturbations have small amplitudes compared to those of long period effects, expansions to low order are all that is necessary except in the case of the moon for a high-altitude spacecraft. Application of perturbation theory using Lie series yields a canonical transformation that separates out only the short-period terms from the new Hamiltonian and allows a straightforward analytic integration of the new Hamiltonian to obtain a short-period generating function. A new set of variables that are noncanonical are then defined to eliminate a division by zero in the case of near-circular orbits. The new short-period coordinates are computed analytically from partials of the short-period generating function at the time they are needed and are added to the numerically computed, averaged coordinates.

The resulting averaged equations of motion and the literal representation of the short-period contributions have been implemented in a preliminary orbit determination program. Some comparisons on the basis of accuracy have been made with results from a traditional numerical model. The procedure is as follows: A mean state vector—one from which all short-period terms are removed—is used in the averaged equations of motion. These equations are numerically integrated using time steps of multiple orbits, thereby obtaining a mean ephemeris of the orbit. Whenever a position is desired, the mean state is obtained from the ephemeris by interpolation and is transformed to the new coordinates. The more accurate state is obtained by adding the short-period contributions represented by the partial derivatives of the short-period generating function. The result is then transformed back to the original coordinates.

Comparing the accuracy of the semianalytic method with a standard numerical one was done by generating position data with the numerical program and then fitting these data with the semianalytic method. Two cases are shown in the figures. Figure 9 shows the square root of the

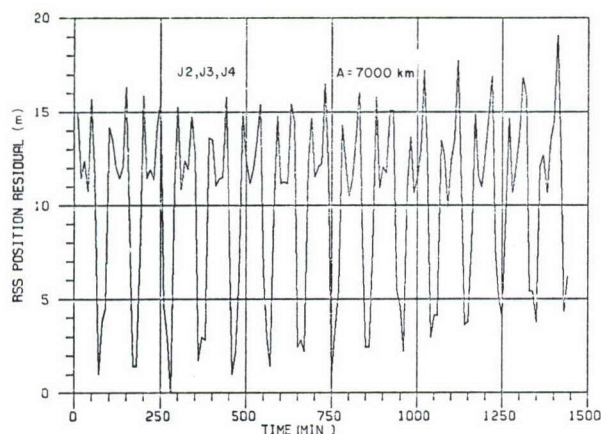


Figure 9. Low-orbit comparison with Cowell numerical integration; data fit over 1/2 day.

sum of the squares (rss) of the position-vector difference obtained by fitting the position data from the numerical method over one-half day and then extrapolating for one-half day. The orbit used in Figure 9 is nearly circular, with a 7000-km radius; the perturbations were the zonal terms J_2 , J_3 and J_4 . As can be seen, the deviation ranges from near zero to about 16 m with an average of about 9 to 10 m. Figure 10 is an example of an orbit that is highly perturbed by the moon and sun. Again, the orbit is nearly circular, with a radius of 20000 km, and the data are fitted over the entire day. The residuals in this case are about what is to be expected for this type of orbit fit over a one-day span of data. No computer time comparisons were made, because no attempt has yet been made to optimize the semianalytic method.

Future work on this method will involve higher order terms for the moon and the zonals, accurate interpolators, and optimization of the

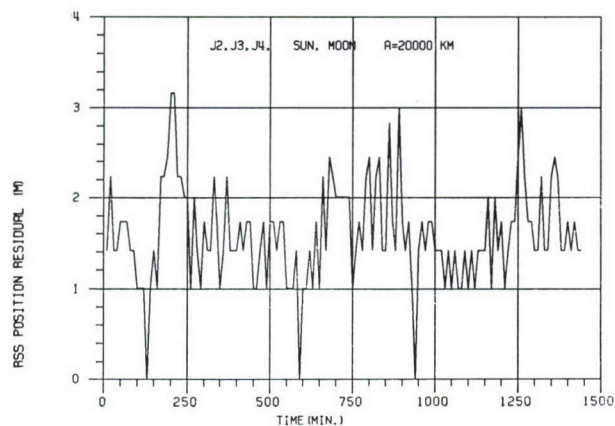


Figure 10. High-orbit comparison with Cowell numerical integration; data fit to one day.

computation of individual terms. Inclusion of atmospheric drag and tesseral harmonics will also be investigated.

[Sponsored by ONR]

Reference

1. B. Kaufman and R. Dasenbrock, "Semianalytic Theory of Long-Term Behavior of Earth and Lunar Orbiters," *J. Spacecraft Rockets* **10**, 377–383 (1973).

Parametric Wave-spectra Measurements from Aerospace Platforms, by D.T. Chen, *Space Systems Division*

For many years there has been a recognized need for remote sensing techniques to gather information about surface waves from aircraft and satellites. Synoptic data gathered over broad ocean areas can be used by the Navy in operational planning, system design and development, and in research and experimental programs.

Despite this recognized need and considerable effort over many years, the present capability is limited. For example, there is no proven technique for obtaining surface-wave spectra from data that have been gathered by satellites. Synthetic-aperture radars such as the one on SEASAT-1 can provide wavelength measurements, but there is no accepted technique for determining wave amplitudes from the data. Linear relationships between ocean-wave spectra and phase spatial spectra of *nadir-looking*, satellite-borne radar have been derived theoretically, but the ocean-wave spectra calculated from such a relationship would be the *encountered* spectra of the waves along the track of the satellite. These spectra would be skewed relative to the *true* spectra (a) by the angles between the orthogonals to the wavefronts and the direction of satellite ground track and (b) by the angular distribution functions of waves at the ocean surface.

Another mechanism has been proposed through which ocean-wave spectra can be derived from measurements made by nadir-looking satellite radars. Based on this mechanism, a spectral model has been derived at the NASA Wallops Flight Center. The spectral function obtained from this model is independent of the local wind conditions, provides an estimate of spectral bandwidth, calculates the ocean-wave spectrum (not the encountered spectrum), and is based on two parameters (mean-squared surface-wave

amplitude and skewness) that can be derived from the returned waveform in the nadir-looking satellite radar. Validation of the Wallops spectral model requires data gathered from aircraft altitudes for extremely high sea conditions. Significant steps toward this validation were taken at NRL in 1980.

The NRL analysis used data obtained from an airborne experiment conducted by the Laboratory in February and March 1976 to provide calibration (ground truth) for the GEOS-III satellite. Significant wave heights of 4 to 8 m were measured by radar and laser instruments. With aircraft motion data obtained from a vertical accelerometer and an inertial navigation system, the measurements made by NRL's laser profilometer are well suited to verifying the Wallops spectral model.

The results of analyses of data taken on February 20, 23 (sets a and b), 28, and March 3 are presented in Figure 11. The horizontal axis is the ratio of dominant wavelength λ_0 to significant wave height $H_{1/3}$. This ratio is equal to the inverse of the significant slope divided by 4. The solid curve is the theoretical relationship between the skewness coefficient and the ratio; it has been substantiated in wind-tank measurements. The dotted curves represent upper and lower bounds obtained analytically. The wave spectra show that there was a considerable amount of wave energy due to swells. The data for February 20 and 28 and March 3 show that there were distinctly different peaks for swells and wind-waves on those dates. The Wallops spectral model accommodates the presence of either wind-wave or swell separately, but not both simultaneously. Efforts have been made to remove the effects of swells on the significant wave height but, because of theoretical difficulty at this time, not on the skewness. The revised wind-wave peaks, also shown in Figure 11, are in better agreement with the theoretical curve and the upper and lower bounds than were the original wave peaks.

If not taken into account, the presence of a lot of energy due to swells will invalidate the Wallops spectral model. Therefore, additional

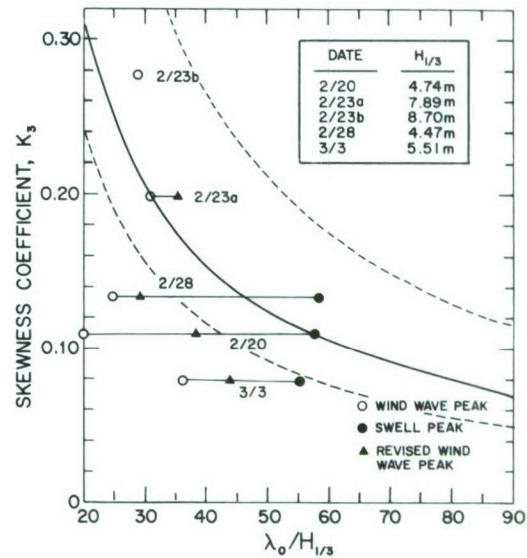


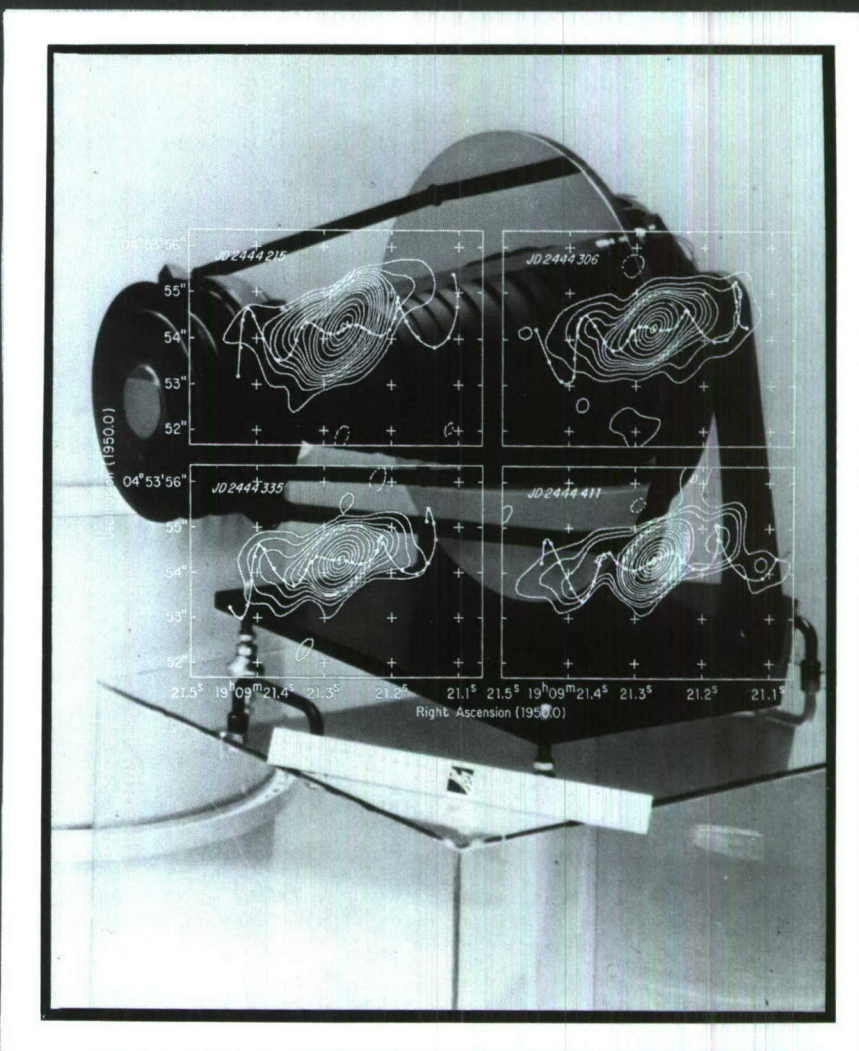
Figure 11. Theoretical relationship (solid curve) and its upper and lower bounds (dotted curves) between the skewness coefficient K_3 and the ratio of dominant wavelength λ_0 to significant wave height $H_{1/3}$.

work is required to solve this problem. Otherwise, the revised wind-wave peaks are well within the theoretical bounds. Except for the case where the effects on the skewness and the significant wave height due to swells are large, the theoretical relationship shown in Figure 11 can be used to parameterize ocean-wave spectra, through the Wallops spectral model. This can be done using skewness and significant-wave-height measurements from nadir-looking radars.

An airborne experiment is currently being planned at NRL to apply this model in resolving the direction of the dominant-wave component by use of active microwave radar measurements over the ocean. The results of this experiment will contribute to the scientific and technological efforts toward the measurement of directional ocean-wave spectra from aircraft and, ultimately, from satellites.

[Sponsored by NAVAIRSYSCOM]

HIGH-POWER TECHNOLOGY AND ASTROPHYSICS



HIGH-POWER TECHNOLOGY AND ASTROPHYSICS

Among the long-range objectives of work in these areas are new and improved techniques for power generation, weaponry, and navigation. Their ultimate realization will depend, in large measure, on basic understanding and innovative utilization of the complex, high-energy phenomena involved. NRL recognizes these major scientific and technical challenges and has continued its productive research in these areas during 1980.

SS433—A Peculiar Galactic Object	129
New Payload for Far-infrared Sky Survey	131
Rapid Variability from X-ray Emitting Galaxies	132
XUV Radiation Modeling of Dense Plasmas	135
An Ultra-high-power Magnetron for Air Breakdown Studies	138

SS433—A Peculiar Galactic Object, by K.J. Johnston, *Space Science Division*

The positions of extragalactic radio sources make up a grid that defines an almost inertial reference frame against which motions of the earth, i.e., Universal Time and polar motion, may be precisely measured. With recent advances in radio interferometry, the positions of sources making up this reference frame have been defined to an order-of-magnitude higher precision than those of the stars making up the optical reference frame. In addition, the radio frame is inherently more stable because its component sources are extragalactic, i.e., farther away. This reference frame consists of strong radio sources that are optically very faint, and it is therefore very difficult to use it to improve the *optical* reference frame of bright stars that are used quite often in guidance systems.

To improve the optical reference frame requires that common sources of intense optical and radio emissions be found. One such galactic object is SS433. An initial investigation by NRL and the U.S. Naval Observatory (USNO) using the Green Bank interferometer and the Observatory's Flagstaff facility indicated that the optical and radio radiations from this object are coincident to $0.2''$. Further investigations showed variations of the radio intensity occurring on time scales of days. Figure 1 displays the variations in the 11.1-cm radiation from July 1979 through August 1980. There is a quiescent phase in which the radiation level decays very slowly, and an active "flaring" phase in which it increases abruptly ($\sim 30\%$ per day) and decays to the quiescent level in a few days. In the figure, the quiescent behavior is seen during the first 21 days and again from J.D. 2444240 for 160 days. This quiescent and flaring behavior may be modeled as due to a plasma with an exponent (γ) of the energy distribution ($E^{-\gamma}$) of 1.2.

To investigate the spatial structure of this source, NRL personnel in collaboration with investigators of the National Radio Astronomy Observatory (NRAO) obtained measurements using the Very Large Array. This instrument, the most powerful radio telescope in the world, consists of 27 antennas located on the plains of St. Augustine, New Mexico. Measurements of the radio emission made at four dates in 1979–1980 showed structure, with size scales between $0.1''$ and $5''$, that changed significantly on time scales of 1 to 2 wk. This structure showed that jets with 8 to 20% linear polarization are ejected on oppo-

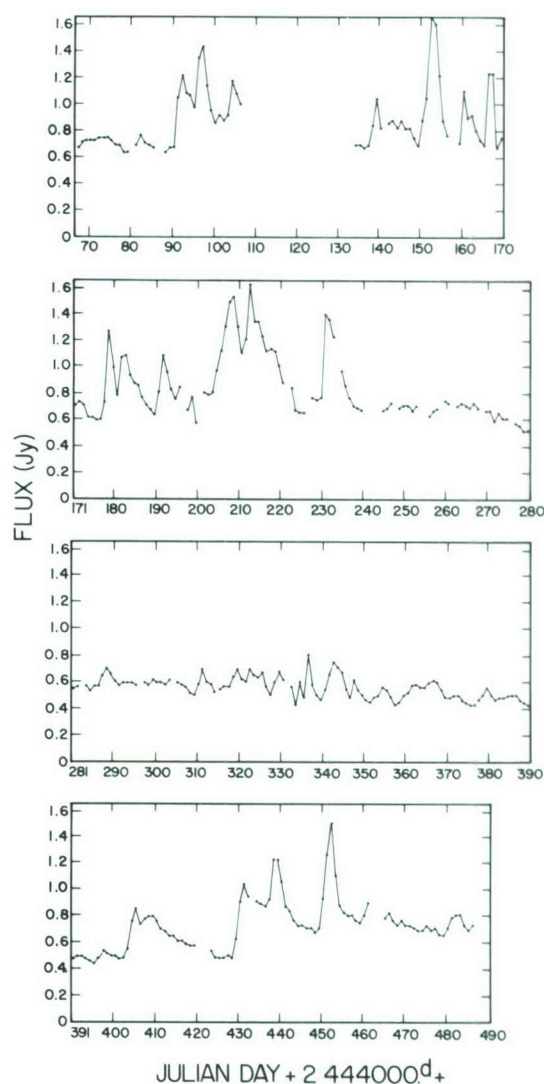


Figure 1. The daily averaged flux density of SS433 measured at 11.1 cm using the 2.4-km baseline of the Green Bank interferometer. The data spans Julian days 2444067 to 2444487. The flux density is in janskys.

site sides of the central radio source that is coincident with the optical image. Maps of the 4885-Hz radiation are shown in Figure 2.

Earlier optical observations at other laboratories of SS433 showed that the Doppler shifts of the hydrogen and helium emission lines varied by 50 000 to $-30\,000\text{ km s}^{-1}$. An explanation for these variations, advanced by Fabian and Rees of Cambridge, attributed the Doppler-shifted lines to jets of gas ejected in opposite directions from a central compact object. Milgrom of the Weizmann Institute of Science in Israel independently made this same suggestion and further stated that the Doppler shift variations may be periodic on

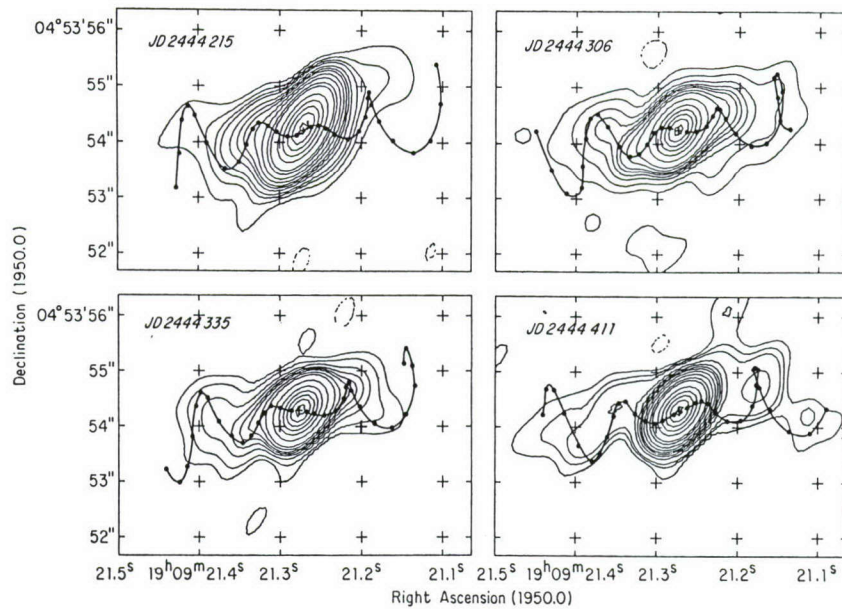


Figure 2. Very Large Array (VLA) contour maps of SS433 at 4885 MHz for Julian dates 2444215, 2444306, 2444335, and 2444411 are displayed in a form where the unresolved core radio source coincident with the central object is removed and the proper motion paths of material ejected are drawn with filled circles at 20-day intervals. The contour levels correspond to 90, 80, 70, 60, 50, 40, 30, 20, 15, 10, 5, and -5 (noise) percent of the peak flux values of 0.070, 0.030, 0.029, and 0.032 Jy, respectively, for the four maps.

time scales of a few months. Abell and Margon of the University of California modeled the Doppler variations with a period of 164 days and attributed this variation to a precessing beam of gas emanating from a compact object. The radio observations provided conclusive support for this explanation of the optical phenomenon.

The optical observations of Margon and his co-workers yield the line-of-sight motions of the gas in SS433. The radio observations now allow us to study the tangential motions and complete the picture. The radio jets are seen to move perpendicular to the line of sight at a rate of $3.0''/\text{yr}$. More important, since the plasma and gas associ-

ated with the jets are moving at $0.26c$ (where c is the velocity of light), there are significant special relativity, time travel effects between the two jets. These time travel effects allow one to obtain independently a velocity of $0.26c$ for the jets, yielding a distance of 5.5 kpc. The radio observations enable us to construct a model of the complete kinematic parameters for the jets of SS433, i.e., their inclination, cone angle, velocity, and period. These are illustrated in Figure 3. In addition, the mechanisms that give rise to this radiation can be studied. The radiation displayed in Figure 2 has a half-life of ~ 30 days, whereas the flares of Figure 1 have a half-life of 2 days.

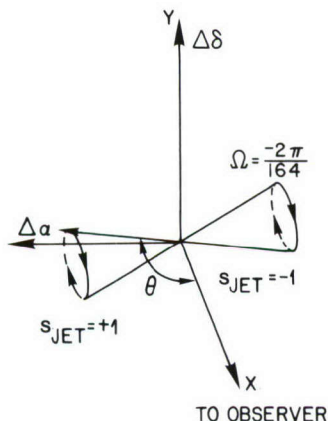


Figure 3. Kinematic model for SS433. The z - and y -axes correspond to displacement in right ascension ($\Delta\alpha$) and in declination ($\Delta\delta$), respectively. The approximately correct geometry of the rotating twin jets of SS433 is shown with $s_{\text{jet}} = +1$ and -1 for the nearer (approaching) and the farther (receding) jet axes, respectively. The correct angular frequency, $\Omega = -2\pi/164$ rad per day is shown, and the correct values of $\chi = 10^\circ$, $\psi = 20^\circ$, and $i = 80^\circ$ were used to obtain an approximate schematic representation of the SS433 radio and optical jets.

SS433 is believed to be a binary system with a period of revolution of 13 days. One member of the system is a massive star, and the other is a neutron star with an accretion disk. The observed jets are attributed to material being ejected along the rotation axis of the accretion disk. The flaring radio emission is due to a stellar wind originating from the massive star. The beam from the accretion disk radiates into an inhomogeneous medium, and, when it encounters a dense globule, it causes it to become relativistic (velocities approaching the speed of light) and radiate, producing a flaring event.

With the kinematic behavior of the radio jets in SS433 understood, we are developing a detailed model of the radio source emission. The understanding of the jet model for SS433 will lead to a better understanding of this phenomenon, which also takes place in radio galaxies and quasars. As such, it may be a "Rosetta stone" in our understanding of the general problem of relativistic jets. The understanding of the kinematics of quasars will allow the prediction of the stability of the inertial reference frame defined by these extragalactic sources. The discovery of further SS433-type galactic objects will allow refinements, improving the accuracy of optical reference frames.

[Sponsored by ONR]

A New Payload for Far-infrared Sky Survey, by D.P. McNutt, K. Shivanandan, and M. Daehler, *Space Science Division*

There will soon be a new catalog of stars for astronomers to ponder. The far-infrared (far-IR) spectral region between $14\ \mu\text{m}$ and $1\ \text{mm}$ has been a difficult one to explore because of a lack of good detectors and because the atmosphere radiates throughout the band. However, several current experiments, including the Far Infrared Sky Survey Experiment (FIRSSE), are now expected to provide data in this range. Potential rewards are great. Observations from balloons have shown that there are complex, distributed sources in the galactic plane, especially near the galactic center. Some discrete sources are bright enough at $100\ \mu\text{m}$ to be seen from NASA's Kuiper Airborne Observatory (KAO) (a C-141 aircraft equipped with a 1-m telescope).

According to currently accepted theory, most of the radiation originates as blackbody radiation from dust heated by shorter wavelength radiation from obscured stars. Also, in the early stages of

star formation, a dust cloud undergoing gravitational collapse may radiate at $100\ \mu\text{m}$ because of heating associated with compression. Our knowledge of star and associated planet formation can be improved by the study of such objects, should they be found. Several hundred sources have already been discovered by observations (from balloons or the KAO) of places where star formation is expected. A full-scale survey will provide an unbiased picture of the distribution of sources.

Extrinsic photoconductive detectors using gallium as an impurity in a germanium crystal, developed in the early 1960s by Moore and Shenker at NRL, are suitable for astronomical work in the far IR. However, in order to operate they must be cooled to 3 K, a temperature considerably below that required to eliminate the thermal background from telescope mirrors.

The only fundamental limit to detection sensitivity is the quantum fluctuations present in the radiation being observed. This sets a signal-to-noise ratio at $1/\sqrt{N}$, where N is the number of photons detected. (Readers familiar with the use of IR detectors within the atmosphere should note that the fluctuations in the background are not important in space.) With background radiation from mirrors and optics eliminated by cooling and the atmospheric effects eliminated by use of a rocket, the current state of the art is a factor of 10 to 100 away from the quantum limit and is set by the amplifiers used.

Since no photocathodes are effective at $100\ \mu\text{m}$, there is no electron multiplier available; therefore, the highly successful photomultiplier tube technology cannot be used. Detector impedance in the dark is generally too high to measure, and certainly too high to match to an electronic amplifier. So current-sensitive "trans-impedance" designs are used. The load resistor and a metal-oxide semiconductor field-effect transistor (MOSFET) are operated at the temperature of the detector with short wires and are coupled through long wires of low thermal conductance to a warm operational amplifier. The circuit is stabilized by feedback through the load resistor.

The first cryogenically cooled telescope was built and flown in the late 1960s when M. Harwit was visiting NRL as an E. O. Hulburt Research Fellow from Cornell University. Since then, the Air Force has made sky surveys from rockets in the 10- to $30\text{-}\mu\text{m}$ band where, because of the short wavelength, they were able to use liquid

neon and supercritical helium as coolants with a high degree of latent heat.

The new rocket payload for project FIRSSE was conceived as a merger of Air Force short-wave technology with NRL's long-wave experience. The responsible Air Force group is directed by S. Price and T. Murdock at the Air Force Geophysical Laboratory (AFGL), Bedford, Massachusetts. The sensor is a superfluid helium dewar with a 30-cm telescope and an array of 71 detectors to be flown on an Aries rocket. The AFGL scanning system will lock the spinning rocket onto a guide star near the zenith, and the telescope will be gimbaled to the side of the rocket so that it scans small circles of ever-increasing diameter as the flight progresses (Figure 4).

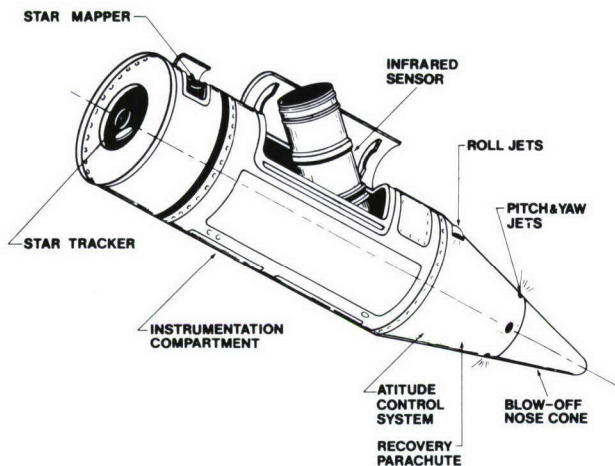


Figure 4. The payload-sensor configuration during the experiment. The star tracker is locked to a star near local zenith, the telescope is deployed to a specified zenith angle, and the payload rotates about the optical axis of the tracker. The star mapper provides azimuth reference during the roll maneuver.

Figure 5 shows the telescope and dewar. The optical design is a folded Gregorian system chosen because the first image is real and can accommodate a field stop to improve baffling against off-axis light from the horizon. The dewar is aluminum with stainless steel plumbing and is filled with liquid helium, which is converted to superfluid by pumping over the vapor. At equilibrium the focal plane is below 3 K, but the telescope is allowed to rise to a maximum of 10 K.

The scanning motion of the rocket causes sources of light to move in the focal plane and, as a star crosses a detector, a pulse of photoconductive carriers is created. The amplifiers are capaci-



Figure 5. The FIRSSE dewar and telescope. The dewar keeps the optics and detectors at cryogenic temperature (liquid helium). The cover, shown here at the bottom of the dewar, is removed above the atmosphere and is replaced before re-entry. The telescope is a folded Gregorian system of all-beryllium construction.

tively coupled to reject any isotropic background, so that each sensing of a star goes to the telemetry as a differentiated pulse. Later analysis can recreate the intensity distribution in the sky. The first FIRSSE launch is scheduled for 1981.

[Sponsored by ONR and AFGL]

Rapid Variability from X-ray Emitting Galaxies, by K.S. Wood and W.A. Snyder, *Space Science Division*

It has been recognized since the 1960s that quasars and active galaxies release tremendous amounts of energy from very small volumes. These objects undergo the most violent forms of energy release known to astronomy, but the physical processes responsible remain poorly understood. It is believed that relativistic states of

matter and plasma conditions not readily reproducible in the laboratory are involved. The compact objects at the cores of these galaxies are near the point of gravitational collapse and may even contain collapsed regions (black holes). They thus provide a testing place for ideas in relativistic astrophysics, where we stand to gain improved understanding of high-energy physical processes by detailed observation. BL Lacertae (BL Lac) objects are especially apt choices for study. These are elliptical galaxies containing intense sources of nonthermal radiation at their cores and are distinguished by high luminosities and extreme variability. They also have relatively little gas surrounding the active core, which means that the site of energy release itself is most directly exposed for our view.

It is especially desirable to observe the x-ray emissions from BL Lac objects because the x-ray photons are thought to be generated close to the center of the system. NRL's X-ray Astronomy program has developed highly sensitive proportional counters, culminating in the largest array of such counters ever flown on a satellite, the A-1

Experiment on NASA's High Energy Astronomy Observatory (HEAO-1). Figure 6 shows this array undergoing integration with the spacecraft at TRW, Inc. in Redondo Beach, California. The mission lifetime was from August 12, 1977 to January 9, 1979. NRL's experiment returned roughly 10^{11} bits of telemetry data that are still being analyzed at NRL by the X-ray Astronomy group and by guest investigators from a number of universities.

Because BL Lac objects are very distant, they appear as faint x-ray sources in spite of their prodigious luminosities. They are all known to be variable in optical and radio wavelengths, on time scales ranging from days to years. Thus, to monitor their variability in x-rays calls for a highly sensitive instrument with broad time coverage. This combination is uniquely provided by NRL's HEAO A-1 Experiment. Sensitive to photons in the 0.5- to 25-keV range, the experiment observed a great-circle band 8° wide every 30 min in continuous scanning. During a 6-month period, this permitted a survey of about 60 BL Lac objects, because the scan plane advanced

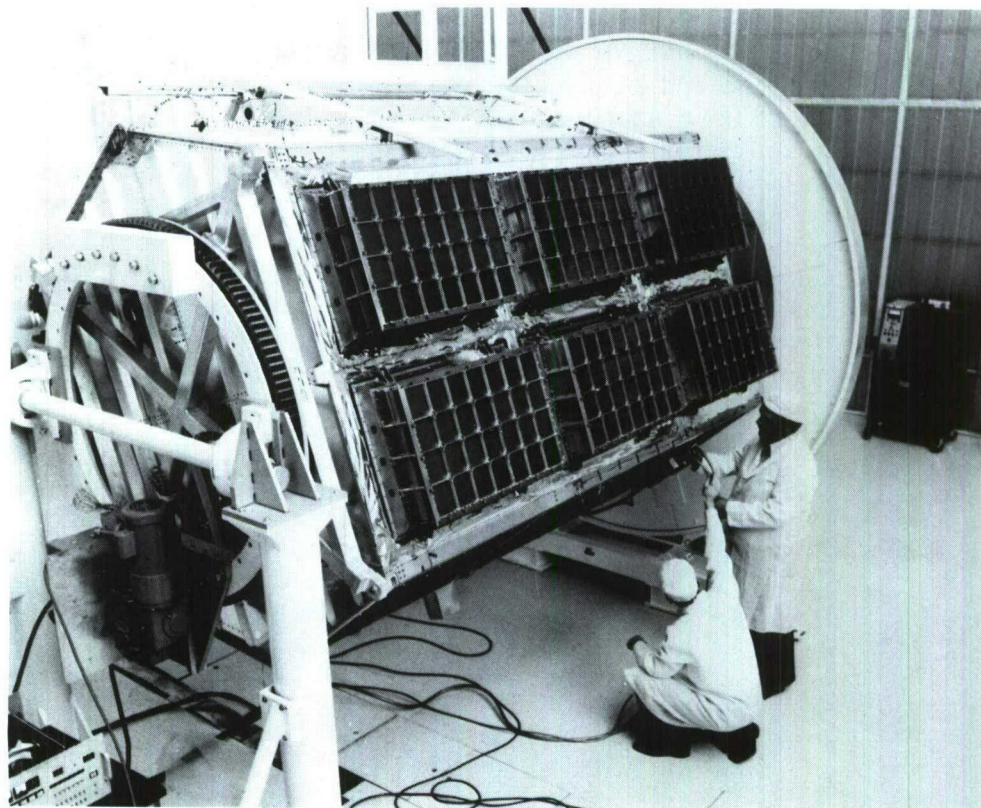


Figure 6. NRL's HEAO A-1 Experiment during spacecraft integration and testing at TRW in 1976. Shown are six of the seven NRL proportional counters, mounted on one side of the HEAO-1 Observatory. (Courtesy of TRW.)

daily by 1° in such a way that the entire sky was surveyed. The regular scanning pattern also provided regular sampling of source intensity during the time the objects were in the field of view. This kind of sampling is ideal for variability studies. Source intensities are determined by representing x-ray counts as a function of phase angle in the scan and fitting them with the instrumental response function. If the source is too faint to be seen on a single scan, data from several scans are summed prior to fitting. This improves the signal-to-noise ratio at a sacrifice of temporal resolution. X-ray fluxes so derived are used to help build physical models of the source. If the distance to the source is known, the observed flux can be converted to absolute luminosity and used to establish overall source energetics. Variations in flux serve to establish source dimensions. Comparisons of x-ray flux with measurements at other wavelengths provide information about radiation mechanisms.

Among the BL Lac objects detected by HEAO A-1, PKS2155-304 and 3C371 stand out as being of particular interest. PKS2155-304 is a southern hemisphere radio source that was so bright in x-rays that it was detectable in single-scan observations. Because of earth occultation of the source, observations of 10-s duration were typically available once every hour and sometimes every 30 min. The light curve (x-ray intensity vs time) obtained for the source is seen in Figure 7. Changes in intensity of 100% are apparent on time scales as short as 6 h. The peak luminosity of this object is estimated at 2×10^{47} erg s $^{-1}$, or about 100 times the luminosity of the entire Milky Way galaxy. Variability of 6 h implies that the emitting region producing this luminosity is small enough to fit within the orbit of Neptune.

Moreover, the source must be subject to severe dynamical instabilities.

The second BL Lac object, 3C371, was situated at a location that permitted 80 consecutive days of observations. Because it is considerably fainter than PKS2155-304, many scans had to be summed to give sufficient signal for intensity determination. Threefold or larger intensity variations were observed in the 0.5- to 20-keV flux (see Figure 8), with one variation exhibiting more than a 100% increase in intensity over 8 days, whereas decays were typically found to occur over 20 days. Optical variations have also been noted in 3C371 by other observers. While optical flares typically rise at the same rapid rate as observed in x-rays, they decay more slowly. Although the variability time scales are somewhat different for PKS2155-304 and 3C371, the basic temporal behavior in x-rays is similar: the emission appears to consist of a succession and partial superposition of individual events or bursts. Consideration of the optical variability and the apparent agreement between the extrapolated optical and x-ray flux suggests models in which both the optical and x-ray emissions are produced by a beam of relativistic electrons radiating by the synchrotron mechanism. The time scale of variation would then imply that the magnetic field in the emission region is a few tens of milligauss.

Light curves such as Figures 7 and 8 represent a major advance over earlier x-ray results from smaller satellites, where all available data had to be summed to establish that the source had been seen in x-rays at all. These light curves not only provide the best characterization of temporal structure yet obtained at x-ray wavelengths, but are also superior in some ways to what is obtainable at visible wavelengths

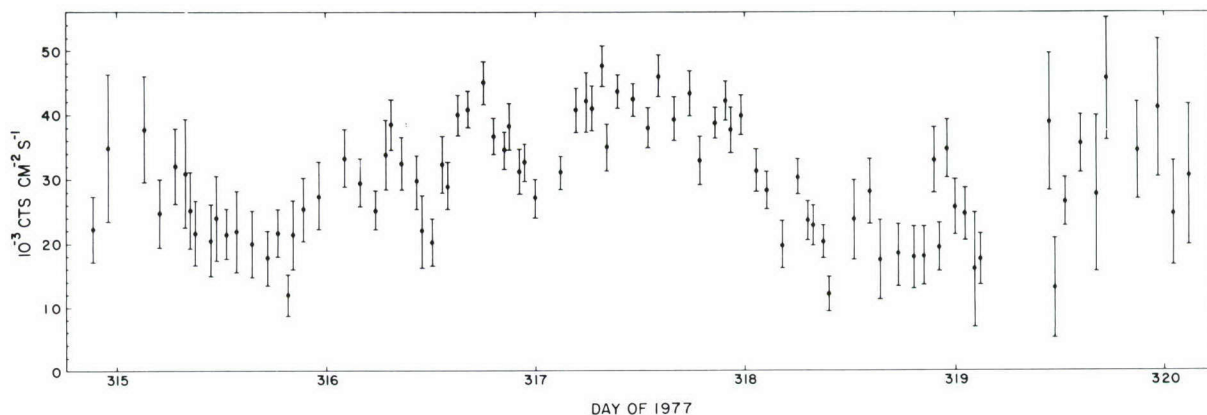
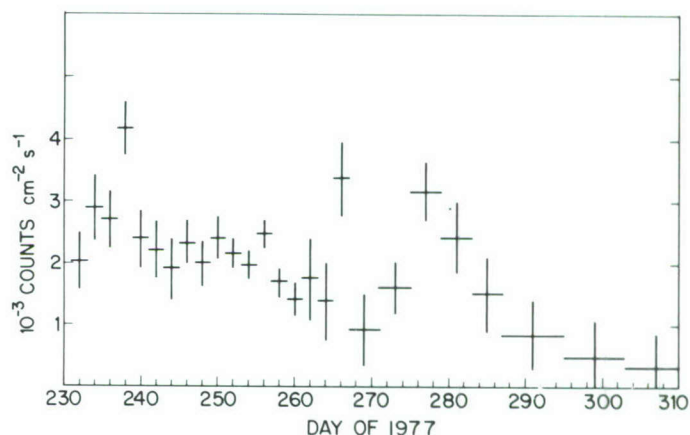


Figure 7. X-ray light curve for PKS2155-304 showing intensity variations on time scales of 6 h. Each data point is a single 10-s observation.

Figure 8. X-ray light curve for 3C371 showing intensity variations on time scales of one to two weeks. This source is considerably fainter than PKS2155-304, requiring that the data be summed over 2-, 4-, and 8-day intervals.



(where, for example, the 6-h variability of PKS2155-304 would not readily be accessible because of the alternation of day and night and the changes in observing conditions). We are continuing to survey BL Lac objects using the HEAO data in an attempt to establish a typical brightness and characteristic time scale of variability for each source, in addition to other ensemble characteristics of the population. We are also continuing to analyze the light curves shown here in order to achieve better characterization of the flaring behavior.

[Sponsored by NASA]

XUV Radiation Modeling of Dense Plasmas, by D. Duston and J. Davis, *Plasma Physics Division*

In recent years, the creation of an intense source of short-wavelength radiation from a hot plasma has been of extreme interest to the scientific community because of the application for such a device in studying wideband radiation effects on materials as well as for inertial confinement fusion research. In an effort to provide theoretical guidance in this area, NRL scientists have constructed detailed models of these hot, dense plasma sources to analyze the experimental spectral data for diagnostic purposes and to predict energy conversion efficiencies as functions of material, load configuration, and power delivered to the load.

The most recent model developed at NRL is unique in that it explicitly treats a large number of atomic levels of an aluminum plasma in collisional-radiative equilibrium (CRE) in order to calculate the soft x-ray and extreme ultraviolet (XUV) emission as a function of plasma density, temperature, and size. The model is based on the solution of the time-independent rate equa-

tions describing the dominant particle-particle and photon-particle collisions that determine the populations of each ground state and of approximately 100 excited states in a hot, dense aluminum plasma. These excited states are from all ions between Al III and Al XIII, and it is the radiation resulting from transitions among these states that lies in the region of interest, typically 50 to 2200 eV (25.0 to 0.56 nm). In addition to collisional couplings between states, absorption and emission of plasma radiation are calculated using a probability-of-escape algorithm that self-consistently couples the collision and radiation physics in the calculation. Hence, this model permits accurate predictions of both line and continuum emission energies, as well as calculation of a detailed emission spectrum over a wide range of wavelengths for direct comparison with experimental plasma-radiation signatures.

One interesting aspect of this work is the comparison between the results of this detailed model and those predicted by the coronal (low density limit) and the local thermodynamic equilibrium (LTE) (high density limit) models that are used extensively in astrophysical and plasma communities. In Figure 9, the line-radiation power coefficient (the product of radiation power density, ion density, and electron density) is plotted as a function of electron temperature for all three models. The plasma described here has a density of 10^{19} ions cm^{-3} (typical of dense plasma experiments) and is optically thin (very small radius). Notice the large differences in the *L*-shell (Al IV — Al XI) peak at ~ 100 eV as predicted by the coronal model and the CRE model. The LTE model predicts the peak power level of the *L*-shell radiation satisfactorily, but the temperature at which it is predicted to occur (~ 70 eV) is incorrect. For the

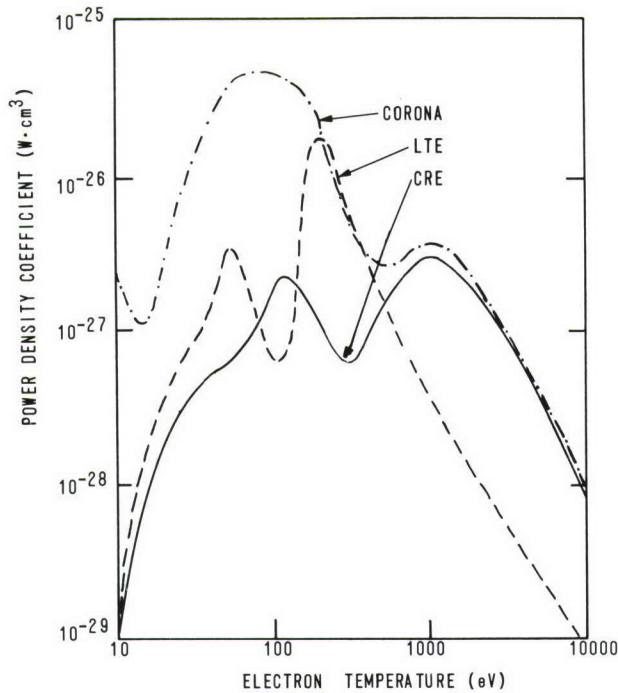


Figure 9. Total line emission power coefficient vs electron temperature for an aluminum plasma of 10^{19} ions cm^{-3} (optically thin). Results from three radiation-ionization models are shown: LTE, corona, and NRL's CRE.

K -shell (Al XII — Al XIII) peak at about 1000 eV, the coronal result is accurate but the LTE model is seriously in error (by an order of magnitude) and has the wrong temperature distribution as well. Therefore, at the densities that are common in the dense plasma experiments being studied, neither the LTE model nor the corona model yields accurate results over the wide range of temperatures the plasma may span.

A typical theoretical CRE spectrum is shown in Figure 10 for a cylindrical aluminum plasma. The emission lines lying below 17.5 nm (71 eV) are due primarily to transitions from excited states of principal quantum number $n = 3$ to states of $n = 2$; above 17.5 nm, the lines are due predominantly to transitions among the $n = 2$ levels. Notice the rise in the continuum radiation at lower wavelengths as characterized by the various electron-ion recombination edges, shown as several sharp increases in intensity well below the line intensities.

Another aspect of this work that should prove valuable to experimentalists is the capability of the model to predict line-intensity ratios as a function of temperature. Shown in Table 1 is a list of transition pairs that form lines whose ratios are temperature sensitive. (Some of the lines are

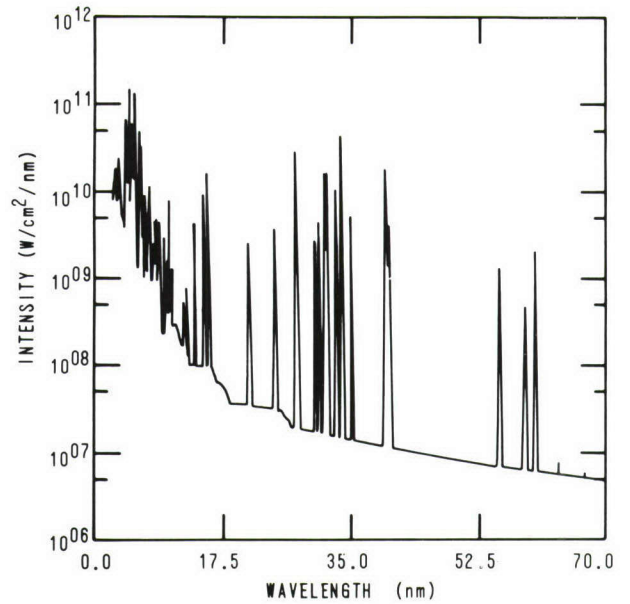


Figure 10. Emission spectrum calculated with NRL's CRE model for an aluminum plasma with 1-mm radius, 10^{19} ions cm^{-3} , and a linear temperature gradient from 80 eV on axis to 30 eV at the outer plasma boundary

represented in the table by several wavelengths, since these transitions are multiplets and each line is actually a manifold of lines.) The ratios of these line pairs as predicted by the model for an optically thin plasma at 10^{19} ions cm^{-3} are shown in Figure 11. In addition, each pair of transitions consists of lines that lie very close to one another in the spectrum. This eliminates experimental difficulties arising from variable film or crystal response when analyzing the spectral data. The ratios shown in Figure 11 allow one to diagnose aluminum plasma temperatures from 10 to 150 eV. In a previous work [1], line ratios were studied that provided a temperature diagnosis from 400 to 1200 eV. The intervening temperature region from 150 to 400 eV is relatively undiagnosable with this technique, because little line intensity is emitted at these temperatures. (Note the minimum in the curve between the K - and L -shells in Figure 9.)

With the successful completion of this aluminum model, similar calculational techniques are now being applied to construct an argon K - and L -shell model. It will be used to diagnose and predict conversion efficiencies of argon plasmas as an intense radiation source and as a seed element in laser-imploded microballoons used as targets in inertial confinement fusion experiments. Having a detailed calculation of dense plasma radiation energetics, such as provided by

Table 1. Atomic Transitions and Wavelengths that Comprise the Temperature Sensitive/Line Intensity Ratios Shown in Figure 11

Key	Ion	Transition	Wavelengths (nm)
1	Al IV	$2s^22p^6(^1S) - 2s^22p^53d(^3D)$	12.9729
	Al V	$2s^22p^5(^2P) - 2s2p^4(^3P)3s(^2P)$	13.0413, 13.0848, 13.1003, 13.1441
2	Al V	$2s^22p^5(^2P) - 2s2p^4(^3P)3d(^2D)$	10.7945, 10.8057, 10.8462
	Al VI	$2s^22p^4(^3P) - 2s^22p^3(^4S)3s(^3S)$	10.9514, 10.9843, 10.9974
3	Al VI	$2s^22p^4(^3P) - 2s^22p^3(^4S)3d(^3D)$	9.2626, 9.2636, 9.2875, 9.297
	Al VII	$2s^22p^3(^2P) - 2s^22p^2(^1D)3s(^2D)$	9.063
4	Al VII	$2s^22p^3(^4S) - 2s^22p^2(^3P)3d(^4P)$	7.527, 7.5320, 7.536
	Al VIII	$2s2p^3(^3D) - 2s2p^2(^2D)3s(^3D)$	7.5577
5	Al VIII	$2s2p^3(^5S) - 2s2p^2(^4P)3d(^5P)$	6.6704, 6.6731, 6.6771
	Al IX	$2s^22p(^2P) - 2s^23s(^2S)$	6.6624, 6.6836
6	Al IX	$2s2p^2(^4P) - 2s2p3d(^4D)$	6.0504, 6.0549, 6.0588, 6.0645
	Al X	$2s2p(^1P) - 2s3d(^1D)$	5.9107
7	Al X	$2s^2(^1S) - 2s3p(^1P)$	5.1979
	Al XI	$2p(^2P) - 3s(^2S)$	5.439

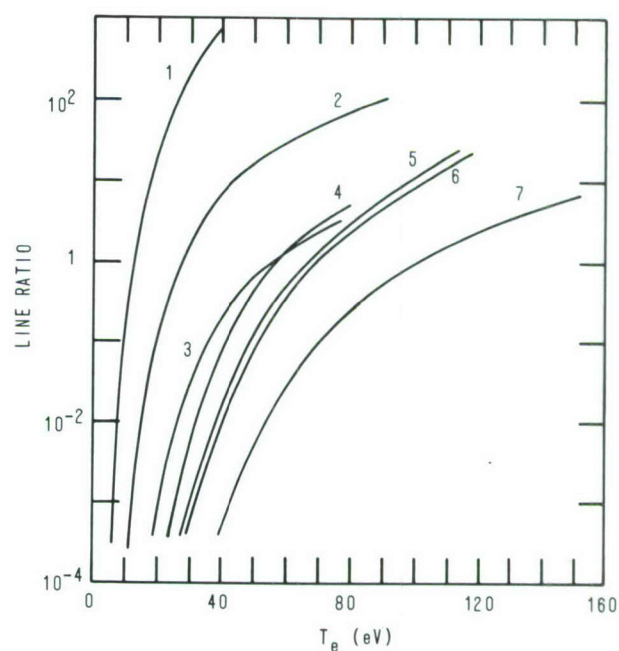


Figure 11. Temperature-sensitive line intensity ratios for selected L-shell lines for an optically thin aluminum plasma at 10^{19} ions cm^{-3} . (See Table 1 for key.)

this CRE model, should be of great assistance to plasma experimentalists who previously had to rely on LTE or corona models for radiation calculations in the XUV region of the spectrum [2].

[Sponsored by DNA]

Reference

1. D. Duston and J. Davis, *Phys. Rev. A* **21**, 1664 (1980).
2. D. Duston and J. Davis, *Phys. Rev. A* **23**, 2620 (1981).

An Ultra-high-power Magnetron for Air Breakdown Studies, by R.K. Parker and W.M. Black, *Plasma Physics Division*

A renewed interest in military applications for high-power microwave systems has been stimulated by the development of new sources with gigawatt output levels of peak pulse power. An innovative NRL device called a hybrid inverted coaxial magnetron is being used to study the microwave breakdown of the atmosphere. For the first time, critical experimental data can be obtained concerning the breakdown and subsequent deposition of microwave energy in the breakdown plasma and the formation and recovery of the breakdown channel.

The basic design philosophy for the magnetron was to develop a practical, reliable device to produce high levels of microwave power in a single mode. The magnetron has long been recognized as an attractive approach to the efficient production of high radiative power levels at centimeter wavelengths. In contrast to linear beam tubes, the magnetron functions by having a large number of power-generating sections (anode cavities) operating in parallel. When scaled to very high voltages, magnetrons offer an additional advantage in that the electron potential energy, rather than kinetic energy, is converted to microwave power. In an efficient magnetron, the electron kinetic energy is determined primarily by the rotational drift velocity. Because this velocity is much less than that associated with the applied voltage, relativistic effects detrimental to the electron dynamics are minimized.

Recent experiments by researchers such as Bekefi at M.I.T. have dramatically demonstrated the adaptation of the conventional magnetron geometry to short-pulse production of gigawatt power levels by scaling to high voltage. In these experiments, the impedance associated with the electron flow was lowered by reducing the diode separation to values substantially less than the

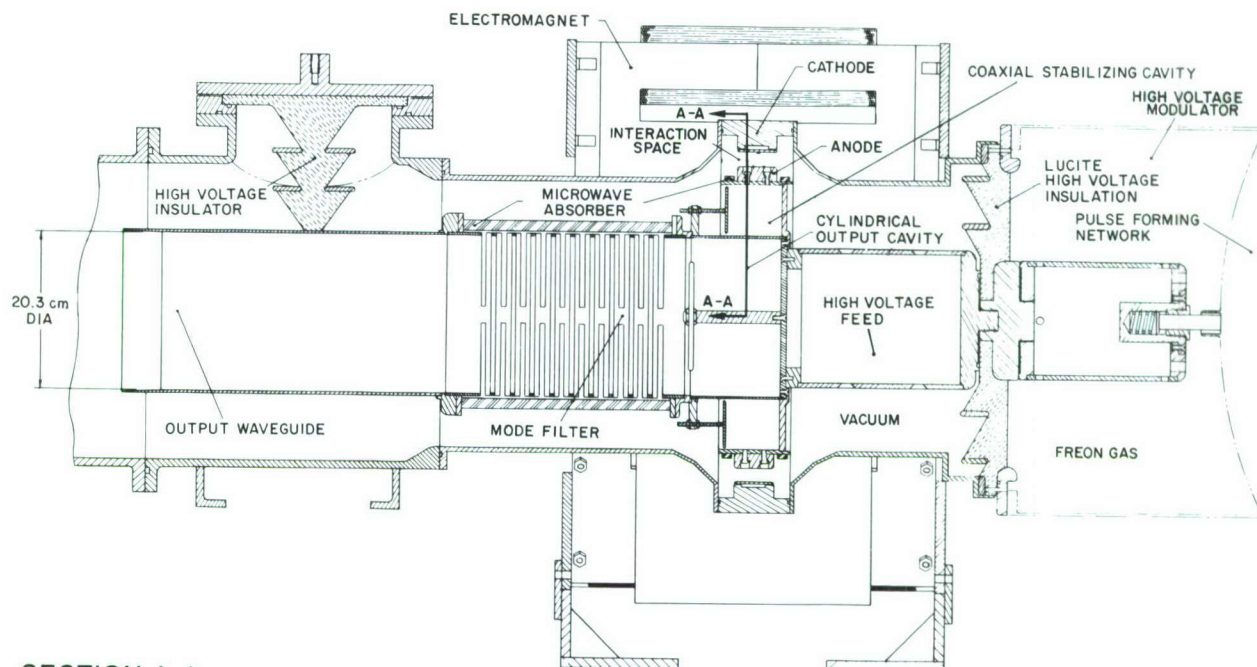
periodic spacing of the slow-wave structure. Mode separation was enhanced by keeping the number of anode cavities to a minimum, typically six or eight. Although these initial experiments have yielded their expected peak powers, further improvement in performance will become increasingly difficult to achieve. Problems result from the effects of reduced electrode separation and from perturbations to the applied magnetic field. At applied voltages of hundreds of kilovolts, the operable electron emission mechanism is plasma-induced field emission. The maximum achievable pulse duration will therefore be determined by the radial diffusion of cathode plasma across magnetic field lines. Reduced electrode separation consequently results in a more rapid gap closure.

The constraints imposed by these problems emphasize the need to consider alternate techniques for high-power scaling. Since power flow in a diode can be increased either by reducing the electrode separation or by increasing the electrode area, the obvious alternative is to substantially increase the circumference of the interaction space and, consequently, the number of anode cavities. Since the frequency separation between adjacent modes decreases with increasing number of cavities, mode control and stability will be a predominant design problem.

The new NRL magnetron is based on the hybrid inverted coaxial design shown in Figure 12. The increased electrode area (600 cm²) is achieved by reversing the polarity of the device and inserting a coaxial stabilization cavity between the anode slow-wave structure and the cylindrical output waveguide. The use of graphite as the cathode material ensures the rapid formation of the cathode plasma required for plasma-induced field emission.

To date, peak microwave powers of 500 to 800 MW have been measured with calibrated sidewall couplers and RF crystal detectors. A high-voltage modulator provides a 600-kV single-pulse duration of 50 ns, with a measured diode current of roughly 4 kA. Consequently, the efficiency in producing the microwave power is roughly 25%. Accurate measurements have verified the design frequency of 3.2 GHz.

The large peak microwave fields generated by this system provide a unique capability for studying air breakdown and the subsequent deposition of microwave energy in the breakdown plasma. When the incoming microwave frequency equals the electron plasma frequency (ω_{pe})



SECTION A-A

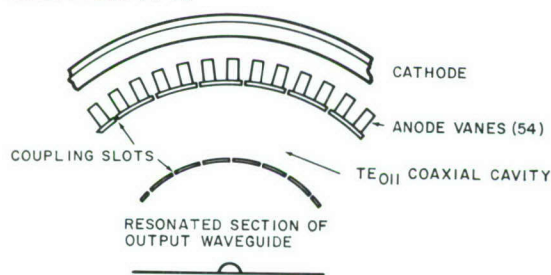


Figure 12. The NRL hybrid inverted coaxial magnetron. Microwave power generated in the 54 anode cavities is coupled through slots between every other anode vane to a coaxial stabilizing cavity. This power is then fed into the output cylindrical waveguide through a mode filter designed to pass only the desired TE_{01} mode, which has a circular electric field that is zero on axis and at the guide wall.

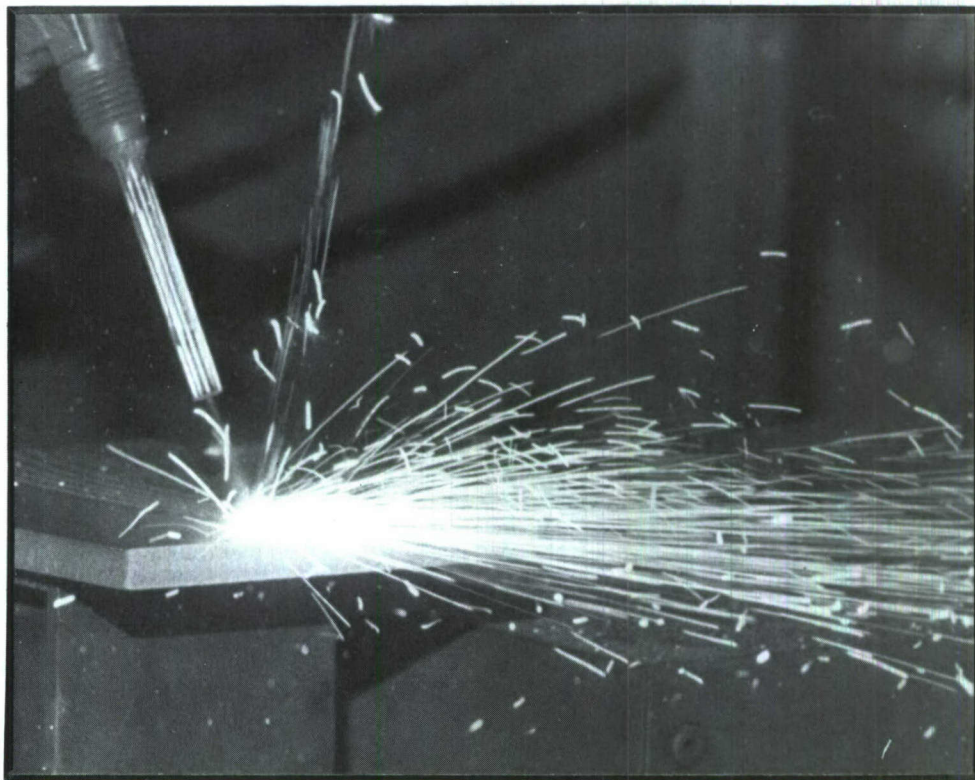
$\approx 5.6 \times 10^4 \sqrt{n}$, n in cm^{-3}), the corresponding electron density n is said to be critical and the air has broken down. At atmospheric pressure, the evolution of the microwave-generated plasma is dominated by electron neutral collisions. When the collision frequency for electron neutral momentum transfer is large compared to the microwave frequency, strong absorption of the incident radiation is predicted by theory. This strong coupling should produce an electron density in the breakdown plasma that is substantially greater than the critical value in a collisionless plasma (low particle densities). In the initial experiments, with M. Bollen of Mission Research Corp., conducted at atmospheric pressure using a 150-MW, 30-ns pulse, we observed densities of

more than 100 times the value corresponding to $\omega_{pe} \approx \omega$.

The magnetron modulator is now being replaced to increase the pulsewidth to ~ 250 ns. Tests will be conducted to investigate the feasibility of scaling the magnetron to even greater pulsewidths ($\geq 1 \mu\text{s}$). Breakdown studies will include measuring the degradation of the high-power pulse as it passes through air and measuring the density by interferometry techniques. The initial objective, however, of developing a practical source of S-band radiation to conduct breakdown studies, has been successfully achieved. The valuable assistance of R. Tobin of B-K Dynamics is gratefully acknowledged.

[Sponsored by NAVAIRSYSCOM]

MATERIALS MODIFICATION AND BEHAVIOR



MATERIALS MODIFICATION AND BEHAVIOR

The Navy is engaged in a never-ending search for improved capabilities with which to carry out its many mission responsibilities. An all-pervading aspect of the search is the development of new or improved materials and processes that can contribute to enhanced performance. The needs and corresponding opportunities are endless, and NRL programs continue to address many of them through research directed toward new modification techniques and improved understanding of the behavior of materials.

A New Metal-surface Cleaning Method	143
Ion Implantation, a New Method to Modify Polymers	144
Corrosion Behavior of Laser-processed Metal Surfaces	146
Ion Implantation for Improved Corrosion Resistance	147
A New Class of Amorphous Magnetic Alloys	149
InP Planar Transferred-electron Devices	150

A New Metal-surface Cleaning Method, by D.L. Venezky and R. Panayappan, *Chemistry Division*

Protective coatings and coating technologies play an important role in reducing maintenance and extending the useful lives of naval vessels and shipboard machinery. For maximum protection, a coating must be applied on a clean, uncorroded surface and maintain its integrity for long periods of time. The surface cleaning and pretreatment technology required to ensure the integrity of coatings has shown little improvement over the years, despite indications that 90% of all coating failures occur because of inadequate pretreatment methods. Surface preparation by the time-honored chipping and wire brushing approach is often nonuniform and always time-consuming. Sandblasting and chemical cleaners are often used in the shipyard, but they pose health and safety problems that require the inconvenience of protecting shipboard items by covering or even removal. Consequently, NRL scientists have been working to develop new cleaning chemicals and precoating procedures that can be applied safely and efficiently to prepare shipboard surfaces for protective coatings.

At NRL a new procedure has been developed that provides a marked improvement in pretreatment technology. A paste that consists of a water-soluble organic polymer combined with a chelant is applied to the dirty corroded surface. During cure times of minutes to hours, depending on the formulation, an outer plastic film encapsulates the cleaning ingredients, keeps them in contact with the dirty surface, prevents dripping, and permits the chelant (and sometimes the polymer) to dissolve the metal ions. The thick hard film that results can be peeled off like a strip of tape, bringing the dirt and corrosion products with it. The film can be disposed of as solid waste.

NRL scientists have studied a number of chelating agents that are capable of forming strong complexes with iron, such as ethylenediaminetetraacetic acid (EDTA), nitrilotriacetic acid, iminodiacetic acid, and hydroxyethyliminodiacetic acid. The chelating agents were used in amounts ranging from 1 to 10% by weight of the entire solution. After many tests, EDTA was selected as the preferred chelating agent for the iron system being investigated.

The second component needed for the new system was a water-soluble polymer that could be cross-linked with iron ions to form an insoluble

material. Methacrylic and acrylic acid polymers and polyvinylpyrrolidone (PVP) were investigated as candidates. A 5- to 30-% (by weight) solution or paste of PVP that was combined with EDTA was found to be particularly suitable for iron surfaces. Surfactants were included in the composition to improve the surface wetting properties. The exact proportions of the various components in the cleaning formulation are influenced by the amount of rust on the surfaces, the ambient humidity and temperature, and the time allowed for the cleaning and coating activity.

The cleaning process is illustrated in Figures 1 through 3. The cleaning formulation is applied as a thick paste (Figure 1) to a typical oxidized iron surface that has a layer of magnetite (Fe_3O_4) and rust (Fe_2O_3). The outer surface of the cleaning composition then forms a solid polymeric film that encapsulates the cleaning fluid in contact with the dirty surface (Figure 2). The applied cleaning material is allowed to clean and to harden over a period of 2 to 24 h (with PVP, preferably 8 to 12 h at about 24°C (75°F)). The result is a thick strip of plastic material that protects the clean metal surface and contains the iron ions from the dissolved rust as well as other loose material. When the cured strip is peeled away (Figure 3), it leaves a clean metal surface with a thin magnetite layer that affords temporary protection from rusting until the permanent protective coating is applied.



Figure 1. Dr. Panayappan applying the PVP/EDTA cleaning formulation to a typical rusty surface

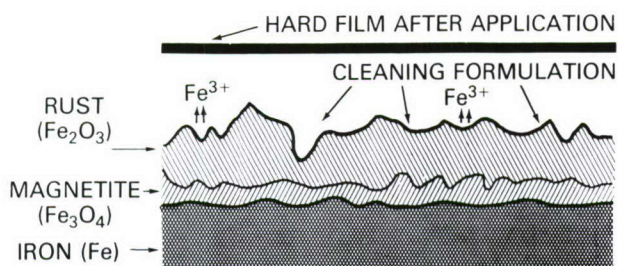


Figure 2. Encapsulating process with film holding the cleaning formulation in contact with the rust



Figure 3. Removing the cleaning strip that contains the rust and other corrosion products

The advantages of NRL's new cleaning formulation and technique over existing methods are substantial. A shipboard metal surface now can be effectively and easily cleaned with a minimum of effort. If a large area such as a bilge or tank is cleaned, the thin adherent layer of magnetite that remains should make the surface resistant to rust for at least a day, until the protective coating is applied. Finally, the chemicals suggested for iron surfaces are both economical and nontoxic, and the polymeric film formed can be disposed of easily and safely as solid waste.

Many modifications and variations of the formulation reported for iron surfaces and the removal of rust are possible. We are investigating the mechanism of the reactions that are

important in the encapsulating, solubilizing, hardening, and peeling steps of the new process. In addition, we are developing formulations for Navy applications that require specific characteristics for such variables as the area of application, type of metal, temperature, humidity, and the surface quality required before the protective coating can be applied. When the formulations are optimized, shelf life and cost estimates will be determined.

[Sponsored by ONR]

Ion Implantation, a New Method to Modify Polymers, by D.C. Weber and P. Brant, *Chemistry Division*; and C. Carosella, *Radiation Technology Division*

Ion implantation is an established technique for modifying the physical and electrical properties of metals, alloys, and semiconductors. We have extended its use to polymers and have demonstrated for the first time the unique potential of this technique in the chemical and physical modification of organic polymers. We will present results for the halogen cations (F^+ , Cl^+ , Br^+ , I^+) implanted into free-standing films of polyacetylene, $(CH)_x$.

Polyacetylene, a conjugated polymer, is being investigated by several research groups because of its electrical properties as well as other interesting properties. (See, for example, *NRL Review*, issued July 1980, pp. 179–180.) In a typical experiment, the ion beam energy was ~ 10 to 40 keV, the total ion dose ranged from 1×10^{15} to 3×10^{17} ions cm^{-2} , and the beam current was $1 \mu A$. These beam parameters produce implanted ion concentrations of 0.1 to 10 at.% in the region of highest ion concentration (~ 1 to 2 nm thick). The ion beam was swept across the sample at a rate sufficient to keep local heating effects to a minimum while also ensuring a uniform ion concentration across each sample.

The characteristics of implanted $(CH)_x$ films were investigated by x-ray photoelectron spectroscopy (XPS), electron spin resonance (ESR), ^{19}F NMR, IR- and UV-visible spectroscopies as well as He^+ backscattering and scanning electron microscopy (SEM) (~ 10 nm resolution). Pristine $(CH)_x$ films decompose in air, losing their characteristic metallic luster in a matter of days. However, most *implanted* films retain the silvery appearance of pure $(CH)_x$ and exhibit relatively high reflectivities through the visible region after long exposures to air (up to a year in many cases). Other films implanted at 25 keV with 0.3 ,

1.0 and $3.1 \times 10^{17} \text{ F}^+ \text{ cm}^{-2}$, respectively, turned red, brown and blue. Studies are under way to determine whether these color changes are caused by a bulk interference pattern or by local chemically induced "color centers." We believe that ion implantation results in one or both of the two ion-substrate interactions shown in Figure 4.

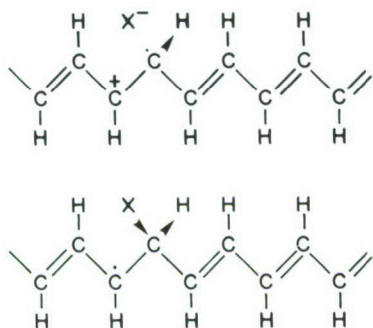


Figure 4. Two possible ion-substrate interactions. X represents the halogen atom used in the ion beam. Arrowheads indicate nonplanar bonds.

Various spectroscopic techniques were used to determine which of the above results is obtained after implantation. The following analysis pertains to the F^+ -implanted $(\text{CH})_x$. Transmission and attenuated total reflectance IR spectra (4000 to 400 cm^{-1}) are identical with those of pure $(\text{CH})_x$. One film, doped with $3.1 \times 10^{17} \text{ F}^+ \text{ cm}^{-2}$ at 25 keV , was examined by both X- and Q-band ESR and showed no difference from pure $(\text{CH})_x$ analyzed in a similar manner.

X-ray photoelectron spectroscopy is useful for detecting and examining the implanted ions. For example, Figure 5 shows the F 1s spectrum of F^+ -implanted $(\text{CH})_x$ for four different F^+ fluences. The narrow (full width at half-maximum of 1.7 eV) symmetric F 1s peak indicates the presence of a single fluorine-type interaction with the sample. Narrow single peaks are also found for samples implanted with Cl^+ (Cl 2p), Br^+ (Br 3d), and I^+ (I 3d $_{5/2}$). The C 1s line in implanted $(\text{CH})_x$ retains the peak shape and position recorded for pure $(\text{CH})_x$. There are no new C 1s peaks, which indicates that no damage has occurred to the polymer. Lower kinetic energy photoelectrons are preferentially attenuated with respect to the higher energy photoelectrons in the implanted samples, in accord with the strong depth dependence of the ion concentration. In addition, we find that F 1s signals

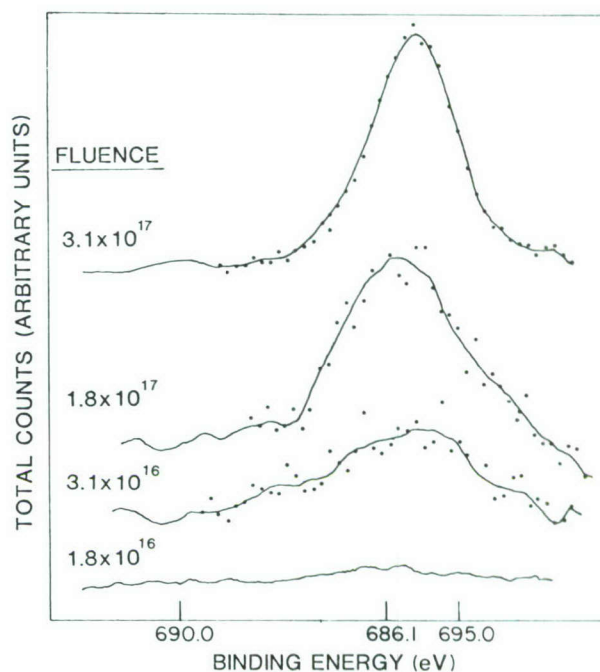


Figure 5. F 1s XPS spectra at 25 keV with various fluences. Peaks indicate a single fluorine-type interaction with the sample. Note that the F 1s signals increase with fluence.

increase with increasing fluence. Thus, the XPS results suggest that there is no significant ion diffusion after implantation. These findings are substantiated by high-energy helium backscattering spectra which demonstrate that the implanted species remain in a thin near-surface layer. A ^{19}F NMR was obtained at 4.9 K for a F^+ -implanted $(\text{CH})_x$ sample in which the total fluence of $4 \times 10^{18} \text{ F}^+ \text{ cm}^{-2}$ was distributed homogeneously to a depth of approximately 180 nm . The NMR signal is similar in intensity, position, and bandwidth to the signal recorded under the same conditions for a polytetrafluoroethylene (PTFE) sample containing 10^{18} fluorine atoms. However, at present signal/noise levels there is no indication of ^{19}F – ^{19}F coupling as is observed for PTFE.

These results demonstrate that ion implantation can be used to modify polyacetylene. These modifications include the unique, spatially resolved chemical addition to the polymer backbone, controlled alteration of the optical reflectivity, and stabilization of the modified polymer. We can control the extent or type of the modification by appropriate selection of the ion beam, energy of the beam, and total fluence. We are continuing to study the ion-substrate interaction in $(\text{CH})_x$. The study will be expanded to include graphite, polyparaphenylene sulfide,

and other materials with electrical properties that can be tailored by ion implantation to control conductivity over a wide range. Such materials have been used for a variety of electrical applications, including photovoltaic cells, PN junctions, and even a totally organic battery that incorporated electrodes that had been doped with (CH)_x.

[Sponsored by ONR]

Corrosion Behavior of Laser-processed Metal Surfaces, E. McCafferty, P.G. Moore, and J.D. Ayers, *Material Science and Technology Division*

Laser processing of a metal can modify its surface properties, including its corrosion resistance. The interaction between a laser beam and a metal entails rapid melting followed by rapid solidification in a surface region, with melting depth typically 10 to 100 μm . Such laser processing modifies the metal surface by changing its microstructure and/or chemical composition. At the Naval Research Laboratory, recent studies have been made of several metal systems in which surfaces have been modified by laser alloying, laser melting, or laser remelt consolidation of porous coatings.

Surface composition can be altered by a relatively new process, called laser alloying, in which a metallic coating and the underlying metal substrate are rapidly melted by a high-power, continuous-wave CO₂ laser. The rapid melting and the concomitant mixing, followed by rapid resolidification, produce a surface alloy of the coating and substrate metals. Initial research at NRL on laser-surface alloying has concentrated on the preparation and characterization of iron/chromium alloys, because much is known about the corrosion behavior of the corresponding bulk alloys.

Figure 6 shows the electrochemical behavior of 1018 steel and several iron/chromium surface alloys. With increasing positive potential (right to left), the steel substrate displays increasing current output (i.e., an increasing corrosion rate). By contrast, the three Fe/Cr surface alloys exhibit lower currents (up to +0.8 V), because of the formation of passive surface films. In the passive region, the current densities decrease with increasing Cr content, somewhat similarly to the behavior of conventional bulk stainless steels. The increases in current above +0.8 V are not indicative of increased corrosion rates, but of the onset of a new anodic reaction (i.e., oxygen evolution).

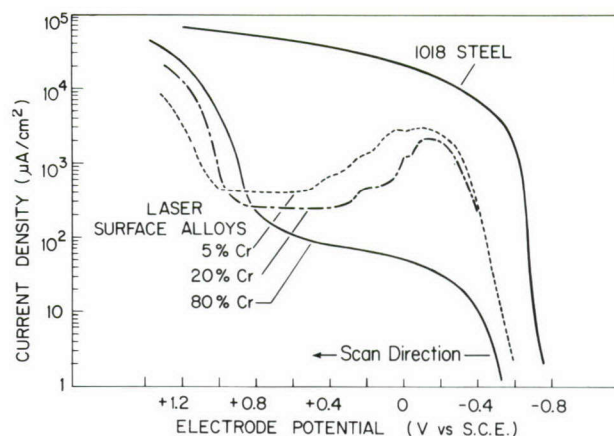


Figure 6. Electrochemical behavior of Fe/Cr laser surface alloys and 1018 stainless steel subjected to increasing positive potential in 0.1 M sodium sulphate solution.

The corrosion resistance can also be enhanced by using the laser to modify physical, rather than chemical, surface properties. For example, porous titanium coatings formed on steel by plasma spraying have been remelted by the laser to eliminate the pores. The remelted coating of pure titanium then provides corrosion protection to the underlying steel in seawater. Figure 7 shows cross-sections through the porous and consolidated coatings after 15 days of immersion in natural seawater at the NRL Marine Corrosion Laboratory at Key West, Florida. The unconsolidated sample in Figure 7a shows pitting of the steel at the coating-substrate interface. The sample in Figure 7b was consolidated, with the laser melting approximately one-third of the coating thickness, and shows no evidence of corrosion.

In another study, a laser surface-melted aluminum-1% manganese alloy showed improved resistance to uniform corrosion because of a change in microstructure. This is attributed to the redistribution of second phases, normally present as discrete particles in the bulk alloy, into layers that are parallel to the surface in the melted region.

Present NRL efforts coupling corrosion research and laser processing are directed toward improving the corrosion resistance of naval alloys exposed to the marine environment. Advanced stainless steel surface alloys containing high concentrations of nickel, chromium, and molybdenum for improved pitting resistance are being produced by laser-surface alloying. The alloys are

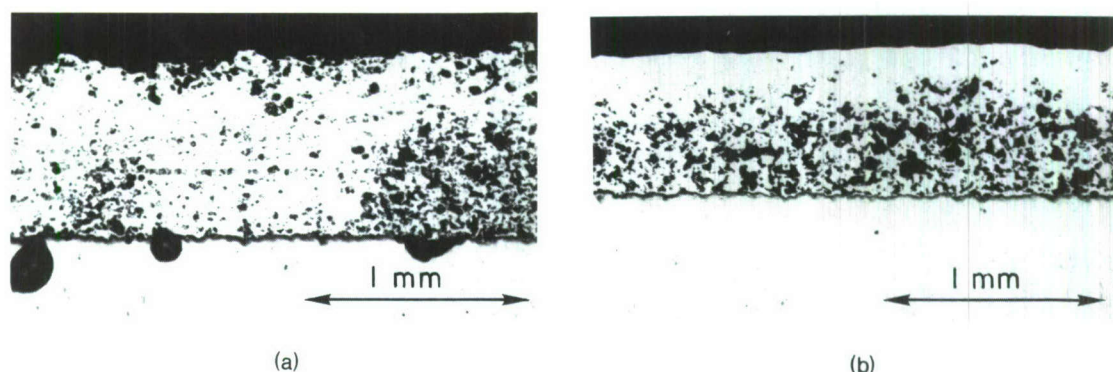


Figure 7. Cross-sectional views through (a) the porous and (b) laser-consolidated titanium coatings on steel after 15 days of immersion in seawater. Part (a) shows pitting (dark spots) at the coating-substrate interface.

used for a variety of purposes including turbine blades, propeller shafts, and naval machinery.

[Sponsored by ONR]

Ion Implantation for Improved Corrosion Resistance by G.K. Hubler and J.K. Hirvonen, *Condensed Matter and Radiation Sciences Division*

Corrosion is one of the most common reasons for rejection of aircraft bearings during periodic scheduled overhaul in the Navy. Corrosion also causes premature (catastrophic) in-service failures and unacceptably short shelf life for new unused bearings. For example, the majority of bearings reconditioned at the Naval Air Rework Facilities (NARFs) are unused spares that have corroded on the shelf, not those from used aircraft engines. It is estimated that the Navy spends over \$1 million per year for the replacement of turbojet main-shaft engine bearings alone, excluding labor costs.

Turbojet engines that are used only intermittently exhibit the worst corrosion problems, consisting of local corrosion pits formed at the contact points between the rollers or balls and the inner or outer race. These pits act as initiation sites for catastrophic fatigue failures. In responding to these problems, NRL has established research programs to investigate the application of ion implantation to produce corrosion-resistant bearings made of 52100 and M-50 steel, two of the most commonly used alloys for Navy equipment.

Ion implantation is a process by which virtually any element can be injected into the near-surface region of a solid by directing a beam of high-velocity ions onto it in a vacuum chamber.

Energies usually range from tens to hundreds of keV. One distinct advantage of ion implantation is that thin surface layers of corrosion- or wear-resistant alloys can be formed on a metal without altering its desirable bulk properties. In addition, the surface alloy has a graded composition, i.e., no well-defined interface, and hence has no adhesion problems. These differences are important when compared with depositional techniques, which produce coatings that can degrade mechanical performance of the bearings.

The research programs include the development of bearing implantation treatments and subsequent corrosion tests that simulate the conditions in an engine compartment under field service. Quantitative electrochemical testing of the bearing is conducted to measure the corrosion kinetics and resistance to localized corrosion (pitting) in chlorine-contaminated environments (such as salt water) to which Navy equipment is generally exposed. In addition, the mechanical stability of the implanted surfaces is measured to determine whether the implantation process degrades the rolling-contact fatigue lifetime of the bearings.

The implantation energies and ion fluences used for the anticorrosion implantation treatments were chosen to produce a 15- to 30-at.% concentration of the implanted elements in a region extending from the surface to a depth of about 80 nm. The choice of ions is determined primarily by the known anticorrosion behavior of the ions in bulk materials. Some examples of this behavior include the production of stainless steel by the addition of chromium, improved pitting resistance in steels by addition of molybdenum, formation of a stable corrosion-resistant

oxide by titanium, and stabilization of an amorphous corrosion-resistant phase by phosphorus when suitably quench-alloyed with iron. The implanted species are profiled by ion beam techniques and by sputter etching used in combination with Auger electron spectroscopy.

Figure 8 shows the corrosion test geometry used to simulate the field-service conditions for M-50, a high-temperature turbojet-engine bearing alloy. The photomicrographs show the flat surface (simulating the race) both before and after being tested. Implantation with ions of chromium, molybdenum, and nitrogen improved

the corrosion resistance markedly, as evidenced by well-developed pits seen on the unimplanted sample and the absence of any form of corrosion on the implanted sample.

Tests in chloride ion solutions are being performed to measure the resistance of the ion-implanted surface alloy to localized corrosion (pitting). These tests were conducted in a pH 6 buffered, 0.01-*M* salt (NaCl) solution. Figure 9 presents potentiodynamic polarization scans for the 0.01-*M* NaCl solution for tantalum implants in the 52100 steel alloy. The pertinent characteristic of each curve is the breakdown potential

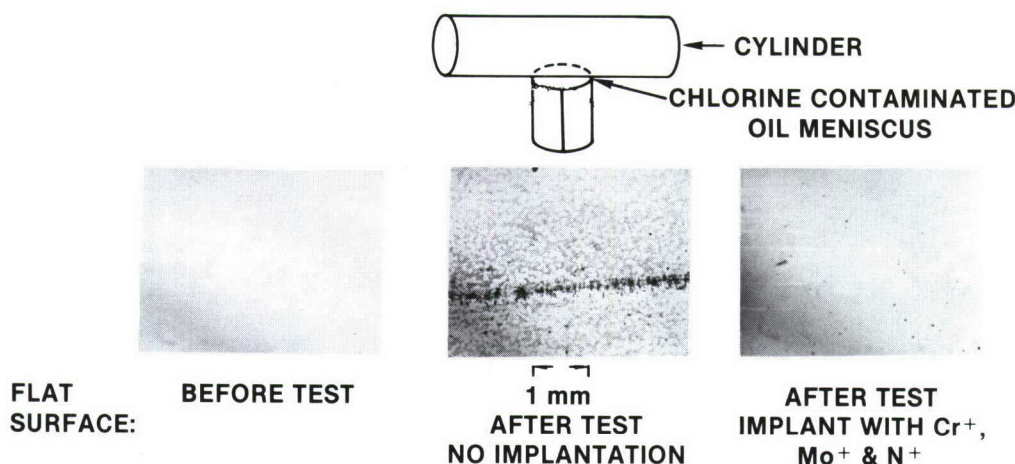


Figure 8. Simulated field-service corrosion test of M-50 steel. Flat samples were placed on top of the vertical cylinder and were statically loaded by a horizontal cylinder. After being immersed in oil contaminated with chlorine and water, the system was exposed to moist air and cycled daily between 4° and 60°C for 7 wk, with the results shown in the photomicrographs.

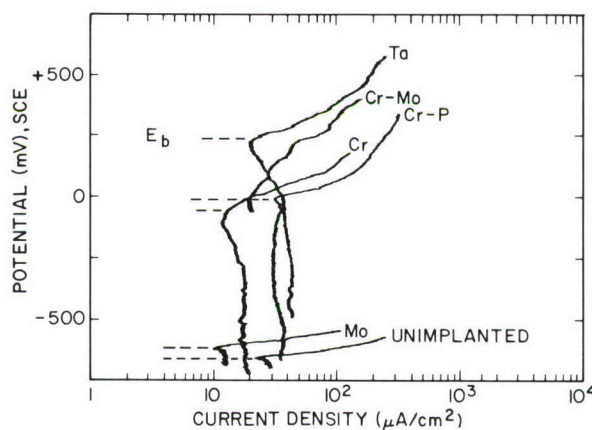


Figure 9. Anodic polarization curves of implanted 52100 bearing steel in 0.01-*M* NaCl solution buffered at pH 6. E_b is the breakdown potential (voltage at which current density suddenly begins to increase). The higher the E_b , the greater the corrosion resistance.

E_b , which characterizes the metal's ability to withstand pitting (a higher E_b indicates better protection). The breakdown potential is that voltage on the curve where there is a sudden increase in current density. Note the large improvement in E_b following Ta implantation.

In addition to these corrosion tests, 20 M-50 bearings for an H46 helicopter turbojet engine have been implanted with the most promising species (10 with Cr and 10 with Cr plus P). Results of fatigue endurance tests were compared with those of a control group of 10 unimplanted bearings. No significant differences in fatigue endurance appeared between the two groups. These findings demonstrate that the ion implantation process does not degrade the mechanical performance of the bearings. In addition, implanted jet aircraft and helicopter engine bearings have passed endurance tests in a test engine for 400 h (minimum period for operational use) at conditions simulating the speeds, loads, and temperatures experienced by engines in operational use.

These programs have demonstrated that ion implantation improves the corrosion resistance of 52100 and M-50 bearings without degrading their mechanical performance. They have also suggested that production-line implantation of bearings could be feasible. For the production line, the technique has the important advantage of not affecting the macroscopic dimensions of the precision bearings. The implantation process should be applicable to otherwise finished components, and thus can become part of an existing production line. In addition, the cost associated with implanting aircraft-quality bearing components is estimated to be but a small fraction of their initial cost.

[Sponsored by ONR, NAVAIRSYSCOM, and NAPC]

A New Class of Amorphous Magnetic Alloys, by N.C. Koon and B.N. Das, *Condensed Matter and Radiation Sciences Division*

Amorphous magnetic materials have received a great deal of attention in recent years, mainly because of their potential for use in high-performance, low-loss transformers. The use of amorphous alloys is attractive for such applications partly because a material that lacks a regular crystal structure cannot have conventional magnetic anisotropy. Because amorphous alloys combine low magnetic anisotropy with a very uniform microstructure, they are generally very easy to

magnetize, often requiring only fractions of an oersted to achieve almost complete saturation.

Amorphous metallic ribbons can be prepared by combining a magnetic transition metal such as iron, cobalt, or nickel with a metalloid glass-forming element such as boron, phosphorous, silicon, or carbon. The resultant alloy is melted in a quartz crucible, then quenched by squirting it as a stream of molten metal onto the polished surface of a rapidly rotating copper wheel. Because of the fast cooling rate ($\sim 10^6$ K s⁻¹), together with the effect of glass-forming elements in retarding crystallization, the atoms do not have time to arrange themselves in a regular crystalline array. They remain in a metastable amorphous state with no long-range crystallographic order.

One recent goal of NRL research has been to produce amorphous melt-quenched alloys that combine a strongly magnetic transition metal/metalloid glass (such as Fe₈₂B₁₈) with relatively small quantities (~ 10 at.%) of rare-earth elements such as terbium, dysprosium, holmium, praseodymium, or neodymium. Because the magnetic electrons of the rare earths are highly localized and anisotropic, their introduction into a crystalline material generally provides a very high degree of magnetic anisotropy and large distortions of the lattice when the magnetization is rotated (magnetostriction). In fact, the central problem in producing good magnetostrictive alloys is finding a method that will impart both high magnetostriction and low magnetic anisotropy. An amorphous alloy, however, already has low anisotropy and the magnetostriction can still be large. Therefore, amorphous transition metal/metalloid/rare-earth alloys can have significant potential for use in magnetostrictive devices.

Perhaps a more important use of these alloys is to make permanent magnets. Crystallization from the amorphous state provides an excellent way to produce a very fine-grained crystal structure in which the grains can have a randomly oriented magnetic anisotropy. Rare-earth additions can make this anisotropy quite large. If the grains are small enough so that each is effectively a single-domain particle, then very large magnetic fields may be required to change the magnetic state of the material, in contrast to the case when the alloy is fully amorphous.

We have recently solved the problem of how to add significant amounts of rare-earth elements to strongly magnetic transition metal/metalloid glasses while keeping the alloy amorphous. This

was accomplished by the discovery that small amounts of lanthanum (La) strongly inhibit the formation of rare-earth/transition-metal intermetallic compounds during quenching. As an example, the largest amount of terbium (Tb) that can be added to $\text{Fe}_{82}\text{B}_{18}$ without detectable crystallinity is about 1 at.%. The addition of just 2% La raises this limit to about 8 at.% Tb ($\sim 25\%$ by weight), which is enough to have a large effect on the magnetostriction and magnetic anisotropy of the glass.

One alloy of special interest is $(\text{Fe}_{82}\text{B}_{18})_{.9}\text{Tb}_{.05}\text{La}_{.05}$. Figure 10 shows the magnetization of this alloy in both the amorphous and crystallized states as a function of applied magnetic field. In the amorphous state, this alloy is very easily magnetized, as is the corresponding alloy without rare earths. Yet the calculated magnetostrictive strains are quite large (about 250 to 300×10^{-6}), compared to those typically observed for transition metals (e.g., 33×10^{-6} for Ni). Even more interesting is the effect of crystallization of the alloy by heating it for 16 h at 650°C in a magnetic field. The alloy develops an enormous hysteresis; that is, it retains much of the magnetization induced in it by an applied field even after the field is removed. In fact, once the alloy has been fully magnetized, a magnetic field of nearly 10 kOe in the opposite direction is required just to bring it back to the demagnetized

state. Naturally, this is a very desirable characteristic for a permanent magnet. In fact, these hysteretic properties are actually superior to some permanent magnet materials used commercially, and probably can be further improved.

Therefore, this new alloy class appears to be useful in two almost opposite kinds of applications. In the amorphous state, the alloys are magnetically soft and easily magnetized, yet still have high magnetostriction; therefore, they could be useful for transducers or high-speed switches. In the crystallized state, they develop very large hysteresis and thus have potential for use as permanent magnets. Future research will focus on understanding the mechanisms responsible for the interesting behavior of these alloys and on learning how to improve their desirable properties.

[Sponsored by ONR]

InP Planar Transferred-electron Devices, by K.J. Slegler, H.B. Dietrich, and R.L. Henry, *Electronics Technology Division*

Indium phosphide (InP) solid state devices offer the possibility of providing superior components for future Navy electronic warfare and communications systems operating at millimeter-wave frequencies (30 to 1000 GHz). Current work at NRL is directed toward developing a monolithic integrated circuit (MIC) technology in InP with performance superior to that of Si or GaAs MICs at millimeter wavelengths. As a first step toward this objective, we have fabricated the first all-ion-implanted planar InP transferred-electron devices (TEDs) for use as free-running oscillators [1]. Fundamental to this success is the NRL in-house materials technology for the growth of high-quality semi-insulating InP substrates upon which the TEDs and MICs are built. These substrates provide electrical isolation between various electronic devices and therefore allow for ease of circuit fabrication not available in much of the silicon integrated-circuit technology.

The types of InP TEDs that have been fabricated are illustrated in Figure 11. These devices can operate as free-running oscillators in the 1- to 40-GHz frequency range. The two-terminal device operates at the higher end of the frequency range, since its dimensions are smaller than those of the three-terminal device. The gate in the three-terminal device can be used as a switch or to control the oscillation frequency. Both types of TEDs were fabricated on semi-insulating InP

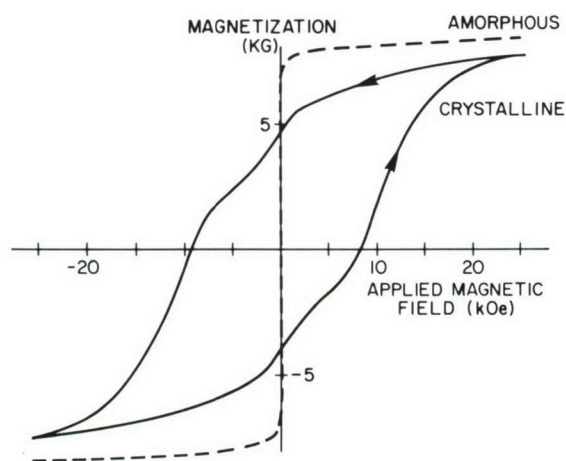


Figure 10. Intrinsic magnetization ($B_i = 4\pi M$) of $(\text{Fe}_{82}\text{B}_{18})_{.9}\text{La}_{.05}\text{Tb}_{.05}$ alloy as a function of applied magnetic field H . The alloy is easily magnetized in the amorphous state (dashed line), and shows large hysteresis (retained magnetization at zero field) in the crystalline state. The measurement sequence, indicated by arrows, began and ended with a large positive applied field.

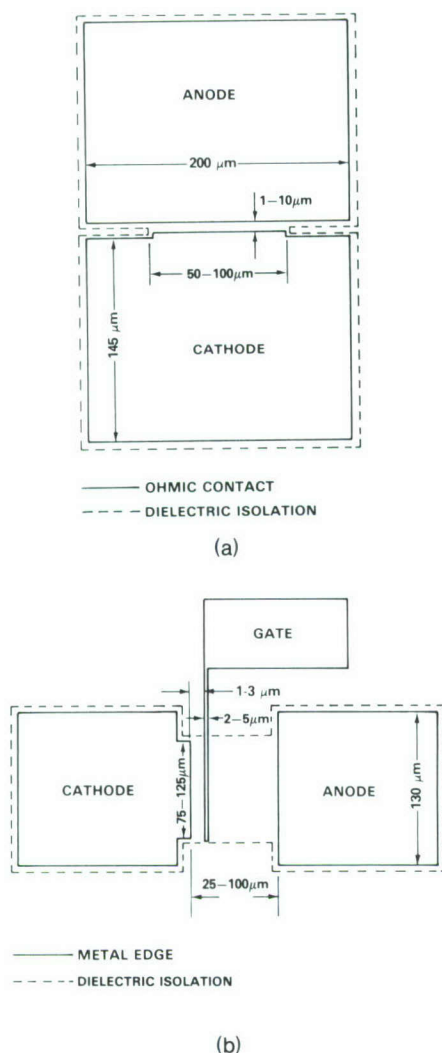


Figure 11. Geometries (map view) of NRL-developed transferred-electron devices (TED): (a) Two-terminal TED is a free-running oscillator (5-40 GHz); (b) Three-terminal TED is a free-running oscillator or high-speed switch (1 to 5 GHz) [1].

substrates grown at NRL; however, their active or conducting regions were produced differently.

The two-terminal TEDs were produced by growing a thin (0.3 to $0.4\ \mu\text{m}$) conducting n-type InP layer on the InP substrate using chemical vapor phase deposition. Commonly referred to as vapor phase epitaxy (VPE), this was performed at Varian Associates, according to NRL's specification of a free carrier (electron) concentration of $8 \times 10^{16}\ \text{cm}^{-3}$. Since VPE is a somewhat more mature technology than ion implantation in InP, it provided a baseline by which the ion implantation results could be judged.

The three-terminal TEDs had NRL ion-implanted active regions $0.3\ \mu\text{m}$ thick with free carrier concentrations of $2 \times 10^{17}\ \text{cm}^{-3}$. These were produced by a triple ^{29}Si implant followed by a $700^\circ\text{C}/20\text{-min}$ anneal with a plasma-deposited Si_3N_4 cap. This reordered the crystal lattice to produce free electrons from the Si. In the ion-implanted TEDs, the free carrier concentration of the active layers was significantly larger than the level ($8 \times 10^{16}\ \text{cm}^{-3}$) that is generally accepted as producing optimum microwave performance in these planar devices. Attempts to lower carrier concentrations were unsuccessful, presumably because of the iron incorporated in the substrate. The iron is necessary to absorb any free electrons contributed by background impurities and thereby ensure that the substrate is semi-insulating. However, it will also absorb free carriers from intentionally added impurities (such as silicon), and generally is present at levels sufficient to prevent the activation of implants designed to produce carrier concentrations less than about $10^{17}\ \text{cm}^{-3}$.

A similar phenomenon has been observed in ion-implanted GaAs TEDs fabricated on NRL semi-insulating GaAs substrates [2]. In the case of GaAs, however, the materials technology is more mature, and GaAs semi-insulating substrates have been produced at NRL without an intentionally added absorbing agent. This permits electrical activation of low-level ^{29}Si implants in the $2 \times 10^{16}\ \text{cm}^{-3}$ range. The activation of low-level TED-type implants in semi-insulating InP and GaAs is a subject of intense study by NRL scientists, with special efforts being made to investigate alternate absorbing agents such as chromium.

TEDs were processed by Dr. T. Weng and M. Bark of NRL. Figures 12a and b are representative of the pulsed current/voltage (I/V) characteristics of these InP devices. Pulsed operation eliminated undesirable thermal heating. The current dropback from maximum to minimum (differential negative resistance) was observed on both types of devices and is necessary to sustain microwave oscillations. The gate bias (voltage between gate and cathode) of the three-terminal TEDs controls the anode voltage at which differential negative resistance begins.

Completely fabricated TEDs were evaluated as free-running pulsed oscillators. Two-terminal devices delivered power outputs up to $4.1\ \text{mW}$ at $15.7\ \text{GHz}$. Three-terminal TEDs delivered their best performance at $2.1\ \text{GHz}$ with $106\ \text{mW}$ power

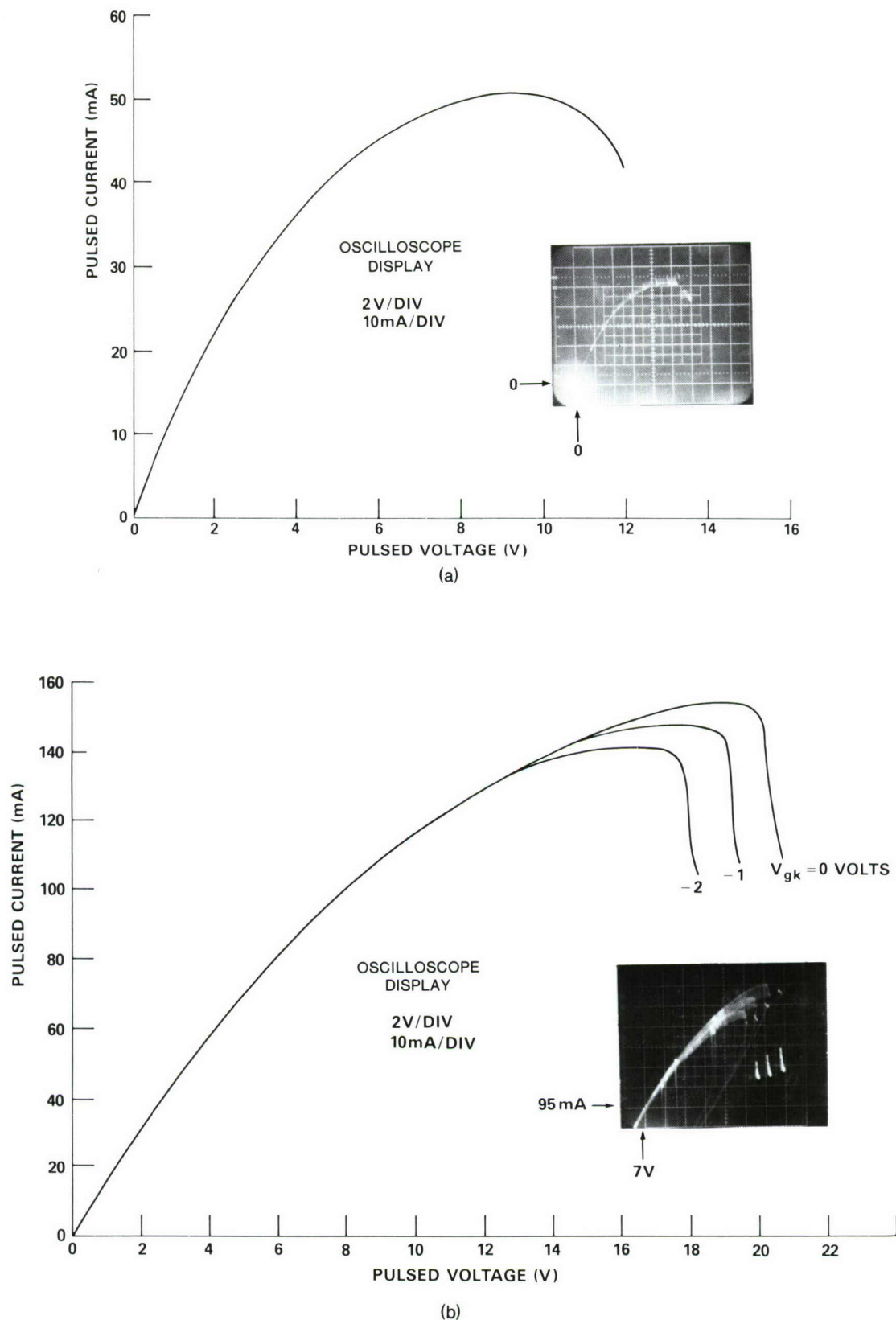


Figure 12. Current/voltage characteristics of TEDs based on iron-doped NRL semi-insulating substrates (a) Two-terminal device with active layer grown by vapor phase epitaxy; (b) Three-terminal device produced by ion implantation [1].

output. The higher power output of the three-terminal device is attributed to the device geometry and the presence of the gate. Such power levels are adequate for many microwave applications of interest to the Navy. These results suggest that ion-implanted InP TEDs can deliver performance equivalent to that of their VPE channel counterparts and that direct implantation into semi-insulating InP substrates is a viable alternative to VPE. Better performance of the ion-implanted devices is anticipated when improved semi-insulating substrates become available.

In summary, Si implants into semi-insulating InP have been successfully activated. These activations were repeatable and have been used to fabricate the first all-ion-implanted planar InP TEDs. Although their carrier concentrations generally were higher than optimum, the performance of ion-implanted TEDs compared well with that of VPE TEDs that was achieved with

lower carrier concentrations. These results represent a major step forward in achieving a planar IC technology in InP suitable for circuit operations above 20 GHz. It is now possible to consider ion implantation realistically as an important technology for InP TED-based MICs.

[Sponsored by ONR and NAVMATCOM]

References

1. T. Weng, K.J. Slegler, H.B. Dietrich, E.D. Cohen, M.L. Bark, and R.L. Henry, "Two and Three Terminal Planar InP TEDs," *IEEE Electron. Dev. Lett.* **EDL-1**, 69-71 (1980).
2. W.T. Anderson, H.B. Dietrich, E.W. Swiggard, S.H. Lee, and M.L. Bark, "Gallium Arsenide Transferred-electron Devices by Low-Level Ion Implantation," *J. Appl. Phys.* **51**, 3175-3177 (1980).

MATERIALS ANALYSIS AND PROPERTIES



MATERIALS ANALYSIS AND PROPERTIES

The development of improved materials and structures to enhance all phases of Navy operations is an important and continuing aspect of NRL research. An intrinsic and essential part of these efforts is the ability to identify, measure, model, and understand those properties and processes that affect or determine the behavior of the materials. These investigations cover a wide range of topics and frequently are essential adjuncts to other research programs. As such, they typify the strength and value of a truly multidisciplinary laboratory.

Anomalous-scattering Analysis of Macromolecular Structure	157
Signal-enhanced NMR for Materials Analysis	158
Partially Stabilized Zirconia Crystals	159
The As Antisite Defect in GaAs	161
Toward a Novel Red Blood Cell Surrogate	163

Anomalous-scattering Analysis of Macromolecular Structure, by W.A. Hendrickson, *Laboratory for the Structure of Matter*

Life processes, including responses to disease, injury, and environmental stress, are governed by biological macromolecules. A basic understanding of the essential roles of these complicated molecules demands structural knowledge of a kind that can be gained only by the diffraction analysis of crystals. X-ray crystallography provides definitive and comprehensive structural data, but such diffraction analyses of macromolecules have until recently required time-consuming and experimentally demanding indirect methods. Advances at NRL in the theory and experimental methods for using anomalous-scattering effects have made possible for the first time the direct analysis of protein structures.

The magnitude of x-ray scattering by free electrons is independent of x-ray wavelength. However, since the scattered radiation arises from the acceleration of electrons excited by the x-ray wave, resonance with natural frequencies of vibration for bound electrons in atoms can be expected to modify the scattering. This wavelength-dependent perturbation to the free-electron scattering is *anomalous* scattering (or dispersion).

One manifestation of anomalous scattering is small departures from Friedel's law of diffraction symmetry. It has long been understood that such departures have implications for crystallographic structure determination, but heretofore, anomalous scattering has played only an auxiliary role in structure analysis. However, recent advances made at NRL in the theory and experimental methods for treating the symmetry deviations due to anomalous scattering have greatly enhanced the power of such methods. The partial structure of anomalous scatterers is used to resolve ambiguities inherent in the direct anomalous-scattering information. As a result of these advances, anomalous scattering can play a central and decisive role in structure analysis.

The newly devised methods were first applied to crambin. This hydrophobic protein is found in seeds of *Crambe abyssinica*, a plant closely related to cabbage and mustard. The biological function of crambin is still unknown, but the chemical structure deduced during the crystallographic analysis is remarkably similar to that in certain plant toxins. Attempts to determine the structure by the conventional method of isomor-

phous replacement failed, because heavy-atom derivatives could not be prepared. However, the three-dimensional structure of crambin (at 0.15 nm resolution) was solved directly from the anomalous scattering of the six sulfur atoms in crambin. This is the first protein structure, and the largest atomic structure of any kind, ever to be determined *de novo* from the diffraction data of a single crystalline species. Figure 1 is a schematic of crambin.

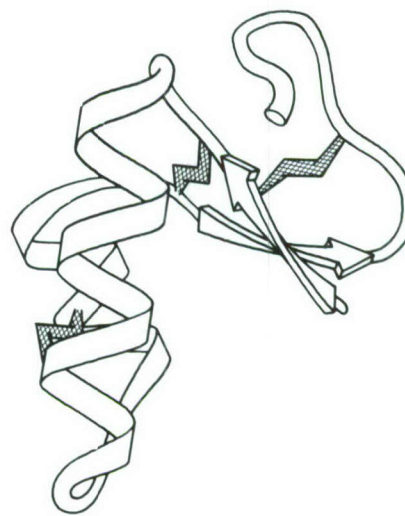


Figure 1. Molecular structure of crambin. This schematic traces the polypeptide backbone of the protein. Arrows represent the course of strands in β -sheet structure, flat ribbons represent the α -helices, and the tube represents a stretch of irregular structure. The shaded "lightning flashes" represent disulfide bonds that interconnect the backbone.

A second application of the new anomalous-scattering methods was in the elucidation of the structure of a trimeric hemerythrin. Hemerythrins are reversible oxygen carriers found in the blood of certain marine worms. They serve as a model for the development of synthetic oxygen-carrying molecules that might be used in artificial resuscitation fluids. A variety of attempts to solve this structural problem by molecular repositioning of a related known structure had failed to produce definitive results. In contrast, the new methods, coupled with molecular averaging about the noncrystallographic, threefold axis, have given a clean answer. The resulting structure (at 0.55 nm resolution) is shown schematically in Figure 2.

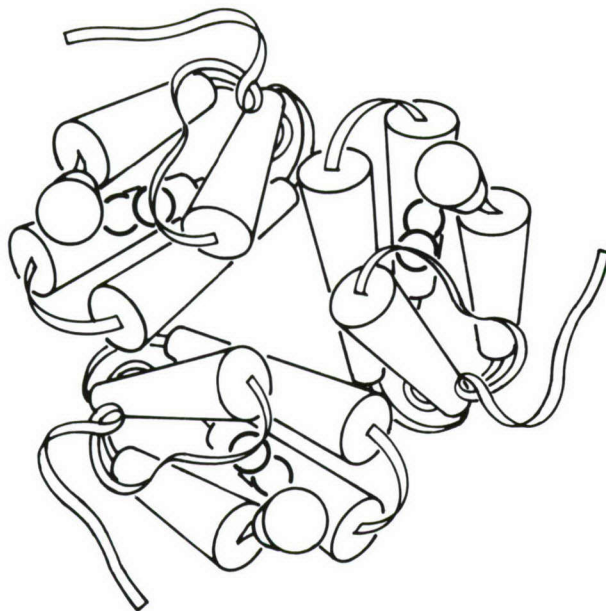


Figure 2. Molecular structure of trimeric hemerythrin. This schematic shows helices as cylinders, interconnections as ribbons, and each iron center as two small spheres. The view is along the threefold axis.

These initial applications of anomalous-scattering methods serve as a benchmark for other studies. It is clear that these methods have great potential, both for structures with native anomalous scatterers and for heavy-atom complexes. The possibility of performing experiments with multiple wavelengths from synchrotron sources further enhances the promise for anomalous-scattering applications. This work provides an improved readiness to solve complicated structural problems that have an impact in biomedical studies of naval interest.

[Sponsored by ONR]

Signal-enhanced NMR for Materials Analysis,
by B.S. Holmes and G.C. Chingas, *Chemistry Division*

Hundred-fold reductions in the time required to obtain nuclear magnetic resonance (NMR) spectra for important but weakly magnetic nuclei have been achieved using a signal-enhancement technique, adiabatic J cross-polarization (AJCP), developed at NRL. Such time savings permit application of NMR to the chemical analysis of materials that would otherwise require impractically long experiment times. Polymer characterization by NMR spectroscopy provides analytical methods and quality control techniques urgently needed for Navy polymeric

materials such as acoustic tiles and coatings. Our goal is to improve the quality control and reliability of materials used in Navy operations.

We have applied AJCP to a nitrogen-15 study of nylons (polyamides) in solution to enhance our understanding of how polymers interact with solvents.

The J cross-polarization (JCP) technique applies to liquid-state molecules that have two types of nuclei; the weakly magnetic species (A) of interest, and another highly magnetic species (X), such as hydrogen, fluorine, or phosphorus. When the A and X nuclei are in the same host molecule, they may interact magnetically via the spin coupling (J coupling) which appears as a splitting of the resonance line into discrete components. In 1962, S.R. Hartmann and E.L. Hahn [1] demonstrated that this J interaction can cause an interchange of magnetic polarization when both species are irradiated simultaneously at their respective resonant frequencies. In this way, the signal of the weaker A species can be enhanced by transferring to it the easily detected polarization of the X species.

Under carefully controlled experimental conditions, a complete exchange occurs and the A signal strength can be increased by the ratio of the X to A magnetic strength. The averaging time required to achieve an acceptable signal-to-noise (S/N) ratio is reduced by the square of the ratio. For the hydrogen/nitrogen-15 systems of the polyamides the ratio is about 10, and time savings of ~ 100 or more have been achieved with the JCP technique for nitrogen-15 spectroscopy.

Despite this obvious potential, the basic JCP method was considered too difficult for routine application because the signal enhancement is substantially reduced unless the frequency, duration, and power levels of the radio-frequency (RF) pulses are properly adjusted. On closer examination of these difficulties late in 1979, we found that controlled mismatch of the RF power levels could actually be used to improve performance of JCP. This discovery eventually led us to develop an adiabatic JCP technique, in which the matched RF condition is passed through by slowly increasing the power applied to the A species while simultaneously decreasing the power applied to the X species. This method still provides full polarization transfers, yet is insensitive to the problems mentioned above.

During the spring of 1980, we applied the AJCP technique to a nitrogen-15 (^{15}N) NMR

spectroscopic study of various types of nylon systems to correlate the ^{15}N resonant-frequency shifts with nylon chain length. Acceptable signal strength was achieved after about 1 h of signal averaging. This time period compares favorably with that required by conventional methods, despite the fact that space limitations forced us to use samples only one-tenth of the conventional size. A larger coil capable of accommodating a bigger sample could shorten the time needed for the same experiments to about 40 s.

In the nylon study, we were able to differentiate between the nitrogen-15 nuclei in nylon 6 and in nylon 6,12 because of their characteristic resonance-frequency shifts (^{15}N shifts) (see Figure 3). In the temperature study of a copolyamide consisting of 15% nylon 6 and 85% nylon 6,12, the individual components were still distinguishable. The large resonance-frequency shift of the nylon 6,12 component at higher temperatures (50 to 57°C) indicates a decrease in the extent of hydrogen bonding that is probably caused by a change in the conformation (rearrangement) of the polymer. Understanding such changes in polymeric materials under various conditions will enable the Navy to develop better and more efficient materials.

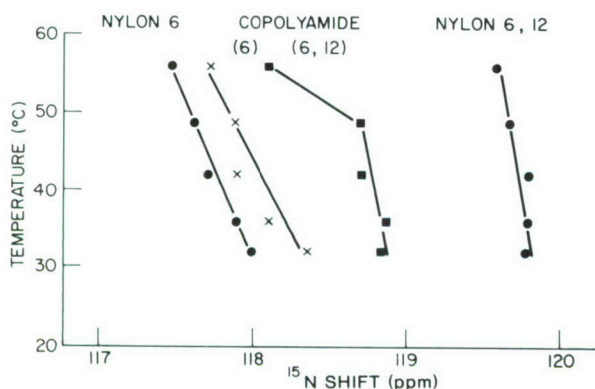


Figure 3. Temperature study of nylon 6 and nylon 6,12 in trifluoroacetic acid (CF_3COOH) solution. The copolyamide is a mixture of 15% nylon 6 and 85% nylon 6,12. The plot shows the change in the resonance frequency shift of the ^{15}N nuclei in the nylon chains with respect to temperature and length of the nylon chain.

Major industrial and academic laboratories generally have bypassed such studies involving ^{15}N NMR of polymers because the standard methods have been so time consuming. This situation is by no means limited to ^{15}N NMR studies. There are many other nuclei for which NMR spectroscopy could provide useful analytical

Table 1. Time Savings Achieved with J Cross-polarization

Nucleus (A)*	Time Savings Factor (X^2/A^2)
Carbon-13	1/16
Silicon-29	1/25
Mercury-100	1/32
Nitrogen-15	1/97
Tungsten-183	1/578
Silver-107	1/611
Rhodium-103	1/1009

*Coupled to hydrogen (X).

information, e.g., for fossil fuel studies and for improved semiconductor materials. These nuclei are neglected because of the impractically long data acquisition times. Table 1 lists these nuclei and shows the reduction in experimental time resulting from using JCP when the nucleus (A) is coupled to hydrogen (X), as compared to experimental time for normal NMR techniques. The time savings factor equals the square of the ratio of the X to A magnetic strengths. We are now expanding our spectroscopic capabilities to include additional weakly magnetic nuclei systems to which we will apply JCP.

[Sponsored by ONR]

Reference

1. S.R. Hartmann and E.L. Hahn, *Phys. Rev.* **128**, 2042 (1962).

Partially Stabilized Zirconia Crystals, by R.P. Ingel and R.W. Rice, *Material Science and Technology Division*

Zirconium dioxide (ZrO_2), or zirconia, is an important ceramic because of its toughness, moderate density, and electrical and thermal properties. However, zirconia changes at 1100°C from the higher-temperature cubic or tetragonal phase to a more stable monoclinic form at lower temperatures. This tetragonal-monoclinic transformation results in expanded volume, commonly causing severe cracking and a loss of mechanical integrity. Past studies have shown that other oxides (such as MgO , CaO , Y_2O_3), if added in sufficient quantities, would form a solid solution with ZrO_2 , resulting in a high-temperature cubic phase that is stable, that is, does not transform upon cooling to the tetragonal or the monoclinic phase. This material is called fully stabilized zirconia (FSZ).

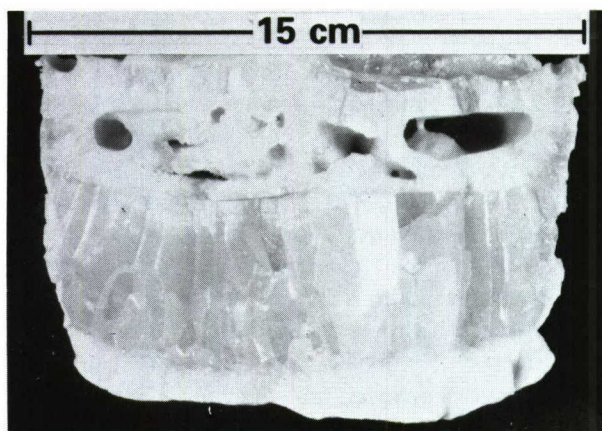
Recently at NRL, various studies investigated the production of a two-phase partially stabilized zirconia (PSZ) material formed with yet smaller percentages of oxide additions. In this procedure, the matrix, consisting of a solid solution of zirconia and yttria, is in the stable cubic phase, and the second-phase precipitates occur as either the metastable tetragonal or the monoclinic phase.

Investigations of PSZ alone or in combination with other materials such as alumina (Al_2O_3) and mullite ($3\text{Al}_2\text{O}_3 \cdot 2\text{SiO}_2$) have shown significant improvements in mechanical properties, particularly fracture toughness, as compared to fully stabilized ZrO_2 . Although a substantial amount of work has been done on PSZ, all of it has been concerned with conventionally processed polycrystalline bodies. Results from these studies have been limited because of significant problems with processing defects and the grain boundaries inherent in polycrystalline bodies.

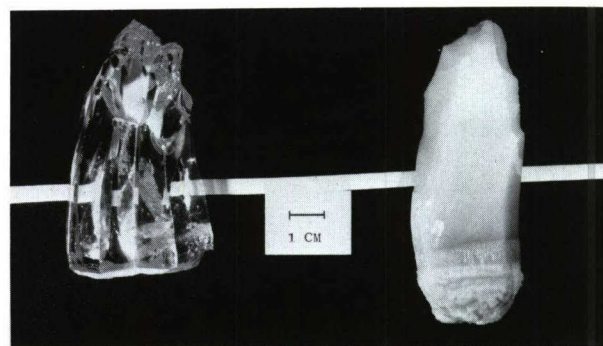
Fully stabilized cubic ZrO_2 has been grown in single crystal form on a commercial scale because its high refractive index and hardness make cubic zirconia an excellent simulation of diamonds in jewelry. The crystals are grown by the skull melting technique, that is, from a melt contained in a sintered "skull" of the same composition as the liquid (Figure 4a). Use of this technique allows the growth of single crystals of refractory oxides that have melting temperatures above 2000°C without unwanted chemical reactions and the danger of contamination. Through a combination of recent technical and theoretical advances in crystal growth and ceramic alloying, we have obtained large single crystals of PSZ (see Figure 4b) produced by an industrial supplier who used the skull melting technique.

Although the material was not yet optimized, our preliminary testing of mechanical properties showed excellent results. At room temperature, we measured a peak flexure strength (see Figure 5a) of about 1400 Mpa (2×10^5 psi). This is four times the 350 Mpa measured for the FSZ (high yttria) crystals, and two to three times greater than values for conventional polycrystalline PSZ material. Further, this result was unaffected by heat treatment at 1500°C . Similarly, the fracture toughness data in Figure 5b show a significant increase with decreasing yttria content (i.e., from FSZ to PSZ crystals).

The results of flexure strength tests at elevated temperatures (Figure 6) show that PSZ has great potential in high-temperature applica-



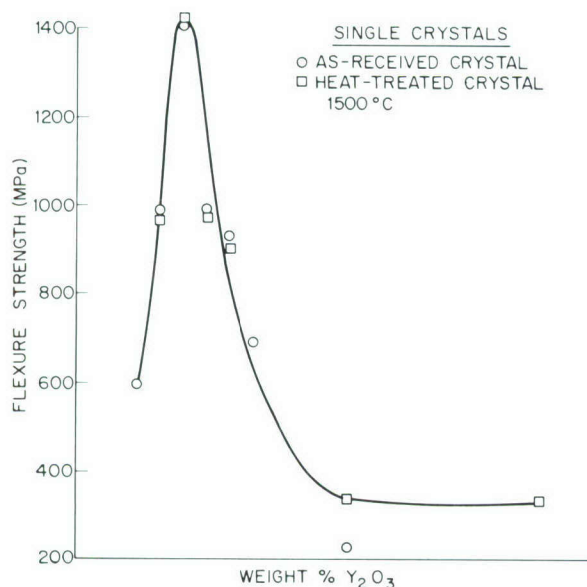
(a)



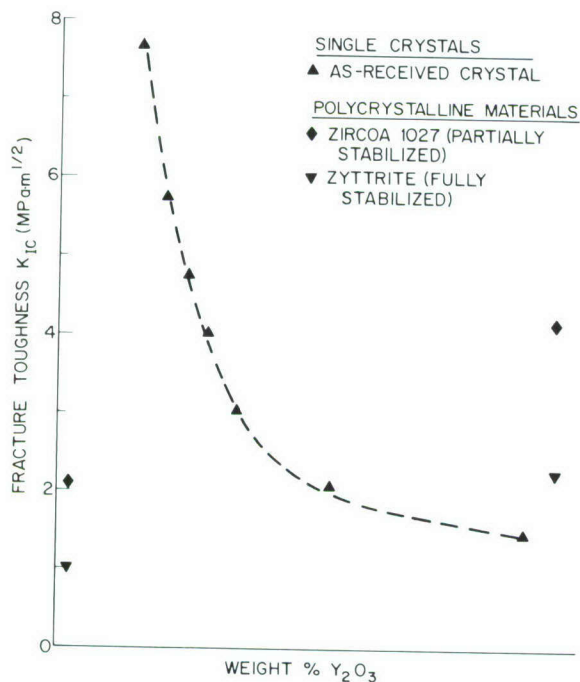
(b)

Figure 4. (a) Cross section of as-received skull (ZrO_2 with low Y_2O_3 content), (b) Individual as-received single crystals. Note the transparency of fully stabilized crystals (left) with a high Y_2O_3 content. The partially stabilized crystals (right) have a low Y_2O_3 content.

tions, for example, 690 Mpa (10^5 psi) strengths at 1500°C for some PSZ single crystal compositions. These elevated temperature strengths were obtained without elaborate surface preparation such as chemical polishing and are significantly greater than those of other ceramics such as Si_3Ni_4 , which has a strength of 480 Mpa (68 500 psi) at 1100°C but loses its strength almost completely at 1500°C . Furthermore, plastic deformation of FSZ and PSZ crystals observed at high temperatures has confirmed that both materials can be press forged at temperatures above 1500°C . The experiments show the efficacy of forging these PSZ crystals into complex shapes with good retention of flexure strength and fracture toughness, thus minimizing the costly and prolonged machining required for other materials.



(a)



(b)

Figure 5. (a) Flexure strength vs percent (by weight) of yttria, (b) Fracture toughness vs percent by weight of yttria as compared with polycrystalline materials.

The high strength, hardness, toughness, thermal shock resistance (greater than sapphire), and especially the favorable IR transmission qualities, suggest the use of PSZ single crystals as IR windows and domes. Furthermore, the National Bureau of Standards tested PSZ single crystals provided by NRL; the results indicated that the

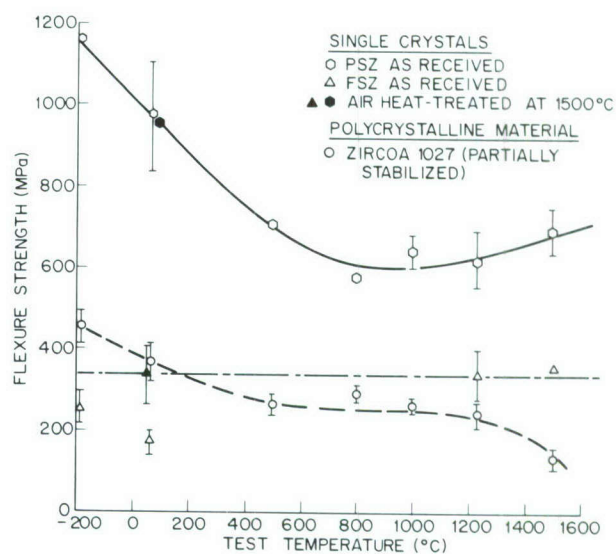


Figure 6. Flexure strength vs test temperature of single crystals and polycrystalline material. The PSZ crystals (solid curve) have a significantly higher strength at all temperatures as compared to fully stabilized single crystals (horizontal line) or PSZ polycrystalline materials (dashed line). Note that the flexure strength of the FSZ crystal (at 1500°C) has increased because of plastic deformation.

electrical conductivity of the single crystals is significantly higher than that of polycrystalline zirconia. These crystals, therefore, have potentially important applications in oxygen sensors and fuel cells for which ZrO_2 is being used.

These investigations of PSZ single crystal properties indicate important opportunities for high technology application as well as for the development of a basic understanding of toughening mechanisms in ceramics. The production costs for crystals of various sizes that are needed for different applications are reasonable. Thus, partially stabilized zirconia single crystals may well become an important ceramic material.

[Sponsored by NAVAIRSYSCOM and ONR]

The As Antisite Defect in GaAs, by R.J. Wagner, J.J. Krebs, and G.H. Stauss, *Electronics Technology Division*

Recent efforts to develop small, high-speed electronic devices have been focused on the III-V compound semiconductor family. The success of such a program depends on the availability of well-characterized, semi-insulating substrate material. To this end, the electrical, optical, and microwave electron paramagnetic resonance (EPR) properties of a number of the

more promising III—V semiconductors are being studied intensively at NRL. These studies have clarified the doping properties (charge states and energy levels) of a number of transition metals in GaAs crystals. Until recently, the existence of native defects (growth displacements of Ga and As atoms) in GaAs has escaped experimental observation. However, we have used another type of analytical tool, submillimeter laser EPR, to observe a center that has the anticipated properties of an As antisite defect, i.e., an As atom on a Ga site. This is the first observation of a native defect in GaAs.

In terms of the underlying physics, conventional microwave EPR and submillimeter laser EPR are identical. A necessary requirement for any type of EPR is the existence of electrons with unpaired spins. When a magnetic field is applied to a sample, it interacts with the electronic spins to produce a difference in energy between spins aligned with the field and those opposed to it (the Zeeman effect). In addition, the unpaired electron will interact with the spin of the nucleus around which it is localized (the hyperfine interaction). When microwave or submillimeter radiation is applied to the defect center and the magnetic field is varied, a resonant absorption occurs when the photon energy (the product of the radiation frequency, ν , and Planck's constant, h) equals the difference, induced by the Zeeman and hyperfine effects, between the energies of the two electron spin states:

$$h\nu = g\mu_B H + AI_Z,$$

where g is the electron g -value, μ_B is the Bohr magneton, H is the applied magnetic field, A is the hyperfine interaction parameter, and I_Z is the component of the nuclear spin aligned along the magnetic field.

Whereas the differences between microwave and submillimeter EPR are due only to the relative magnitudes of frequency and magnetic field, there are substantial differences in experimental apparatus. The submillimeter source is a pulsed, optically pumped laser rather than a microwave klystron. In the present case, the high magnetic field is obtained with a Bitter-type solenoid (0 to 14 Tesla) of the NRL High Magnetic Field Facility, rather than a conventional electromagnet (0 to 1.5 T). Because of limitations inherent in submillimeter spectroscopy, the radiation makes a single pass through a rather thick (1 cm) sample.

The initial motivation for developing the submillimeter EPR technique was to provide a

new approach to the determination of the electron ground state energy levels of the charge state ($2+$) of the Cr ion in GaAs. The Cr^{2+} resonance was easy to observe, and therefore it was possible to test various schemes for signal-to-noise enhancement. With an optimized field-modulation technique, a field derivative of the absorption was obtained. Figure 7 shows resonances caused by the Cr^{2+} center and, in addition, a new four-line spectrum. A number of deductions concerning this new spectrum can be made. First, the similarity of the 11.236 cm^{-1} curves shows that it is independent of the orientation of the field with respect to the crystallographic axes. Hence, the unpaired electron is localized on a center with cubic symmetry. Second, the field splitting (i.e., separation) of the four lines is the same for both laser frequencies. This implies that the splitting is due to a (field-independent) hyperfine interaction between the electron and a nucleus with nuclear spin, $I = 3/2$.

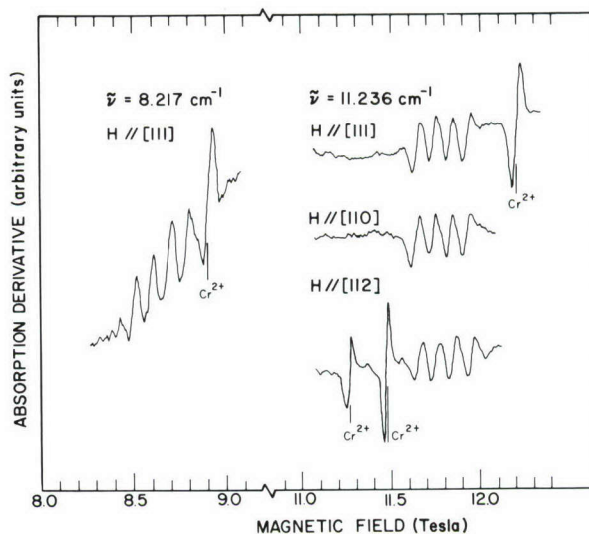


Figure 7. High-field isotropic resonant absorptions observed in semi-insulating GaAs:Cr at three orientations and two wavelengths (1.217 and 0.890 mm). H is the applied magnetic field. The absorption derivative is obtained by applying a small (0.01 T) audiofrequency magnetic field to the sample and observing the effect on the radiation transmitted by the sample. Cr^{2+} resonances were used to enhance the signal-to-noise ratio and to calibrate the magnetic field.

Accurate analysis based mainly on the large magnitude of the hyperfine parameter A and theoretical estimates of its value for various $I = 3/2$ nuclei showed that only ^{75}As is a viable source of the observed spectrum. Based on the

cubic symmetry deduced above and the fact that As in a normal location would not have an unpaired spin, it is concluded that the center is at a Ga site.

There is additional supporting evidence for this conclusion. Earlier, the P antisite in GaP was observed via microwave EPR [1]. As in the present case, a quantitative measure of both g and A was made. By using theoretical considerations regarding the dependence of these parameters on such factors as s-wave function overlap at the respective nuclei (P or As) and the spin-orbit interaction parameters on the nearest neighbors, the characteristics of the As antisite can be estimated from those of the P antisite in GaP. This estimate agrees well with the experimentally determined results.

The As antisite has been observed in some but not all samples studied. In the sample used for the experiment shown in Figure 1, the concentration is found to be as high as $8 \times 10^{15} \text{ cm}^{-3}$. When As at the antisite location has satisfied the bonding requirements, it has two extra electrons. Thus antisite As can act as an n-type dopant and may become a significant factor in the design of semi-insulating GaAs.

[Sponsored by ONR]

References

1. U. Kaufmann, J. Schneider, and A. Räuber, *Appl. Phys. Lett.* **29**, 312 (1976).
2. R.J. Wagner, J.J. Krebs, G.H. Stauss, and A.M. White, *Solid State Commun.* **36**, 15 (1980).

Toward a Red Blood Cell Surrogate, by B.P. Gaber and J.P. Sheridan, *Optical Sciences Division*

In support of the Navy's blood research program, we are attempting to develop a stable, universal red blood cell (RBC) substitute for short-term resuscitation of casualties. Our RBC surrogate relies on the entrapment of the natural oxygen transport protein, hemoglobin, in large (ca. 200 nm) phospholipid vesicles. Our objective is a nontoxic product that is suitable for field administration, restores both effective tissue oxygenation and plasma volume, withstands prolonged storage with little or no refrigeration, and requires minimal reconstitution.

Phospholipids are polar molecules consisting of a hydrophilic head group and two hydrophobic hydrocarbon chains (Figure 8). When hydrated, phospholipids spontaneously organize into the

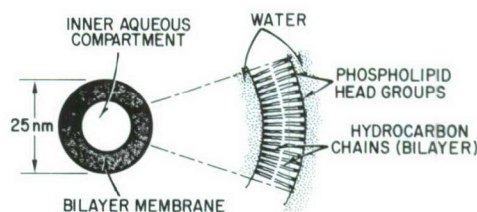


Figure 8. A single phospholipid vesicle. Uniform in size, these vesicles provide excellent models for studies of membrane structure and functions.

tail-to-tail bilayer structure characteristic of all biological membranes. Although permeable to water and oxygen, the phospholipid bilayer forms an impenetrable barrier to the passage of salts, sugars, proteins—virtually all of the material that must be retained within (or kept outside) a cell. Under proper laboratory conditions, bilayers may be induced to close upon themselves in such a way that discrete spherical vesicles are formed. Remarkably homogeneous in size, phospholipid vesicles have proven to be excellent models for studies of membrane structure and function.

Recently, the biomedical community has become interested in the potential of vesicles as carriers for delivery of entrapped therapeutic agents to specific tissues. Cancer chemotherapy, for example, is an area that could benefit enormously from the development of a "targetable" drug delivery system.

We reasoned that if drugs can be encapsulated in vesicles, perhaps hemoglobin can also. The result would be an artificial red cell. Indeed, other laboratories had reported limited success with entrapment of proteins, but none had systematically approached the idea of hemoglobin encapsulation.

One major barrier to the practical encapsulation of proteins has been the small size of the vesicle formed by the usual techniques; vesicles of 25 nm diameter do not possess sufficient volume to trap significant amounts of protein. Newly developed procedures produce vesicles on the order of 100 nm, and modifications developed in our laboratory have extended the diameter to 220 nm. This corresponds to an internal volume of 7.5 liters per mole of phospholipid. It is interesting to note that the diameter of a single vesicle comprised of one mole of lipid would be about 100 m—longer than a football field!

The preparation of large vesicles relies upon the controlled separation of a 2:1 molar mixture of phospholipid and a biological detergent. As

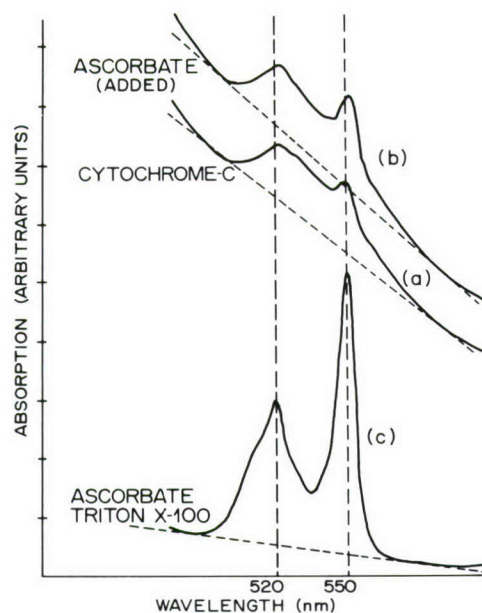


Figure 9. Visible absorption spectrum of vesicle-encapsulated cytochrome-c (curve (a)). The addition of ascorbate to vesicle suspension shows no change in absorption (curve (b)), indicating that all the protein is trapped within the vesicles. Addition of Triton X-100, however, ruptures vesicles, thereby exposing cytochrome-c to ascorbate, resulting in reduction of the protein and a substantial increase in absorption as indicated by the increased height of the peaks above the reference baseline (curve (c)).

the detergent is removed, vesicles form, entrapping a portion of any protein that is present in the solution. Separation of vesicles from detergent is accomplished by gel filtration, a chromatographic procedure that separates the components according to their molecular weights. A second gel filtration step separates the protein-containing vesicles from the protein remaining in solution. The size of the vesicles is determined by an advanced optical measurement called photon correlation spectroscopy.

Free of the red blood cell, the hemoglobin tetramer is readily susceptible to dissociation into dimers and monomers, which subsequently cease

to function properly (in fact one goal of encapsulation is to assure the protein's stability). Thus, we chose a hardier protein, cytochrome-c, for our initial attempts to characterize and optimize the encapsulation procedure. Like hemoglobin, cytochrome-c has an iron-containing heme group, and the two proteins have similar spectroscopic properties. Chemical reduction of oxidized cytochrome-c results in a significant change in its optical absorption spectrum. Using this fact, we have developed a simple assay to demonstrate that cytochrome-c is *inside* the vesicle.

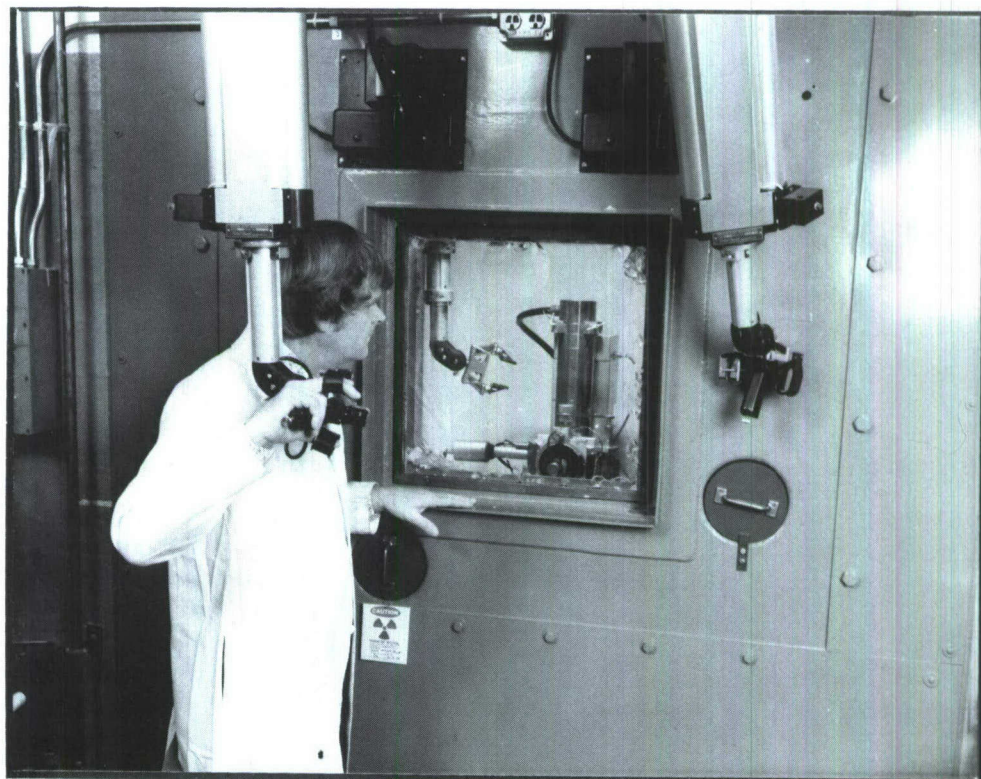
The absorption spectrum of vesicle-encapsulated cytochrome-c is shown by curve (a) of Figure 9. The sloping baseline results from light scattering due to the large vesicles. The bilayer is known to be completely impermeable to ascorbate (vitamin C), which is an excellent reducing agent for cytochrome-c. Thus, when the addition of ascorbate results in little or no spectral change (Figure 9, curve (b)), we conclude that nothing on the outside of the vesicles is reduced. However, when a strong detergent (Triton X-100) is added, the vesicles are completely disrupted and an intense band appears at 550 nm (Figure 9, curve (c)), indicating reduction of the cytochrome-c that had been entrapped. Repeated assays show that the vesicles remain stable and intact for several weeks.

Most significantly, using similar methods we have recently demonstrated the incorporation of hemoglobin into vesicles. What lies ahead is improvement and simplification of our encapsulation technique as well as detailed studies of the biophysical properties of encapsulated hemoglobin.

The development of an effective blood surrogate is no small task, requiring determined effort at both basic and applied levels. Toward this goal we have successfully solved a basic problem by developing a reliable and efficient entrapment procedure and by demonstrating the principle of hemoglobin encapsulation.

[Sponsored by ONR]

STRESS AND RADIATION EFFECTS



STRESS AND RADIATION EFFECTS

It is axiomatic that the Navy's ability to perform effectively depends heavily upon the capabilities of the systems with which its people must train, work, and fight. Many of these systems are constrained by intrinsic or design considerations of strength, weight, temperature, and radiation tolerance that limit their utility and service. During 1980, NRL continued its strong tradition of research contributions to improved understanding and performance in this area.

Creep-fatigue Crack Propagation in Stainless Steel	167
Prediction of High-temperature Fatigue Crack Growth	168
Low-cycle Fatigue Life of Titanium Alloys	170
Sulfur Trioxide Factor in Low-temperature Hot Corrosion	171
Damage Cascades in Semiconducting Material	174
Cosmic-Ray Effects on Microelectronics	175

Creep-fatigue Crack Propagation in Stainless Steel, by D.J. Michel, *Material Science and Technology Division*

The performance of structural materials has become increasingly important with the higher operating temperatures of advanced energy-conversion systems. Frequently, these systems encounter applications where combined cyclic and static loading conditions are expected in service at sustained elevated temperatures. For many materials, however, exposure to sustained elevated temperatures can produce metallurgical changes that degrade their mechanical properties. Systematic studies of the relationship between such metallurgical changes and the fatigue and

creep performance of the materials are being conducted by NRL scientists. Recently, these studies revealed that, when certain critical conditions are satisfied, the new phenomenon of accelerated crack propagation can occur during combined creep-fatigue loading at elevated temperatures.

The experiments were conducted with specimens of austenitic stainless steel that were previously subjected to thermal aging at 593°C for 5000 h. The aging produced a stable alloy carbide precipitate on the grain boundaries of the test specimens. During tests at the aging temperature, notched specimens of the steel were subjected to fatigue cycles in which the maximum tensile load was held constant for preselected

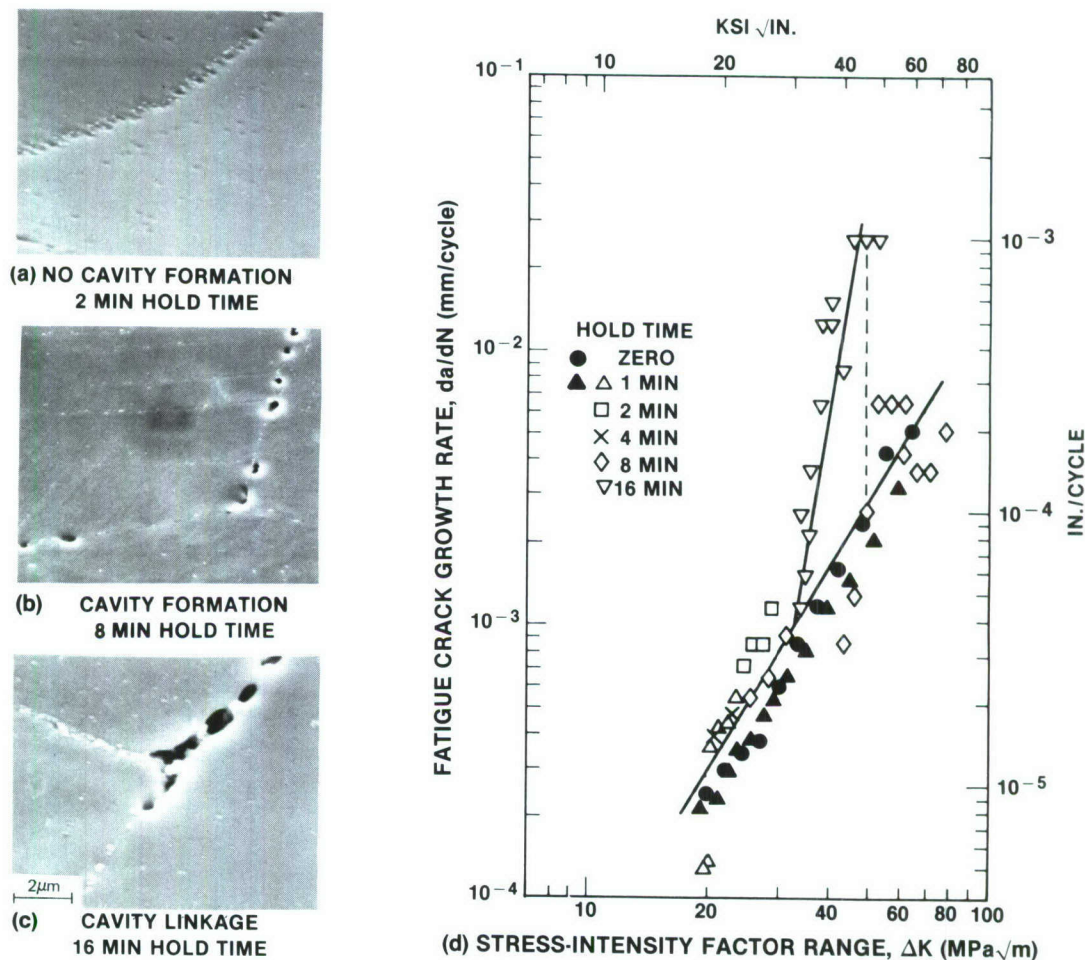


Figure 1. Accelerated crack propagation and microstructure of annealed, thermally aged (593°C for 5000 h) Type 316 stainless steel. Figures 1a, 1b, and 1c present scanning electron micrographs of grain boundary precipitates and associated cavities for three different hold times. Figure 1d shows the fatigue-crack growth rate in air as a function of the stress-intensity factor range. Solid symbols represent results from tests conducted with a constant hold time. The open symbols represent results from tests in which hold times were sequentially increased to 16 min (1, 2, 16 or 4, 8, 16) and then reduced to 8 min. The dashed line indicates the decrease in the crack propagation rate to previously observed values that accompanied the hold time reduction from 16 to 8 min.

time periods (hold times). The test results for Type 316 stainless steel for various hold times are shown in Figure 1.

The macroscopic test results, Figure 1d, indicate that the longest hold time (16 min) accelerated the rate of crack propagation, whereas shorter hold times did not. Indeed, reduction of the hold time to 8 min produced an immediate decrease in crack propagation rate to the rate previously observed (see dashed line, Figure 1d). Microscopic investigation of the grain boundary regions of the specimen revealed that the onset of the accelerated crack propagation rate (with the 16-min hold time) coincided with the linkage of intergranular cavities (or holes) associated with the grain boundary precipitates (Figure 1c). With shorter hold times (Figures 1a and 1b), the microscopic evidence shows that cavities did form, but with no linkage. Using quantitative evidence obtained from the microstructural studies, we were able to demonstrate that the critical condition for the occurrence of the accelerated crack propagation was the presence of grain boundary precipitates of the proper size and spacing for cavity growth and linkage.

We are conducting further experiments to define the limits of the conditions under which the phenomenon of accelerated fatigue-crack propagation occurs at elevated temperatures. The objective is to provide a basis for determination of those service conditions for elevated-temperature energy-conversion materials where accelerated crack propagation would be expected. Equally important, the results should increase the understanding of the basic mechanism responsible for accelerated crack propagation phenomenon.

[Sponsored by ONR]

Prediction of High-temperature Fatigue Crack Growth, by K. Sadananda and P. Shahinian, *Material Science and Technology Division*

To ensure more reliable performance and increased efficiency of naval energy systems such as gas turbines requires an accurate prediction of the life cycle of high-temperature components. Fatigue is one of the most common processes by which structural components fail, and it is accentuated by high temperatures and aggressive environments. Since fatigue failure of such components occurs by propagation or growth of a single crack that initiates from pre-existing cracklike flaws or weld defects, we have been exploring the utility of fracture mechanics techniques to quan-

tify and predict the growth behavior in service. For this, validity of the techniques at high temperature needs to be established with different loads, specimen geometries, and temperatures. When these techniques are used, the number of fatigue cycles required for a small crack to reach the critical size for catastrophic failure can be calculated from crack growth data.

The applicability of fracture mechanics techniques at high temperatures is complicated by the fact that nonlinear plasticity effects become increasingly important with increasing temperature, due to a lowering of flow stress and the incipience of time-dependent creep and environmental effects. The validity of linear elastic fracture mechanics techniques that are successful at low temperatures, therefore, becomes questionable for high temperatures. Recent developments in the use of elastic-plastic fracture mechanics techniques have stimulated the present research effort. In particular, we are evaluating the J -integral technique as a valid measure of the energy required for fatigue crack growth at high temperatures.

Most fatigue-crack-growth data are generated in laboratories where the load amplitudes can be controlled for each cycle. However, no successful technique has been available to determine J . NRL has developed such a procedure and has shown the J -integral to be analogous to the linear elastic stress-intensity parameter K , within the limits of small plastic strains. Figure 2 shows the method of determining the correct J value for fatigue using load-displacement curves for crack length increments from a to $a + da$. In particular, the rising parts of the loops in Figure 2a are displaced to a common origin, and the J -value is then given by the shaded area between the two curves in Figure 2b. The approach has been validated by demonstrating the equivalency of J values with K for a gas turbine material under conditions where crack growth is essentially elastic.

The validated ΔJ -integral approach can be more useful because it includes the plasticity factor at higher temperatures, whereas the ΔK parameter is limited to linear elastic conditions. Even at room temperature, the ΔJ -integral approach has advantages over ΔK for predicting the fatigue life of thin sections on components subjected to high loads where plasticity effects become significant.

The J -integral approach provides a powerful technique for correlating high-temperature

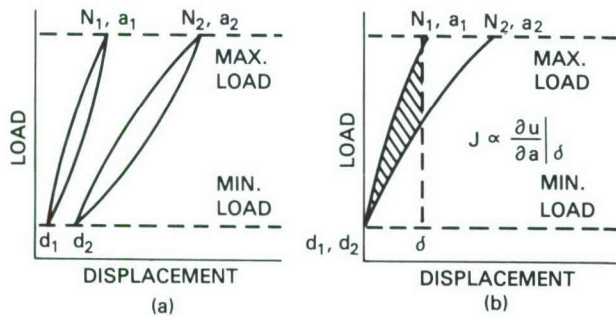


Figure 2. Procedure for the determination of J for load-controlled fatigue: (a) Load-vs-displacement loops for a cracked specimen at cycles N_1 and N_2 corresponding to crack lengths a_1 and a_2 ; (b) Rising parts of the loops are displaced to a common reference. J is proportional to the shaded area.

fatigue-crack-growth rate data with J , particularly for materials that undergo slow changes in their stress-vs-strain response during service. This correlation can be seen clearly in Figure 3. Cold-worked stainless steel undergoes slow recovery and loses some of its strength at the test temperature. Therefore, crack growth rates at

low loads (long time tests) differ considerably from those at high loads (short time tests) when represented in terms of the stress-intensity factor range ΔK . On the other hand, the J -integral correlates the data for all loads, because changes in the material are reflected in the load displacement curves that provide the basis for the values of the J -integral.

Because such metallurgical changes during service are normal, particularly at high temperatures, the use of J -integral techniques for correlating crack-growth rate data are necessary. Furthermore, the use of J -integral techniques makes it possible to predict crack growth behavior at high temperatures, even for long-time service applications, from the short-time test data generated in the laboratory. Efforts are under way to explore further the utility of the J -integral technique in conditions where crack growth occurs simultaneously by cycle-dependent and time-dependent creep processes that are sometimes encountered during high-temperature applications.

[Sponsored by ONR]

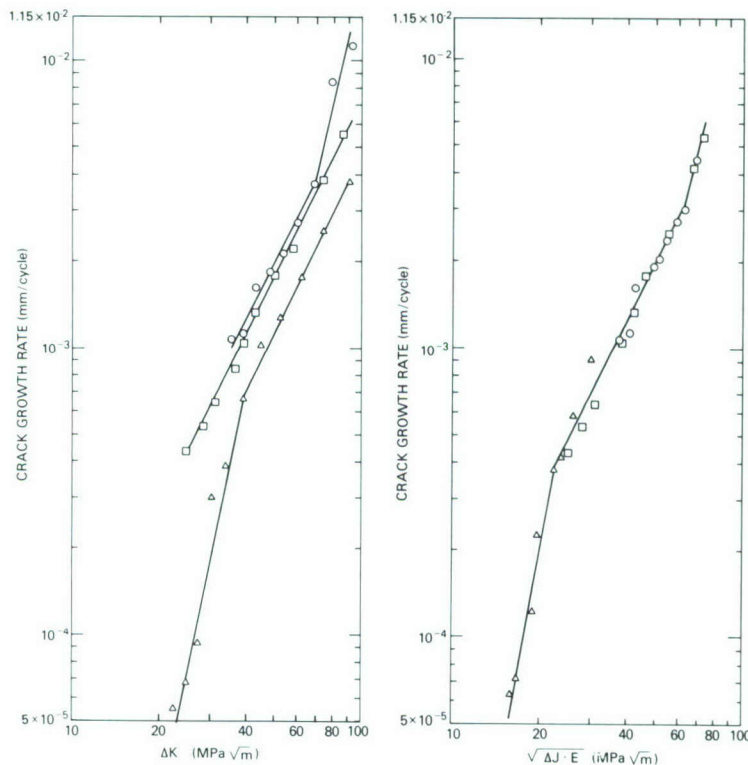


Figure 3. Advantages of ΔJ over ΔK for correlating high-temperature fatigue-crack-growth data for type 316 cold-worked stainless steel at 593°C and with different loads. The single ΔJ curve at the right unifies crack growth data taken as a function of load and is analogous to the three ΔK curves at the left. (The J -integral approach also accommodates various geometries.)

Low-cycle Fatigue Life of Titanium Alloys, by J.M. Krafft, *Marine Technology Division*

Low-cycle fatigue (LCF) is a material failure mode in which cracking results from repeated applications of large stresses. The high-performance flight tactics of naval fighter aircraft subject the rotating parts of the jet engines to such stresses. Jet-engine rotors and blades are often constructed of titanium alloys because of the high stiffness and low weight of these materials. Resistance of titanium alloys to LCF is a concern in both advanced engine design and testing of operational engines for safe service life.

Previous NRL work has shown that the resistance of titanium alloys to the propagation of cracks is extremely sensitive to grain size. It was found that increased grain size retarded the propagation of cracks significantly, with little adverse effect on static strength. Another important factor is the amount of interstitial oxygen, which acts as a hardening agent, that the alloy contains. However, little is known about how these factors affect initiation of fatigue cracks.

Tests for LCF resistance in the life range less than 10 000 cycles are usually conducted by imposing a fixed strain (deformation) excursion rather than a fixed stress (load) excursion. Records of stress vs strain made during such tests form closed, convex, hysteresis-like loops as the material is alternately cycled through excursions first in tension, then in compression. Figure 4

shows two loops, one taken early in the test and one later on, for each of three alloys. When tension is applied from rest, the specimen first exhibits a linear, elastic response, and then a non-linear, plastic response out to maximum excursion. As the tension is unloaded, the material contracts linearly and therefore has a residual plastic strain remaining at zero load. When compression is then applied, the material again responds first elastically, then plastically. As the cycle is completed by unloading the compression, the material responds elastically in returning to zero net load. This sequence continues until a crack is initiated, shortly after which the loops collapse markedly, signaling failure of the specimen.

An established way of evaluating LCF resistance is to plot the plastic strain excursion vs the fatigue life (number of cycles to crack initiation). Plastic strain excursion is measured by the horizontal distance between the elastic loading and unloading lines in Figure 4. The data points shown in Figure 5 are for seven alloys selected from those tested to date. Each data point represents the results of one specimen subjected to the plastic strain excursion indicated on the ordinate for the number of cycles to fatigue crack initiation shown on the abscissa. The connected line segments also shown in this figure will be discussed later in the article. For a given plastic strain excursion, LCF resistance is measured by

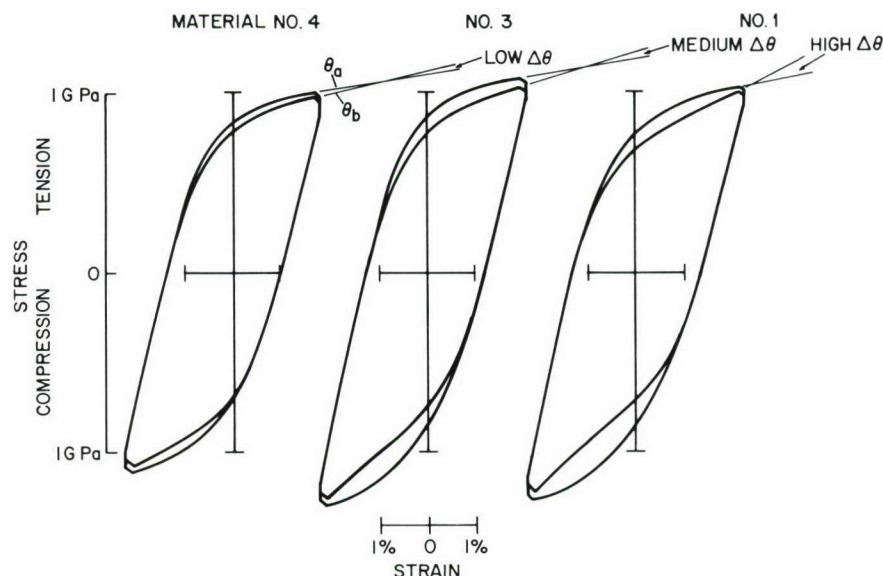


Figure 4. The three pairs of cyclic stress-strain loops typify the range of strain-hardening evolution as measured by the change in terminal slope $\Delta\theta$. The numbers index the materials relative to their order in Figure 5.

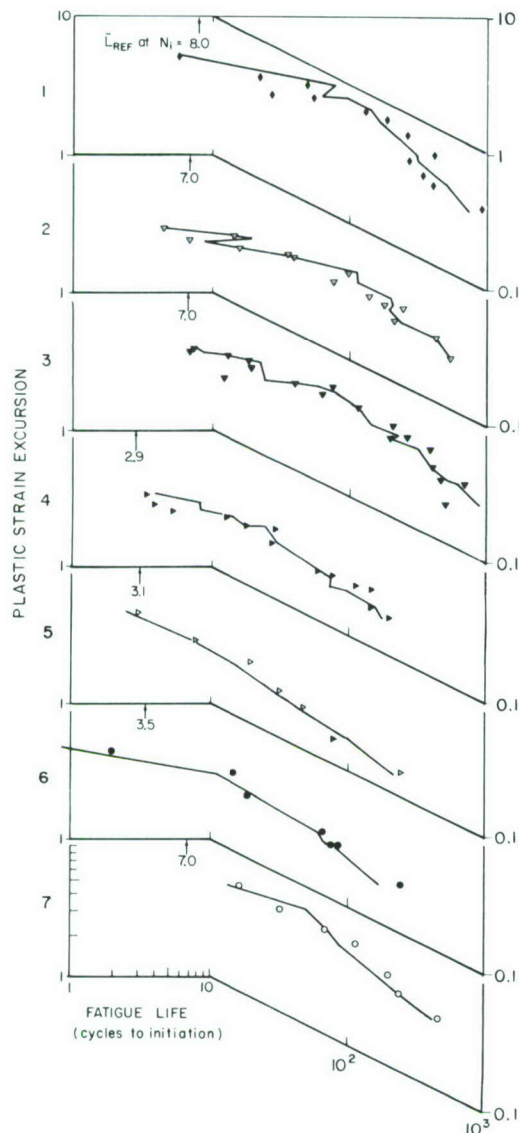


Figure 5. Low-cycle fatigue data for seven different titanium alloys. Each frame contains a set of LCF data, cycles to initiation with respect to the applied strain range. The segmented lines connect points of a calculated LCF life factor \bar{L} , obtained from the evolving shape of the cyclic stress-strain curve in each fatigue test.

the number of cycles that the material can endure before crack initiation. Thus, materials 1 and 7 have the best LCF resistance of this set, whereas materials 4, 5, and 6 are the poorest.

The search for an explanation of the variability observed in Figure 5 revealed a curious evolution in the shape of the cyclic stress-strain loops. The three materials in Figure 4 correspond, from left to right, to low, medium, and high LCF resistance samples from Figure 5. In each case, the

loop made later in the test falls inside the earlier loop. As illustrated by the loop pairs shown here, it was found that, after a few cycles, the strength of the material (as measured by the stress it supports) always fell off early in the plastic part of the loading phase but was restored to near coincidence toward the end of the loading. The terminal slope of the curve is indicated on the figure by θ , and the difference $\Delta\theta$ between the two cycles is seen to increase with increasing LCF resistance. This correlation of $\Delta\theta$ with LCF resistance was generally observed for most cycles on all specimens used throughout the tests.

The slope θ is a measure of the strain-hardening rate of the material. The larger strain-hardening rate observed in the better materials is thought to be beneficial, in that high strain hardening tends to stabilize plastic deformation and reduce creep strain. It was reasoned that if creep strain were the damage mechanism, then it should be inversely correlated with fatigue endurance; that is, the less the creep strain the greater the endurance. Accordingly, the average creep strain per cycle, calculated from the stress-strain loops obtained for each cycle during the test, was determined for each specimen. The reciprocal of the average creep strain per cycle was then plotted and the points were connected by straight line segments. These lines are designated \bar{L} , for fatigue life factor. The \bar{L} curves were matched to the raw fatigue data in Figure 5 by sliding the curves laterally to the position of best fit. The amount of the displacement is indicated by the reference value L_{REF} , and it is a virtue of the model that only one such fitting parameter is required.

The agreement seen in Figure 5 between the derived inverse creep strain per cycle data and the raw fatigue life endurance data is encouraging. Work is continuing to validate and extend this damage model. If successful, it will provide a means of predicting LCF endurance through the full cyclic life range of a material with minimal laboratory or field testing. This would greatly improve our ability to predict the safe service life of Navy jet fighter engines.

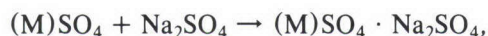
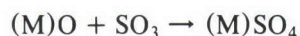
[Sponsored by NAVAIRSYSCOM]

Sulfur Trioxide Factor in Low-temperature Hot Corrosion, by R.L. Jones and S.T. Gadomski, Chemistry Division

The operational success of the Navy's new DD 963-class destroyers and FFG 7-class frigates

depends on the protection of their gas turbine engines against hot corrosion. Hot corrosion is caused by reaction of ingested sea salt and sulfur from the fuel with the hot blade surfaces. To develop resistant blade metals and coatings requires an understanding of the chemical reactions involved in hot corrosion.

Research at NRL has shown that sulfur trioxide (SO_3) in the engine gas produces molten, mixed-sulfate deposits on gas turbine blades at 600 to 750°C, which cause low-temperature hot corrosion (LTHC) [1]. The critical reactions are



where (M) represents either cobalt (Co) or nickel (Ni); (M)O is the metal oxide; and $(\text{M})\text{SO}_4 \cdot \text{Na}_2\text{SO}_4$ is a low-melting eutectic cobalt or nickel-sodium mixed sulfate. Similar iron oxide- SO_3 -sulfate deposit reactions are postulated as the cause of fireside boiler tube corrosion in steam-generating boilers.

Sulfur trioxide and sulfur dioxide exist in combustion gases and are related by the equilibrium equation



Below 700°C, sulfur trioxide is predicted by thermodynamics to be favored. The equilibrium SO_3/SO_2 ratio in air at 627°C, for example, is 3.08. However, measurements of boiler flue gases show low SO_3/SO_2 ratios (0.01–0.05), as do gas turbine exhausts (<0.10), despite postcombustion temperatures below 700°C that should promote SO_3 formation. To understand how SO_3 can yield corrosive mixed sulfates while it is present in such apparently low concentrations has been a long-standing problem in fireside corrosion [2] and now becomes crucial in understanding Navy marine gas-turbine corrosion.

The results of recent NRL studies of the reactions of Co_3O_4 - Na_2SO_4 deposits with mixtures of SO_2 and SO_3 (i.e., SO_x) in air provide an explanation for the low SO_3 concentrations. The experiments used a gas furnace fitted to allow controlled SO_2 input and SO_x analysis of the exhaust gas. The reactions took place at 625°C in the presence of 100 ppm SO_x , which ranged from essentially 100% to less than 25% SO_2 .

The rates of formation of CoSO_4 - Na_2SO_4 mixtures from Co_3O_4 and Na_2SO_4 were virtually identical for SO_x gaseous environments up to 24 h, as seen in Figure 6. However, the SO_3 -rich

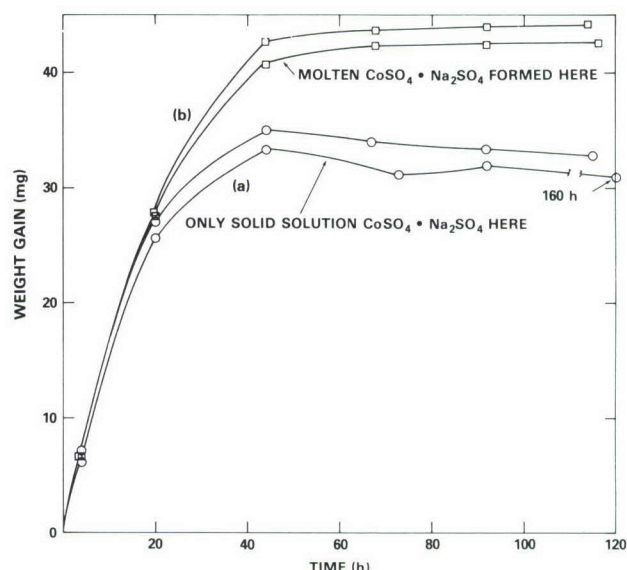


Figure 6. Rate of formation of CoSO_4 - Na_2SO_4 , the cause of LTHC. Weight gain vs time for two 250-mg specimens of 50 mol % Co_3O_4 - Na_2SO_4 exposed at 625°C (a) under 100 ppm SO_2 in air; (b) under ~75 ppm SO_3 , 25 ppm SO_2 in air.

environment yielded a higher ultimate conversion, producing a mixed sulfate of ~34 mol % as compared to ~27 mol % produced in a pure SO_2 environment. The higher yield was molten and the lower yield solid, in general agreement with the CoSO_4 - Na_2SO_4 phase diagram. The difference of state is vital in causing LTHC, as will be explained below. Analyses for SO_2 and SO_3 revealed that SO_3 was produced in the SO_2 trials, and subsequent experiments verified the strong catalytic activity of Co_3O_4 for the $\text{SO}_2 \rightarrow \text{SO}_3$ reaction. Tests using 300 and 1200 ppm SO_2 proved that molten CoSO_4 - Na_2SO_4 could be produced with SO_2 alone if the concentrations were high enough, with the Co_3O_4 catalysis evidently generating sufficient SO_3 (~75 ppm) at the Co_3O_4 - Na_2SO_4 surface to form the molten sulfate mixture.

This behavior shows clearly that SO_3 is critical in molten sulfate formation. The effective SO_3 pressure is the sum of the SO_3 in the gas stream and that produced catalytically at the oxide-sulfate surface. The latter reacts essentially in situ, with little escaping to increase the gas stream SO_3/SO_2 ratio, especially for high-gas-volume machines. It becomes understandable, therefore, that molten mixed sulfates can form in gas streams that show little or no SO_3 , given sufficient surface catalysis and SO_2 gas-stream concentration.

Further experiments demonstrated that LTHC takes place only when the mixed sulfate is molten, and that, even for the same SO_x concentration and temperature, the occurrence of LTHC depends on whether the local SO_3 concentration is such as to form either a molten or solid mixed sulfate. For these experiments, beads of $\text{Co}_3\text{O}_4\text{--Na}_2\text{SO}_4$ were placed on gas-turbine-blade specimens, which were then exposed under 100 ppm SO_2 , or 100 ppm SO_3 -rich gas mixture, as described above. The mixed sulfate produced under SO_2 remained solid throughout the 115-h run (although extensive solid solution of $\text{CoSO}_4\text{--Na}_2\text{SO}_4$ formed), and no corrosion occurred. Conversely, under the SO_3 -rich gas, sufficient CoSO_4 was formed after 24- to 48-h exposure (just as with the bulk $\text{Co}_3\text{O}_4\text{--Na}_2\text{SO}_4$ samples) to yield a molten $\text{CoSO}_4\text{--Na}_2\text{SO}_4$ mixed sulfate. Rapid LTHC then followed, with the reaction between the blade metal and molten sulfate causing decomposition of the sulfate and locally high SO_3 pressures (SO_3 bubbles form) at the sulfate-metal interface. This high SO_3 concentration produces pitting. X-ray analysis shows that the initial pit is heavily loaded across its breadth with a sulfur species, presumably SO_3 . Later, this sulfur species reacts or diffuses away, and sulfur is found only in a concentrated band (probably as a metal sulfide) at the pit perimeter,

the morphology usually seen on corroded turbine blades. This sulfide is the cause of further corrosion.

Corrosion pits on turbine blades in service at sea usually show this morphology, i.e., sulfur only at the pit front. However, smaller pits with sulfur across the pit breadth are found (Figure 7). This indicates, in accord with our laboratory findings, that LTHC pits are in fact initiated in service by decomposition of mixed sulfate deposits.

These results establish several points that previously were uncertain in low-temperature hot corrosion: (a) SO_3 is in fact the critical species; (b) catalytic oxidation of SO_2 to SO_3 on turbine surfaces is an important, perhaps crucial, factor; (c) very small increases in SO_3 level can greatly enhance LTHC by causing the sulfate to change from solid to liquid; and (d) LTHC is initiated by a process of formation and decomposition of mixed sulfates on the blade surface. These points have been very helpful in defining development test conditions and explaining seemingly contradictory corrosion behavior in Naval Sea Systems Command programs for LTHC-resistant alloy development and engine-corrosion monitoring.

[Sponsored by NAVSEASYS COM]

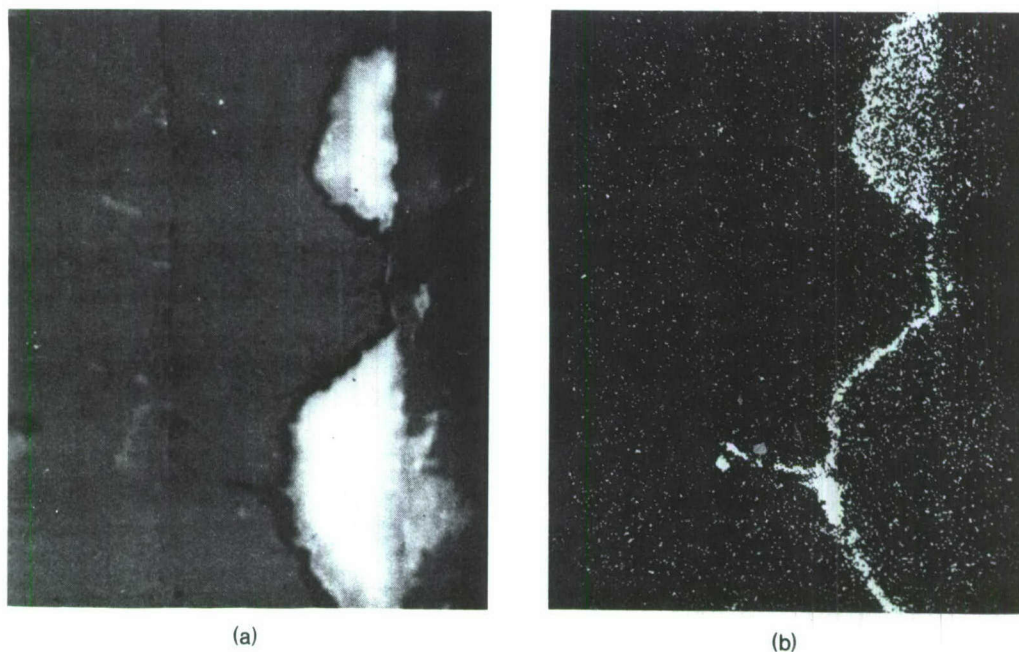


Figure 7. Electron microprobe cross-sections of pits on a gas-turbine blade: (a) Current scan and (b) X-ray scan for sulfur. Note the difference in sulfur distribution in Figure 7b between large and small pits, as indicated by the density of white spots. Magnification is 200 \times . (From Ref. 3.)

References

1. R.L. Jones and K.H. Stern, *Ind. Eng. Chem. Prod. Res. Dev.* **19**, 158 (1980).
2. W.T. Reid, *Trans ASME, J. Eng. Power* **89**, Ser. A, 283 (1967).
3. G.F. Case, "Evaluation of Hot-Section Components from FT4C-1 Aboard *Asiafreighter*," DTNSRDC Report MAT-76-29, Aug. 1976.

Damage Cascades in Semiconducting Material,
by G.P. Mueller and C.S. Guenzer, *Condensed Matter and Radiation Sciences Division*

Future Navy systems will incorporate electronics of far greater complexity and density than those in currently operational systems. Some of these systems will operate in an environment of nuclear radiation, such as occurs naturally in space or near a nuclear weapon burst. Recent work at NRL and elsewhere has shown that ultraminiaturized integrated circuits in the presence of nuclear radiation are subject to new failure mechanisms, called single-event radiation effects, that will affect their operational reliability. Several kinds of single-event mechanisms have been observed.

There is one single-event mechanism, the permanent damage of a transistor by a nuclear particle, that has not yet been observed but may ultimately limit the use of advanced microcircuits in radiation environments. This mechanism is expected to become important when the cascade of displacement damage (lattice atoms displaced from their native sites) that the particle creates as it traverses an electronic device occupies a significant fraction of the active volume of that device. Unfortunately, the size and shape of displacement cascades in the most common semiconducting material, silicon, are not well known. Both experimental and theoretical results have been based on unrealistic assumptions that include spherical damage volumes and amorphous silicon models.

To investigate the form of damage volumes in silicon, we used the simulation code MARLOWE developed by Robinson and Torrens [1]. This code maintains a model of a crystalline silicon lattice and follows the effects on the lattice due to an irradiating particle. In our mode of use, a MARLOWE calculation is started by giving a significant velocity to an atom at a lattice site. The direction of the atom's motion is chosen randomly with respect to the crystal directions. MARLOWE follows the collisions of this atom

with atoms immediately in its path. The code assesses the momenta of both atoms in the initial collision and all subsequent collisions. Each collision produces additional moving atoms that also collide, creating the cascade of displaced, moving atoms. Each displaced atom leaves a vacancy at its original lattice site, and each collision reduces the energy of the striking atom. MARLOWE successively monitors the collisions of the moving atoms until their energies are reduced to some predetermined minimum.

During 1980, we made twenty such simulations using an initial particle energy of 100 keV in order to picture the effects of large cascades. We assumed that if an ion came to rest sufficiently close to a vacancy, it would fill the vacancy. Examples of displacement damage are shown in Figures 8 and 9. The size of the boxes in these figures represents the amount of local damage produced in that region. In both cases, we selected the viewing angle that best portrays the cascade.

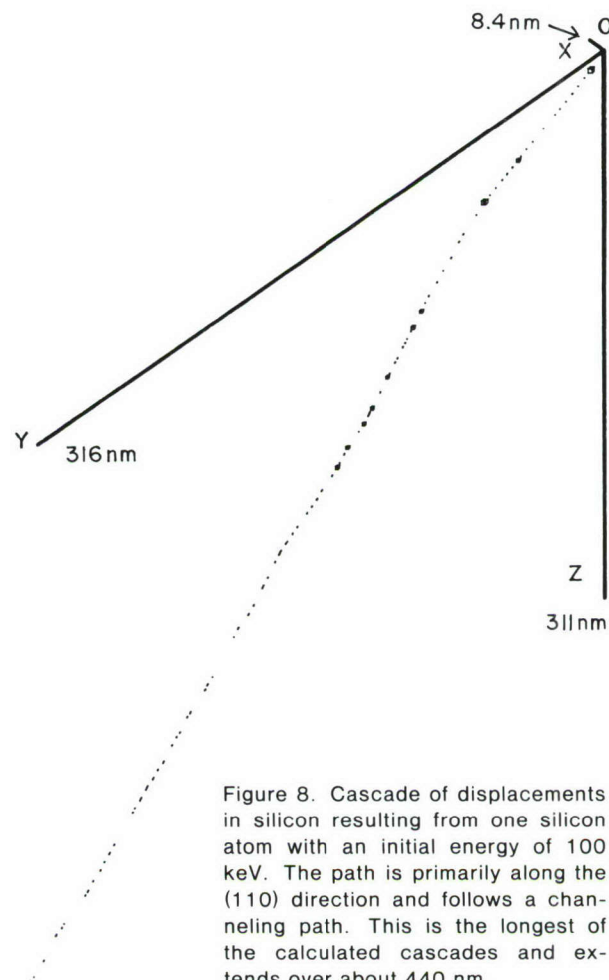


Figure 8. Cascade of displacements in silicon resulting from one silicon atom with an initial energy of 100 keV. The path is primarily along the (110) direction and follows a channeling path. This is the longest of the calculated cascades and extends over about 440 nm.

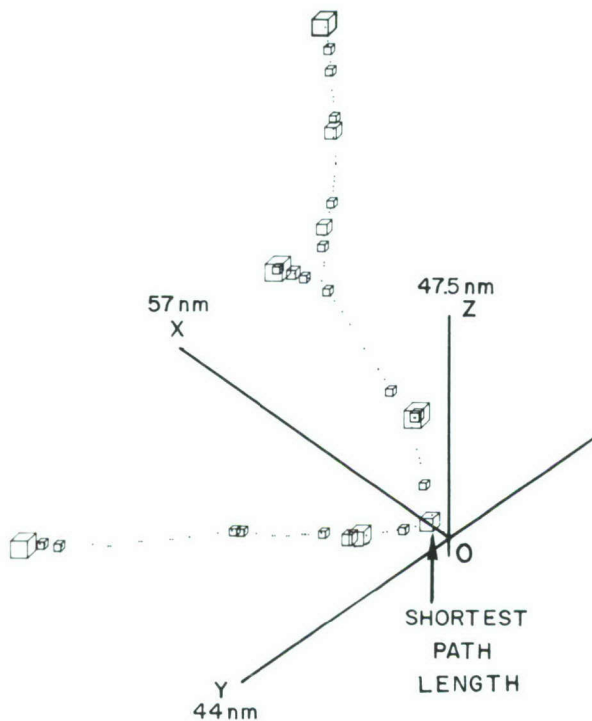


Figure 9. Cascade of displacements in silicon resulting from a 100-keV silicon atom that suffered a strong interaction near the origin. This is one of the most dense and most treelike of the calculated cascades and extends over about 80 nm; the shortest path is only 10 nm. The sizes of the boxes are proportional to the local damage.

The twenty cascades display considerable variety. No individual cascade is typical. The two represented in Figures 8 and 9 are those for which the initial atom traveled the longest and shortest paths, 440 nm and 10 nm, respectively, before the minimum energy level was reached. In the example of Figure 8, the atom started from the origin in a direction nearly parallel to the large channel in the (110) direction. Such channels or open corridors occur because the atoms of the lattice are in a regular array. Atoms moving in a channel undergo little scattering, and the moving atom in this case produced a number of displacements but was gradually directed into the channel. It produced no significant number of displacements past about 310 nm.

In contrast, the initial atom in Figure 9 suffers a nearly head-on collision shortly after leaving its lattice site and generates the treelike structure traditionally associated with cascades. There is a large difference of scale between the figures. The cascade in Figure 8 is 440 nm in extent, and the one in Figure 9 extends a maximum of 80 nm from the origin even though one

of the two principal branches (the one between the x - and y -axes) is focused into a channel. Further, because of channeling and the filling of nearby vacancies by stopped atoms, there are large gaps in the branches of the trees. Prior calculations of cascade structure were based on amorphous models, which were incapable of detecting the more discrete character that is evident in these full-lattice calculations.

In summary, the nature of the collision cascade simulation is changed dramatically when the effects of channeling and focusing are included. The damage cascades resulting from 100-keV silicon vary widely in structure and size. By making many calculations with a code such as MARLOWE, one can determine average properties of a damage cascade; but the average cascade may be neither typical nor elucidative with regard to potential damage to electronic devices. However, such model calculations do provide an important tool in efforts to relate the structure of the damage volumes to degradation of electronics, and eventually to predict the radiation vulnerability of advanced integrated circuits. Of current interest is the application of MARLOWE to studies of damage volume effects on channel conductance and on transistor gain.

[Sponsored by DNA]

Reference

1. M.T. Robinson and I.M. Torrens, *Phys. Rev. B* **9**, 5008 (1974).

Cosmic-ray Effects on Microelectronics, by J.H. Adams, Jr., R. Silberberg, and C.H. Tsao, *Laboratory for Cosmic Ray Physics*

The digital integrated circuits currently used in satellite electronics have such small, sensitive circuit elements that the passage of a single intensely ionizing particle through an element can change its logic state without damaging the circuit. Cosmic rays from outer space contain such intensely ionizing particles and thus are capable of causing these so-called soft errors in a variety of circuit designs.

The rate at which soft errors occur depends on how frequently the circuit is struck by a cosmic-ray particle capable of producing the required ionization. It is therefore necessary to know the energy spectra and elemental composition of these particles in the vicinity of earth.

The published experimental measurements in the near-earth charged-particle environment

have been compiled and used to construct an analytic model of the composition and energy spectra of these nuclear particles. Figure 10 shows the model spectra we have fitted to the existing data for galactic cosmic-ray hydrogen, helium, and iron nuclei. Each spectra has two branches at low energies. The upper branch corresponds to periods of minimum solar activity, and the lower one applies to the maximum of the solar cycle, when the enhanced solar wind makes it more difficult for cosmic rays to penetrate the solar system. The spectral amplitude varies between these extremes, with an 11-yr period.

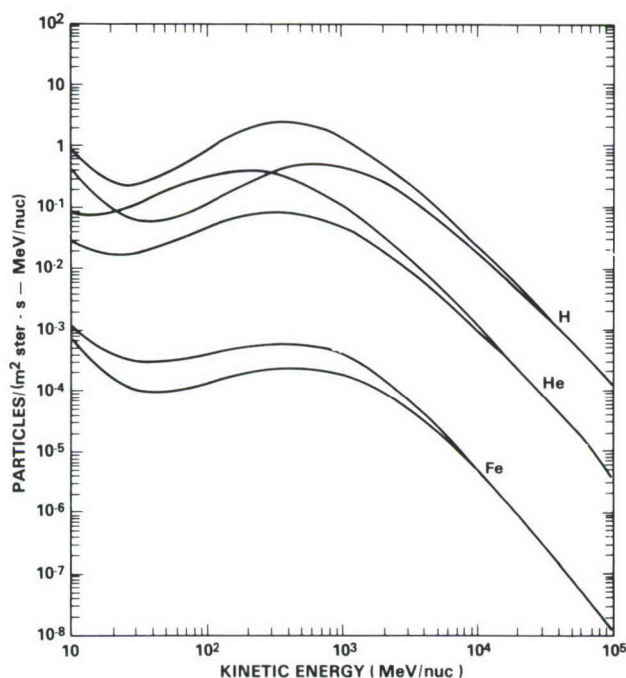


Figure 10. The galactic cosmic-ray differential energy spectra for hydrogen (H), helium (He), and iron (Fe)

The primary cosmic rays consist of all the elements in the periodic table, though elements beyond nickel are quite rare. We have accounted for the fluxes of the other elements up to nickel by scaling from the helium or iron spectra according to their measured relative abundances.

In addition to cosmic rays, which are always present in the interplanetary medium, the particle environment occasionally is much enriched by large solar flares. Figure 11 shows the proton spectrum from a series of very large flares that occurred in August 1972. Shown for comparison are the spectra of cosmic-ray protons that would have accumulated during the time of these flares

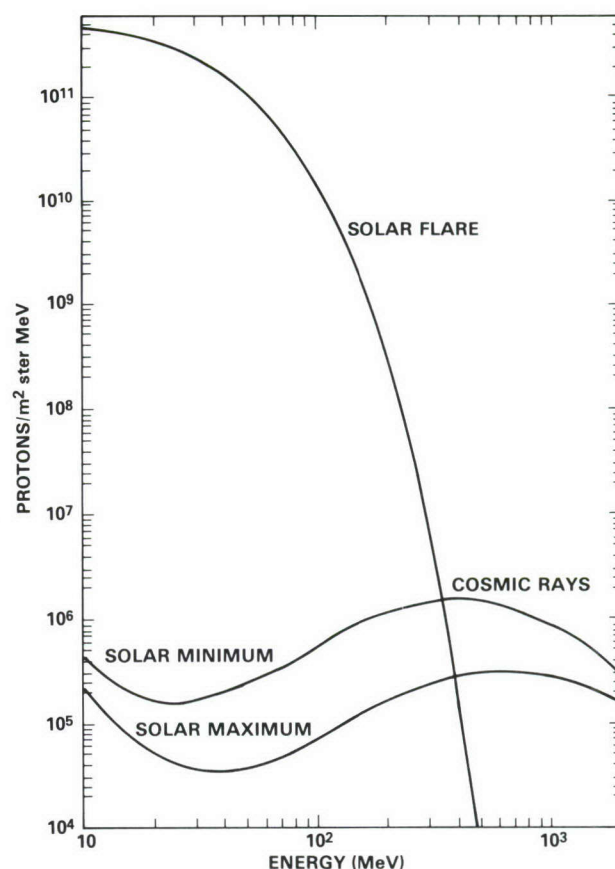


Figure 11. The accumulated hydrogen differential-energy spectrum for the solar flares of August 4-11, 1972. This is compared with the spectra of galactic cosmic-ray hydrogen accumulated for one week in periods of maximum and minimum solar activity.

had they occurred during solar maximum and minimum, respectively.

In addition to these energetic particle components found in interplanetary space, there are particles trapped in the earth's magnetosphere. Figure 12 shows flux contours for protons with energies greater than 10 MeV in the inner Van Allen belt [1]. Helium, carbon, nitrogen, and oxygen nuclei also are present in the belts in much smaller numbers.

The rate at which soft errors occur on a satellite depends on its orbit, the amount of shielding around the electronics, and the critical amount of charge that must be liberated by the ionization from a single cosmic ray to induce an error. To compare the error rates to be expected under different conditions, we have chosen to model a 256-kbit memory. Each bit in the memory has a sensitive volume whose average cross section is $100 \mu\text{m}^2$. Three values were considered for the critical charge required to change

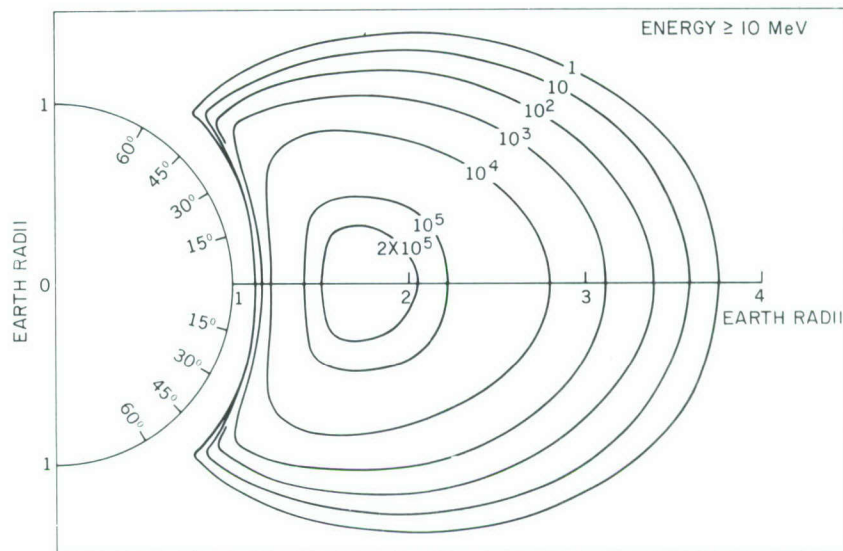


Figure 12. The inner Van Allen radiation belt protons with energies ≥ 10 MeV; flux contours are shown in protons $\text{cm}^{-2} \text{s}^{-1}$ [1].

the state of a memory bit, $10^4 e^-$, $10^5 e^-$, and $10^6 e^-$ (where e^- is the charge carried by a single electron). The shielding around the electronics was assumed to be of a uniform thickness, and aluminum of two thicknesses was considered, 25 and 580 mils. Finally, three different cases were considered: (1) synchronous orbit, no flares; (2) synchronous orbit, one very large flare, and (3) 1500 nmi in a 30° circular orbit. The results are

shown in Table 1. The error rates, given in soft errors per day, are attributed to H (hydrogen) nuclei, He (helium) nuclei, HN (all nuclei heavier than helium), and Int. (errors caused by the products of a nuclear interaction initiated by the cosmic ray), respectively.

For each case, the error rate drops dramatically with increasing critical charge. Shielding is of little help for case 1, because the errors

Table 1. Soft Errors per Day in a 256-kbit Memory

Case	Damaging Components	Critical Charge					
		$10^4 e^-$		$10^5 e^-$		$10^6 e^-$	
		Shield Thickness (mils)					
		25	580	25	580	25	580
1. Synchronous orbit	H	200	100	—	—	—	—
	He	1500	1500	100	2	—	—
	HN	600	600	300	300	10	5
	Int.	3	3	3	3	3	3
2. Synchronous plus very large flare	H	2×10^9	2×10^8	—	—	—	—
	He	4×10^7	5×10^5	4×10^7	5×10^5	—	—
	HN	1×10^6	1×10^4	1×10^6	1×10^4	1×10^5	1×10^4
	Int.	1×10^5	1×10^4	1×10^5	1×10^4	1×10^5	1×10^4
3. 1530 nmi in a 30° orbit	H	8×10^8	1×10^7	—	—	—	—
	He	small	small	2×10^6	small	—	—
	HN	small	small	small	small	small	small
	Int.	1×10^4	500	1×10^4	500	1×10^4	500

are caused by galactic cosmic rays. Additional shielding is effective in cases 2 and 3, especially in case 3 at $10^5 e^-$. This is because the shielding completely stops the low-energy trapped heavy ions, and cosmic-ray heavy ions that would be slow enough to stop in the satellite are excluded by the earth's magnetic field. It should be noted that as the critical charge increases, heavier nuclei in the cosmic rays are required to produce soft errors. It will also be seen that there is no critical charge at which the heavy nuclear fragments from interactions dominate, in cases 1 and 2, as a cause of soft errors. This is because galactic cosmic rays and solar flare particles contain significant numbers of heavy nuclei, which themselves cause soft errors. For case 3 it is the trapped particles that produce soft errors, and these are almost entirely protons, especially at higher energies. Consequently, interaction pro-

ducts are the dominant source of soft errors for $10^6 e^-$ and $10^5 e^-$ in the heavily shielded case.

It is clear that many details of the spacecraft and its orbit go into determining the soft-error rate. Future research on this topic will be directed to developing a means of accurately computing soft-error rates on various satellites.

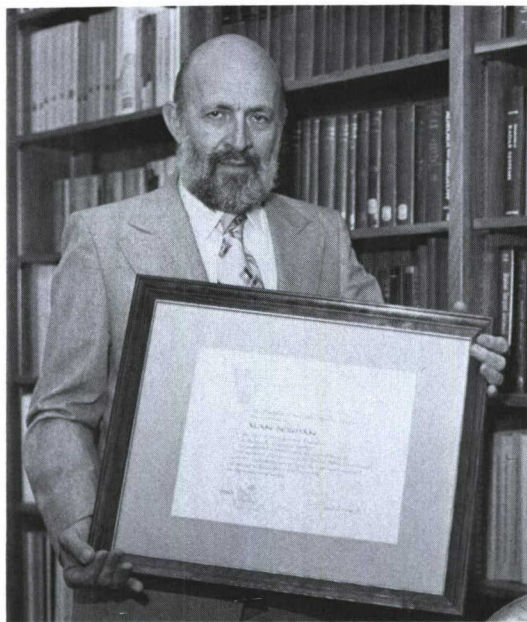
[Sponsored by NAVELEXSYSCOM and ONR]

Reference

1. D.M. Sawyer and J.I. Vette, "AP-8 Trapped Proton Environment for Solar Maximum and Solar Minimum," National Space Science Data Center Report NSSDC/WDA-A-R&S 76-06, Greenbelt, Md. (1976).

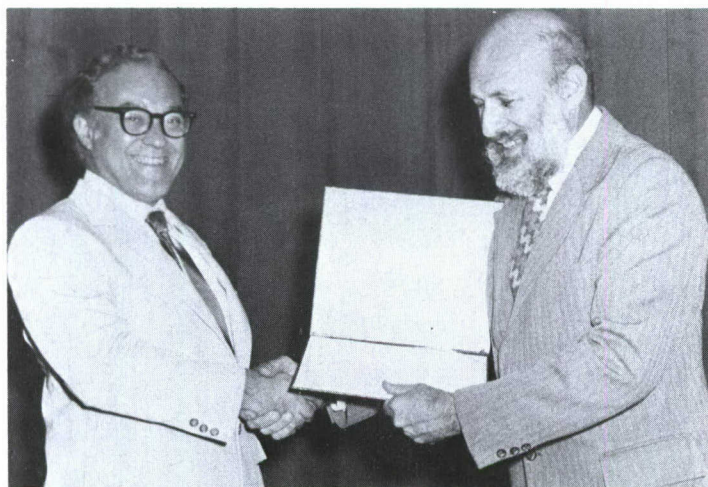
RECOGNITION HONORS, AWARDS, AND TRAINING





Dr. Alan Berman received the rank of Distinguished Executive in the Senior Executive Service, conferred by the President, "for sustained extraordinary accomplishment in management of programs of the United States Government and for leadership exemplifying the highest standards of service to the public, reflecting credit on the career civil service."

Dr. J.P. Boris receiving from Rear Adm. A.J. Baciocco the Navy Distinguished Achievement in Science Award for his pioneering research in computational physics. Dr. Boris is known as the originator of the flux-correct transport (FCT) algorithm and is recognized for his innovative applications in reactive flow, FCT, and plasma physics.



Dr. Victor Granatstein receiving from Dr. A. Berman the Laboratory's E.O. Hulburt Award for 1980 for "contributions to the experimental and theoretical studies of coherent electromagnetic radiation from relativistic electron beams and advanced concepts in millimeter wave tubes." He also received the Navy Superior Civilian Service Award.

RECOGNITION

HONORS, AWARDS, AND TRAINING

HONORS AND INCENTIVE AWARDS

During 1980 NRL staff members earned 1902 awards under the Federal Incentive Awards program. These awards are summarized in the following table.

Distribution of
Federal Incentive Awards During 1980

President's Distinguished Senior Executive Award	1
Arthur S. Flemming Award	1
DoD Distinguished Civilian Service Award	1
Navy Distinguished Civilian Service Award	1
Navy Award for Distinguished Achievement in Science	1
Navy Robert Dexter Conrad Award	1
Navy Superior Civilian Service Award	7
Navy Meritorious Civilian Service Award	10
NRL E.O. Hulburt Annual Science Award	1
Outstanding Performance Ratings	289
Special Achievement Awards	175
Quality Salary Increases	282
Research Publication Awards	67
Invention and Patent Disclosures	211
Employee Suggestions	22
Length of Service Awards	628
Safety Certificates	107
Blood Donor Certificates	95
Commanding Officer's Award for Achievement in EEO	1
Commanding Officer's Award	1
TOTAL	1902

In addition, Laboratory employees received numerous scientific medals, military service awards, academic honors, and other forms of recognition, including election and appointment to offices in technical societies. The following is an alphabetical list of the persons receiving such recognition in 1980.

R.L. Aberg: *Chairman, Navy Radar/Electronic Warfare Technical Group; member, DoD/IDA Avionics, Navigation, and Naval Equipment Technical Working Group; member, NAVMAT R&D Structuring Group*

G. Abraham: *IEEE United States Activities Board Citation of Honor; member, Editorial Board, IEEE Press*

S. Ahn: *Editor, Proceedings of the KSEA Washington Conference on Science and Technology; editor, Collection of Papers on the Electron Cyclotron Masers (Gyrotron)*

K.T. Alfried: *Appointed to Editorial Board, Celestial Mechanics*

C.A. Bartholomew: *Chairman, Technical Program Committee, 12th Annual Precise Time and Time Interval (PTTI) Applications and Planning Meeting*

R.L. Beard: *Chairman, Navy Critical Technology Committee on Guidance and Control at NRL*

A. Berman: *Awarded Rank of Distinguished Senior Executive by the President*

L.S. Birks: *Elected Honorary Member, Society for Applied Spectroscopy; invited lecturer, Australian X-Ray Society*

S.G. Bishop: *Member, Navy Technical Review Committee, Joint Services Electronics Program; session chairman, Semi-Insulating III-V Materials Conference (Nottingham, U.K.); invited paper, NATO InP Workshop (Cape Cod)*

T.V. Blanc: *NATO Air-Sea Interaction Study Visit Grant*

D.J. Blome: *Navy Meritorious Civilian Service Award*

J.E. Blue: *Appointed to Membership Committee, Acoustical Society of America; elected President, Central Florida Federal Management Association*

R.J. Bobber: *Navy Superior Civilian Service Award*

D.J. Bogan: *Chairman, Chemical Kinetics Session, Fall 1980 Technical Meeting of Combustion Institute, Eastern States Section (Princeton, N.J.)*

D.L. Book: *Translation Editor, Soviet Journal of Plasma Physics; appointed to Board of Editors, 50th Anniversary Physics Handbook*

RECOGNITION



Robert Doerflein receiving the CHINFO Merit Award from Capt. E.E. Henifin, given by the Chief of Naval Information.



Dr. Herbert Friedman wearing the medal for the Navy Distinguished Civilian Service Award presented to him in March 1980.



Dr. Isabella L. Karle, of NRL's Laboratory for the Structure of Matter, was awarded the Navy Capt. Robert Dexter Conrad Award for her contributions to methods of molecular and crystal structure analysis, for fundamental analyses of the structure of many substances of Navy interest, and for her publishing and teaching achievements on these subjects. Rear Adm. A.J. Baciocco, Chief of Naval Research, presented the award.

J.P. Boris: *Navy Award for Distinguished Achievement in Science; appointed to Executive Committee, Plasma Physics Division, American Physical Society*

H. Bress: *Navy Meritorious Civilian Service Award*

G.E. Brueckner: *Elected Fellow, American Association for the Advancement of Science*

J.A. Buisson: *Session chairman, 12th Annual Precise Time and Time Interval (PTTI) Applications and Planning Meeting*

J.W. Butler: *Member, Organizing Committee, and session chairman, 6th Conference on the Application of Accelerators in Research and Industry (Denton, Tex.)*

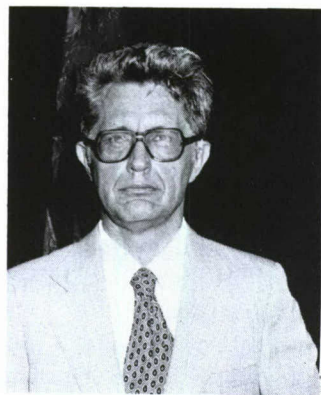
F.J. Campbell: *Elected Fellow, American Institute of Chemists; Certified Professional Chemist, National Certification Commission in Chemistry and Chemical Engineering; Chairman, Commit-*

tee on Radiation Effects, Electrical Insulation Society, IEEE; Chairman, Committee on Radiation Effects on Electrical Insulation, International Electrotechnical Commission; invited paper, International Meeting on Radiation Processing; invited paper, Gordon Research Conference on Science of Adhesion; listed in American Men and Women of Science and Who's Who in Technology Today

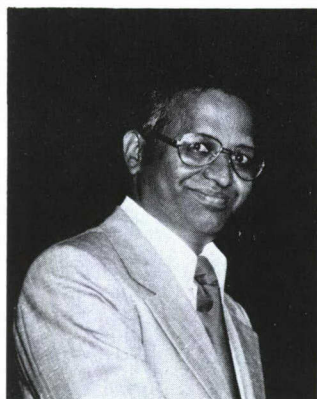
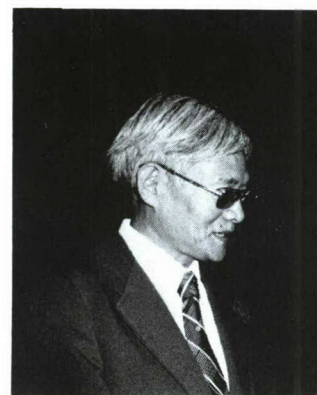
W.H. Carter: *Appointed Chairman, Technical Council, Society of Photo-Optical Instrumentation Engineers (SPIE); appointed Associate Editor, Journal of the Optical Society of America, for 6-year term; Chairman and proceedings editor for SPIE seminar, Applications of Speckle Phenomena*

C.I. Chang: *Co-Chairman, Structural Hardening Subgroup, Tri-Service Laser Hardening Materials and Structural Group; member, Executive*

- Committee, Washington Chapter, American Society for Metals; member, Executive Committee, Army Solid Mechanics Symposium; member, ASTM Pipe Flaw Evaluation Task Group
- T.A. Chubb: *Elected Secretary-Treasurer, Biology and Chemistry Topical Division of the American Section of the International Solar Energy Society*
- T. Coffey: *Elected Fellow, American Physical Society; elected to Commission H of International Union of Radio Science (URSI)*
- S.C. Collins: *Centennial Award (1880-1980), American Society of Mechanical Engineers, Washington Section*
- G. Cooperstein: *Elected member, Plasma Science and Applications Executive Committee, IEEE Nuclear and Plasma Science Society for 3-year term*
- C.D. Crandall: *Chairman, Nominating Committee, IEEE Washington Section; member, IEEE National Membership Development Committee; member, Board of Directors, EASCON, 1980-1983*
- K.L. Davis: *Member, 1980 IEEE Ultrasonics Symposium Technical Program Committee; Chairman, IEEE Sonics and Ultrasonics Group, Washington Chapter*
- J.A. DeSanto: *Co-editor (with A.W. Sáenz and W.W. Zachary) of Mathematical Methods and Applications of Scattering Theory, Lecture Notes in Physics, Vol. 130, Springer-Verlag; member, National Science Foundation Review Panel on Tomography in the Ocean; invited participant, Oberwolfach Conference on Scattering Theory; elected to Commission B of International Union of Radio Science (URSI)*
- N. Djeu: *Associate Editor, IEEE Journal of Quantum Electronics*
- R. Doerflein: *Navy Chief of Information (CHINFO) Merit Award, Graphics*
- L.F. Drummeter, Jr.: *Navy Superior Civilian Service Award*
- H.G. Eaton: *Chairman, Committee of Management, Silver Spring YMCA; member, review panel for membership and allocations for United Way agencies*
- R.C. Elton: *Executive Secretary, 6th International Conference on Vacuum UV Radiation Physics (Charlottesville); appointed to International Advisory Board for International Conference on Vacuum UV Radiation Physics; appointed Associate Editor, Physical Review A, for 3-year term*
- B.J. Faraday: *Session chairman, Second European Symposium on Photovoltaic Generators in Space (Heidelberg, West Germany); session chairman, 11th International Conference on Defects and Radiation Effects in Semiconductors (Osaka, Japan)*
- S. Flannelly: *Annual research award, National Space Club*
- J.L. Flippen-Anderson: *Member, Selection Committee for the First A.L. Patterson Award, American Crystallographic Association*
- R.B. Fox: *Elected Secretary, Interdivisional Committee on Nomenclature and Symbols, International Union of Pure and Applied Chemistry (IUPAC); associate member, Commission on Macromolecular Nomenclature, IUPAC; elected Regional Director, American Chemical Society (ACS); member, Ad Hoc Committee on ACS Subsidies; member, Board of Managers of Washington Section, ACS; Chairman, Washington Section Councilors Committee*
- W.B. Fox: *Deputy Assistant for Research to the Deputy Under Secretary of Defense for Research and Advanced Technology*
- T.L. Francavilla: *Session chairman, 1980 Applied Superconductivity Conference; member, Interagency Advanced Power Group Superconductivity Panel; editor, AIP Conference Proceedings #58, Inhomogeneous Superconductors—1979*
- E.J. Friebele: *1979 Washington Academy of Sciences Award in physical science*
- H. Friedman: *Navy Distinguished Civilian Service Award*
- W.D. Garrett: *Member, United Nations Group of Experts on the Scientific Aspects of Marine Pollution (GESAMP); Chairman, GESAMP Working Group on the Interchange of Pollutants between the Atmosphere and the Oceans; invited participant, U.N. meeting on the Global Investigation of Pollution in the Marine Environment (Monterey, Calif.); invited seminar on mosquito control, United Nations Development Program (New York, N.Y.); session chairman, Conference on Air-Sea Interactions (Los Angeles, Calif.)*
- T.G. Giallorenzi: *Elected Fellow, Optical Society of America; Program Chairman, International Conference on Integrated Optics and Optical Fiber Communications; member, Program Committee, Conference on Laser Engineering and Applications; keynote address, Two-Dimensional Optical Signal Processing Symposium (Washington, D.C.); five other invited conference addresses on fiber optics*



The Sigma Xi award winners are (top) the Pure Science Award, Dr. Rein Silberberg (left) and Dr. Chen H. Tsao of the Laboratory for Cosmic Ray Physics, and (bottom) the Applied Science Award, Dr. K. Sadananda (left) and Dr. Paul Shahinian of the Material Science and Technology Division.



- R.J. Goode: *Re-elected 2nd Vice Chairman of ASTM Committee E-24 on Fracture Testing*
- C.M. Gordon: *President, NRL Chapter of Sigma Xi, Research Society of America; member, ONR Advisory Group for HEBBLE (High Energy Benthic Boundary Layer Experiment)*
- D.F. Grady: *Navy Superior Civilian Service Award*
- V.L. Granatstein: *Navy Superior Civilian Service Award; E.O. Hulburt Award for 1979; invited to present lectures in Relativistic Electronics at Institute of Electronics, Chinese Academy of Science (Peking, China)*
- O.M. Griffin: *Keynote speaker, Symposium on Vortex Flows, ASME Winter Annual Meeting; co-editor, Ocean Engineering for OTEC, published by ASME, February 1980*
- D.U. Gubser: *Associate Professorial Lecturer, George Washington University; member, Program Committee, and session chairman, 1980 Applied Superconductivity Conference; member, Interagency Advanced Power Group Superconductivity Panel; elected Fellow, American Physical Society; editor, AIP Conference Proceedings #58, Inhomogeneous Superconductors—1979*
- C.S. Guenzer: *Conference Chairman, DNA/DARPA Single Event Upset Workshop*
- G.A. Haas: *Special editor, Application of Surface Science, Special Issue for Tri-Service Cathode Conference (Rome, N.Y.); session chairman, Tri-Service Cathode Workshop (Rome, N.Y.); invited speaker, Vacuum Devices Conference (Cavendish Laboratory, Cambridge, England)*
- A.B. Harvey: *Member, Committee on Atomic and Molecular Physical Data; member, Organizing Committee, Gordon Conference on Vibrational Spectroscopy; member, Selection Committee for 1980 Coblentz Award; session chairman, Special Symposium on Combustion, 35th Annual Symposium on Molecular Spectroscopy; member, NSF Review Panel on Combustion; Chairman, Sigma Xi Pure and Applied Science Award Selection Committee; invited lecturer, Special Symposium on Laser Spectroscopy sponsored by Spectroscopy sponsored by Spectroscopy Society of Pittsburgh*
- J.R. Hawthorne: *Appointed to Program Committee, Fourth ASTM-EURATOM Symposium (American Society for Testing and Materials-European Communities Commission) on Reactor Dosimetry; appointed to Program Committee, ASTM Symposium on Radiation Effects; elected Second Vice President, ASTM Committee E-10 on Nuclear Technology and Applications*

- W.A. Hendrickson: *Elected Co-Chairman, Gordon Research Conference on Diffraction Methods in Molecular Biology; member, Molecular Biology Advisory Panel of National Science Foundation; member, Proposal Review Panel for Stanford Synchrotron Radiation Laboratory*
- J.K. Hirvonen: *Session chairman, 2nd International Conference on Ion Beam Modification of Materials (Albany, N.Y.)*
- V.J. Hollings: *Navy Meritorious Civilian Service Award*
- D.D. Howard: *Navy Meritorious Civilian Service Award*
- E.O. Hulburt: *Honorary Doctor of Humane Letters, Johns Hopkins University*
- B.G. Hurdle: *Co-organizer and invitational speaker, Norway—United Kingdom, United States sponsored NORSE WORKSHOP (Bergen, Norway)*
- E.J. Jablonski: *Navy Meritorious Civilian Service Award*
- R.K. Jeck: *Temporary appointment to Faculty, U.S. Naval Academy, as NAVAIR Research Professor in Meteorology for academic year 1980-81*
- W.M. Jewett: *Navy Meritorious Civilian Service Award*
- A.K. Jordan: *Appointed chairman, Inverse Scattering Review Committee for Commission B (Fields and Waves) of URSI (International Union of Radio Science)*
- I.L. Karle: *Navy Robert Dexter Conrad Award; appointed to Editorial Board, International Journal of Peptide and Protein Research; appointed member, Board of International Organizations and Programs, National Academy of Sciences; program co-chairman, Symposium on Structure of Large Drugs and Biomolecules, Experimental and Theoretical (Houston); listed in Who's Who and Who's Who in American Women; biography in Who's Who in Technology Today; 1963 paper selected as Citation Classic for Science Citation Index*
- J. Karle: *Member, Advisory Panel of Biotechnology Center, Stanford Synchrotron Radiation Laboratory; member, Audit Committee, National Academy of Sciences*
- P.F. Kennedy: *Navy Superior Civilian Service Award*
- T.A. Kennedy: *Invited paper, American Physical Society Meeting (New York); invited paper, NATO InP Workshop (Cape Cod); invited paper, Materials Research Society (Boston)*
- C. Kim: *Treasurer, Korean Scientists and Engineers Association in America (KSEA); member, Editorial Committee, KSEA News Letter*
- E.L. Kline: *Chief U.S. member, NATO Task Group of Experts on Narrowband Digital Speech; Chairman, NATO Task Group of Experts on HF Voice Communications; U.S. member, NATO Senior Working Group on Narrowband Digital Speech*
- N.C. Koon: *Elected Fellow, American Physical Society; President, Greater Washington Solid State Physics Colloquium 1979-80*
- J.J. Krebs: *Elected Vice President, NRL Chapter of Sigma Xi*
- J.D. Kurfess: *Elected Secretary-Treasurer Division of Cosmic Physics, American Physical Society; member, Scientific Advisory Panel, Long Duration Balloon Program; member, Scientific Advisory Panel, Australian Balloon Launching Station; session chairman, Conference on Cosmic Ray Astrophysics and Low Energy Gamma Ray Astronomy*
- J.M. Lambert: *Member, Organizing Committee, and session chairman, 6th Conference on the Application of Accelerators in Research and Industry (Denton, Tex.)*
- T.J. Lennox, Jr.: *Appointed to National Association of Corrosion Engineers President's Government Affairs Committee (1980-1983); Navy representative to DoD/IDA Critical Technology Technical Working Group on Chemicals and Materials; member, Navy Critical Technology Committee on Materials at NRL*
- F.K. Lepple: *Appointed member, American Meteorological Society Committee on Interaction of the Sea and Atmosphere*
- J. Lescault: *Navy Superior Civilian Service Award*
- H. Lessoff: *Invited speaker, Gallium Arsenide Integrated Circuit Symposium; session chairman and member, Program Committee, Electronic Materials Conference; liaison representative, National Material Advisory Board on Assessment of HgCdTe*
- V.J. Linnenbom: *Navy Meritorious Civilian Service Award*
- W.T. Manheimer: *Navy Meritorious Civilian Service Award*
- E. McCafferty: *Chairman, National Capital Section, Electrochemical Society; divisional editor, Journal of the Electrochemical Society; member, Executive Committee, Corrosion Division of the Electrochemical Society; member, Honors and Awards Committee of the Electrochemical Society*
- B.D. McCombe: *Session chairman and invited speaker, American Physical Society Meeting*

- (New York, N.Y., March 1980); session chairman, American Vacuum Society Meeting (Detroit, Mich.); invited speaker, Gordon Research Conference, July, 1980; invited speaker, Workshop on the Physics of Sub-Micron Devices, Colorado State University; Chairman, Physics of Compound Semiconductor Interfaces (PCSI-8) Conference
- J.R. McDonald: Plenary lecture, Sixth International Symposium on Gas Kinetics (Southampton, England)
- J.R. McGrath: Awarded Humanitarian Services Medal for USMCR participation in Cuban Alien Relocation Program
- E.A. McLean: Member, Administrative Committee, IEEE Nuclear and Plasma Sciences Society; session organizer, 1980 IEEE International Conference on Plasma Science (Madison, Wis.)
- S.K. Meads: Navy Meritorious Civilian Service Award
- D.J. Michel: Chairman, Nuclear Metallurgy Committee, The Metallurgy Society of the American Institute of Mining, Metallurgical and Petroleum Engineers (AIME); member, Task Force on Crack Propagation Technology, American Society of Mechanical Engineers, Boiler and Pressure Vessel Code Subcommittee on Properties of Metals
- R.B. Moore: Member, Technical Program Committee, 12th Annual Precise Time and Time Interval (PTTI) Applications and Planning Meeting
- D. Mosher: Elected Fellow, American Physical Society
- J.C. Munson: Elected Fellow, IEEE
- J.A. Murray: Navy representative to DoD Technical Working Group on Electronic Instrumentation Critical Technology; Chairman, Navy Instrumentation Critical Technology Committee at NRL
- D.J. Nagel: Invited to write major review on "Plasma Technology" for Encyclopedia of Chemical Technology
- K.L. Ngai: Invited speaker, Annual Meeting, European Physical Society (Antwerp, Belgium); invited speaker, International Symposium on 1/f Noise (Orlando, Fla.)
- M. Nisenoff: Member, Organizing Committee, Conference on Refrigeration for Cryogenic Sensors and Electronic Systems (Boulder, Colo.); member, Organizing Committee for Navy Review of Superconducting Magnetometry and Gravimetry (Annapolis, Md.)
- E.S. Oran: Arthur S. Flemming Award
- S.L. Ossakow: Member, National Research Council Committee on Solar-Terrestrial Research Panel on the Jicamarca Radio Observatory in Peru; member, Doctoral Thesis Committee, Physics Department, Boston College
- E.D. Palik: Co-Chairman, Program and Editorial Committee, Topical Conference on Basic Optical Properties of Materials (NBS, Gaithersburg)
- P.J. Palmadesso: Editor, Commission H section, International Union of Radio Science (URSI) publication Review of Radio Science 1978-1980
- D.A. Papaconstantopoulos: Elected Fellow, American Physical Society
- G.E. Perez: NRL Equal Employment Opportunity Award
- H. Rabin: DoD Distinguished Civilian Service Award
- B.B. Rath: Chairman, Editorial Board, Metallurgical Transactions-A; Chairman, Flow and Fracture Activity Committee, American Society for Metals; member, Board of Directors, Maryland Institute of Metals; member, planning committee, and co-editor of seminar proceedings on Fundamentals of Friction and Wear of Materials; member, Navy Steering Committee on Rapid Solidification Technology; member, ONR Steering Committee on Titanium; member, Electrical, Optical and Magnetic Phenomena



Dr. Elaine S. Oran, shown with Dr. Flemming, received one of the Arthur S. Flemming Awards given annually by the District of Columbia Junior Chamber of Commerce to ten young Federal employees nationwide who have performed outstanding work of distinct benefit to the government.



Dr. Herbert Rabin, a former Associate Director of Research, was presented the Department of Defense Distinguished Civilian Service Award on July 10, 1980 by Deputy Secretary of Defense W. Graham Claytor, Jr.. The award, based on his work at NRL, was for his contributions to solid state and optical physics, for management in basic and applied research programs, and for contributions to advanced technology in space systems.

Committee, Titanium Committee of American Society for Metals and American Institute of Metallurgical Engineering; member, DARPA/AF Review Board on RSR program; member, Proposal Review Board, National Science Foundation

C. Rauscher: *Member, Steering Committee, 1980 IEEE International Microwave Symposium*

H.A. Resing: *Co-editor, Magnetic Resonance in Colloid and Interface Science, NATO Advanced Study Institute Series C61; lecturer, National Research Council of Canada*

L.T. Rhodes: *Navy Meritorious Civilian Service Award*

B.H. Ripin: *Elected Fellow, American Physical Society; Chairman, Plasma Science Application*

Committee of IEEE; Associate Editor, Physics of Fluids; Physics of Fluids Review Committee, American Institute of Physics

A.E. Robson: *Member, Editorial Board, Plasma Physics; member, Overview Committee for the 5-Year Plan, Applied Plasma Physics Division, Department of Energy; elected Fellow, American Physical Society*

P.H. Rogers: *1980 Biennial Award, Acoustical Society of America; A.B. Wood Medal and Prize, Institute of Acoustics, Great Britain*

L.H. Ruhnke: *Secretary, International Commission on Atmospheric Electricity, 1980-1985*

K. Sadananda: *Sigma Xi Applied Science Award; Program Chairman, Symposium on Crack Propagation, American Society for Metals; member, Task Group on High Temperature Crack Growth, American Society for Testing and Materials*

A.W. Sáenz: *Co-editor (with J.A. Desanto and W.W. Zachary) of Mathematical Methods and Applications of Scattering Theory, Lecture Notes in Physics, Vol. 130, Springer-Verlag; invited participant, Oberwolfach Conference on Scattering Theory*

R.J. Sanford: *Elected Fellow, Society for Experimental Stress Analysis (SESA); member, Committee of Fellows, SESA*

A.I. Schindler: *Appointed Chairman, Technical Panel PTP-4 (Materials Performance in Systems) of Subgroup P (Materials), Technical Cooperation Program*

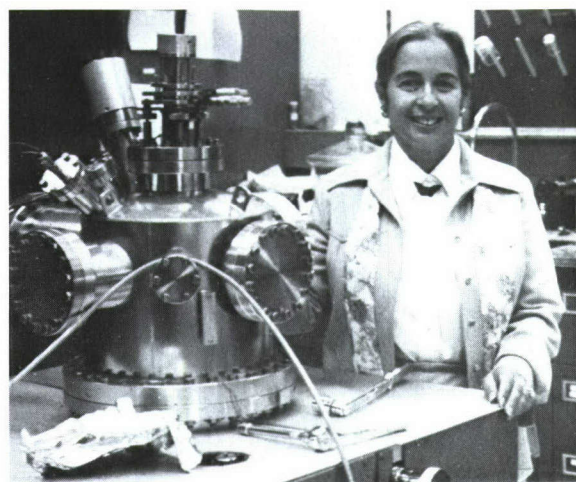
J.T. Schriempf: *Elected Fellow, American Physical Society; briefings to JASON Group and ARPA; organizer and Co-Chairman, Fourth DoD Conference on Laser Vulnerability, Effects, and Hardening*

J.W. Schwartz: *Technical Program Chairman, U.S. Commission C (Signals and Systems), International Union of Radio Science (URSI)*

Dr. Peter H. Rogers, while assigned at USRD, was chosen recipient of the 1980 Biennial Award of the Acoustical Society of America. This honor is presented in part for substantial contribution, through published papers, to the advancement of theoretical or applied acoustics. Dr. Rogers is the first NRL staff member to receive the award, and also the first Navy employee to be given the award for a career in naval research.



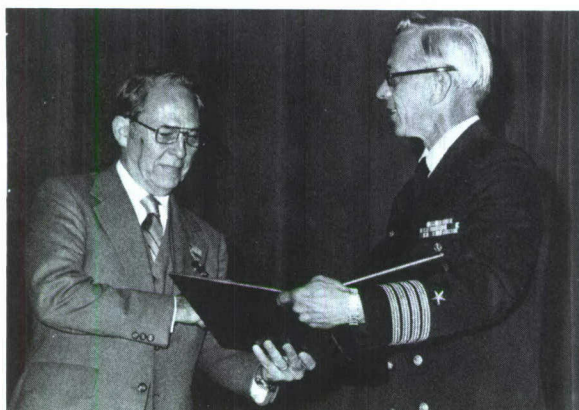
- E.G. Shafrin: *Community Service Award, Chemical Society of Washington; Washington Academy of Sciences plaque, "For Encouragement of Science Talent, 1965-1980"*
- P. Shahinian: *Sigma Xi Applied Science Award; appointed Chairman, Task Force on Cyclic and Fracture Behavior, Pressure Vessel Research Council*
- M.M. Shapiro: *Vice-Chairman and Chairman-Elect, High-Energy Astrophysics Division, American Astronomical Society; interviewed by American Institute of Physics for Archives, "Oral History of Physics," on early research in cosmic rays; member, Executive Committee, DUMAND Consortium; member, ad-hoc International Committee for DUMAND; member, Scientific Advisory Committee, and Rapporteur for Cosmic-Ray Workshop, Texas International Symposium on Relativistic Astrophysics (Baltimore, Md., Dec. 1980); member, International Executive Committee for the Texas Conferences; representative, Division of Cosmic Physics, to Council Committee on International Freedom of Scientists, American Physical Society (APS); member, panel of Publications Committee, APS, on review procedures; member of the Board, Einstein Foundation International*
- B.P. Shay: *Member, ONR Technical Review Committee for Joint Services Electronics Program; member, DoD Protocol Standards Technical Panel*
- S.D. Shulman: *Member, Advanced X-Ray Astrophysics Facility Working Group, sponsored by National Aeronautics and Space Administration Headquarters*
- R. Silberberg: *Sigma Xi Pure Science Award; co-director (with M.M. Shapiro) of course, "Acceleration of Particles in Nature," International School of Cosmic-Ray Astrophysics, Erice, Italy; invited by Deputy Undersecretary of Defense (DDR&E) to contribute a résumé on Biological Effects of Cosmic Rays for presentation to the Congress*
- E.F. Skelton: *Yuri A. Gagarin Award, Satellite Communication Committee of the RSF, USSR*
- J.R. Slagle: *Member, Editorial Board, for special issue of IEEE Transactions on Pattern Analysis and Machine Intelligence, "Computer Intelligence: Three Decades"; member, Executive Committee, IEEE Computer Society Technical Committee on Machine Intelligence and Pattern Analysis*
- F.A. Smidt: *Secretary, Technical Cooperative Program, Technical Panel-4 (TTCP TP-4),*



Chemist Elaine Shafrin received the Chemical Society of Washington's Community Service Award, a plaque from the Washington Academy of Sciences for the encouragement of science talent, and a certificate of appreciation as advisor from the Washington Junior Academy of Sciences.

- "Materials Performance in Systems"; member, Executive Committee, Washington Chapter, American Society for Metals; member, Program Committee, Second Topical Meeting on Fusion Materials*
- B.E. Spielman: *Chairman, IEEE MTT-S Technical Committee on Microwave Integrated Circuits*
- L.E. Steele: *Appointed Chairman, American Society for Testing and Materials (ASTM) Board of Directors Standing Committee on Technical Committee Activities; editor, Assuring Structural Integrity of Steel Reactor Pressure Vessels, Applied Science Publishers, London; organizer and Chairman, First ASTM Energy Emphasis Week (New Orleans, La., Jan. 1980)*
- K.H. Stern: *Co-editor, Phase Diagrams for Ceramicists, 1979 and 1984 Editions*
- R.R. Stone, Jr.: *Navy Distinguished Civilian Service Award*
- D.F. Strobel: *Appointed member, Committee on the Upper Atmosphere, American Meteorological Society*
- E.P. Szuszczewicz: *Session chairman and invited speaker, International Symposium on Equatorial Aeronomy (Aguadilla, Puerto Rico); member Proposal Review Panel for National Aeronautics and Space Administration's OPEN (Origin of Plasmas in the Earth's Neighborhood) Program*
- P.C. Taylor: *Member, Organizing Committee and Program Committee, International Topical*

Dr. Fred A. Smidt, Jr., head of NRL's Damage and Failure Mechanics Section, received the Charles B. Dudley Medal Award from the American Society for Testing and Materials for work on irradiation effects in reactor structural materials.



Robert R. Stone was awarded the Navy Distinguished Civilian Service Award, presented by Capt. E.E. Heniffin. Stone, a research physicist in the Communication Sciences Division, was cited for his work in frequency control and synthesis techniques.

Conference on Tetrahedrally Bonded Amorphous Semiconductors (Carefree, Ariz.)

R.E. Thomas: *Session chairman, Tri-Service Cathode Workshop (Rome, N.Y.)*

P.A. Treado: *Member, Organizing Committee, and session chairman, 6th Conference on the Application of Accelerators in Research and Industry (Denton, Tex.)*

D.D. Triantos: *Arranger and chairman of symposium "How Much Does the Defense Department Advance Science?" at Annual Meeting, American Association for the Advancement of Science*

C.H. Tsao: *Sigma Xi Pure Science Award*

G.R. Valenzuela: *Co-opted member, Working Group on Remote Sensing, International Union of Radio Science (URSI); listed in 1979 Year Book of International Council of Scientific Unions*

N.R. Vanderplaats: *Member, Subcommittee P457 on Nonlinear, Active, and Nonreciprocal Waveguide Components of IEEE/MTT*

D.L. Venezky: *Appointed member, American Chemical Society Council Committee on Divisional Activities and Chairman, Formation of New Divisions Subcommittee*

R.W. Waynant: *Member, Organizing Committee, First International Conference on Lasers (Peoples Republic of China, May 1980); organizer and Chairman, Washington Chapter, IEEE Quantum Electronics and Applications Society*

D.C. Webb: *Program Committee member and session chairman, 1980 IEEE International Microwave Symposium*

L.R. Whicker: *Deputy member, Advisory Group on Electron Devices, Working Group A; member, IEEE Energy Committee; member, IEEE Research and Technology Committee; member, IDA Group D on Critical Technologies*

F.W. Williams: *Appointed to Executive Panel, NAVSEA Submarine Fire Protection Research and Development Committee*

N.D. Wilsey: *Session chairman, International Conference on Defects and Radiation Effects in Semiconductors (Osaka, Japan); invited paper, NATO InP Workshop (Cape Cod)*

L.M. Winslow: *Associate Editor, IEEE Transactions on Electron Devices (Electron Tubes); Navy representative, DoD Technical Working Group 5 B on Critical Technologies; Chairman, Navy Critical Technology Export Control Committees; appointed associate member, Main Group and Microwave Working Group, DoD Advisory Group on Electron Devices*

J.M. Witting: *Appointed Visiting Professor of Oceanography, U.S. Naval Academy, for 1980-1981*

S.A. Wolf: *Associate Professorial Lecturer, George Washington University; member, Advisory*

RECOGNITION



Five of the 134 Publications Awards winners (clockwise from upper left) are Drs. T.G. Giallorenzi, Wayne A. Hendrickson, Ming Chang Lin, George H. Sigel, and Jay P. Boris.



Committee, 1980 Applied Superconductivity Conference; member, Interagency Advanced Power Group Superconductivity Panel; editor, AIP Conference Proceedings #58, Inhomogeneous Superconductors—1979

E.A. Wolicki: *Appointed Chairman, Hardness Assurance Committee of Space Parts Working Group sponsored by NASA and U.S. Air Force Space Division*

I. Wolock: *Organizer and Chairman, Session on Advanced Composites for Naval Applications, 12th National Technical Conference, Society for the Advancement of Material and Process Engineering*

L. Young: *President and Chairman of the Board, IEEE; President and Chairman of the Board, IEEE Foundation; Governor, American Association of Engineering Societies; member, U.S. National Committee, International Union of Radio Science (URSI); member, Organizing Committee, URSI General Assembly; guest editorial in Science (AAAS); member, Evaluation Panel for Electronics and Electrical Engineering, National Bureau of Standards; member, Advisory Board, Department of Electrical and Computer Engineering, University of California at Santa Barbara; Certificate of Recognition, IEEE Society on Electromagnetic Compatibility*

W.W. Zachary: *Co-editor (with J.A. DeSanto and A.W. Sáenz) of Mathematical Methods and Applications of Scattering Theory, Lecture Notes in Physics, Vol. 130, Springer-Verlag; invited participant, Oberwolfach Conference on Scattering Theory*

RESEARCH PUBLICATION AWARDS

Each year the Director of Research presents cash awards and certificates to the authors of the best NRL scientific or technical papers of the year. This practice was established in 1968 by Dr. Alan Berman, Director of Research, as a means of encouraging and rewarding outstanding scientific writing by the Laboratory staff. Committees for each of 16 major research units nominated a total of 156 papers that were published in 1980; 34 of these ultimately earned Research Publication Awards. Each of the divisions was permitted \$600, which in one case went to a single author, in another was shared by 10 authors, and in the other divisions went to varying numbers of authors in between these extremes.

The Office of the Director of Research awarded a smaller sum, and an extra prize was presented to the authors of two special publications. On March 6, 1981, the awards were presented to the 67 NRL authors at the 13th Annual Research Publication Awards Dinner held at the Bolling Air Force Base Officers' Club. In addition to the check, each winner received a certificate and a bronze paperweight.

The unclassified winning papers are included in the following section under "Papers in Periodicals, Books, and Proceedings of Meetings" and are designated by daggers in the margin. NRL authors are listed below by their research units. There were 16 non-Laboratory coauthors, who are not named.

PUBLICATION AWARDS WINNERS

Office of the Director of Research (1001)

Jay Paul Boris	John H. Konnert
Wayne A. Hendrickson	Elaine S. Oran

Space Science Division (4100)

George A. Doschek	John T. Mariska
Uri Feldman	Robert R. Meier

Environmental Sciences Division (4300)

Hermann E. Gerber	Gaspar R. Valenzuela
-------------------	----------------------

Plasma Physics Division (4700)

Jack Davis	Robert E. Pechacek
Joseph R. Greig	Michael Raleigh
Verne L. Jacobs	Ihor M. Vitkovitsky

Acoustics Division (5100)

Stephen N. Wolf

Radar Division (5300)

William F. Gabriel	Robert D. Tompkins
--------------------	--------------------

Tactical Electronic Warfare Division (5700)

James H. Edwards	Leo W. Lemley
Robert L. Goodwin	Roger McAlevey

Marine Technology Division (5800)

Henry H. Chaskelis	George A. Keramidas
Alfred V. Clark, Jr.	

RECOGNITION

Underwater Sound Reference Detachment (5900)

Steven W. Meeks
Robert W. Timme

David H. Trivett

Chemistry Division (6100)

Robert L. Jones
Ming Chang Lin
Kurt H. Stern

Larry D. Talley
David E. Tevault

Material Science and Technology Division (6300)

Jack D. Ayers
Laurent Beaubien
Philip W. Mast
Kuntimaddi Sadananda

Paul Shahinian
Ray W. Thomas, Jr.
Irvin Wolock

Optical Sciences Division (6500)

Thomas G. Giallorenzi
Richard G. Priest

George H. Sigel
Edward J. West

Condensed Matter and Radiation Sciences Division (6600)

Larry L. Boyer

Norman C. Koon

Electronics Technology Division (6800)

John H. Claassen
James J. Krebs

George H. Stauss
Robert J. Wagner

Communications Sciences Division (7500)

Ronald M. Bauman
John R. Davis
Robert J. Dinger
Joseph A. Goldstein

Charles E. Hobbis
William D. Meyers
Richard K. Royce

Space Systems Division (7900)

James Diggs
Richard Eilbert

Frederick Fine
Bernard Kaufman

Commanding Officer's Special Awards

Walter A. Buczek
Peter H. MacGahan
Philip J. Moser

George E. Price
Jay W. Schwartz
Dean S. Watkeys

CONTINUING EDUCATION AND TRAINING

During 1980, members of the civilian staff participated in 3602 individual training incidents.



Mary Coughlin utilizes one of the Employee Development Branch's well-equipped study booths.

Many of these training opportunities were presented as in-house courses and video tape packages.

The most common study procedure was for participants to work full time at the Laboratory and take job-related scientific courses at universities and schools in the Washington area. There were also the following formal programs in which 8 persons were enrolled: Advanced Graduate Research, Edison Memorial, and Select Graduate. There are two additional programs that exemplify the Laboratory's continuing associations with higher education and the academic community. They are the National Research Council-NRL postdoctoral Cooperative Research Associateship Program, which had 24 new participants in 1980, and the Navy-ASEE Summer Faculty Research Program, which had 6 participants.

The five postgraduate programs and the participation in 1980 are described in the remainder of this section.

Advanced Graduate Research Program

The Advanced Graduate Research Program, which was started in 1964, enables selected employees to devote full time to research or course work in their own or a related field for one academic year at an institution of their choice without the loss of regular salaries, leave, or fringe benefits. From the inception of the program through 1980, 128 employees have participated in this program. Criteria for eligibility include professional stature consistent with the applicant's opportunities and experience, a satisfactory program of study, and acceptance by the

institution selected by the applicant. The program is open to midlevel (and above) employees who have completed six years of federal service, including four years at NRL.

The following NRL staff members began their programs in the fall of 1980. The student's division and chosen institution are given following each name.

Carmine Vittoria (Electronics Technology), Philips Research Laboratory, Hamburg, Germany

Chet B. Opal (Space Science), University of Texas, Austin Texas

Edison Memorial Graduate Training Program

This program enables employees to pursue advanced studies in their fields at local universities. Eligible employees who are selected for participation in this program normally spend 24 hours per week in their work at the Laboratory and 16 hours per week in their studies. The criteria for eligibility include a minimum of one year of service at NRL, a bachelor's or master's degree in an appropriate field, and professional standing in keeping with the candidate's opportunities and experience.

From 1963 through 1980, 137 employees have studied under the Edison Program. The following began study as Edison Scholars in 1980:

Carmela A. Bailey (Environmental Sciences), American University

William R. Barger (Environmental Sciences), University of Maryland

William E. Howell (Tactical Electronic Warfare), Catholic University of America

Patricia A. Tatem (Chemistry), George Washington University

Select Graduate Student Program

To be eligible for this program, employees must have a college degree in an appropriate field and must have maintained at least a B average in undergraduate study. Accepted students devote a full academic year to graduate study. While actually attending school, they receive one half of their salaries, and NRL pays for tuition, books, and laboratory expenses. During the summer, they work at the Laboratory and receive normal pay and fringe benefits.

Thirty-four staff members have enrolled in the program since it began in 1967. There were no new students during 1980.

NRC-NRL Cooperative Research Associateships

Selected Research Associates, who are not NRL employees, spend up to two years here conducting research in their chosen fields in association with NRL scientists. The responsibility for evaluating and selecting the best qualified applicants rests with the National Research Council of the National Academy of Sciences and the National Academy of Engineering. The 24 new postdoctoral Associates appointed in 1980 are listed below with their degree-granting universities and the NRL Divisions in which they are working.

James H. Beall (University of Maryland), Space Science

Michael R. Berman (University of California-Berkeley), Chemistry

Joseph E. Campana (Pennsylvania State University), Chemistry

Benjamin M. DeKoven (University of Chicago), Chemistry

Thomas G. DiGiuseppe (Boston College), Chemistry

Michael T. Duigan (Brandeis University), Chemistry

Michael D. Duncan (Stanford University), Optical Sciences

Wendy W. Fuller (University of California-Los Angeles), Material Science and Technology

John B. Hoover (Johns Hopkins University), Environmental Sciences

Judith T. Karpen (University of Maryland), Space Sciences

Carolyn M. Kramer (University of California-Davis), Chemistry

Marc J. Lipman (Dartmouth College), Acoustics

Steven C. Moss (North Texas State University), Optical Sciences

Herbert H. Nelson (University of California-Berkeley), Chemistry

William L. Nikolai III (University of Utah), Optical Sciences

John H. Paul (University of Miami), Environmental Sciences

Dale L. Peebles (University of Pennsylvania), Chemistry

Christopher Reiser (Massachusetts Institute of Technology), Optical Sciences

Gary S. Selwyn (University of California-Berkeley), Chemistry

Benjamin V. Shanabrook (Pennsylvania State University), Electronics Technology

RECOGNITION

George F. Spooner, Jr. (University of Washington), Environmental Sciences

Paul A. Sutor (University of Southern California), Chemistry

Robert W. Williams (Washington State University), Optical Sciences

Paul Yager (University of Oregon), Optical Sciences

Navy—ASEE Summer Faculty Research Program

This ONR-sponsored program affords selected university faculty members the opportunity to work for 10 summer weeks with professional peers in participating Navy laboratories on research of mutual interest. Administered by the

American Society for Engineering Education, the program in 1980 (its second year) involved 7 Navy R&D centers and 26 faculty participants. The 6 participants at NRL are listed below with their universities and host NRL divisions.

Robert L. Carroll, George Washington University (Space Systems)

Mark S. Cramer, Virginia Polytechnic Institute and State University (Environmental Sciences)

Charles M. Gilmore, George Washington University (Material Science and Technology)

Arthur Linz, Massachusetts Institute of Technology (Optical Sciences)

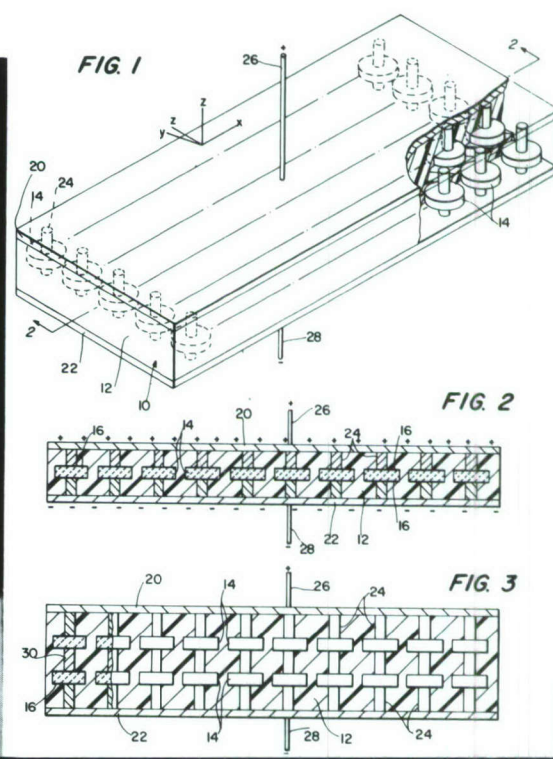
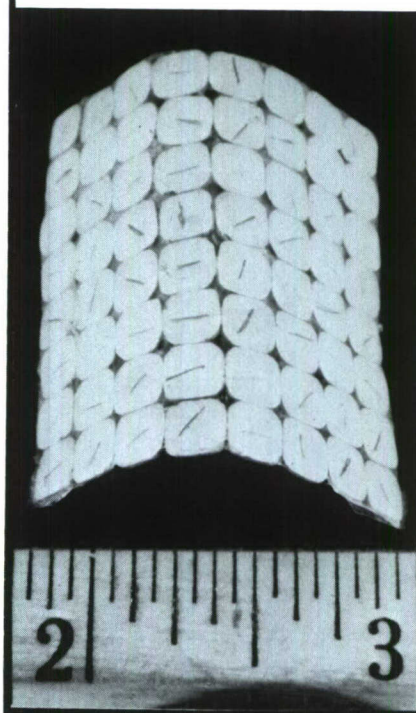
Charles K. Manka, Sam Houston State University (Plasma Physics)

Michael L. Morrell, Clemson University (Marine Technology)

CONTRIBUTIONS

PAPERS, REPORTS, AND PATENTS

U.S. Patent Nov. 11, 1980 4,233,477



CONTRIBUTIONS

PAPERS, REPORTS, AND PATENTS

NRL's scientists document the results of their research with reports for their sponsors and others concerned with each particular area of investigation. Every year they contribute to a variety of scientific periodicals and books and prepare many special reports, both classified and unclassified. In 58 years, NRL's pioneering research has led to 2810 patents. The following table summarizes the Laboratory's contributions during 1980 in these areas.

Laboratory staff members are active in most major scientific societies and contribute to them by holding office and serving on committees (see

the individual honors under "Recognition, Honors, Awards, and Training") and by making presentations. The latter normally number upward of 1500 and are too numerous to list here. The bibliography that follows contains only the unclassified papers and reports in the table below, grouped according to scientific categories. NRL Memorandum Reports are not listed, except for two that won Research Publication Awards. A dagger preceding a title indicates a prize-winning publication; an asterisk identifies an author who is not on the NRL staff. This section concludes with a list of patents issued to NRL inventors in 1980.

Type of Contribution	Unclass.	Class.	Total
Papers in periodicals, books, and proceedings of meetings	594	8	602
NRL Reports	71	21	92
NRL Memorandum Reports	226	41	267
Patents granted			48

PAPERS IN PERIODICALS, BOOKS, AND PROCEEDINGS OF MEETINGS

ACOUSTICS

- A Mobility Analogy Equivalent Circuit of a Magnetostrictive Transducer in the Presence of Eddy Currents, by S.W. Meeks, *J. Acoust. Soc. Am.* 67:683
- A Precision TVG for Echo Ranging Sonar, by F.W. Heemstra, *Oceans '80*, IEEE, New York, p. 277,
- † Acoustic Resonance of a Rare Earth Iron Magnetostrictive Rod in the Presence of Large Eddy Currents, by S.W. Meeks and R.W. Timme, *IEEE Trans. Sonics Ultrason.* SU-27(2):60

- Acoustic Sensing with a Single Coiled Monomode Fiber, by S.C. Rashleigh, *Opt. Lett.* 5:392
- Application of Ferrofluids as an Acoustic Transducer Material, by P.S. Dubbelday, *IEEE Trans. Magn.* MAG-16:372
- Book Review: Sound Transmission through a Fluctuating Ocean, ed. by S.M. Flatte, by J.A. DeSanto, *Nature* 284:380
- Calculations of Sound Propagation through an Eddy, by R.N. Baer, *J. Acoust. Soc. Am.* 67:1180
- Environmental Influences on Acoustic Array Design and Performance in Shallow Water,

- by A.I. Eller and J.F. Miller, *ICASSP80, IEEE International Conference on Acoustics, Speech and Signal Processing*, IEEE, New York, Vol. I, p. 115
- Filled Rubber Materials System: Application to Echo Absorption in Waterfilled Tanks**, by R.D. Corsaro, J. Jarzynski, and J.D. Klunder, *J. Acoust. Soc. Am.* 68:655
- Impact of the Ocean Acoustic Transfer Function on the Coherence of Undersea Propagations**, by A.A. Gerlach, *IEEE Trans. Acoust., Speech Signal Process.* ASSP-28:145
- Measured Noise Levels for a Laboratory Fiber Interferometric Hydrophone**, by J.H. Cole and J.A. Bucaro, *J. Acoust. Soc. Am.* 67:2108
- Resonating Fields inside Elastic Scattering Objects**, by L. Flax, J. George,* P.K. Raju,* and H. Überall,* *J. Acoust. Soc. Am.* 68:973
- Spatial Correlation of Surface Generated Noise in a Stratified Ocean**, by W.A. Kuperman and F. Ingenito, *J. Acoust. Soc. Am.* 67:1988
- Static Pressure Sensitivity Amplification in Interferometric Fiber-Optic Hydrophones**, by R. Hughes and J. Jarzynski, *Appl. Opt.* 19:98
- † **Ultrasonic Nondestructive Bond Evaluation: An Analysis of the Problem**, by H.H. Chaskelis and A.V. Clark, Jr., *Mater. Eval.* 38(4):20
- Use of a Microsphere Probe for Pressure Field Measurements in the Megahertz Frequency Range**, by P.L. Edwards* and J. Jarzynski, *J. Acoust. Soc. Am.* 68:356
- Heights at the Coastal Zone**, by R.E. Larson and D.J. Bressan, *J. Geophys. Res.* 85:4107
- Improved Model of Mie Scattering Contribution to Tropospheric and Stratospheric Photodissociation Fluxes**, by D.E. Anderson, J.B. Kumer, and R.R. Meier, *Appl. Opt.* 19:1230
- Molecular Hydrogen in the Urban Troposphere: Measurement of Seasonal Variability**, by M.Z. Scranton,* W.R. Barger, and F.L. Herr, *J. Geophys. Res.* 85:5575
- Numerical Simulation of Sudden Stratospheric Warmings**, by M.R. Schoeberl and D.F. Strobel, *J. Atmos. Sci.* 37:214
- Radon-222 as an Indicator of Continental Air Masses and Air Mass Boundaries over Ocean Courses**, by R.E. Larson and D.J. Bressan, *Natural Radiation Environment III*, DoE Symposium Series 51, CONF-780422, U.S. Department of Energy, p. 308
- Resonant Planetary Waves in a Spherical Atmosphere**, by M.R. Schoeberl and J.A. Clark, *J. Atmos. Sci.* 37:20
- Sudden Stratospheric Warming Forced by Mountains**, by M.R. Schoeberl and D.F. Strobel, *Geophys. Res. Lett.* 7:149
- The Relative Contribution of Fluctuations in Relative Humidity and Particulate Concentrations to the Variability of the Scattering Coefficient over the North Atlantic**, by J.W. Fitzgerald, *Atmos. Environ.* 14:71
- The Secondary Circulation Associated with a Vertically Aligned Planetary Wave Critical Line**, by M.R. Schoeberl, *Geophys. Res. Lett.* 7:153

ATMOSPHERIC SCIENCES

- Air Mass Characteristics over Coastal Areas as Determined by Radar Measurements**, by R.E. Larson and D.J. Bressan, *Second Conference on Coastal Meteorology*, American Meteorological Society, Boston, Mass., p. 94
- Angle-Dependent Frequency Redistribution in a Plane Parallel Medium: External Source Case**, by J.-S. Lee and R.R. Meier, *Astrophys. J.* 240:185
- Comparison of Laboratory and Numerical Model Studies of the Initial Phase of Cloud Droplet Growth by Condensation**, by J.W. Fitzgerald, S.G. Gathman, E.J. Mack,* and U. Katz,* *Proceedings of the 8th International Conference on Cloud Physics*, University of Clermont II, Aubiere, France, p. 67
- Diurnal Variations of Radon and Mixing**

BIOSCIENCE

- Control of Culex Mosquitos in Sewage Treatment Systems of Southwestern Florida with Monomolecular Organic Surface Films**, by R. Levy,* J.J. Chizzonite,* and W.D. Garrett, *J. Am. Mosq. Control Assoc.* 40:26
- Deep Ocean Microbiology**, by J.W. Deming, P.S. Tabor, and R.R. Colwell, *Advanced Concepts in Ocean Measurements for Marine Biology*, Belle W. Baruch Library in Marine Science, Vol. 10, p. 285
- Effects of Chain Packing and Chain Mobility on the Raman Spectra of Biomembranes**, by R.G. Snyder,* J.R. Scherer,* and B.P. Gaber, *Biophys. Acta* 601:47
- Effects of UV-B on Algal Growth Rate and Trace Gas Production**, by P.J. Hannan, J.W.

Swinnerton, and R.A. Lamontagne, *Aquatic Toxicology*, ASTM STP 707, American Society for Testing and Materials, Philadelphia, Pa., p. 177

Species Composition and Barotolerance of Gut Microflora of Deep-Sea Benthic Macrofauna Collected at Various Depths in the Atlantic Ocean, by K. Ohwada, P.S. Tabor, and R.R. Colwell, *Appl. Environ. Microbiol.* 40:746

The Use of Small Culture Tubes for Testing Microbial Viability and Growth under High Hydrostatic Pressure, by K. Ohwada, P.S. Tabor, and R.R. Colwell, *Bull. Japan. Soc. Sci. Fish.* 46:1293

CERAMICS, GLASSES, AND PLASTICS

Anomalous Fluorescence Linewidths in Glasses, by T.L. Reinecke, *J. Non-Cryst. Solids* 35-36:1145

Dependence of Thermal Stress Resistance on Material Parameters: Ceramic Composite Systems, by P.F. Becher, D. Lewis, W.J. McDonough, R.W. Rice, G.E. Youngblood,* and L. Bentsen,* *Thermal Stresses in Severe Environments*, Plenum Publishing Corp., New York, p. 397

Electron Spin Resonance in Glasses. Part II. Magnetic Properties, by D.L. Griscom, *J. Non-Cryst. Solids* 40:211

Electron Spin Resonance Studies of Iron-Group Impurities in Beryllium Fluoride Glasses, by D.L. Griscom, M. Stapelbroek,* and M.J. Weber,* *J. Non-Cryst. Solids* 41:329

Experimental Investigation of Defect States in Amorphous Chalcogenide Glasses, by G. Pfister* and P.C. Taylor, *J. Non-Cryst. Solids* 35-36:793

Ferromagnetic Resonance of Fine Grained Precipitates in Glass: A Thumbnail Review, by D.L. Griscom, *J. Non-Cryst. Solids* 42:287

Fracture Process in Ferroic Materials, by R. C. Pohanka,* S. W. Freiman,* and R. W. Rice, *1979 IEEE International Symposium on Applications of Ferroelectrics*, Gordon and Breach, New York, p. 337

Processing Defects in a Partially Stabilized Zirconia, by D. Lewis, *Bull. Am. Ceram. Soc.* 59:244

The Dependence of Strength-Controlling Fracture Energy on the Flow-Size to Grain-Size Ratio, by R.W. Rice, S.W. Freiman, and J.J. Mecholsky, *J. Am. Ceram. Soc.* 63:129

The Grain Size Dependence of Spontaneous Cracking in Ceramics, by R.W. Rice and R.C. Pohanka,* *J. Am. Ceram. Soc.* 62:559

Thermal Shock of Ceramics: Size and Geometry Effects, by R.F. Becker,* D. Lewis, R. Carman,* and A. Gonzalez,* *Bull. Am. Ceram. Soc.* 59:542

Thermal Structural Ceramic Composites, by R.W. Rice, *Ceram. Eng. Sci. Proc.* 1:424

CHEMISTRY

A Flow Tube Investigation of the Temperature Dependence of the Chemi-Ionization Reaction between Antimony Pentafluoride and Benzyl Chloride, by A. Auerbach, *J. Chem. Phys.* 73:2003

A Gradient Heat Desorption Technique of Preconcentrated Tenax-GC Tubes for Use in GC-MS Analysis, by H.G. Eaton, *J. Chromatogr. Sci.* 18:580

Abrasive Wear Resistance of Titanium- And Nitrogen-Implanted 52100 Steel Surfaces, by I.L. Singer, R.N. Bolster, and C.A. Carosella, *Thin Solid Films* 13:283

Adiabatic J Cross-Polarization in Liquids for Signal Enhancement in NMR, by G.C. Chingas, R. Bertrand,* A.N. Garroway, and W.B. Moniz, *J. Am. Chem. Soc.* 102:2526

Adsorption of O₂ on the SrTiO₃ (100) - (1 x 1) Surface, by V. M. Bermudez and V. H. Ritz, *Chem. Phys. Lett.* 73:160

Alkane Chain Conformation as a Function of Pressure, by P.E. Schoen and S.L. Wunder, *High Pressure Science and Technology*, Pergamon Press, New York, Vol. 2, p. 676

Applications of Multiphoton Dissociation and Laser Induced Fluorescence to Combustion: Reactions of CH Radicals with Unsaturated Hydrocarbons, by J.W. Fleming, G.T. Fujimoto, M.C. Lin, and A.B. Harvey, *Lasers '79*, STS Press, McLean, Va., p. 246

ArF Excimer Laser Multiphoton-Ionization Mass Spectrometry of Organic Molecules, by M. Seaver, J.J. DeCorpo, and J.W. Hudgens, *Int. J. Mass Spectrom. Ion Phys.* 34:159

Atmospheric Monitoring in Submersibles, by J.J. DeCorpo, J.R. Wyatt, and F.E. Saalfeld, *J. Am. Soc. Mech. Eng.* 80:1

Atomic Volume Contraction in Intermetallic Hydride Formers: A Valuable New Clue, by F.L. Carter, *J. Less-Common Met.* 74:245

- Atomic Volume Contraction in Rare Earth Nickel Intermetallics as a Function of Partial Coordination Number Coefficient**, by F.L. Carter, *The Rare Earths in Modern Science and Technology*, Plenum Publishing Corp. New York, Vol. 2, p. 299
- Autoignition: The Importance of the Cool Flame in the Two-Stage Process**, by W.A. Affens and R.S. Sheinson, *Loss Prev. Tech. Man.* 13:83
- Carbon Isotope Enrichment by Retention of Isotopic Excitation Selectivity in VV Ladder Climbing Collisions**, by D. Hsu and T.J. Manuccia, *Chem. Phys. Lett.* 76:16
- Carbon Monoxide Laser Resonance Absorption Studies of $O(^3P) + 1$ -Alkynes and Methylene Radical Reactions**, by W.M. Shaub and M.C. Lin, *Laser Probes for Combustion Chemistry*, ACS Symposium Series 134, American Chemical Society, Washington, D.C., p. 403
- Carbon-13 NMR Investigation of Surface Modified Silica Gels**, by D. Slotfeldt-Ellingsen and H.A. Resing, *Magnetic Resonance in Colloid and Interface Science*, Proceedings of a NATO Advanced Study Institute and The Second International Symposium, p. 577
- Central Atmosphere Monitor (CAMS)**, by J.J. DeCorpo, J.R. Wyatt, and F.E. Saalfeld, *J. Am. Soc. Nav. Eng.* 92:231
- Characteristics of CO_2 - CH_4 Reforming-Methanation Cycle Relevant to the Sol-chem Thermochemical Power System**, by T.A. Chubb, *Sol. Energy* 24:341
- Characterization of Ligand-Binding Systems by Continuous Affinity Distributions of Arbitrary Shape**, by A.K. Thakur,* D.L. Huns-ton, P.J. Munson, and D. Rodbard, *Analyt. Biochem.* 130:240
- Characterization of Multiphoton-Ionization Mass Spectrometry**, by J.J. DeCorpo, J.W. Hudgens, M.C. Lin, F.E. Saalfeld, M.E. Seaver, and J.R. Wyatt, *Adv. Mass Spectrom.* 8:133
- Chemical Demulsification of Seawater in Residual Oil Emulsions**, by R.N. Bolster and R.C. Little, *Environ. Int.* 3:163
- Chemical State of Ion-Implanted Nitrogen in Fe18 Cr8 Ni Steel**, by I.L. Singer and J.S. Murday, *J. Vac. Sci. Technol.* 17:327
- Chemically Modified Electrodes, Radiofrequency Plasma Polymerization of Vinylferrocene on Glassy Carbon and Platinum Electrodes**, by R.J. Nowak, F.A. Schultz, M. Umana, R. Lam, and R.W. Murray, *J. Anal. Chem.* 52:315
- $CH_3O(\tilde{X}^2E)$ Production from 266 nm Photolysis of Methyl Nitrite and Reaction with NO** , by N. Sanders, J.E. Butler, J.R. McDonald, and L.R. Pasternack, *Chem. Phys.* 48:203
- Chromate Film Used for Chemical Corrosion Control on Gold-Plated PCB Connectors**, by E.G. Shafrin, J.D. Guttenplan,* L.N. Hashimoto,* and J.S. Murday, *Appl. Surf. Sci.* 4:456
- Coal Liquefaction 2. Controlled Oxidations and Thermolysis of Coal in Pyridine**, by J. Solash, R.N. Hazlett, J.C. Burnett, P.A. Climen-sen, and J.R. Levine, *Fuel* 59:667
- Combustion Promotors for Safe Disposal of Carbon Fiber Reinforced Plastics**, by J. Rear-don, S. Kaufman, and L. Johnson, *Environ. Sci. Technol.* 14:325
- Comparison of Laboratory Techniques for Evaluating the Fracture Toughness of Glassy Polymers**, by R.Y. Ting and R.L. Cottingham, *J. Appl. Polymer Sci.* 25:1815
- $C_2O(\tilde{X}^3\Sigma^-)$: Absolute Reaction Rates Measured by Laser Induced Fluorescence**, by V.M. Donnelly,* J.R. McDonald, and W.M. Pitts,* *Chem. Phys.* 49:289
- Creation of J-Ordered Magnetic States by Adiabatic Demagnetization in the Rotating Frame**, by A.N. Garroway and G.C. Chin-gas, *J. Magn. Reson.* 38:179
- Desorption Kinetics of Methyl Iodide from Impregnated Charcoal**, by L.A. Jonas,* V.R. Deitz, and J.B. Romans, *Nucl. Technol.* 48:77
- Detailed Modelling of Combustion: a Nonin-terfering Diagnostic Tool**, by E.S. Oran, J.P. Boris, and M.J. Fritts, *Laser Probes for Combustion Chemistry*, ACS Symposium Series 134, American Chemical Society, Washington, D.C., p. 331
- Dynamics of Oxygen Atom Reactions**, by M.C. Lin, *Adv. Chem. Phys.* 42:113
- Dynamics of Reactions of $O(^3P)$ Atoms with 1-Alkynes as Studied by a CO Laser Reso-nance Absorption Technique**, by W.M. Shaub, T.L. Burks, and M. C. Lin, *Chem. Phys.* 45:455
- Dynamics of the Quenching of $Na(3^2P_{1/2})$ by $CO(X^1\Sigma^+, v=0)$** , by D.S. Hsu and M.C. Lin, *J. Chem. Phys.* 73:2188
- Effect of Room-Temperature Aging on Graphite/Polyimide Prepreg Materials**, by H.C. Nash, C.F. Poranski, and R.Y. Ting, 199

- Resins for Aerospace*, ACS Symposium Series 132, American Chemical Society, Washington, D.C., p. 469
- Effects of Competitive Hydrogen Halide Elimination on CO Production from the Reaction of O(³P) Atoms with Propargyl Chloride and Bromide**, by G.T. Fujimoto, M.E. Umstead, and M.C. Lin, *Chem. Phys.* **51**:399
- Effects of Molecular Structure on the Mechanical Properties of Phthalocyanines**, by R.Y. Ting and R.L. Cottingham, *Org. Coatings Plast. Chem. Prepr.* **42**:496
- Electrical Conductivity of TCNQ Salt Dispersions in Electron Donor Poly(vinyl acetal) Matrices**, by O.-K. Kim and R.B. Fox, *Polym. Prepr.* **21** (2):255
- Electron Spectroscopic Analysis of Lubricant-Treated Steel Surfaces after Solvent Cleaning**, by M.K. Bennett and H. Ravner, *Microstruct. Sci.* **8**:85
- Failure in Elastomer-Toughened Epoxies: Viscoelastic Effect**, by D.L. Hunston, J.L. Rushford, J.L. Bitner, J. Oroshnik, and R.S. Rose, *J. Elastomers Plast.* **12**:133
- Flow-Assisted Degradation in Dilute Polystyrene Solutions**, by D.L. Hunston and J.L. Zakin,* *Polym. Eng. Sci.* **20**:517
- Fouling Release Coatings**, by J.R. Griffith and J.D. Bultman, *Nav. Eng. J.* **92**:129
- Fouling Release Coatings: Comment and Discussion**, by D.E. Field, *Nav. Eng. J.* **92** (3):89
- High-Performance Secondary Ion Mass Spectrometer**, by R.J. Colton, J.E. Campana, T.M. Barlak, J.J. DeCorpo, and J.R. Wyatt, *Rev. Sci. Instrum.* **51**:1685
- Identification of Intercalated Species in AsF₅-NO₂SbF₆ Intercalated Graphite Using ¹⁹F NMR; Fluorine Exchange Between the Various Species**, by G.R. Miller, H.A. Resing, P. Brant, M.J. Moran, F.L. Vogel,* T.C. Wu,* D. Billaud,* and A. Pron,* *Synth. Met.* **2**:236
- Infrared Chemiluminescence Investigation of Reactions of Methyl Radicals with Oxygen and Fluorine**, by M.G. Moss, J.W. Hudgens, and J.D. McDonald, *J. Chem. Phys.* **72**:3486
- Investigation of Lubricated Bearing Surfaces by X-Ray Photoelectron and Auger Electron Spectroscopy**, by I.L. Singer and J.S. Murday, *Fundamentals of Tribology, Proceedings of the International Conference*, MIT Press, Cambridge, Mass., p. 239
- Ion Implantation Studies of (SN)_x and (CH)_x**, by W.N. Allen, P. Brant, C.A. Carrosella, J.J. DeCorpo, C.T. Ewing, F.E. Saalfeld, and D. Weber, *Synth. Met.* **1**:151
- † **Landau Phenomenological Theory of One and Two Component Phospholipid Bilayers**, by R.G. Priest, *Mol. Cryst. Liq. Cryst.*, **60**:167
- Laser Applications to Heterogeneous Catalysis: Reactant Excitation and Product Diagnostics**, by M.E. Umstead, M.C. Lin, L.D. Talley, and D.E. Tevault, *Opt. Eng.* **19** (1):94
- Laser Probes for Combustion Applications**, by J.R. McDonald, *Laser Probes for Combustion Chemistry*, ACS Symposium Series 134, American Chemical Society, Washington, D.C., p. 19
- Lead-Acid Battery Overview**, by S.M. Caulder and A.C. Simon, *Materials for Advanced Batteries*, Plenum Press, New York, p. 199
- Logic Aided Fire Detection System**, by T.T. Street, J.I. Alexander, and F.W. Williams, *J. Fire Flammability* **11**:212
- Mass Resolved Detection of Multiphoton Ionization: Mechanistic Insight**, by M. Seaver, J.J. DeCorpo, and J.W. Hudgens, *6th International Conference on Vacuum Ultraviolet Radiation Physics, Extended Abstracts*, University of Virginia, Charlottesville, Vol. II, paper II-33
- Mass Spectral Studies of Electroactive Polymers**, by F.E. Saalfeld, J.J. DeCorpo, W.N. Allen, D. Weber, and J.R. Wyatt, *Adv. Mass Spectrom.* **8**:1913
- Mass Spectrometric Characterization of Halogen Doped Polyacetylene**, by W.N. Allen, J.J. DeCorpo, F.E. Saalfeld, J.R. Wyatt, and D.C. Weber, *Synth. Met.* **1**:371
- † **Matrix Isolation and Laser Diagnostic Studies of Catalytic Oxidation of H₂ and D₂ on Platinum**, by D.E. Tevault, M.C. Lin, and L.D. Talley, *J. Chem. Phys.* **72**:3314
- Motions of Phenyl Groups Chemically Bound to Silica-Gel Carbon-13 Nuclear Magnetic Resonance**, by D. Slotfeldt-Ellingsen and H.A. Resing, *J. Phys. Chem.* **84**:2204
- † **New Eras in Molten Salt Corrosion Research**, by R.L. Jones and K.H. Stern, *I&EC Prod. Res. Dev.* **19**:158
- New Opportunities in Tribology**, by I.L. Singer, J.S. Murday, H. Ravner, J.K. Hirvonen, and N.L. Jarvis, *Nav. Res. Rev.* **32**:4
- Nuclear Magnetic Resonance Characterization of Some Polyphthalocyanine Precursors**, by C.F. Poranski and W.B. Moniz, *Resins for Aerospace*, ACS Symposium Series 132, American Chemical Society, Washington,

- D.C., p. 337
- OH($X^2\Pi_1$) Product Internal Energy Distribution Formed in the Reaction of O(1D_2) with H₂** by G.K. Smith and J.E. Butler, *J. Magn. Reson.* 73:2243
- 193 nm Laser Dissociation of CS₂, Prompt Emission from CS and Internal Energy Distribution of CS($X^1\Sigma^+$),** by J.E. Butler, W.S. Drozdowski, and J.R. McDonald, *Chem. Phys.* 50:413
- Order Parameter from Chemical Shift Anisotropy Patterns in Two-Dimensional Systems,** by H.A. Resing and D. Slotfeldt-Ellingsen,* *J. Magn. Reson.* 38:401
- Oxide Ion Titrations in Molten NaCl with the Zirconia Electrode,** by K.H. Stern, *J. Electrochem. Soc.* 127:2375
- Photonitration of Hydrocarbons with Lasers,** by M.E. Umstead, J.W. Fleming, and M.C. Lin, *IEEE J. Quantum Electron.* QE-16:1227
- Polaron and Bipolaron States in Si- Inversion Layers: Possible Origins and Effects,** by C.T. White and K.L. Ngai, *Surf. Sci.* 98:227
- Polymerization Studies on Aromatic Bis(phthalonitrile) Monomers,** by T.M. Keller, T.R. Price, and J.R. Griffith, *Org. Coatings Plast. Chem. Prepr.* 43:804
- Possible Contributions of Electron Pairing (-u) Centers to the Normal-State Resistivity and Superconductivity in Nonsimple Metals,** by C.S. Ting,* K.L. Ngai, and C.T. White, *Phys. Rev. B* 22:2318
- Pressure Effects on the Resistivity of Pristine and Doped Polyacetylene,** by J.P. Ferraris,* P. Brant, E.R. Carpenter, W.B. Fox, A.W. Webb, and D.C. Weber, *Solid State Commun.* 35:15
- Problems Encountered with Antistatic Packaging for Miniature Bearings,** by B.J. Kinzig and H. Ravner, *Lubr. Eng.* 36:219
- Production of OH Radicals in the Catalytic Oxidation of H₂ by NO₂ over Pt,** by L.D. Talley and M.C. Lin, *Lasers '79*, STS Press, McLean, Va., p. 270
- Pure Rotational Coherent Anti-Stokes Raman Scattering of Simple Gases,** by L.P. Goss,* J.W. Fleming, and A.B. Harvey, *Opt. Lett.* 5:345
- Quantitative Determination of Surface Composition of Sulfur Bearing Anion Mixtures by Auger Electron Spectroscopy,** by N.H. Turner, J.S. Murday, and D.E. Ramaker, *Anal. Chem.* 52:84
- Radiation Lifetimes and Collisional Deactivation Rate Constants of Excited Ne ($2p^53p$) States,** by R.S.F. Chang and D.W. Setser,* *J. Chem. Phys.* 72:4099
- Radiative Lifetimes and Two-Body Collisional Deactivation Rate Constants in Argon for Kr ($4p^55p$) and Kr ($4p^55p^1$) States,** by R.S.F. Chang, H. Horiguchi,* and D.W. Setser,* *J. Chem. Phys.* 73:778
- Reconstruction vs. Magnetism at (111) Si and Ge Surfaces,** by C. White and W. Carlos, *Ordering in Two Dimensions*, S.K. Simha, ed., North-Holland, New York, p. 421
- Remarks Concerning the Interpretation of Coherent Anti-Stokes Raman Spectroscopy Spectral Profiles,** by W.M. Shaub and A.B. Harvey, *Appl. Spectrosc.* 34:381
- Short-Resistant Two-Stage Electrostatic Precipitator Designs,** by G.H. Fielding, J.K. Thompson, and R.C. Clark, *IAS Conference Record*, Industry Applications Society, IEEE, New York, p. 930
- Silicone Amine Cured Fluoroepoxy Resins,** by J.R. Griffith and J.G. O'Rear, *Resins for Aerospace*, ACS Symposium Series 132, American Chemical Society, Washington, D.C., p. 35
- SIMS Fragmentation Patterns from Organic Overlayers on Metal Surfaces,** by J.J. DeCorpo, R.J. Colton, J. Murday, F.E. Saalfeld, and J.R. Wyatt, *Adv. Mass Spectrom.* 8:522
- Summary Abstract: Quantitative Determination of the Surface Composition of Sulfur-Bearing Anion Mixtures by Auger Electron Spectroscopy,** by N.H. Turner, J.S. Murday, and D.E. Ramaker, *J. Vac. Sci. Technol.* 17:214
- Surface Analysis of Bearing Steels after Solvent Treatments,** by M.K. Bennett, B.J. Kinzig, J.S. Murday, and H. Ravner, *ASLE Trans.* 24:98
- Surface Hardness and Abrasive Wear Resistance of Nitrogen-Implanted Steels,** by I.L. Singer and R.N. Bolster, *Ion Implantation Metallurgy*, Metallurgical Society of AIME, Warrendale, Pa., p. 116
- Synthesis and Trimerization of Fluorinated Tertiary Cyanates,** by A.W. Snow and J.R. Griffith, *J. Fluorine Chem.* 15:471
- Synthesis of Phthalonitriles by Nitro Displacement,** by T.M. Keller, T.R. Price, and J.R. Griffith, *Synthesis* 8:613
- Temperature Dependence of the C₂($a^3\Pi_u$) + CH₄ Reaction from 337 to 605 K,** by L.

- Pasternack, A.P. Baronavski, and J.H. McDonald, *J. Chem. Phys.* 73:3508
- The Application of Gas Phase and Solid State Photoelectron Spectroscopy to the Investigation of Derivatives Containing the Repeating SN Unit**, by P. Brant, D.C. Weber, C.T. Ewing, F.L. Carter, and J.A. Hashmall, *Synth. Met.* 1:161
- The Dynamic Mechanical Properties and Fracture Behavior of Phthalocyanine Polymers**, by W.D. Bascom, R.L. Cottingham, and R.Y. Ting, *J. Mater. Sci.* 15:2097
- The Effect of Silica on the Thermal Decomposition of Sodium Sulphate**, by J.C. Halle and K.M. Stern, *Corros. Sci.* 20:1139
- The Identification of PF_6^- Ions in Intercalated Graphites by ^{19}F and ^{31}P NMR Spectroscopy**, by G.R. Miller, H.A. Resing, F.L. Vogel,* A. Pron,* T.C. Wu,* and D. Billaud,* *J. Phys. Chem.* 84:3333
- The Loading-Rate Dependent Fracture Property of a Toughened Epoxy Polymer**, by R.Y. Ting and R.L. Cottingham, *Polym. Bull.* 2:211
- The Synthesis of a New Class of Polyphthalocyanine Resins**, by T.M. Keller and J.R. Griffith, *Resins for Aerospace*, ACS Symposium Series 132, American Chemical Society, Washington, D.C., p. 25
- The Use of the Width-Tapered Double-Cantilever Specimen for Assessing the Interlaminar Toughness of Woven Reinforcement Laminates**, by W.D. Bascom, J.L. Bitner, R.J. Moulton, and A.R. Siebert, *Composites* 11:132
- The X-ray Photoelectron Spectrum of S_2N_2 Gas**, by P. Brant, F.L. Carter, C.T. Ewing, J.A. Hashmall,* and D.C. Weber, *Inorg. Chem.* 19:2829
- Use of Stabilized Zirconia Electrodes to Transport Oxide Ion into and out of Molten Salts**, by M.L. Deanhardt* and K.H. Stern, *J. Phys. Chem.* 84:2831
- Vaporization and Decomposition of Na_2SO_4 . Thermodynamics and Kinetics**, by J.C. Halle and K.H. Stern, *J. Phys. Chem.* 84:1699
- Vibrational Spectra and Bonding in Nitrocyclopropane**, by J.R. Holtzclaw, W.C. Harris, and S.F. Bush, *J. Raman Spectrosc.* 9:257
- Viscoelastic Characterization of Structural Adhesive via Force Oscillation Experiments**, by D.L. Hunston, W.D. Bascom, J.L. Bitner, J.D. Fahey, and E.E. Wells,* *Adhesion and Adsorption of Polymers*, Plenum Press, New York, p. 321

- Voltammetric and Chronopotentiometric of $\text{Na}_2\text{O-NaCl}$ Melts**, by M.L. Deanhardt* and K.H. Stern, *J. Electrochem. Soc.* 127:2600
- X-Ray Photoelectron Spectra of Dopant Molecules for Conducting Polymers. Vapor Phase Core Level Binding Energies for Arsenic and Antimony Pentafluorides**, by P. Brant, M.J. Moran, and D.C. Weber, *Chem. Phys. Lett.* 76:529

COMMUNICATIONS

- † **A New Wide-Band System Architecture for Mobile High Frequency Communication Networks**, by J.R. Davis, C.E. Hobbs, and R.K. Royce, *IEEE Trans. Commun.* COM-28:1580
- Axiomatic Derivation of the Principle of Maximum Entropy and the Principle of Minimum Cross Entropy**, by J.E. Shore, *IEEE Trans. Inf. Theory* IT-26:26
- On Single-Sample Robust Detection of Known Signals with Additive Unknown Mean Amplitude-Bounded Random Interference**, by J.M. Morris, *IEEE Trans. Inf. Theory* IT-26:199
- SQUID Magnetometer Measurements of the Spatial Coherence of Atmospheric Noise from 0.3 to 40 Hz**, by R.J. Dinger and J.A. Goldstein, *1980 Digests of the Intermag Conference*, IEEE, New York, Paper 10-3m

COMPUTER SCIENCES

- Specifying Software Requirements for Complex Systems: New Techniques and Their Application**, by K.L. Heninger, *IEEE Trans. Software Eng.* SE-6:2

COSMIC RAYS

- Detection Processes of Cosmic Neutrinos with an Underwater Astronomical Observatory**, by R. Silberberg, *Proceedings of the Marine Technology 80 Conference*, Marine Technology Society, Washington, D.C., p. 353
- Sources of Cosmic Neutrinos to be Detected in an Underwater Astronomical Observatory**, by M.M. Shapiro, *Proceedings of the Marine Technology 80 Conference*, Marine Technology Society, Washington, D.C., p. 344

ELECTRONICS AND ELECTRICITY

- A New Technique for Hardening CCD Images by Suppression of Interface State Generation**, by N.S. Saks, *IEEE Trans. Nucl. Sci.* NS-27:1727
- † **A Radiation Thermoelectric Power Converter**, by L.W. Lemley, *Proceedings of the Third International Conference on Thermoelectric Energy Conversion*, IEEE, New York, p. 20
- Analysis of the Gyrotron Amplifier for Azimuthally Varying TE Modes**, by S. Ahn and J. Choe, *IEEE Electron. Device Lett.* EDL-1:20
- Broadband Varactor Tuned GaAs F.E.T. Oscillator**, by C. Rauscher, *Electron. Lett.* 16:534
- CCD and SAW Technology**, by K. Davis, *Signal* 34:56
- Charge-Coupled Devices**, ed. by D.F. Barbe, Springer-Verlag, New York
- Compact Coaxial Diode Electron Beam System: Carbon Cathodes and Anode Fabrication Techniques**, by J.G. Eden and D. Epp, *Rev. Sci. Instrum.* 51:781
- Comparison of Reactivation Following Shelf Life Poisoning of the Impregnated and Coated Powder Cathodes**, by G.A. Haas, C. Hor, J.T. Jensen, and A. Shih, *Appl. Surf. Sci.* 5:73
- Gain of the Gyrotron with High Circular Waveguide Mode (Whispering Gallery Mode)**, by S. Ahn and J. Choe, *1980 IEEE MTT-S International Microwave Symposium Digest*, IEEE, New York, p. 102
- Measurement of Noise Sources in p-Surface Channel Charge Coupled Device (CCD) Multiplexers for Infrared Focal Plane Arrays**, by W.C. Jenkins, J.M. Killiany, and J.A. Modolo, *IR Image Sensor Technology*, SPIE, Bellingham, Wash., Vol. 225, p. 136
- Multistable Integrated Circuits for Variable RADIX Systems Design**, by G. Abraham, *12th Annual Southeastern Symposium on System Theory*, IEEE, New York, p. 200
- Nonlinear Interactions in Degenerate Surface Acoustic Wave Elastic Converters**, by A.K. Ganguly and K.L. Davis, *J. Appl. Phys.* 51:920
- NTS-2 Solar Cell Experiment after Two Years in Orbit**, by R.L. Statler and D.H. Walker, *14th IEEE Photovoltaic Specialists Conference -1980*, IEEE, New York, p. 1234
- On the Relationship between Thermal Noise and the Dielectric Response of Pyroelectric**

Materials, by S.T. Liu,* K.L. Ngai, and S. Teitler, *1979 IEEE International Symposium on Applications of Ferroelectrics*, Gordon and Breach, New York, p. 369

On the Relationship Between Thermal Noise and the Dielectric Response of Pyroelectric Materials, by K.L. Ngai, S.T. Liu,* and S. Teitler, *Ferroelectrics* 28:369

Optimum Larger-Signal Design of Fixed-Frequency and Varactor-Tuned GaAs FET Oscillators, by C. Rauscher, *1980 IEEE MTT-S International Microwave Symposium Digest*, IEEE, New York, p. 373

Radiation Effects in Silicon Charge-Coupled Devices, by J.M. Killiany, *Charge-Coupled Devices*, Springer-Verlag, New York, p. 147

Science and Engineering, by L. Young, *Science* 209:1475

Signal Processing with Charge-Coupled Devices, by D.F. Barbe, W.D. Baker, and K.L. Davis, *Charge-Coupled Devices*, Springer-Verlag, New York, p. 91

Study of High Work Function Materials Needed for Close-Spaced Grid Applications, by G.A. Haas and A. Shih, *Appl. Surf. Sci.* 4:104

Submillimeter Laser Cyclotron Resonance of Inversion Layers at Low Electron Densities, by R.J. Wagner and D.C. Tsui,* *Surf. Sci.* 98:256

Synthesis of Distribution Networks with Applications to the Design of Ultra-Wideband GaAs MESFET Power Amplifiers, by W.H. Ku and H.A. Willing, *1980 IEEE MTT-S International Microwave Symposium Digest*, IEEE, New York, p. 390

GEOSCIENCES

Morphology and Magnetic Anomalies North of Iceland, by P.R. Vogt, G.L. Johnson,* and L. Kristjansson,* *J. Geophys.* 47: 67

INSTRUMENTATION

- A Fluid Insulator Used in the Investigation of Gas Phase Ions with an Electrometer**, by A. Auerbach, *Rev. Sci. Instrum.* 51:254
- † **A Saturation Hygrometer for the Measurement of Relative Humidity between 95 and 105%**, by H.E. Gerber, *J. Appl. Meteorol.* 19:1196
- Spectral Distortion Inherent in Airborne Profilometer Measurements of Ocean Wave-Heights**, by D.L. Hammond and C.R. McClain,* *Ocean Eng.* 7:99

LASER SCIENCE

- A Flow Tube Investigation of the Temperature Dependence of the Chemi-Ionization Reaction between Antimony Pentafluoride and Benzyl Chloride**, by A. Auerbach, *J. Chem. Phys.* 73: 2003
- Comparison of CO₂ Laser Extinctions to HITRAN Calculations for 80 Lines—9.2 to 10.8 μ m**, by R.F. Horton, *Atmospheric Effects on Radiative Transfer*, SPIE, Bellingham, Wash., Vol. 195, p. 46
- Destruction of Ground State XeCl Molecules by HCl and Rare Gas Collisions**, by R.W. Waynant and J.G. Eden, *Appl. Phys. Lett.* 56:262
- Dissociative Excitation of HgBr₂ by Rare-Gas Metastable Atoms and N₂(A³ Σ_u^+)**, by R.S. Chang and R. Burnham, *Appl. Phys. Lett.* 36:397
- Enrichment of Deuterium Using Vibrationally Sensitized Reaction of Methane**, by D.S. Hsu and T.J. Manuccia, *Appl. Phys. Lett.* 36:714
- 406-nm Laser on the C \rightarrow B Band of N₂**, by J.G. Eden, *Appl. Phys. Lett.* 36:393
- Frequency and Focal Volume Dependence of Laser-Induced Breakdown in Wide Band Gap Insulators**, by M.J. Soileau,* M. Bass,* and P.H. Klein, *Laser Induced Damage in Optical Materials: 1979*, NBS SP 568, G.P.O., Washington, D.C., p. 497
- High-Power Picosecond Molecular Fragmentation and Rapid X-X Radical Formation**, by B.B. Craig,* W.L. Faust, L.S. Goldberg, P.E. Schoen, and R.G. Weiss,* *Picosecond Phenomena II*, Springer-Verlag, New York, p. 253
- IR Cascade Solid State Lasers**, by L. Esterowitz, R.C. Eckardt, and R.E. Allen, *Lasers '79*, STS Press, McLean, Va., p. 632
- Isotope Separation Using CW Infrared Lasers**, by D.S.Y. Hsu and T.J. Manuccia, *Lasers '79*, STS Press, McLean, Va., p. 276
- Kinetics of the XeCl ($\beta \rightarrow X$) Laser**, by T.G. Finn,* L.F. Champagne, R.S.F. Chang, and L.J. Palumbo, *Appl. Phys. Lett.* 36:789
- Laser Damage in Yttrium Orthophosphate**, by R. Allen, L. Esterowitz, P.H. Klein, V.O. Nicolai,* and W.K. Zwicker,* *Laser Induced Damage in Optical Materials: 1979*, NBS SP 568, G.P.O., Washington, D.C., p. 137
- Low-Frequency Laser Noise of Several Commercial Lasers**, by J. H. Cole, *Appl. Opt.* 19:1023

- Low Frequency Noise in Fiber Coupled Diode Lasers**, by R.O. Miles, W.K. Burns, and T.G. Giallorenzi, *Topical Meeting on Integrated and Guided Wave Optics*, IEEE, New York, p. TuC 3-1
- Passive Mode-Locking of the Nd-Glass Oscillator at High Repetition Rate with Thermally Compensated Phosphate Glasses**, by T.R. Royt, *Opt. Commun.* 35:271
- Rare Gas Halides: The Lasers of the 70's**, by N. Djeu, *Nav. Res. Rev.* 32(2):32
- Repetitive Mode-Locking in Thermally Compensated Phosphate Glasses at 5H₂**, by T.R. Royt, *Picosecond Phenomena II*, Springer-Verlag, New York, p. 3
- The General Non-Linear Theory of Free-Electron Laser and Efficiency Enhancement**, by P. Sprangle, W.M. Manheimer, and C.M. Tang,* *Free-Electron Generators of Coherent Radiation*, Addison-Wesley, Reading, Mass., p. 207
- Transient Absorption in Electron-Beam-Excited Rare Gases at XeF Laser Wavelengths**, by R.S. Chang and L.P. Champagne, *Appl. Phys. Lett.* 36:879
- Transverse Electrodeless RF Discharge Excitation of High-Pressure Laser Gas Mixtures**, by C.P. Christensen, F.X. Powell, and N. Djeu, *IEEE J. Quantum Electron.* QE-16:949
- Violet Laser from E-Beam Excited Ar-N₂**, by J.G. Eden, *Lasers '79*, STS Press, McLean, Va., p. 642
- XeF(C) State Lifetime and Quenching by Rare Gases and Fluorine Donors**, by R. W. Waynant, *Appl. Phys. Lett.* 36:493

MAGNETISM

- A Method for the Calculation of the Magnetization of Random High Anisotropy Amorphous Materials**, by L.M. Pecora and D.I. Paul,* *J. Non-Cryst. Solids* 40:447
- Applications of Magneto-Optics in Ring Laser Gyroscopes**, by J.J. Krebs, W.G. Maisch, G.A. Prinz, and D.W. Forester, *1980 Digests of the Intermag Conference*, IEEE, New York, Paper 38-1; and *IEEE Trans. Magn.* MAG-16:1179
- Calculations of the Atomic Magnetic Moments and Short Range Order in Iron at High Temperature**, by V. Heine,* A.J. Holden,* P.J. Lin-Chung, and M.V. You,* *J. Magn. Mater.* 15-18:69
- Linear Electric Field Effects In Magnetic Anisotropy and Ferromagnetic Resonance**, by

- G.T. Rado, *J. Magn. Magn. Mater.* **15-18**:542
Magnetism In Iron At High Temperatures, by M.V. You,* V. Heine*, A.J. Holden,* and P.J. Lin-Chung, *Phys. Rev. Lett.* **44**:1282
Spin Wave Lifetime in the Antiferromagnet RbMnF_3 , by T.L. Reinecke and R.B. Stinchcombe,* *J. Magn. Magn. Mater.* **15-18**:341

MATHEMATICS

- A Note on "Queuing Models with Lane Selection," by D. Roque, *Oper. Res.* **28**:419
 A Scoring Procedure for the Multiple Target Correlation and Tracking Problem, I.R. Goodman, *19th IEEE Conference on Decision and Control, Including the Symposium on Adaptive Processes*, IEEE, New York, p. 829
 A Surface Wave Interpretation for the Resonances of a Dielectric Sphere, by J.D. Murphy, P.J. Moser, A. Nagl, and H. Überall, *IEEE Trans. Antennas Propag.* **AP-28**:924
 Asymptotic Completeness in Classical Three-Body Scattering, by W.W. Zachary, *Mathematical Methods and Applications of Scattering Theory*, Springer-Verlag, New York, p. 182
 Coherent Scattering from Rough Surfaces, by J.A. DeSanto, *Mathematical Methods and Applications of Scattering Theory*, Springer-Verlag, New York, p. 60
 † First Order Semianalytic Satellite Theory with Recovery of the Short Period Terms due to Third Body and Zonal Perturbations, by B. Kaufman, *31st Congress, International Astronautical Federation, IAF 80*, Paper E-204
 Functional Equation of Inverse Scattering for the Schrödinger Equation with Continuous and Discrete Spectra (Short Note), by S. Ahn, *Mathematical Methods and Applications of Scattering Theory*, Springer-Verlag, New York, p. 327
 Identification of Fuzzy Sets with a Class of Canonically Induced Random Sets, by I.R. Goodman, *19th IEEE Conference on Decision and Control, Including the Symposium on Adaptive Processes*, IEEE, New York, p. 352
 Inverse Scattering Theory: Exact and Approximate Solutions, by A.K. Jordan, *Mathematical Methods and Applications of Scattering Theory*, Springer-Verlag, New York, p. 318
 Mathematical Methods and Applications of Scattering Theory, ed. by J.A. DeSanto, A.W. Sáenz, and W.W. Zachary, *Proceedings of a Conference held at Catholic University,*

Washington, D.C., May 21-25, 1979, *Lecture Notes in Physics*, Vol. 130, Springer-Verlag, New York

- † Numerical Modeling for Convection-Dispersion Problems, by G.A. Keramidas, *Proceedings of the International Conference on Numerical Methods for Non-Linear Problems*, p. 985
 Numerical Simulation of the Anomalous Transport Process in Radically Compressed Reversed-Field Configurations, by S. Hamasaki* and D.L. Book, *Nucl. Fusion* **20**:289
 On a Characteristic Property of Periodic Entire Functions, by C.C. Yang and H. Urabe,* *Kodai Math. J.* **3**:253
 On n-Dimensional Sampling Theorem, by C.C. Yang and K.H. Chen,* *Appl. Math. Comput.* **7**:247
 On Right and Left Factors of a Certain Class of Entire Functions, by C.C. Yang and F. Gross, *J. Math. Anal. Appl.* **77**:416
 One-Dimensional Velocity Inversion for Acoustic Waves: Numerical Results, by S. Gray and N. Bleistein,* *Mathematical Methods and Applications of Scattering Theory*, Springer-Verlag, New York, p. 311
 Resonance Theory and Application, by L. Dragonette and L. Flax, *Mathematical Methods and Applications of Scattering Theory*, Springer-Verlag, New York, p. 95
 Some Triangle Inequalities and Generalizations, by C.C. Yang, C.E. Carroll,* and S. Ahn, *Can. Math. Bull.* **23**:267
 The Chebyshev Method for Solving Nonself-Adjoint Elliptic Equations on a Vector Computer, by B.E. McDonald, *J. Comput. Phys.* **35**:147
 The Markov Property Viewed as the Huygens' Principle of Random Processes, by P.J. Crepeau, *IEEE 1980 Southeastcon*, IEEE, New York, p. 207
 Wave Operators for Multichannel Long-Range Scattering, by A.W. Sáenz, *Mathematical Methods and Applications of Scattering Theory*, Springer-Verlag, New York, p. 175

MECHANICS

- An Experimental Study of Flow Generated Waves on a Flexible Surface, by R.J. Hansen, D.I. Hunston, C.C. Ni, and M.M. Reischman,* *J. Sound Vib.* **68**:317

Application of the Least-Squares Method to 205

- Photoelastic Analysis**, by R.J. Sanford, *Exp. Mech.* 20:1
- Failure of Polymer Composites**, by D.R. Mulville and I. Wolock, *Developments in Polymer Fracture 1*, Applied Sciences Publishers, Ltd., London, Chapter 8, p. 263
- † **Fracture Criteria of Fibrous Laminated Composites Under In-Plane Multidirectional Loading**, by P.W. Mast, J. Tirosh,* L. Beaubien, D. Mulville,* S. Sutton,* R.W. Thomas, Jr., and I. Wolock, *J. Appl. Mech., Trans. ASME Ser. E*, 47:563
- Guyed Towers under Arbitrary Loads**, by F. Rosenthal and R.A. Skop, *J. Struct. Div. ASCE* 106(ST3):679
- Hydrodynamic Drag and Surface Deformations Generated by Liquid Flow and Flexible Surfaces**, by R.J. Hansen, D.L. Hunston, C.C. Ni, M.M. Reischman,* and J.W. Hoyt,* *Viscous Drag Reduction*, Progress in Astronautics and Aeronautics, Vol. 72, AIAA, New York, p. 439
- Photoelastic Holography — A Modern Tool for Stress Analysis**, by R.J. Sanford, *Exp. Mech.* 20:421
- Resonant Scattering of Elastic Waves from Spherical Solid Inclusions**, L. Flax, H. Überall,* and O.M. Griffin, *J. Acoust. Soc. Am.* 67:1432
- Ultrasonic Nondestructive Bond Evaluation: An Analysis of the Problem**, by H.H. Chaskelis and A.V. Clark, *Mater. Eval.* 38:20
- Universal Similarity in the Wakes of Stationary and Vibrating Bluff Structures**, by O.M. Griffin, *Wind Engineering*, Pergamon Press, New York, p. 607
- Vortex-Excited Cross-Flow Vibrations of a Single Cylindrical Tube**, by O.M. Griffin, *Trans. ASME, J. Pressure Vessel Technol.* 102:158
- Vortex-Excited Vibration of Marine Cables**, by O.M. Griffin, J.H. Pattison,* R.A. Skop, S.E. Ramberg, and D.J. Meggitt,* *J. Waterway, Port, Coastal, Ocean Div. ASCE* 106:183
- What Price Speed? Revisited**, by S. Teitler and R.E. Proodian, *J. Energy* 4:46
- ica*, Claitor's Publishing Co., Baton Rouge, La., p. 328
- A Computerized Data Acquisition System for High-Temperature, Pressurized-Water, Fatigue Test Facility**, by W.H. Cullin, B.H. Menke, H.E. Watson, and F.J. Loss, *Computer Automation of Materials Testing*, ASTM STP 710, ASTM, Philadelphia, Pa., p. 127
- A Method for Determining Depth Profiles of Transition Elements in Steels**, by C.R. Gossett, *Nucl. Instrum. Methods* 168:217
- A Reduction in the Coefficient of Friction for Ti-6Al-4V**, by J.D. Ayers, R.C. Bowers, and T.R. Tucker, *Scr. Metall.* 14:549
- Acceleration Creep-Fatigue Crack Propagation in Thermally Aged Type 316 Stainless Steel**, by D.J. Michel and H.H. Smith, *Acta Metall.* 28:999
- Assuring Structural Integrity of Steel Reactor Pressure Vessels**, by L.E. Steele and K.E. Stahlkopf,* Applied Science Publishers, Ltd., London
- Autoklaven zur Prüfung und bestrahlter Proben**, by D. Sturm,* F.J. Loss, and W.H. Cullen, *Materialprüfung* 22:5
- Consolidation of Metal Coating by Electron Beam Melting**, by T.R. Tucker, J.D. Ayers, and R.J. Schaefer,* *Laser and Electron Beam Processing of Materials*, Academic Press, New York, p. 760
- Consolidation of Plasma-Sprayed Coatings by Laser Remelting**, by J.D. Ayers and R.J. Schaefer,* *Laser Applications In Materials Processing*, SPIE, Bellingham, Wash., Vol. 198, p. 57
- † **Crack Growth under Creep and Fatigue Conditions**, by K. Sadananda and P. Shahinian, *Creep-Fatigue-Environment Interactions*, American Institute of Mining and Metallurgical Engineers, p. 88
- Creep-Fatigue-Environment Interactions on Crack Propagation in Alloy 718**, P. Shahinian and K. Sadananda, *Proceedings of International Conference on Engineering Aspects of Creep*, The Institution of Mechanical Engineers, London, Vol. 2, p. 1
- Discussion—Influence of Grain Size and Yield Strength on Threshold Fatigue Behaviour in Low-Alloy Steel**, by G.R. Yoder, L.A. Cooley, and T.W. Crooker, *Metal Sci.* 14(7):283.
- Ductile Fracture Analysis and Safety of Nuclear Pressure Vessels**, by F.J. Loss, *Risk and Failure Analysis for Improved Performance and*

METALLURGY

- A Comparison of Neutron and Nickel Ion Irradiation of Some Binary Nickel Alloys**, by J.A. Sprague, K.B. Roarty,* R.A. Johnson, and F.A. Smidt, *Proceedings, 18th Annual Meeting Electron Microscopy Society of Amer-*

- Reliability*, Plenum Publishing Corp., New York, Chapter 5, p. 93
- Dynamic Fracture Analysis of Notched Beam Specimens**, by S. Mall,* A.S. Kobayashi,* and F.J. Loss, *Crack Arrest Methodology and Applications*, ASTM STP 711, ASTM, Philadelphia, Pa., p. 70
- Effect of Environment on Crack Growth Behavior in Austenitic Stainless Steels under Creep and Fatigue Conditions**, by K. Sadananda and P. Shahinian, *Metall. Trans. A*, 11A:267
- Effect of Microstructure on Creep-Fatigue Crack Growth in Alloy 718**, by K. Sadananda and P. Shahinian, *Res Mech.* 1:109
- Elastic-Plastic Fracture Mechanics for High-Temperature Fatigue Crack Growth**, by K. Sadananda and P. Shahinian, *Fracture Mechanics: Twelfth Conference*, ASTM STP 700, ASTM, Philadelphia, Pa., p. 152
- Improvement of Environmental Crack Propagation Resistance in Ti-8Al-1Mo-1V through Microstructural Modification**, by G.R. Yoder, L.A. Cooley, and T.W. Crooker, *Advances in Materials Technology in the Americas — 1980*, Vol. 2, *Materials Processing and Performance-MD-2*, ASME, New York, p. 135
- J-R Curve Characterization of Irradiated Nuclear Pressure Vessel Steels**, by F.J. Loss, B.H. Menke, R.A. Gray, and J.R. Hawthorne, *Proceedings of CSNI Specialists Meeting on Plastic Tearing Instability*, NUREG/CP-0010, CSNI Report No. 39, p. 292
- Laser Induced Thermal Stresses in Brittle Materials**, by J.J. Mecholsky, P.F. Becher, R.W. Rice, J.R. Spann, and S.W. Freiman, *Thermal Stresses in Severe Environments*, Plenum Publishing Corp., New York, p. 567
- Laser Surface Melting with Carbide Particle Injection**, by R.J. Schaefer,* J.D. Ayers, and T.R. Tucker, *Laser and Electron Beam Processing of Materials*, Academic Press, New York, p. 754
- Notch Ductility Degradation of Low Alloy Steels with Low-to-Intermediate Neutron Fluence Exposure**, by J.R. Hawthorne, *Dosimetry Methods for Fuels, Cladding and Structural Materials*, Proceedings of the Third ASTM-EURATOM Symposium on Reactor Dosimetry, Vol. 1, p. 108
- Orientation Relationships for Twinned Massive α Precipitates in Cu-Zn and Ag-Zn**, by J.D. Ayers, *Acta Metall.* 28:1513
- † **Particulate-TiC-Hardened Steel Surfaces by Laser Melt Injection**, by J.D. Ayers and T.R. Tucker, *Thin Solid Films* 73:201
- Pulsed CO₂ Laser Interaction with a Metal Surface at Oblique Incidence**, by J.A. McKay, T.L. Cronburg,* J.E. Eninger,* J.T. Schriempf, and J.A. Woodroffe,* *Appl. Phys. Lett.* 36:125
- Surface Alloying Using High-Power Continuous Lasers**, by P.G. Moore and L.S. Weinman,* *Laser Applications in Materials Processing*, SPIE, Bellingham, Wash., Vol. 198, p. 120
- Surface Hardness and Abrasive Wear Resistance of Nitrogen-Implanted Steels**, by R.N. Bolster and I.L. Singer, *Appl. Phys. Lett.* 36:208
- The Corrosion Behaviour and Rutherford Backscattering Analysis of Palladium-Implanted Titanium**, by G.K. Hubler and E. McCafferty, *Corros. Sci.* 20:103
- The Effect of Environment on the Creep Crack Growth Behavior of Several Structural Alloys**, by K. Sadananda and P. Shahinian, *Mater. Sci. Eng.* 43:159

NUCLEAR SCIENCE

- Steels and Welds Used for Water-Cooled Nuclear Reactor Vessels**, by L.E. Steele, *Proceedings of IAEA Technical Committee Meeting on Correlation Accuracy in Properties with Exposure Data*, International Atomic Energy Agency, p. 6

OCEAN SCIENCE AND TECHNOLOGY

- † **An Asymptotic Formulation for SAR Images of the Dynamical Ocean Surface**, by G.R. Valenzuela, *Radio Sci.* 15:105
- Characteristics of Surface Temperature Structure and Subsurface Mesoscale Features**, by J.P. Dugan, *Remote Sensing Environ.* 9:109
- Design Features and Test Results of an Unmanned Free Swimming Submersible**, by H.A. Johnson, *Oceans '80*, IEEE, New York, p. 304
- Forecast of Remote Underwater Sensing Technology**, by V.A. Del Grosso, P.B. Alers, and L.J. Nivert,* *Proceedings of the Marine Technology 80 Conference*, Marine Technology Society, Washington, D.C., p. 463
- Gulf Stream Ground Truth Project: Results of the NRL Airborne Sensors**, by C.R.

McClain,* D.T. Chen, and D.L. Hammond,
Ocean Eng. 7:55

In-Water Testing of an Autonomous Submersible, by H.A. Johnson, E.W. Carey, and E.C. Czul, *7th Annual Symposium, Association for Unmanned Vehicle Systems*, p. 44

Modeling of Large Gulf Stream Rings in the Northeast Sargasso Sea, by R.P. Mied and G.J. Lindemann, *Proceedings of the Marine Technology 80 Conference*, Marine Technology Society, Washington, D.C., p. 126

Motion Stabilization for Towed Oceanographic Sensors, by B.S. Okawa, T.P. Dugan, W.D. Morris, B.S. Stalcup, and E.E. Rudd, *Proceedings of the Marine Technology 80 Conference*, Marine Technology Society, Washington, D.C., p. 529

Ocean Wave — Radar Modulation Transfer Functions from the West Coast Experiment, by J.W. Wright, W.J. Plant, W.C. Keller, and W.L. Jones,* *J. Geophys. Res.* 85:4957

On Obtaining Maximum Performance from Liquid Surface Levitation Holography, by A.V. Clark, *Acoustic Imaging*, Vol. 8, *Ultrasonic Visualization and Characterization*, Plenum Press, New York, p. 417

On the Steady-State Energy Balance of Short Gravity Wave Systems, by W.J. Plant, *J. Phys. Oceanogr.* 10:1340

Phase Speeds of Upwind and Downwind Trailing Short Gravity Waves, by W.J. Plant and J.W. Wright, *J. Geophys. Res.* 85:3304

Remote Sensing of the Sea Surface Using One- and Two-Frequency Microwave Techniques, by W.J. Plant and D.L. Schuler, *Radio Sci.* 15:605

Surface Microlayer Samplers, by W.D. Garrett and R.A. Duce, *Air-Sea Interaction*, Plenum Publishing Corp., New York, p. 471

The Fraction of Vertical Isotherm Deflections Associated with Eddies: An Estimate from Multiship XBT Surveys, by W.J. Emery, C. Ebbesmeyer, and J.P. Dugan, *J. Phys. Oceanogr.* 10:885

Theory of Scattering from Multilayered Bodies of Arbitrary Shape, by J.A. DeSanto, *J. Wave Motion* 2:63

OPTICAL SCIENCES

AIDER (Angle-of-Incidence Derivative Ellipsometry and Reflectometry)—Implementation and Application, by V.M. Bermudez,

Surf. Sci. 94:29

An 0.8 Meter Infrared Tracking Optical System Design, by R.F. Horton, *1980 International Lens Design Conference*, Society of Photo-Optical Instrumentation Engineers (SPIE), Bellingham, Wash., Vol. 237, p. 412

An RF Field Strength Measurement System Using an Integrated Optical Linear Modulator, by H.J. Bassen,* C.H. Bulmer, and W.K. Burns, *1980 IEEE MTT-S International Microwave Symposium Digest*, IEEE, New York, p. 317

Analysis of the Changes in Efficiency Across the Ruled Area of a Concave Diffraction Grating, by M. Neviere* and W.R. Hunter, *Appl. Opt.* 19:2059

Application of Advanced Light Scattering Techniques to the Study of Polymer Properties, by J.M. Schnur, P. Schoen, and S.L. Wunder, *Fundamentals of Tribology, Proceedings of the International Conference*, MIT Press, Cambridge, Mass., p. 787

Applications of Digital Processing to Calibrated Infrared Imagery, by T.H. May, G.L. Stamm, and T.A. Blodgett, *Infrared Systems*, SPIE, Bellingham, Wash., Vol. 256, p. 55

Applications of Ion Implantation to Integrated Optical Spectrum Analyzers, by W.K. Burns, J. Comas, and R.P. Moeller, *Opt. Lett.* 5:45

Applied Optics and Optical Engineering, by W.R. Hunter, *Appl. Opt.* 19:227

Calibration and Testing of Optical Single-Particle-Size Spectrometers with Monofilament Fibers as Substitute Particles, by R.K. Jeck, *Appl. Opt.* 19:657

Compositional Effects on the Radiation Response of Ge-Doped Silica-Core Optical Fiber Waveguides, by E.J. Friebele, P.C. Schultz, and M.E. Gingerich, *Appl. Opt.* 19:2910

Controlled Fabrication of Multilayer Soft X-Ray Mirrors, by E. Spiller,* A. Segmuller,* J.C. Rife, and R.P. Haelbich,* *Appl. Phys. Lett.* 31:1048

Correction to "Approximate Calculation of Leaky-Mode Loss Coefficients for Ti-Diffused LiNbO₃ Waveguides", by W.K. Burns, A.F. Milton, and S.K. Sheem, *IEEE J. Quantum Electron.* QE-16:685

Diffraction Gratings for the Vacuum Ultraviolet Spectral Region, by W.R. Hunter, *Nucl. Instrum. Methods* 172:259

Dual-Input Fiber-Optic Gyroscope, by S.C.

- Rashleigh and W.K. Burns, *Opt. Lett.* 5:482
- Effect of Irradiation on Evaporated ZnS Films**, by G. Hass,* J.B. Heaney,* W.R. Hunter, and D.W. Angel, *Appl. Opt.* 19:2480
- Electroluminescence**, by M.N. Kabler, *Encyclopedia of Physics*, Addison-Wesley, Reading, Mass., p. 227
- Elimination of Drift in a Single-Mode Optical Fiber Interferometer Using a Piezoelectrically Stretched Coiled Fiber**, by D.A. Jackson, R. Priest, A. Dandridge, and A.B. Tveten, *Appl. Opt.* 19:2926
- Extreme Ultraviolet Picosecond Pulses**, by J. Reintjes, *Philos. Trans. R. Soc. London* A298:273
- Fiber Optical Gyroscope with (3 × 3) Directional Coupler**, by S.K. Sheem, *Appl. Phys. Lett.* 37:869
- Fiber Transmission Losses in High-Radiation Fields**, by G.H. Sigel, *Proc. IEEE* 68:1236
- Four Definitions for the Term Emittance**, by W.H. Carter, *Appl. Opt.* 19:3419
- Frequency Mixing in the Extreme Ultraviolet**, by J. Reintjes, *Appl. Opt.* 19:3889
- Generation of Coherent Tunable VUV Radiation near the Ly- β Transition of Atomic Hydrogen**, by J. Reintjes, *Opt. Lett.* 5:342
- High Birefringence in Tension-Coiled Single-Mode Fibers**, by S.C. Rashleigh and U. Ulrich,* *Opt. Lett.* 5:354
- High-Efficiency Flip-Chip Coupling between Single-Mode Fibers and LiNbO₃ Channel Waveguides**, by C.H. Bulmer, W.K. Burns, R.P. Moeller, and S.K. Sheem, *Appl. Phys. Lett.* 37:351
- High Efficiency Single-Mode Fiber/Channel Waveguide Flip-Chip Coupling**, by S.K. Sheem, C.H. Bulmer, W.K. Burns, and R.P. Moeller, *Topical Meeting on Integrated and Guided Wave Optics*, IEEE, New York, p. MA 4-1
- Influence of Broadband Photocoupling on K-Shell Excitation in Aluminum**, by K.G. Whitney, J. Davis, and J.P. Apruzese,* *Phys. Rev. A* 22:2196
- Infrared Surveillance. 1: Statistical Model**, by R.A. Steinberg, *Appl. Opt.* 19:77
- Infrared Surveillance. 2: Continuous-Time Signal Processors**, by R.A. Steinberg, *Appl. Opt.* 19:1673
- Instability of Single-Mode Communication Systems Due to Interference and Polarization Effects**, by S.K. Sheem and T.G. Giallorenzi, *Topical Meeting on Integrated and Guided Wave Optics*, IEEE, New York, p. MA 3-1
- Laser Noise in Fiber-Optic Interferometer Systems**, by A. Dandridge, A.B. Tveten, R.O. Miles, and T.G. Giallorenzi, *Appl. Phys. Lett.* 37:526
- Linear Interferometric Modulation for Electromagnetic Field Detection**, by C.H. Bulmer, W.K. Burns, and R.P. Moeller, *Topical Meeting on Integrated and Guided Wave Optics*, IEEE, New York, p. TuC 4-1
- Linear Interferometric Waveguide Modulator for Electromagnetic-Field Detection**, by C.H. Bulmer, W.K. Burns, and R.P. Moeller, *Opt. Lett.* 5:176
- Local Instances of Good Seeing**, by H.H. Szu, J.A. Blodgett, and L. Sica, *Opt. Commun.* 35:317
- Measurement of Small Phase Shifts Using a Single-Mode Optical-Fiber Interferometer**, by D.A. Jackson,* A. Dandridge, and S.K. Sheem, *Opt. Lett.* 5:139
- Measuring Absorption Coefficients in Crystal-line Materials**, by P.H. Klein, *Physical Properties of Materials*, SPIE, Bellingham, Wash., Vol. 204, p. 77
- MO Imagery Techniques Using Arrays of Large Aperture Telescopes**, by H.H. Szu, *Opt. Commun.* 32:229
- Optical Control of Millimeter-Wave Propagation in Dielectric Waveguides**, by C.H. Lee,* A.P. DeFonzo, and P.S. Mak,* *IEEE J. Quantum Electron.* QE-16:277
- †Optical Fibre Magnetic Field Sensors**, by A. Dandridge,* A.B. Tveten,* G.H. Sigel, E.J. West, and T.G. Giallorenzi, *Electron. Lett.* 16:408
- Optical Heating in Semiconductors**, by J.R. Meyer, F.J. Bartoli, and M.R. Kruer, *Phys. Rev. B* 21:1559
- Optical Heating in Semiconductors: Laser Damage in Ge, Si, InSb, and GaAs**, by J.R. Meyer, M.R. Kruer, and F.J. Bartoli, *J. Appl. Phys.* 51:5513
- Optical Waveguide Channel Branches in Ti-Diffused LiNbO₃**, by W.K. Burns, C.H. Bulmer, R.P. Moeller, and H. Yajima,* *Topical Meeting on Integrated and Guided Wave Optics*, IEEE, New York, p. TuE 5-1, and *Appl. Opt.* 19:2890
- Photodichroics as Active Devices for Optical Correlation**, by W.C. Collins, *Active Optical Devices*, SPIE, Bellingham, Wash., Vol. 202, p. 132
- Photographic Image Enhancement Using Pho-**

- ton Induced Fission of Uranium**, by K.M. Murray, *Photogr. Sci. Eng.* 24:166
- Preparation and Testing of Reflectance Coatings for Diffraction Gratings in the Extreme Ultraviolet**, by W.R. Hunter and G. Hass,* *Phys. Thin Films* 11:1
- Properties of Electromagnetic Radiation from a Partially Correlated Current Distribution**, by W.H. Carter, *J. Opt. Soc. Am.* 70:1067
- Radiation Induced Optical Absorption Bands in Low Loss Optical Fiber Waveguides**, by E.J. Friebele and M.E. Gingerich, *J. Non-Cryst. Solids* 38-39:245
- Reflectance, Fluorescence and Photoelectron Spectroscopy of CaF_2 in the 10 to 100 eV Range**, by R.T. Williams, D.J. Nagel, and M.N. Kabler, *J. Phys. Colloque* C6:439
- Replication of Wolter Lens Components**, by W.R. Hunter, D.J. Michels, C.M. Fleetwood,* J.D. Mangus,* and B.W. Bach,* *Appl. Opt.* 19:2128
- Single-Mode Fiber Wavelength Multiplexer**, by S.K. Sheem and R.P. Moeller, *J. Appl. Phys.* 51:4050
- 6^1S_0 - 6^3P_0 Transition in ^{199}Hg : Determination of the A Coefficient and Self-Pressure Broadening**, by B.L. Wexler, N. Djeu, and B.E. Wilcomb, *J. Opt. Soc. Am.* 70:863
- Spectra and Redox Photochemistry of Crown Ether Complexes of Lanthanides**, by T. Donohue, *The Rare Earths in Modern Science and Technology*, Plenum Publishing Corp., New York, Vol. 2, p. 105
- Spot Size and Divergence for Hermite Gaussian Beams of any Order**, by W.H. Carter, *Appl. Opt.* 19:1027
- The Range of Speckle Metrology**, by V.J. Parks, *Exp. Mech.* 20:181
- Thermally Induced Optical Phase Effects in Fiber Optic Sensors**, by R. Hughes and R. Priest, *Appl. Opt.* 19:1477
- Transient Absorption in Pure and Mixed Rare Gases in the 350 nm Region**, by L.F. Champagne, R.S.F. Chang, L.J. Palumbo, and T.G. Finn,* *Lasers '79*, STS Press, McLean, Va., p. 49
- UV Absorption Cross Section and Fluorescence Efficiency of HgBr_2** , by B.E. Wilcomb, R. Barnham, and N. Djeu, *Chem. Phys. Lett.* 75:239
- VUV Population Inversions in Laser-Produced Plasmas**, by R.H. Dixon, R.L. Denningham, R.C. Elton, and J.F. Seely, *6th International Conference on Vacuum Ultraviolet Radiation Physics, Extended Abstracts*, University of Virginia, Charlottesville, Va., Vol. III, Paper III-58
- Wavelength Monitoring of Single-Mode Diode Laser Using Guided-Wave Interferometer**, by S.K. Sheem and R.P. Moeller, *Opt. Lett.* 5:179

PLASMA PHYSICS

- A Coherent Nonlinear Theory of Auroral Kilometric Radiation I. Steady State Model**, by C.L. Grabbe,* K. Papadopoulos, and P.J. Palmadesso, *J. Geophys. Res.* 85:3337
- A Shear Stabilized Cylindrically Symmetric Mirror Plasma**, by W.M. Manheimer, *Phys. Fluids* 23:1067
- Amplification of Ion Cyclotron Waves via High Frequency Electron Plasma Wave Turbulence**, by J.D. Huba,* P.K. Chaturvedi,* and K. Papadopoulos, *Phys. Fluids* 23:1479
- Atomic Data and Level Populations of Highly Ionized Ti for Tokamak Plasmas**, by A.K. Bhatia,* U. Feldman, and G.A. Doschek, *J. Appl. Phys.* 51:1464
- Computer Simulation of Gradient Drift Instability Processes in Operation Avesfria**, by B.E. McDonald, M.J. Kirkinen, S.L. Ossakow, and S.T. Zalisak, *J. Geophys. Res.* 85:2143
- Dielectronic Recombination Rates, Ionization Equilibrium, and Radiative Emission Rates for Calcium and Nickel Ions in Low-Density High-Temperature Plasmas**, by V.I. Jacobs, J. Davis, J.E. Rogerson, M. Blaha,* J. Cain,* and M. Davis,* *Astrophys. J.* 239:119
- Direct Solution of the Equation of Transfer Using Frequency- and Angle-Averaged Photon Escape Probabilities, with Application to a Multistage, Multilevel Aluminum Plasma**, by J.P. Apruzese,* J. Davis, D. Duston,* and K.G. Whitney, *J. Quant. Spectrosc. Radiat. Transfer* 23:479
- Early Expansion in Exploding Multiple Wire Arrays**, by H.W. Bloomberg,* M. Lampe, and D.G. Colombant, *J. Appl. Phys.* 51:5277
- Electron Beam Channeling**, by R.F. Fernsler and J.R. Greig, *McGraw-Hill Yearbook of Science and Technology*, McGraw-Hill, New York, p. 167
- Erratum: Radial Expansion of a Self-Pinched Beam with Distributed Energy**, by M.I.

- Haftel, J.B. Aviles, and M. Lampe, *Phys. Fluids* 23:1069
- Heating at the Electron Cyclotron Frequency in the ISX-B Tokamak**, by R.M. Gilgenbach, O.G. Eldridge,* A.C. England,* K.E. Hackett,* H.C. Howe,* A.G. Kuichar,* R. Lacey, E. Lazarus, C.M. Loring,* M. Murakami,* M.E. Read, and B. Wilgen, *Phys. Rev. Lett.* 44:647
- High-Power Ion Beam Generation with an Inverse Reflex Tetrode**, by J.A. Pasour, J. Golden, C.A. Kapetanakis, and R.A. Mahaffey,* *Appl. Phys. Lett.* 36:646
- Hydrodynamic Response of Plasma Channels to Propagating Ion Beams**, by D.G. Colombant, S.A. Goldstein, and D. Mosher, *Phys. Rev. Lett.* 45:1253
- † **Interaction of Laser-Induced Ionization with Electric Fields**, by R. Fernsler,* R. Greig, J. Halle,* R. Pechacek, M. Raleigh, and I.M. Vitkovitsky, *13th Fluid and Plasma Dynamics Conference*, American Institute of Aeronautics and Astronautics, p. 1
- Line Emission from Hot, Dense, Aluminum Plasmas**, by D. Duston* and J. Davis, *Phys. Rev. A* 21:1664
- Lower-Hybrid-Drift Instability in Field Reversed Plasmas**, by J.D. Huba,* J.F. Drake, and N.T. Gladd, *Phys. Fluids* 23:552
- Measurement of the Plasma Width in a Ring Cusp**, by R.E. Pechacek, A.W. DeSilva,* J.R. Greig, D.W. Koopman, and M. Raleigh, *Phys. Rev. Lett.* 45:256
- Methods of Efficiency Enhancement and Scaling for the Gyrotron Oscillator**, by K.R. Chu, A.K. Ganguly, and M.E. Read, *IEEE Trans. Microwave Theory Tech.* MTT-28:318
- Modeling of Linus-Type Stabilized Liner Implosions**, by A.L. Cooper, T.M. Pierre, P.J. Turchi, J.P. Boris, and R.L. Burton, *Mega-gauss Physics and Technology*, Plenum Press, New York, p. 447
- † **Multiple Ionization and X-Ray Emission Accompanying the Cascade Decay of Inner-Shell Vacancies in Fe**, by V.I. Jacobs, J.W. Cooper, J. Davis, and B.F. Rozsnyai,* *Phys. Rev. A* 21:1917
- Nonlinear Equatorial Spread F: Spatially Large Bubbles Resulting from Large Horizontal Scale Initial Perturbations**, by S.T. Zalesak and S.L. Ossakow, *J. Geophys. Res.* 85:2131
- Nonlinear Evolution of Diffuse Auroral F Region Ionospheric Irregularities**, by M.J. Keskinen,* B.E. McDonald, and S.L. Ossakow, *Geophys. Res. Lett.* 7:573
- Numerical Study of Optical Ray Retracing in Laser-Plasma Backscatter**, by R.H. Lehmberg and K.A. Holder, *Lasers '79*, STS Press, McLean, Va., p. 466, and *Phys. Rev. A* 22:2156
- Oscillating Two-Stream and Parametric Decay Instabilities in a Weakly Magnetized Plasma**, by H.P. Freund* and K. Papadopoulos, *Phys. Fluids* 23:139
- Preliminary Numerical Study of the Outer Scale Size of Ionospheric Plasma Cloud Striations**, by M.J. Keskinen, B.E. McDonald, and S.L. Ossakow, *J. Geophys. Res.* 85:2349
- Preliminary Report of Numerical Simulations of Intermediate Wavelength Collisional Rayleigh-Taylor Instability in Equatorial Spread F**, by M.J. Keskinen, P.K. Chaturvedi,* and S.L. Ossakow, *J. Geophys. Res.* 85:1775
- Preliminary Report of Numerical Simulations of Intermediate Wavelength $E \times B$ Gradient Drift Instability in Ionospheric Plasma Clouds**, by M.J. Keskinen, P.K. Chaturvedi, and S.L. Ossakow, *J. Geophys. Res.* 85:3485
- Propagation of Intense Ion Beams in Straight and Tapered z-Discharge Plasma Channels**, by P.F. Ottinger,* P.K. Chaturvedi, S.A. Goldstein,* M.J. Keskinen, D. Mosher, and S.L. Ossakow, *Phys. Fluids* 23:909
- Radiation from Localized Langmuir Oscillation in a Uniformly Magnetized Plasma**, by H.P. Freund* and K. Papadopoulos, *Phys. Fluids* 23:1546
- Repetitive Electron-Beam Controlled Switching**, by R.F. Fernsler, D. Conte, and I.M. Vitkovitsky, *IEEE Trans. Plasma Sci.* PS-8:176
- Reply to the Comments of M. Bornatici and F. Engelmann**, by T.M. Antonsen and W.M. Manheimer, *Phys. Fluids* 23:660
- Self-Absorption of Heliumlike Satellite Lines in High-Density Fusion Plasmas**, by D. Duston* and J. Davis, *Phys. Rev. A* 21:932
- Space-Resolved Extreme Ultraviolet Emission from Laser-Produced Plasmas**, by N.A. Ebrahim,* G.A. Doschek, U. Feldman, and M.C. Richardson,* *J. Appl. Phys.* 51:182
- Spatial and Temporal Coherence of a 35GHz Gyromotion Using the TE₀₁ Circular Mode**, by M.E. Read, R.M. Gilgenbach, R.F. Lucey, K.R. Chu, A.T. Drobot, and V.L. Granatstein, *IEEE Trans. Microwave Theory Tech.* MTT-28:875
- Spectroscopy and Atomic Physics of Highly Ion-**

- ized Cr, Fe, and Ni from Tokamak Plasmas, by U. Feldman, G.A. Doschek, C.C. Cheng,* and A.K. Bhatia,* *J. Appl. Phys.* 51:190
- Spontaneous Emission of Radiation Materials from Localized Langmuir Perturbation, by H.P. Freund* and K. Papadopoulos, *Phys. Fluids* 23:732
- Steady-State Magnetic Diffusion from Resistive Interchange Modes in a Plasma, by W.M. Manheimer, *Phys. Rev. Lett.* 45:1249
- Strongly Turbulent Stabilization of Electron Beam - Plasma Interactions, by H.P. Freund,* I. Haber, P. Palmadesso, and K. Papadopoulos, *Phys. Fluids* 23:518
- Systematic Trends in the Radiative Emission Rates for Low- and Medium-Z Elements in High-Temperature Plasmas, by J. Davis and V.L. Jacobs, *J. Quant. Spectrosc. Radiat. Transfer* 24:283
- The Nonlinear Theory of Efficiency Enhancement in the Electron Cyclotron Maser (Gyrotron), by P. Sprangle, *J. Appl. Phys.* 51:3001
- Theory and Simulation of the Gyrotron Traveling Wave Amplifier Operating at Cyclotron Harmonics, by K.R. Chu, A.T. Drobot, P. Sprangle, and H.H. Szu, *IEEE Trans. Microwave Theory Tech.* MTT-28:313
- Theory of Electron Cyclotron Resonance Heating of Tokamak Plasmas, by E. Ott, K.R. Chu, and B. Hui, *Phys. Fluids* 23:1031
- Theory of Second Harmonic Electron Cyclotron Resonance Heating of Tokamak Plasma, by B. Hui, T. Antonsan,* K.R. Chu, and E. Ott, *Phys. Fluids* 23:822
- Transient Magnetic Field Reversal with a Rotating Proton Laser, by C.A. Kapetanakis, J. Golden, R.A. Mahaffey,* S.J. Marshi,* and J.A. Pasour, *Phys. Rev. Lett.* 44:1218
- X-UV Spectra from Z-Pinched Plasma Sources, by P.G. Burkhalter and R.D. Bleach, *6th International Conference on Vacuum Ultraviolet Radiation Physics, Extended Abstracts*, University of Virginia, Charlottesville, Vol. II, Paper II-43
- Rain, by W.B. Gordon, *19th Conference on Radar Meteorology*, American Meteorological Society, Boston, Mass., p. 704
- Aspects of Parallel-Polarized and Cross-Polarized Radar Returns from a Rough Sea Surface, by H. Raemer and D.D. Preis,* *IEEE Trans. Electromagn. Compat. EMC-22:29*
- Comments on "Millimeter-Wave Missile Seeker Aimpoint Wander Phenomenon," by D.D. Howard, *J. Guid. Control* 3:284
- Discriminants for Assigning Passive Bearing Observations to Radar Targets, by J.O. Coleman, *IEEE International Radar Conference*, IEEE, New York, p. 361
- Experimental Study and Theoretical Model of High-Resolution Radar Backscatter from the Sea, by B.L. Lewis and I.D. Olin, *Radio Sci.* 15:815
- Introduction to Radar Systems, by M.I. Skolnik, McGraw-Hill, New York
- Mirror Scan Antenna Technology, by B.L. Lewis and J.P. Shelton, *IEEE International Radar Conference*, IEEE, New York, p. 279
- Multiple Site Radar Tracking System, by B.H. Cantrell and A. Grindlay, *IEEE International Radar Conference*, IEEE, New York, p. 388
- On a Synthesis of Planar Arrays Based on Convolution Technique, by S.R. Laxpati, *Electron. Lett.* 16:918
- Remote Sensing of the Sea Surface Using One- and Two-Frequency Microwave Techniques, by W.J. Plant and D.L. Schuler, *Radio Sci.* 15:605
- Solid-State Radar Switchboard, by P. Thiebaud and D.C. Cross, *Mil. Electron./Countermeas.* 6(7):44
- †Spectral Analysis and Adaptive Array Super-resolution Techniques, by W.F. Gabriel, *Proc. IEEE* 68:654
- Superresolution of Coherent Sources by Adaptive Array Techniques, by W.F. Gabriel, *IEEE International Radar Conference*, IEEE, New York, p. 182
- Three-Dimensional Bootlace Lenses, by J.P. Shelton, *International Symposium Digest, Antennas and Propagation*, IEEE, New York, Vol. II, p. 568
- Topics in Radar Scattering Theory, by W.S. Ament, *Mathematical Methods and Applications of Scattering Theory*, Springer-Verlag, New York, p. 53

RADAR

- A Critique of the Kerr-Siegert-Goldstein Theory of Radar Backscattering from Clouds and

RADIATION TECHNOLOGY

- Comparison of X-Ray Sources for Exposure of Photoresists**, by D.J. Nagel, *Ann. N.Y. Acad. Sci.* 342:235
- Dose and Dose Rate Dependence of 8080A Microprocessor Failure**, by C.M. Dozier, D.B. Brown, and J.W. Sandelin, *IEEE Trans. Nucl. Sci.* NS-27:1299
- Effects of Surface Roughness on Backscattering Spectra**, by A.R. Knudson, *Nucl. Instrum. Methods* 168:163
- Fading of Unannealed LiF (TLD-600) for Thermal Neutrons and γ Rays**, by T.L. Johnson and R.B. Luersen, *Health Physics* 38:853
- Magnetic Electron Scattering from Deuterium at Low-Momentum Transfer**, by E.C. Jones, W.L. Bendel, L.W. Fagg, and R.A. Lindgren, *Phys. Rev. C* 21:1162
- Mechanism of Stimulated Radiation by Charged Particles**, by W.W. Zachary, *Phys. Rev. D* 20:3412
- New Analytical Calculation of Displacement Damage**, by G.P. Mueller, *Nucl. Instrum. Methods* 170:389
- Optical Effects Resulting from Deep Implants of Silicon with Nitrogen and Phosphorus**, by G.K. Hubler, C.A. Carosella, P.R. Malmberg, C.N. Phillipi, W.G. Spitzer,* T.P. Smith, and C.N. Waddell,* *Radiat. Eff.* 48:81
- Pulsed Electron Beam Irradiation of Ion-Implanted Copper Single Crystals**, by J.K. Hirvonen, A. Greenwald,* R. Little,* and J. M. Poate,* *Appl. Phys. Lett.* 36:564
- Simulations of Cascade Damage in Silicon**, by G.P. Mueller and C.S. Guenzer, *IEEE Trans. Nucl. Sci.* NS-27:1474
- Single Event Upsets in RAMS Induced by Protons at 4.2 GeV and Protons and Neutrons Below 100 MeV**, by C.S. Guenzer, R.G. Allas, A.B. Campbell, J.M. Kidd, E.L. Petersen, N. Seeman, and E.A. Wolicke, *IEEE Trans. Nucl. Sci.* NS-27:1485
- Spectra of Mo XIII-XVIII from a Laser-Produced Plasma and a Low-Inductance Vacuum Spark**, by P. G. Burkhalter, R. C. Cowan,* and J. Reader,* *J. Opt. Soc. Am.* 70:912
- Stimulated Electromagnetic Shock Radiation (SESR) when the Angle Between the Electron Velocity and the External Field Direction Is Arbitrary**, by W.W. Zachary, *Free-Electron Generators of Coherent Radiation*,

Addison-Wesley, Reading, Mass., p. 779

Use of Non-Coulomb H Ion Backscattering to Characterize Thick Anodized Aluminum Films, by C.R. Gossett, *Nucl. Instrum. Methods* 168:151

X-UV Spectra from Kr XI-XIV, by R.D. Bleach, *J. Opt. Soc. Am.* 70:861

SOLID STATE

- A Possible Mechanism of Superconductivity in Metal-Semiconductor Eutectic Alloys**, by C.S. Ting, D.N. Talwar,* and K.L. Ngai, *Phys. Rev. Lett.* 45:1213
- Ab Initio Bandstructure of Lead**, by A.D. Zdetsis,* E.N. Economou, and D.A. Papaconstantopoulos, *J. Phys. F* 10:1149
- Absorption Time by a Random Trap Distribution**, by H.B. Rosenstock, *J. Math. Phys.* 21:1643
- Acoustic Anomalies in Amorphous Thin Films of Si and SiO₂**, by M. Von Haumer,*, S. Hunklinger,* and U. Strom, *Phys. Rev. Lett.* 44:84
- Bonding-Failure Analysis with Electron Beam and Nuclear Scattering Techniques**, by A. Christou, H.M. Day, and G. Nelson, *IEEE Trans. Reliab.* R-29:250
- Cathodoluminescence of SiO₂ Films**, by S.W. McKnight and E.D. Palik, *J. Non-Cryst. Solids* 40:595
- Cathodoluminescence Studies of Anodic Oxides on GaAs**, by S.W. McKnight, T.N. Bhar,* and E.D. Palik, *J. Vac. Sci. Technol.* 17:967
- Channeling and Random Equivalent Depth Distributions of 150keV Li, Be, and B Implanted in Si**, by J. Comas and R.G. Wilson, *J. Appl. Phys.* 51:3697
- Chemical Vapour Deposited SiO₂-InP Interface**, by G.W. Wilmsen,* J.F. Wager,* and J.E. Stannard, *Institute of Physics Conference Series No. 50*, Institute of Physics, London, Vol. 4, p. 251
- Close-Contact Annealing of Ion-Implanted GaAs and InP**, by B. Molnar, *Appl. Phys. Lett.* 36:927
- Cyclotron Resonance of Electron Inversion Layers in Si (001) Metal-Oxide-Semiconductor Field-Effect Transistors (MOSFETS)**, by R.J. Wagner, T.A. Kennedy, B.D. McCombe, and D.C. Tsui,* *Phys. Rev. B* 22:945
- Deposition of Thin Refractory MIS Structures: InP**, by A. Christou and W.T. Anderson, *J. Electron. Mater.* 9:585

Diamond Anvil Techniques for Structural and Electrical/Magnetic Measurements at Low Temperature, by I.L. Spain,* F. Rachford,* and E. F. Skelton, *High Pressure Science and Technology*, Pergamon Press, New York, Vol. 1, p. 150

Dielectric Constant of Semi-Insulating Gallium Arsenide, by R.E. Neidert, *Electron. Lett.* 16:244

Doping Effect of Annealed GaAs Surfaces on Vacuum-Epitaxy-Ge/<100> GaAs, by W.F. Tseng, A. Christou, J.E. Davey, and B.R. Wilkins, *Appl. Phys. Lett.* 36:435

Effect of a Varying Density of States on Superconductivity, by W.E. Pickett, *Phys. Rev. B* 21:3897

Effect of Electron-Hole Scattering on Ambipolar Diffusion in Semiconductors, by J.R. Meyer, *Phys. Rev. B* 21:1554

Effects of Deposition Parameters on the Properties of Superconducting rf Reactively Sputtered NbN Films, by S.A. Wolf, E.J. Cukauskas, T.L. Francavilla, I.L. Singer, and E.F. Skelton, *J. Vac. Sci. Technol.* 17:411

Effects of Formation Temperature on the Superconducting Properties of V₃Ga Wires, by D.G. Howe and T.L. Francavilla, *Filamentary A15 Superconductors*, Plenum Publishing Corp., New York, p. 103

Electron-Transfer Model for E¹-Center Optical Absorption in SiO₂, by D.L. Griscom and W.B. Fowler, *The Physics of MOS Insulators, Proceedings of the International Conference*, Pergamon Press, New York, p. 97

ESR Study of Cr³ in Naβ-Alumina, by R. Hundhausen,* H. Sixl,* and U. Strom, *Z. Phys. B* 38:299

Evidence for Exciton Binding at Ni Impurity Sites in ZnSe, by S.G. Bishop, D.J. Robbins,* and P.J. Dean,* *Solid State Commun.* 33:119

† **Exchange and Crystal Field Excitations in Rare-Earth Iron and Rare-Earth Cobalt Laves Phase Compounds**, by N.C. Koon and J.J. Rhyne,* *Crystalline Electric Field and Structural Effects in f-Electron Systems*, Plenum Publishing Corp., New York, p. 125

Exchange-Correlation Effects in Silicon Inversion Layers: Valley Occupancy Phase Transitions, by T. Cole, B.D. McCombe, and W.L. Bloss,* *J. Phys. Soc. Japan* 49(Suppl. A):963

Fluctuations and the Determination of Critical Currents in Granular Microbridges, by T.F.

Refai,* R.A. Peters,* S.A. Wolf, and F.J. Rachford, *Inhomogeneous Superconductors-1979*, AIP Conference Proceedings No. 58, American Institute of Physics, New York, p. 325

GaAs:Cr³⁺ (3d³) — An Orthorhombic Jahn-Teller Center with a Stress-Dependent Reorientation Rate, by G.H. Stauss and J.J. Krebs, *Phys. Rev. B* 22:2050

GaAs FET Failure Mechanisms due to High Humidity and Ionic Contamination, by W.T. Anderson and A. Christou, *IEEE Trans. Reliab. R*-29:222

GaAs Mixer Diode Burnoff Mechanisms at 36-94 GHz, by A. Christou and Y. Anand,* *Reliability Physics 1980*, IEEE, New York, p. 140

Gallium Arsenide Transferred-Electron Devices by Low-Level Ion Implantation, by W.T. Anderson, M.L. Bark, H.B. Dietrich, S.H. Lee, and E.M. Swiggard, *J. Appl. Phys.* 51:3175

Hall-Effect Omission, by G.C. Carter,* A.C. Ehrlich, and A.I. Schindler, *Phys. Today* 33(1):107

Hydrogen-Associated Disorder Modes in Amorphous Si-H Films, by W.E. Carlos and P.C. Taylor, *Phys. Rev. Lett.* 44:358

Inhomogeneous Superconductors-1979, edited by D.U. Gubser, T.L. Francavilla, S.A. Wolf, and J.R. Leibowitz,* AIP Conference Proceedings No. 58, American Institute Of Physics, New York

Intersubband Spectroscopy of Inversion Layers in the Principal Surfaces of Silicon: Many-Body and "Impurity" Effects, by B.D. McCombe and T.L. Cole, *Surf. Sci.* 98:469

Investigations of the Pressure Dependence of Structural, Chemical, Electrical, and Magnetic Properties of Cuprous Chloride (CuCl), by E.F. Skelton, A.W. Webb, F.J. Rachford, and P.C. Taylor, *Phys. Rev. B* 21:5289

† **Josephson Behavior in Granular NbN Weak Links**, by J.H. Claassen, *Appl. Phys. Lett.* 36:771

Josephson Effects in Granular NbN Microbridges, by E.J. Cukauskas, J.H. Claassen, M. Nisenoff, C.H. Galfo,* R.L. Steiner,* and B.S. Deaver,* *Inhomogeneous Superconductors-79*, AIP Conference Proceedings No. 58, American Institute of Physics, New York, p. 233

LEED Study of the Stepped Surface of Vicinal

- Si(100), by R. Kaplan, *Surf. Sci.* 93:145
- Magnetic Anisotropy and Spin Reorientation in $\text{Ho}_x\text{Tb}_{1-x}\text{Fe}_2$, $\text{Dy}_x\text{Tb}_{1-x}\text{Fe}_2$, and $\text{Ho}_x\text{Tb}_{1-x-y}\text{Fe}_2$** , by N.C. Koon and C.M. Williams,* *Crystalline Electron Field and Structural Effects in f-Electron Systems*, Plenum Publishing Corp., New York, p. 75
- Magnetic Excitations in ErCo_2** , by N.C. Koon, B.N. Das, and J.J. Rhyne,* *NBS Reactor: Summary of Activities, July 1978 to June 1979*, NBS TN 1117, National Bureau of Standards, Washington, D.C., p. 61
- Magnetic Excitations in TbFe_2** , by J.J. Rhyne,* H.A. Alperin,* and N.C. Koon, *NBS Reactor: Summary of Activities, July 1978 to June 1979*, NBS TN 1117, National Bureau of Standards, Washington, D.C., p. 66
- Magneto-Optical Studies of PbTe in the Far Infrared**, by S.W. McKnight and H.D. Drew,* *Phys. Rev. B* 21:3447
- Magnetostrictive Effects in Evaporated Nickel Films**, by C. Vittoria and P. Lubitz, *J. Appl. Phys.* 51:1388
- Material Reactions and Barrier Height Variations in Sintered Al-InP Schottky Diodes**, by A. Christou and W.T. Anderson, *Solid-State Electron.* 22:857
- Measurements of the Far Infrared Optical Constants of Disordered Solids**, by U. Strom and P.C. Taylor, NBS Special Publication 574, G.P.O., Washington, D.C., p. 32
- Metal Insulated Semiconductor (MIS) Radiation Effects Considerations for Infrared Focal-Plane Arrays**, by J.M. Killiany and N.S. Saks, *Advances in Focal Plane Technology*, SPIE, Bellingham, Wash., Vol. 217, p. 192
- MNOS Traps and Tailored Trap Distribution Gate Dielectric MNOS**, by K.L. Ngai and Y. Hsia, *Japan. J. Appl. Phys.* 19:245
- † **Nature of Melting and Superionicity in Alkali and Alkaline-Earth Halides**, by L.L. Boyer, *Phys. Rev. Lett.* 45:1858
- New EPR Data and Photoinduced Changes in GaAs: Cr. Reinterpretation of the "Second-Acceptor" State as Cr^{4+}** , by G.H. Stauss, J.J. Krebs, S.H. Lee, and E.M. Swiggard, *Phys. Rev. B* 22:3141
- New High-Energy Luminescence Bands from Co^{2+} in ZnSe**, by D.J. Robbins, P.J. Dean, J.L. Glasper,* and S.G. Bishop, *Solid State Commun.* 36:61
- Nuclear Quadrupole Resonance Probes of Structural and Photostructural Properties of Glassy As_2Se_3 , As_2S_3 and As_2O_3** , by P.C. Taylor, U. Strom, and D.J. Treacy,* *J. Phys. Soc. Japan* 49 (Suppl. A):1155
- On the Absence of Photodarkening in Pnictide Amorphous Semiconductors**, by E. Mytilineou,* P.C. Taylor, and E.A. Davis,* *Solid State Commun.* 35:497
- Optically Induced Transient Electron Paramagnetic Resonance Phenomena in GaAs:Cr**, by A.M. White,* J.J. Krebs, and G.H. Stauss, *J. Appl. Phys.* 51:419
- Photoluminescence and Optically Induced ESR in Pure and K-Doped Glassy Se**, by S.G. Bishop and P.C. Taylor, *J. Non-Cryst. Solids* 35-36:909
- Photoluminescence Excitation Spectroscopy of 3D Transition Metal Ions in GaP and ZnSe**, by S.G. Bishop, P.J. Dean,* P. Porteous*, and D.J. Robbins,* *J. Phys. C: Solid State Phys.* 13:1331
- Photoluminescence Studies of Deep Impurity States in Fe-Doped InP**, by S.G. Bishop, P.B. Klein, R.L. Henry, and B.D. McCombe, *Semi-Insulating III-V Materials*, Shiva Publishing, Kent, England, p. 161
- Photostructural Effects in Glassy As_2Se_3 and As_2S_3** , by D.J. Treacy,* P.B. Klein, T.P. Martin,* U. Strom, and P.C. Taylor, *J. Non-Cryst. Solids* 35-36:1035
- Platinum Hydride: A Possible High Temperature Superconductor**, by D.A. Papaconstantopoulos, *J. Less-Common Met.* 73:305
- Pulsed Magnetic Field Losses and Critical Current Densities Of V_3Ga and Nb_3Sn Multifilamentary Superconductors**, by K. Kwasnitza,* D. Salathe,* D.G. Howe,* and D.U. Gubser, *Cryogenics* 20:101
- Pulsed NMR Studies of Hydrogenated Amorphous Silicon (a-Si:H)**, by P.C. Taylor and W.T. Carlos, *J. Phys. Soc. Japan* 49 (Suppl. A):1193
- RPA Theory of Magnetic Excitation in Rare Earth-Transition Metal Compounds: Application of ErCo_2 and ErFe_2** , by N.C. Koon and J.J. Rhyne,* *J. Magn. Magn. Mater.* 15-18:349
- Semi-Empirical APW Calculations of the Band Structure of Silicon**, by D.A. Papaconstantopoulos and B.M. Klein, *Solid State Commun.* 34:311
- Slater-Koster Parametrization for Si and the Ideal-Vacancy Calculation**, by D.A. Papaconstantopoulos and E.N. Economou,* *Phys. Rev. B* 22:2903

- Spectroscopic Applications of Structures Produced by Orientation Dependent Etching**, by D.J. Nagel, K.E. Bean,* and R.K. Watts,* *Nucl. Instrum. Methods* 172:321
- Spin-Wave Widths in Antiferromagnets: RbMnF_3** , by T.L. Reinecke and R.B. Stinchcombe,* *Phys. Rev. B* 21:5198
- Stability of CuCl-II at Elevated Pressures and Reduced Temperatures**, by E.F. Skelton, F.J. Rachford, A.W. Webb, S.C. Yu,* and I.L. Spain,* *High Pressure Science and Technology*, B. Vodar and Ph. Marteau, eds., Pergamon Press, New York, Vol. 1, p. 400
- † **Submillimeter EPR Evidence for the As Antisite Defect in GaAs** , by R.J. Wagner, J.J. Krebs, G.H. Stauss, and A. White, *Solid State Commun.* 36:15
- Superconducting Properties and Structural Phase Transformation of Nb_2N Induced by C^+ - and N^- -Implantation**, by M.R. Skokan, E.F. Skelton, and E. Cukauskas, *J. Phys. Chem. Solids* 41:977
- Superconducting Transition Temperatures in Pseudobinary Al_5 Compounds**, by D.A. Papaconstantopoulos, L.L. Boyer, D.U. Gubser, and B.M. Klein, *Phys. Rev. B* 21:1326
- The Effects of Ion Implantation and Pulsed Electron Beam Anneal on Ge Films Grown Epitaxially on $\langle 100 \rangle$ GaAs** , by W. Tseng, W.T. Anderson, A. Christou, J. Davey, and H. Dietrich, *J. Electron. Mater.* 9:685
- Thermal Conversion of GaAs** , by P.B. Klein, P.E.R. Nordquist, and P.G. Siebenmann, *J. Appl. Phys.* 51:4861
- Torque Measurements in Single Crystal $\text{Dy}_x\text{Tb}_{x-1}\text{Fe}_2$ Compounds**, by C.M. Williams,* N.C. Koon, and B.N. Das, *J. Magn. Magn. Mater.* 15-18:553
- Treatise on Materials Science and Technology**, Vol.18, *Ion Implantation*, edited by J.K. Hirvonen, Academic Press, New York
- Unified Theory of $1/f$ Noise and Dielectric Response in Condensed Matter**, by K.L. Ngai, *Phys. Rev. B* 22:2066
- Universality of Low Frequency Fluctuation Dissipation and Relaxation Properties of Condensed Matter. Part II**, by K.L. Ngai, *Comments Solid State Phys.* 9:141
- Valence Bond Contributions of Photoluminescence Excitation Spectra of Tightly Bound Holes in Zincblende Semiconductors**, by P.J. Dean and S.G. Bishop, *J. Lumin.* 25:193
- Valley Degeneracy and Intersubband Spectroscopy in (111) and (110) Si Inversion Layers**, by T.L. Cole and B.D. McCombe, *J. Phys. Soc. Japan* 49 (Suppl. A):959
- Vibrational Properties of Amorphous Solids**, by D. Weaire* and P.C. Taylor, *Dynamical Properties of Solids*, Vol. 4, *Disordered Solids, Optical Properties*, North-Holland Publishing Co., New York, p. 1
- ## SPACE SCIENCE AND TECHNOLOGY
- A Classification Scheme for Solar Flare Models**, by J.C. Brown* and D.S. Spicer, *Sol. Phys.* 59:385
- A High Precision Solar Ultraviolet Spectral Irradiance Monitor for the Wavelength Region 120-400 nm**, by J.-D.F. Bartoe, G.E. Brueckner, D.K. Prinz, and M.E. VanHoosier, *Proceedings of the Workshop on Solar UV Irradiance Monitors*, p. 87
- A High-Resolution View of the Solar Chromosphere**, by G.E. Brueckner, *Highlights in Astronomy* 5:557
- A Review of Connected Element Radio Interferometry Directed at Establishing an Almost Inertial Reference Frame**, by K.J. Johnston, *Radio Interferometry Techniques for Geodesy*, NASA Conference Publication 2115, p. 45
- A Study of BL Lacertae Objects**, by K.W. Weiler* and K.J. Johnston, *Mon. Not. R. Astron. Soc.* 190:269
- Absorption Spectrum of CaI Between 1430 and 1340 Å**, by C.M. Brown and M.L. Ginter,* *J. Opt. Soc. Am.* 70:87
- Absorption Spectrum of CuI Between 1570 and 2500 Å**, by M.S. Longmire,* C.M. Brown, and M.L. Ginter,* *J. Opt. Soc. Am.* 70:423
- Ammonia Observations of DR 21, W51, NGC 1333, and Other Sources**, by D.N. Matsakis, J.M. Bologna, P.R. Schwartz, A.C. Cheung,* and C.H. Townes,* *Astrophys. J.* 241:655
- Angle-Dependent Frequency Distribution in a Plane-Parallel Medium, External Source Case**, by J.S. Lee and R.R. Meier, *Astrophys. J.* 240:185
- Applications of Coherent Satellite Link Frequency Standards to Satellite Position Determination**, by S.H. Knowles and W.B. Waltman, *Position Location and Navigation Symposium*, IEEE, New York, p. 154
- Applications of Interferometers in Space to Astrometry and Planetary Detection**, by S.H. Knowles and D.L. Thacker, *Celestial*

- Mech.* 22:197
- Astrometric Radio Source Catalogs**, by K.J. Johnston, J.H. Spencer, G.H. Kaplan,* and W.J. Klepczynski,* *Celestial Mech.* 22:143
- Astrometry Using Basic Mark II Very Long Baseline Interferometry**, by J.H. Spencer, E.B. Waltman, K.J. Johnston, and D.C. Backer,* *Radio Interferometry Techniques for Geodesy*, NASA Conference Publication 2115, p. 181
- Coincident Radar and Rocket Observations of Equatorial Spread F**, by E.P. Szuszczewicz, J.C. Holmes, R. Narcisi,* and R. T. Tsunoda,* *Geophys. Res. Lett.* 7:537
- Comment on "Variability of the Far-Infrared Solar Temperature Minimum with the Solar Cycle"**, by G.E. Brueckner, J.W. Cook, and M.E. VanHoosier, *Astron. Astrophys.* 92:L7
- Compact Radio Sources with Faint Components**, by R.A. Perley,* E.B. Fomalant,* and K.J. Johnston, *Astron. J.* 85:649
- Continuum Observations of Molecular Clouds at 89.6 GHz**, by P.R. Schwartz, *Astrophys. J.* 238:823
- Densities and Mass Motions in Transition-Zone Plasmas in Solar Flares Observed from Skylab**, by C.C. Cheng, *Sol. Phys.* 65:283
- Discovery of a Longitudinal Asymmetry in the H Lyman-Alpha Brightness of Jupiter**, by B.R. Sandel,* A.L. Broadfoot,* and D.F. Strobel, *Geophys. Res. Lett.* 7:5
- Electron Densities in a Solar Flare Derived from X-Ray Spectra**, by D.L. McKenzie,* R.M. Broussard,* P.B. Landecker,* H.R. Rugge,* R.M. Young,* G.A. Doschek, and U. Feldman, *Astrophys. J. Lett.* 238:L43
- F Region above Kauai: Measurement, Model, Modification**, by C.Y. Johnson, P.A. Bernhardt,* A.V. DaRosa,* E.S. Oran, G.W. Siolander,* and T.W. Young, *J. Geophys. Res.* 85:4205
- Future Possibilities for Ultraviolet Observation of Interstellar Molecules**, by G.R. Carruthers, *Interstellar Molecules*, D. Reidel Publishing Company, New York, p. 613
- Galactic Plane H₂O Masers: A Southern Survey**, by R.A. Batchelor,* J.W. Caswell,* W.M. Goss,* R.F. Haynes,* S.H. Knowles, and K.J. Wellington,* *Aust. J. Phys.* 33:139
- High-Resolution X-Ray Spectra of Solar Flares, III. General Spectral Properties of X1-X5 Type Flares**, by G.A. Doschek, U. Feldman, and R.W. Kreplin, *Astrophys. J.* 227:725
- High Resolution X-Ray Spectra of Solar Flares, IV. General Spectral Properties of M-Type Flares**, by U. Feldman, G.A. Doschek, R.W. Kreplin, and J.T. Mariska, *Astrophys. J.* 241:1175
- High-Resolution X-Ray Spectra of the 1979 March 25 Solar Flare**, by U. Feldman, G.A. Doschek, and R.W. Kreplin, *Astrophys. J.* 238:365
- Identification of a Faint X-Ray Source with the W Ursae Majoris Star VW Cephei**, by R.W. Carroll,* E.T. Byram, R.G. Cruddace, H. Friedman, J. Meekins, K. Wood, D. Yentis, G.H. Share, and T.A. Chubb, *Astrophys. J.* 235:L77
- Impulsive Phase of Solar Flares**, by S.R. Kane,* C.J. Crannell,* D. Datlowe,* U. Feldman, A. Gabriel,* and H.S. Hudson, *Solar Flares, A Monograph from Skylab Solar Workshop II*, Colorado Associated Universities Press, Boulder, p. 187
- Initial Observations with the Solwind Coronagraph**, by N.R. Sheeley, Jr., R.A. Howard, M.J. Koomen, and D.J. Michels, *Astrophys. J.* 237:L99
- Mass Electrons**, by D.M. Rust,* M. Dryer,* R.T. Hansen,* E. Hildner,* A.N. McClymont,* S.M.P. McKenna Lawlor,* D.J. McLean,* E.J. Schmahl,* R.S. Steinolfson,* E. Tandberg-Hanssen,* R. Tousey, D.F. Webb,* and S.T. Wu,* *Solar Flares, A Monograph from Skylab Solar Workshop II*, Colorado Associated Universities Press, Boulder, p. 273
- Measurements of Solar EUV and Soft X-Ray Emission during Sudden Frequency Deviation**, by D.M. Horan and R.W. Kreplin, *J. Geophys. Res.* 88:4257
- Observations of the O I 1355.6 Å and C I 1355.8 Å Lines**, by C.C. Cheng, U. Feldman, and G.A. Doschek, *Astron. Astrophys.* 86:377
- Observed L Profiles for Two Solar Flares: 14:12 UT 15 June 1973 and 23:16 UT 21 January 1974**, by R.C. Canfield* and M.E. VanHoosier, *Sol. Phys.* 67:339
- On the L Alpha Isophotes of Comet West (1976 VI)**, by H.U. Keller* and R.R. Meier, *Astron. Astrophys.* 81:210
- On the 2s²S - 2p²P⁰ Resonance Lines of Ovi and the 2s² ¹S₀ - 2s2p³P⁰ Intercombination Line of Ov**, by C.M. Brown, *Astron. Astrophys.* 88:273
- Optimal Control of Large Angle Attitude**

- Maneuvers for Flexible Spacecraft**, by R.W. Longman* and K.T. Alfriend, *Automatic Control in Space, Proceedings of the 8th IFAC Symposium*, Pergamon Press, New York, p. 57
- Orbit-Averaged Behavior of Magnetic Control Laws for Momentum Unloading**, by F.L. Markley and P.J. Camillo,* *J. Guid. Control* 3:563
- Phase Coherent VLBI Using a Satellite Link**, by W.B. Waltman, S.H. Knowles, J.L. Yen,* D.N. Fort,* G.W. Swenson,* W.A. Cannon,* and J. Galt,* *Radio Interferometry Techniques for Geodesy*, NASA Conference Publication 2115, p. 89
- Physical Conditions in the Solar Atmosphere above an Active Region**, by J.T. Mariska, U. Feldman, and G.A. Doschek, *Astrophys. J.* 240:300
- Plans for Phase Coherent Long Baseline Interferometry for Geophysical Application Using the ANIK-B Communications Satellite**, by W.A. Cannon,* W.T. Petrachenko,* J.L. Yen,* J.A. Galt,* W.B. Waltman, S.H. Knowles, and J. Popelar,* *Radio Interferometry Techniques for Geodesy*, NASA Conference Publication 2115, p. 461
- Progress Report on the USNO/NRL Green Bank Interferometer Program**, by W.J. Klepczynski,* G.H. Kaplan,* D.D. McCarthy,* F.J. Josties,* R.L. Branahan,* K.J. Johnston, and J.H. Spencer, *Radio Interferometry Techniques for Geodesy*, NASA Conference Publication 2115, p. 63
- Radiative Energy Output of the 5 September 1973 Flare**, by R.C. Canfield,* C.C. Cheng,* K.P. Dere, G.A. Dulk,* D.V. McLean,* R.D. Robinson,* E.J. Schmahl,* and S.A. Schoolman,* *Solar Flares, A Monograph from Skylab Solar Workshop II*, Colorado Associated Universities Press, Boulder, p. 451
- Rapid X-Ray Variability of PKS 2155-304**, by W.A. Snyder,* A.F. Davidsen,* R. Kinzer, S. Shulman, H. Smathers, and K. Wood, *Astrophys. J.* 237:L11
- Recent Satellite Observations of the Corona**, by M.J. Kooman, D.J. Michels, and N.R. Sheeley, *Sky and Telescope* 60:102.
- Relative Chemical Abundances in Different Solar Regions**, by J. T. Mariska, *Astrophys. J.* 235:268
- Rocket-Ultraviolet Imagery of the North America Nebula**, by G.R. Carruthers, T.R. Gull,* and H.M. Heckathorn, *Astrophys. J.* 237:438
- Satellite Observation of the Outer Corona near Sunspot Maximum**, by D.J. Michels, R.A. Howard, M.J. Koomen, and N.R. Sheeley, *Radio Physics of the Sun*, D. Reidel, Boston, p. 439
- Search for the Intermediate-Scale Anisotropy of the Cosmological Background Radiation**, by R. Fabbri,* B. Melchiorri,* F. Melchiorri,* V. Natale,* N. Caderni,* and K. Shivanandan, *Phys. Rev. D* 21:2095
- SiO Emission in Orion — KL: An Evolved Star in a Region of Star Formation or a Unique Object in the Galaxy?** by R. Genzel,* D. Downes,* P.R. Schwartz, J.H. Spencer, V. Pankonin,* and J.W.M. Baars, *Astrophys. J.* 239:519
- Soft X-Ray Sources in the Bar of the Large Magellanic Cloud**, by J.D. McKee,* G.G. Fritz, R.E. Cruddace, S.D. Shulman, and H. Friedman, *Astrophys. J.* 238:93
- Soft X-Ray Vacuum UV Spectroscopy of Thin Targets Heated by Enhanced Electron Energy Deposition**, by E.J.T. Burns,* J. Chang,* A.V. Farnsworth,* J.P. Vandevender,* M.M. Widner,* S.A. Goldstein,* C.W. Mandel,* J.P. Quintenz,* and G.A. Doschek, *J. Appl. Phys.* 51:2569
- Solar Flare X-Ray Spectra between 7.8 and 23 Å**, by D.L. McKenzie,* P.B. Landecker,* R.M. Broussard,* H.R. Rugge,* R.M. Young,* U. Feldman, and G.A. Doschek, *Astrophys. J.* 241:409
- Solar Observations with a New Earth-Orbiting Coronagraph**, by N.R. Sheeley, Jr., R.A. Howard, D.J. Michels, and M.J. Koomen, *Solar and Interplanetary Dynamics*, M. Dryer and E. Tandberg-Hanssen, eds., D. Reidel, Boston, p. 55
- Solar Physics in the VUV: The Importance of High Resolution Observations**, by G.E. Brueckner, *Appl. Opt.* 19:3994
- Spatial Distribution of XUV Emission and Density in a Loop Prominence**, by C.C. Cheng, *Sol. Phys.* 65:347
- Spatial Imaging of Lyman α Emission from Jupiter**, by J.T. Clarke,* H.A. Weaver,* P.D. Feldman,* H.W. Moos,* W.G. Fastie,* and C.B. Opal, *Astrophys. J.* 240:696
- Stability of the Primakoff-Sedov Blast Wave and Its Generalizations**, by I.B. Bernstein and D.L. Book, *Astrophys. J.* 240:223
- Stark Effect at the Si I Series Limit**, by J.-D. Bartoe and G.E. Brueckner, *Astrophys. J.* 240:702

- Temporal Variations of Loop Structures in the Solar Atmosphere**, by N.R. Sheeley, *Sol. Phys.* 65:79
- The Absorption Spectrum of CuH in the 2350 Å Region**, by C.M. Brown and M.L. Ginter,* *J. Mol. Spectrosc.* 80:145
- The Chromosphere and Transition Region**, by R.C. Canfield,* J.C. Brown,* G.E. Brueckner, J.W. Cook,* J.D. Craig,* G.A. Doschek, A.G. Emslie,* J.C. Henoux,* B.W. Lites,* M.E. Machado,* and J.H. Underwood,* *Solar Flares, A Monograph from Skylab Solar Workshop II*, Colorado Associated Universities Press, Boulder, p. 232
- The Coincidence of the Radio and Optical Emission from SS433**, by G.H. Kaplan,* R.S. Harrington,* V.V. Kallarakal,* K.J. Johnston, and J.H. Spencer, *Astron. J.* 85:64
- The Continuous Spectrum of Markarian 421 during Periods of X-Ray Satellite Observation**, by S.L. Mufson,* W.C. Wisniewski,* K.S. Wood, D.P. McNutt, D.J. Yentis, J.F. Meekins, E.T. Byram, T.A. Chubb, and H. Friedman, *Astrophys. J.* 241:74
- † **The Detection of a Companion Star to the Cepheid Variable Eta Aquilae**, by J.T. Mariska, G.A. Doschek, and U. Feldman, *Astrophys. J.* 238:L87
- The Effects on the Earth's Magnetotail from Shocks in the Solar Wind**, by J. Lyon,* S.H. Brecht,* J.A. Fedder, and P. Palmadesso, *Geophys. Res. Lett.* 7:721
- The Equatorial Latitude of Auroral Activity during 1972-1977**, by N.R. Sheeley, Jr., and R.A. Howard, *Sol. Phys.* 67:189
- The Equatorial Latitude of Auroral Activity during 1972-1977**, by N.R. Sheeley, Jr., R.A. Howard, and B.S. Dandekar,* World Data Center A Publication UAG-78, National Oceanographic and Atmospheric Administration, Boulder, Colo.
- The Evolution of the Polar Coronal Holes**, by N.R. Sheeley and C.C. Cheng, *Sol. Phys.* 65:229
- The Hard X-Ray Pulse Profile of GX H4**, by M.S. Strickman, W.N. Johnson, and J.D. Kurfess, *Astrophys. J.* 240:L21
- The High-Energy X-Ray Spectrum of Scorpius X-1**, by W.N. Johnson, J.D. Kurfess, G.S. Maurer, and M.S. Strickman, *Astrophys. J.* 238:982
- The Millimeter Wavelength Spectrum of MWC 349**, by P.R. Schwartz, *Publ. Astron. Soc. Pac.* 92:534
- The Need for High Resolution in VUV Rydberg Spectroscopy**, by M.L. Ginter,* D.S. Ginter,* and C.M. Brown, *Appl. Opt.* 19:4015
- The Observation of a High-Latitude Coronal Transient**, by N.R. Sheeley, R.A. Howard, M.J. Koomen, D.J. Michels, and A.I. Poland,* *Astrophys. J.* 238:L161
- The Solar Mass Ejection of 8 May 1979**, by D.J. Michels, R.A. Howard, M.J. Koomen, N.R. Sheeley, Jr., and B. Rompolt,* *Solar and Interplanetary Dynamics*, D. Reidel, Boston, p. 387
- The Structure of Interstellar Hydroxyl Masers: VLBI Synthesis Observation of W3(OH)**, by M.J. Reid,* A.D. Hashick,* B.F. Burke,* J.M. Moran,* K.J. Johnston, and G.W. Swenson,* *Astrophys. J.* 239:89
- The Thermal X-Ray Flare Plasma**, by R. Moore,* S.K. Antiochos,* K.P. Dere, H.W. Dodson-Prince,* E. Hiei,* K.R. Krall,* A.S. Krieger,* D.L. McKenzie,* H.E. Mason,* R.D. Petrasso,* G.W. Preuman, J.K. Silk, Z. Svestka,* J.A. Vorpahl, K.G. Widing, and G.L. Withbroe, *Solar Flares, A Monograph from Skylab Solar Workshop II*, Colorado Associated Universities Press, Boulder, p. 342
- † **The Ultraviolet Dayglow I. Far UV Emissions of N and N₂**, by R.R. Meier, P.D. Feldman,* E.P. Gentieu, and D.J. Strickland,* *J. Geophys. Res.* 85:2177
- The UV Dayglow 2, LY α and LY β Emissions and the H Distribution in the Mesosphere and Thermosphere**, by D.E. Anderson, P.D. Feldman,* E.P. Gentieu, and R.R. Meier, *Geophys. Res. Lett.* 7:529
- The X-Ray Light Curve of 4U-2129**, by M.P. Ulmer,* E.T. Byram, T.A. Chubb, W.D. Evans, H. Friedman, D. McNutt, J. Meekins, S. Shulman, K. Wood and D. Yentis, *Astrophys. J.* 235:L159
- Thermal Design of the Second Navigation Technology Satellite**, by D.W. Almgren,* C.W. Buhler, R. Rovinski, and F.E. Ruicia,* *Heat Transfer, Thermal Control, and Heat Pipes*, Vol. 70 of *Progress in Astronautics and Aeronautics*, AIAA, New York, p. 211
- Variability of the Solar Flux in the Far Ultraviolet 1175-2100 Å**, by J.W. Cook, G.E. Brueckner, and M.E. VanHoosier, *J. Geophys. Res.* 85:2257; and 6th International Conference on Vacuum Ultraviolet Radiation Physics, Vol. III, Paper III-38

STRUCTURE RESEARCH

- A New Class of Indolizidine Alkaloids from the Poison Frog *Dendrobates tricolor*. X-Ray Analysis of 8-Hydroxy-8-Methyl-6-(2'-Methylhexylidene)-1-azabicyclo [4.3.0] Ronane**, by J.W. Daly,* T. Tokuyama,* T. Fujiwara,* R.J. Highet, and I.L. Karle, *J. Am. Chem. Soc.* **102**: 830
- † A Restrained-Parameter Thermal-Factor Refinement Procedure**, by J. H. Konnert and W. A. Henderson, *Acta Crystallogr. A* **36**:344.
- Computer Program for Radial Distribution Calculation from Known Bonding Topologies**, by P. D'Antonio and J.H. Konnert, *J. Appl. Crystallogr.* **13**:459
- Conformation of Cyclic Pentapeptides in the Crystalline State: Cyclic (D-Phe-L-Pro-Gly-D-Ala-L-Pro) with 3--1 and 4--1 Intramolecular Hydrogen Bonds**, by I.L. Karle, *Perspectives in Peptide Chemistry*, S. Karger AG, Basel, Switzerland, p. 261
- Conformation of the Cyclic Hexapeptide (D-Phe-Pro-Val)₂:C₃₈H₅₀N₆O₆**, by J.L. Flippen-Anderson, *Peptides: Structures and Biological Function*, Proceedings of the Sixth American Peptide Symposium, p. 145
- Determination of Molecular Formula and Stereoconfiguration of Unique Steroids by X-Ray Diffraction Analysis**, by J. Karle, *Lipids* **15**:793
- Diffraction Analysis of Motion in Proteins**, by W.A. Hendrickson and J.H. Konnert, *Biophys. J.* **32**: 645
- Estimation of the Torsional Potential for Perfluorodimethyl Ether from Electron-Diffraction Data**, by A.H. Lowrey, C. George, P. D'Antonio, and J. Karle, *J. Mol. Struct.* **63**:243
- Stereochemically Restrained Crystallographic Least-Squares Refinement of Macromolecule Structures**, by W.A. Hendrickson and J.H. Konnert, *Biomolecular Structure Confirmation, Function and Evolution*, Pergamon Press, New York, p. 43
- Structural Comparison of m-AMSA, a New Clinically Active Antitumor Agent with Less Active Related Compounds**, by J.M. Karle,* R.L. Cyayk,* and I.L. Karle, *Acta Crystallogr. B* **36**: 3012
- Structural Ordering of Silica Glass Optical Fibers**, by J. H. Konnert and P. D'Antonio, *Am. Ceram. Soc. Bull.* **59**:643
- The Expected Value of Triplet Invariants: Acentric Case**, by J. Karle, *Acta Crystallogr. A* **36**:800
- Trimerization of an Azomethine Imine by Three Successive 1,3-Dipolar Cycloaddition Reactions**, by J.L. Flippen-Anderson, I.L. Karle, R. Huisgen,* and H.U. Reissig,* *Angew. Chem.* **19**:906
- Triplet Phase Invariants: Formula for Acentric Case from Fourth-Order Determinantal Joint Probability Distributions**, by J. Karle, *Proc. Natl. Acad. Sci. U.S.A.* **77**:5

FORMAL REPORTS

ACOUSTICS

- 8365 Transduction with PVF₂ in the Ocean Environment**, by Y. Berlinsky. AD-A084 561.
- 8372 Effective Shear Modulus for Flexural and Extensional Waves in an Unloaded Thick Plate**, by P.S. Dubbelday. AD-A092 149.
- 8429 Modal Acoustic Transmission Loss (MOATL): A Transmission-Loss Computer Program Using a Normal-Mode Model of the Acoustic Field in the Ocean**, by J.F. Miller and S.N. Wolf. AD-A089 367.
- 8431 Traffic Load Factors and Reliability in Two-Line Undersea Barrier Detection Sys-**

tems, by W.C. Dixon and C.R. Rollins. AD-B052 190L.

- 8436 Long Term Variability of Windspeed**, by A.I. Eller and M.L. Blodgett. AD-A091 802.

- 8438 Role of the Sectionalized Fourier Transform in High-Speed Coherence Processing**, by A.A. Gerlach. AD-A091 419.

CHEMISTRY

- 8397 Catalytic Oxidation of Carbon Monoxide at High Humidity and Low Temperature**, by J.K. Musick and F.W. Williams. AD-A087 206.

8403 **Combustion Products Evaluation from Hull Insulation Materials Coated with Fire Retardant Paints**, by H.G. Eaton, F.W. Williams, and P.A. Tatem. AD-A089 973.

8414 **The Smoke Hazards Resulting from the Burning of Shipboard Materials Used by the U.S. Navy**, by B.T. Zinn, R.F. Browner, E.A. Powell, M. Pasternak, and R.O. Gardner. AD-A088 091.

COMMUNICATIONS

8373 **An Abstract Type for Statistics Collection in SIMULA**, by C.E. Landwehr. AD-A084 562.

† 8376 **Experimental Investigations of Transmission, Propagation, and Reception of 3 kHz Electromagnetic Waves for Tactical Communication Applications**, by R.J. Dinger, W.D. Meyers, and J.A. Goldstein. AD-B046 506L.

8385 **Software Engineering Techniques Applied to Protocol Simulation**, by C.E. Landwehr. AD-A083 887.

8393 **Synthesis of MCJ Codes**, by H.M. Beck. AD-A086 778.

8404 **Analysis of Alternative Satellite Channel Management Systems**, by M.E. Melich, C.E. Landwehr, and P.J. Crepeau.

† 8408 **Design and Risk Analysis of a Wideband Architecture for Shipboard HF Communication**, by C.E. Hobbs, R.M. Bauman, R.K. Royce, and J.R. Davis. AD-B053 797L.

8413 **Experimental Measurements of Ambient Electromagnetic Noise from 1.0 to 4.0 kHz**, by R.J. Dinger, W.D. Meyers, and J.R. Davis. AD-A088 090.

8430 **Spatial Coherence Measurements and Evaluation of a Noise Reduction Technique for Ambient Noise from 0.3 to 40 Hz**, by R.J. Dinger and J.A. Goldstein. AD-A092 151.

8445 **Evaluation of the A-7 Requirements Document by Analysis of Change Data**, by V.R. Basili and D.M. Weiss.

8453 **Transmitting/Receiving Subsystem Decoupling Techniques for Shipboard HF Communication Systems**, by R.K. Royce.

COMPUTER SCIENCES

8402 **Naval Ocean-Surveillance Correlation Handbook, 1979**, by I.R. Goodman, H.L.

Weiner, and W.W. Willman. AD-B051 785L.

8444 **Real-Time and Applications Software for the Neil Brown/W.H.O.I. CTD Microprofiler**, by L.J. Rosenblum.

ELECTRONICS AND ELECTRICITY

8361 **Measured Performance Characteristics of Reflective Butler Matrices**, by B. Sheleg and H.E. Heddings. AD-A081 002.

8388 **Interactive Effects of Bond Wires Used for Microwave Semiconductor Device Combining and Matching Circuitry**, by R.E. Neidert, H.A. Willing, and B.E. Speilman. AD-A083 920.

8394 **Computer-Aided Analysis for the Design of Broad Classes of Microwave Couplers, Filters, and Transmission Lines**, by B.E. Speilman. AD-A088 772.

8418 **Physical Limitations and Design Criteria for a Solid State Gyrotron**, by A.K. Ganguly and D.C. Webb. AD-A092 150.

ENVIRONMENTAL SCIENCES

8454 **Experimental Sea Slicks in the MARSEN (Maritime Remote Sensing) Exercise**, by W.D. Garrett and W.R. Barger. AD-A091 850.

8455 **United States Frigate Constellation: Monitoring of Water at Constellation Pier, Baltimore Harbor, for the Presence of Marine Wood-Destroyers—First Year of Observations, from April 1978 to May 1979**, by J.D. Bultman, K.K. Parrish, and C.A. Bailey. AD-A090 944.

MARINE TECHNOLOGY

8205 **Liquid Surface Levitation Holography, Part 1—Theoretical Analysis**, by A.V. Clark, Jr. AD-A088 418.

8459 **The NRL Unmanned Free-Swimming Submersible (UFSS)**, by P.B. Alers and H.A. Johnson.

MATHEMATICS

8415 **Identification of Fuzzy Sets with a Class of Canonically Induced Random Sets and** 221

Some Applications, by I.R. Goodman.
AD-A089 852.

METALLURGY

- 8357 **Notch Ductility Degradation of Low Alloy Steels with Low-to-Intermediate Neutron Fluence Exposures**, by J.R. Hawthorne. AD-A081 003.
- 8370 **Fractographic and Microstructural Analysis of SCC Specimens of HY-100, HY-130, and HY-180 Steel Weldments**, by F.W. Fraser and E.A. Metzbower. AD-A082 301.
- 8391 **Plastic Deformation and Ductile Fracture at an Angled Slit in a Sheet Under Tension**, by S.C. Sanday and O. Richmond. AD-A084 564.
- 8437 **Comparison of the Temperature-Dependent Elastic Modulus of Ti-Fe with H-Doped Ti-Fe in the [111] Direction**, by J.R. Neighbours, A.C. Ehrlich, R.A. Masamura, and C.L. Vold. AD-A091 507.
- 8451 **Fatigue and Fracture Resistance of Stainless Steel Weld Deposits After Elevated-Temperature Irradiation**, by J.R. Hawthorne. AD-A093 090.

OPTICAL SCIENCES

- 8315 **Pocketron-Atmospheric Transmission Code for the HP-97 Programmable Calculation**, by J.L. Walsh.
- 8352 **Unsteady Thermal Blooming of Intense Laser Beams**, by J.T. Ulrich and P.B. Ulrich. AD-A087 207.
- 8367 **Passive Infrared Surveillance, Part II: Threshold-Crossing Receivers**, by R.A. Steinberg. AD-A081 723.
- 8389 **Hybrid Image Processing System**, by T.H. May and J.A. Blodgett. AD-A084 563.
- 8422 **Atmospheric Transmission Measurements at White Sands Missile Range, August 1978**, by S.T. Hanley, J.A. Dowling, R.F. Horton, J.A. Curcio, C.O. Gott, M.A. Woytko, and J. Storvick. AD-A092 445.
- 8446 **Laser-Extinction and High-Resolution Atmospheric Transmission Measurements Conducted at White Sands Missile Range, New Mexico, March 1979**, by J.A. Dowling, S.T. Hanley, J.A. Curcio, C.O. Gott, and M.A. Woytko. AD-A092 702.
- 8450 **Chemical Laser Computer Code Survey**, by C.M. Wiggins, D.N. Mansell, P.B. Ulrich, and J.L. Walsh. AD-A093 540.

PLASMA PHYSICS

- 8261 **A New Theory for Striations with Experimental Verifications**, by E.E. Kempe. AD-A092 058.

RADAR

- 8345 **Nonlinear Spectral Analysis and Adaptive Array Superresolution Techniques**, by W.F. Gabriel. AD-A083 391.
- 8368 **A Pattern-Synthesis Procedure for Regular Planar Arrays**, by J.P. Shelton. AD-A082 798.
- 8369 **An Analytical Study of Radar Returns in the Presence of a Rough Sea Surface**, by H.R. Raemer. AD-A086 157.
- 8377 **Double-Ended Backward-Wave Yagi Hybrid Antenna**, by W.K. Kahn. AD-A082 795.
- 8386 **Observation by HF Radar of the Phillips Resonance Mechanism for Generation of Wind Waves**, by D.B. Trizna, R.W. Bogle, J.C. Moore, and C.M. Howe. AD-A085 473.
- 8387 **A New Class of Pulse Compression Codes and Techniques**, by B.L. Lewis and F.F. Kretschmer. AD-A086 787.
- 8392 **Analysis of Conventional and Reflective Butler Matrices with Imperfect Components**, by J.P. Shelton and J.K. Hsiao. AD-A085 474.
- 8400 **Preliminary Results of Radar Environmental Mapping**, by B.H. Cantrell. AD-A086 788.
- 8409 **Building Block for an Orthonormal-Lattice-Filter Adaptive Network**, by W.F. Gabriel. AD-A088 088.
- 8421 **Bearing-Only Tracking Algorithms**, by A. Grindlay. AD-A088 093.
- 8433 **An Automatic Tracking System for the Fixed Array Surveillance Radar (FASR)**, by J.D. Wilson.
- 8443 **Some Error Probabilities for the Association of Passive DF Measurements with Radar Returns**, by J.O. Coleman. AD-A091 659.
- 8449 **Comparison of Detectors in the Presence of Sidelobe Jamming**, by G.V. Trunk. AD-A092 709.
- 8461 **Real-Time Ship RCS Scintillation and Angle Noise Simulation**, by W.M. Morris.

RADIATION TECHNOLOGY

- 8457 **Storage-Ring Generation of High-Energy Neutrino Beams**, by F.J. Kelly, A.W. Sáenz, and H. Überall.

RESEARCH MANAGEMENT

- 8426 **Proceedings of AAAS Symposium on January 8, 1980: How Much Does the Defense Department Advance Science?** by G. Gamota, A. Berman, E. Salkovitz, E. Teller, G. Wald, and D. Triantos. AD-A092 607.

SPACE SCIENCE

- 8416 **XUV Aluminum Spectra of Laser-Produced Plasmas**, by G.A. Doschek and U. Feldman. AD-A088 107.

SPACE SYSTEMS

- 8360 **The Contribution of Navigation Technology Satellites to the Global Positioning System**, by R.L. Easton, J.A. Buisson, T.B. McCaskill, O.J. Oaks, S. Stebbins, and M. Jeffries. AD-A080 548.
- 8366 **A Comparison of Intercontinental Clock Synchronization by VLBI and the NTS Satellite**, by J.A. Buisson, O.J. Oaks, T.B. McCaskill, W.J. Hurd, S.C. Wardrip, H.E. Warren, and G.G. Whitworth. AD-A081 001.
- 8374 **Refined Filtering of Image Noise Using Local Statistics**, by Jong-Sen Lee. AD-A080 530.
- 8375 **Stability Analysis of the Cesium Frequency Standard on Board Navigation**

Technology Satellite 2 (NTS-2), by T.B. McCaskill, J.A. Buisson, J. White, and S.B. Stebbins. AD-A082 797.

- 8382 **A Heuristic Method of Optimal Generalized Hypercube Encoding for Pictorial Databases**, by C.-C. Yang, S.K. Chang, and K.K. Singh. AD-A081 700.

- 8395 **Submicrosecond Comparisons of Time Standards via the Navigation Technology Satellites (NTS)**, by J.A. Buisson, T.B. McCaskill, and G.G. Whitworth. AD-A086 780.

- 8406 **Precise Analysis of an Optimal Perturbation Estimation and Control Problem**, by W.W. Willman. AD-A091 116.

- 8410 **Elastic Deformations of a Rotating Spheroidal Earth Due to Surface Loads**, by P. Lanzano and J.C. Daley. AD-A088 089.

- 8419 **GPS NAVSTAR-4 and NTS-2 Long Term Frequency Stability and Time Transfer Analysis**, by J.A. Buisson, T.B. McCaskill, O.J. Oaks, M.M. Largay, and S.B. Stebbins. AD-A088 092.

- 8423 **Some Performance Results for Recursive Multitarget Correlator-Tracker Algorithms**, by W.W. Willman. AD-A088 595.

- 8447 **A Method for Specifying the Noise Suppression-Resolution Tradeoff in Digital Image Filtering with Local Statistics**, by W.W. Willman. AD-A093 560.

AWARD-WINNING NRL MEMORANDUM REPORTS

- † 4172 **A Modified Prony Method Approach to Echo-Reduction Measurements of Time-Limited Transient Signals**, by D.H. Trivett.

- † 4317 **Detailed Modelling of Combustion Systems**, by E.S. Oran and J.P. Boris.

PATENTS GRANTED IN 1980

- 4,181,904 — **Acoustic-Wave Convolver Utilizing Diffused Waveguides and Beam Compression Techniques**, January 1, 1980, to Joseph F. Weller, James D. Crowley, and Thomas G. Giallorenzi
- 4,184,078 — **Pulsed X-Ray Lithography**, January 15, 1980, to David J. Nagel and Martin C. Peckerar

- 4,185,274 — **High Speed Electrooptical A/D Converter**, January 22, 1980, to Thomas G. Giallorenzi

- 4,187,796 — **Specific Gravity Equalizer System**, February 12, 1980, to John O. Ess

- 4,188,120 — **Radioiodine Detector Based on Laser-Induced Fluorescence**, February 12,

- 1980, to Jimmie R. McDonald and Andrew P. Baronavski
- 4,188,710 — Ohmic Contacts for Group III-V n-Type Semiconductors Using Epitaxial Germanium Films**, February 19, 1980, to John E. Davey and Aristos Christou
- 4,190,701 — V_3Ga Composite Superconductor**, February 26, 1980, to David G. Howe and Donald U. Gubser
- 4,192,573 — Variable Power Attenuator for Light Beams**, March 11, 1980, to Ray B. Brown
- 4,193,130 — Fiber-Optic Hydrophone for Use as an Underwater Electroacoustic Standard**, March 11, 1980, to A. Mark Young, Theodore A. Henriquez, and Allan C. Tims
- 4,194,139 — Reflex Tetrode for Producing an Efficient Unidirectional Ion Beam**, March 18, 1980, to John A. Pasour, Christos A. Kapetanakis, Redge A. Mahaffey, and Jeffry Golden
- 4,194,244 — Angle-Sensing System**, March 18, 1980, to Bernard L. Lewis
- 4,195,166 — Alkanediamide-Linked Polyphthalocyanines Coordinated With $SnCl_2$** , March 25, 1980, to James R. Griffith and Jacques G. O'Rear
- 4,196,055 — Method of Determining the Presence of Stray Electrical Currents in a Solution**, April 1, 1980, to Thomas J. Lennox, Jr.
- 4,197,510 — Isochronous Cyclotron**, April 8, 1980, to Harold H. Szu
- 4,197,517 — High-Speed Frequency-Tunable Microwave Filter**, April 8, 1980, to Carmine Vittoria
- 4,197,543 — Display Processor for Aircraft Landing System**, April 8, 1980, to Bernard L. Lewis
- 4,198,632 — Transponder Reply Limiting by Means of Recognition of Fixed Interrogation Periods**, April 15, 1980, to Walton B. Bishop
- 4,200,669 — Laser Spraying**, April 29, 1980, to Robert J. Schaefer and Jack D. Ayers
- 4,201,955 — Method of Producing Population Inversion and Lasing at Short Wavelengths by Charge Transfer**, May 6, 1980, to Raymond C. Elton and Robert H. Dixon.
- 4,206,364 — Device for Producing Extended Elongated Plasmas for X-Ray Lasers**, June 3, 1980, to Robert H. Dixon, Raymond C. Elton, and John F. Reintjes
- 4,206,746 — Spiral-Passage Heat Exchanger**, June 10, 1980, to Talbot A. Chubb
- 4,209,458 — Fluorinated Phthalonitriles**, June 24, 1980, to Teddy M. Keller and James R. Griffith
- 4,213,073 — Rod Pinch Diode**, July 15, 1980, to Redge A. Mahaffey, Shyke A. Goldstein, Jeffry Golden, and Gerald Cooperstein
- 4,213,099 — Hydrophone Preamplifier and Calibration Circuit**, July 15, 1980, to Craig K. Brown
- 4,213,670 — Planar Fiber-Optic Star and Access Coupler**, July 22, 1980, to A. Fenner Milton and Thomas G. Giallorenzi
- 4,215,291 — Collective Particle Accelerator**, July 29, 1980, to Moshe Friedman
- 4,217,032 — End-Butt Optical-Fiber Coupler**, August 12, 1980, to Sang K. Sheem
- 4,217,547 — Method for Determining the Compensation Density in n-Type Narrow-Gap Semiconductors**, August 12, 1980, to Filbert J. Bartoli, Leon Esterowitz, Roger E. Allen, and Melvin R. Kruer
- 4,222,051 — Cascaded Digital Cancellor**, September 9, 1980, to Frank F. Kretschmer and Bernard L. Lewis
- 4,223,123 — Aliphatic Phenoxy Polyphthalocyanine**, September 16, 1980, to Teddy M. Keller and James R. Griffith
- 4,223,400 — Low-Frequency Directional Hydrophone**, September 16, 1980, to Joseph F. Zalesak and Robinson A. Zed
- 4,223,576 — Gyrotron Travelling-Wave Amplifier**, September 23, 1980, to Victor L. Granatstein, Phillip Sprangle, Adam T. Drobot, Kwo R. Chu, and Laurence J. Safter
- 4,225,239 — Magneto-Optic Bias of Ring Laser Using Reflective Magneto-Optic Element at Near-Grazing Incidence**, September 30, 1980, to Gary A. Prinz
- 4,226,629 — Method for Epitaxial Growth of GaAs Films and Devices Configuration Independent of GaAs Substrate Utilizing Molecular Beam**, October 7, 1980, to John E. Davey and Aristos Christou
- 4,226,801 — Terminated bis(2,3-Dicyanophenoxy) Alkanes**, October 7, 1980, to Teddy M. Keller and James R. Griffith
- 4,227,170 — Current-Reducing Device**, October 7, 1980, to Moshe Friedman and Michael G. Ury
- 4,228,407 — Ion-Beam-Excited Gas Laser**, October 14, 1980, to A. Wahad Ali, Jeffry Golden, and Gary J. Eden
- 4,228,437 — Wideband Polarization-Transforming Electromagnetic Mirror**, October 14, 1980, to J. Paul Shelton

- 4,230,995 — Electrically Excited Mercury Halide Laser, October 28, 1980, to Ralph L. Burnham
- 4,231,058 — Tungsten-Titanium-Chromium/Gold Semiconductor Metallization, October 28, 1980, to K. Reed Gleason
- 4,233,477 — Flexible, Shapeable, Composite Acoustic Transducer, November 11, 1980, to Roy W. Rice and Robert C. Pohanka
- 4,234,712 — Polyphthalocyanine Resins, November 18, 1980, to Teddy M. Keller and James R. Griffith
- 4,237,428 — 15.9- μ m Acetylene Laser, December 2, 1980, to Bernard L. Wexler, Joseph A. Stregack, and Thomas J. Manuccia
- 4,237,461 — High-Speed Digital Pulse Compressor, December 2, 1980, to Ben H. Cantrell and Bernard L. Lewis
- 4,238,464 — Air-Revitalization Materials, December 9, 1980, to Paul R. Gustafson
- 4,238,601 — Perfluorinated Aliphatic Phenoxy Bisorthodinitriles and Polyphthalocyanines Therefrom, December 9, 1980, to Teddy M. Keller and James R. Griffith
- 4,238,742 — Laser System, December 9, 1980, to Louis P. Champagne
- 4,238,856 — Fiber-Optic Acoustic Sensor, December 9, 1980, to Joseph A. Bucaro and Edward F. Carome

NRL Review Staff

Research Area Editors

D. A. Patterson, *Senior Science Editor*

J. C. Edge and D. J. DeYoung, *Coordination Assistant*

A. Cooper, *General Science and Technology*

J. T. Warfield, Jr., *Systems Research and Technology*

R. Nekritz, *Material Science and Component Technology*

J. W. Schwartz, *Space and Communications Technology*

Technical Information Staff

E. E. Kirkbride, *Division Head*

S. G. Curry, *Publication Coordinator and Staff Editor*

D. R. Nelson and S. Weintraub, *Associate Editors*

D. B. Wilbanks and Staff, *Composition and Layout*

D. Boyd, S. Moorhouse, and T. E. Phillips, *Cover Design*

D. Robbins, R. Doerflein, J. C. Moon, L. Musselman,
and J. Milligan, *Graphics Services*

DIRECTORY OF KEY OFFICES AND PERSONNEL, MAY 1981

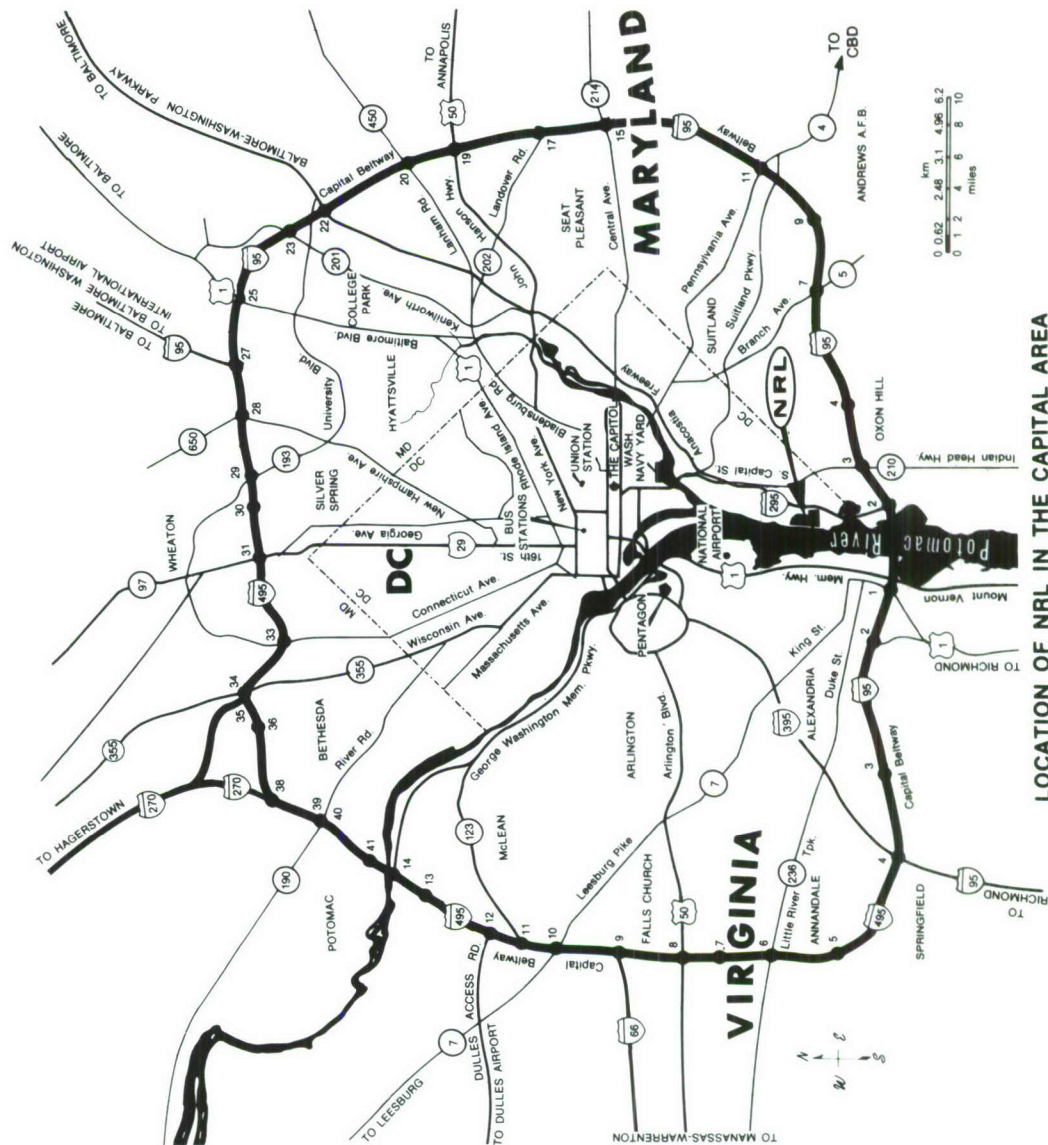
<u>Code</u>	<u>Office and Incumbent</u>	<u>Ext.</u>
OFFICE OF COMMANDING OFFICER/DIRECTOR OF RESEARCH		
1000	Commanding Officer	CAPT E. E. Henifin 73403
1001	Director of Research	Dr. A. Berman 73301
1003	DEEO Officer	Mrs. S. Eaton 72486
1005	Public Affairs Officer	Mr. E. E. Kirkbride 73388
1200	Chief Staff Officer	CAPT E. L. Ebbert 73621
1226	Head, Security Section	Mr. R. E. Abercrombie 73711
1300	Comptroller	Mr. D. T. Green 73405
1400	Head, Management Information Division	Mr. R. E. Ellis 73666
1700	Head, Research Computation Division	Mr. A. B. Bligh 72751
1800	Civilian Personnel Officer	Mr. D. J. Blome 73421
1810	Personnel Operations	Mr. D. J. Blome† 73030
TECHNICAL SERVICES DIRECTORATE		
2000	Associate Director of Research for Technical Services	Dr. H. Q. North 72879
2020	Head, Administrative Office	Mrs. L. V. Dabney 73858
2300	Engineering Services Officer	CDR B. D. Uber 72300
2400	Supply Officer	CDR T. W. Christensen 73446
2500	Public Works Officer	CDR J. W. MacLaughlin 73371
2600	Head, Technical Information Division	Mr. E. E. Kirkbride 73388
2700	Chesapeake Bay Division Officer	CDR K. V. Ruona (301) 259-2111
RESEARCH DIRECTORATES		
4000	Associate Director of Research for General Science and Technology	Dr. T. Coffey 73324
4020	Laboratory for Cosmic Ray Physics	Dr. M.M. Shapiro 72965
4040	Laboratory for Computational Physics	Dr. J. P. Boris 73055
4100	Space Sciences Division Superintendent	Dr. P. W. Mange 73363
4300	Environmental Sciences Division Superintendent	Dr. J. O. Elliot 72974
4700	Plasma Physics Division Superintendent	Dr. T. Coffey* 72723
5000	Associate Director of Research for Systems Research and Technology	Mr. R. R. Rojas 73294
5100	Acoustics Division Superintendent	Dr. J. C. Munson 73482
5300	Radar Division Superintendent	Dr. M. I. Skolnik 72936
5700	Tactical Electronic Warfare Division Superintendent	Mr. L. A. Cosby 72191
5800	Marine Technology Division Superintendent	Dr. R. T. Swim* 73314
5900	Underwater Sound Reference Detachment Superintendent	Dr. J. E. Blue (305) 859-5720 AUTOVON 791-4111)
6000	Associate Director of Research for Material Science and Component Technology	Dr. A. I. Schindler 73566
6030	Laboratory for Structure of Matter	Dr. J. Karle 72665
6070	Health Physics Staff	Mr. J. N. Stone 72232
6100	Chemistry Division Superintendent	Dr. F. E. Saalfeld 73026
6300	Material Science and Technology Division Superintendent	Dr. L. R. Hettche 72926
6500	Optical Sciences Division Superintendent	Dr. T. G. Giallorenzi 73171
6600	Condensed Matter and Radiation Sciences Division Superintendent	Dr. J. B. Aviles, Jr.* 72931
6800	Electronics Technical Division Superintendent	Dr. B. D. McComb* 73525
7000	Associate Director of Research for Space and Communication Technology	Dr. B. Wald 72964
7030	Advanced Projects Office Manager	Dr. R. D. Mayo 72043
7040	Spacecraft Technology Center	Mr. P. G. Wilhelm 72073
7500	Communications Sciences Division Superintendent	Dr. J. R. Davis 72903
7900	Space Systems Division Superintendent	Mr. N. W. Guinard 73468

* Acting

† Additional Duty

Index to Photograph Numbers

<u>Page</u>	<u>Figure</u>	<u>Photo ID Number</u>	<u>Page</u>	<u>Figure</u>	<u>Photo ID Number</u>
iv		78998(4)	79	3	79930(3)
1		80068	83	10	79931
2		P-1708	85	11	79946(4)
3		P-1697(2)	86	13	USRD 1-3666(16)
5		76194(7)	88	16	79946(1)
5		79899			
5		USRD 1-3049-6-75	91		79921(8)
6		79816(103)	97	5a	80014(4)
7		80062	97	5b	80014(3)
10		P-1776	98	6	80014(1)
12		79323(4)	98	7	80014(2)
12		79941			
12		79921(7)	103		80066
12		80052(1)	107	3	80080
12		79559			
13		79778(4)	113		79871(1)
13		79755(1)	115	1	ATM(850)
13		P-1707(8)	118	4	NASA G-80-4346
13		79129(18)			
13		80067(8)	127		79970(1)
13		79832(4)	132	5	79970(1)
14		79797(4)	133	6	TRW 12782-76-10 / 79911
14		79921(4)			
14		79895(1)	141		80081(16)
14		79716(2)	143	1	79964(9)
14		79946(2)	144	3	79766(3)
15		1-3679(18)	147	7	80026(3)
15		79805(2)	148	8	79970(2)
15		80067(2)			
15		79922(1)	155		78648(1)
15		79878(66)	160	4a	80005(2)
			160	4b	80005(1)
21		78383(11)			
24	2	79354(19)	165		79514(2)
24	3	79354(37-38)			
27	7	79685(1)	180		P1788(4)
29	9	79636(4)	180		P-1728(16)
29	10	79636(6)	180		P-1736(2)
			182		P-1704(1)
41	1	79906(2)	182		P-1695(6)
42	2	79906(1)	182		P-1766(2)
46	6	79688(1)	186		79989(2)
47	7	79778(3)	187		P-1711(11)
48	8	79887(3)	188		P-1775
			189		P-1734(2)
58	4	65500	190		80017(67)
68	14	79901(2)	190		80017(64)
69	15	80026(2)	190		80017(11)
70	16	80026(1)	190		80017(66)
75		80004(2)	190		80017(36)
Front Cover		80075	Back cover		79986(2)



LOCATION OF NRL IN THE CAPITAL AREA



varian/extrion



THE NAVAL RESEARCH LABORATORY IS AN
ACTIVITY OF THE OFFICE OF NAVAL RESEARCH